Università degli Studi di Torino
Department of Earth Sciences
PhD Programme in Earth Sciences
XXXV Cycle

In cotutelle with
Univeristé Paris Cité
Institut de Physique du Globe de Paris
ED 560 Ecole Doctorale des Sciences de la Terre et d l'Environnement

Along–strike variations of metamorphic CO_2 outputs from the Nepal Himalaya: Comparison between past production and present emissions

Supervisors:
Prof. Chiara Groppo
Prof. Frédéric Girault
Prof. Franco Rolfo
Prof. Frédéric Perrier

PhD Student: Shashi Tamang

PhD Programme Coordinator:
Francesco Dela Pierre

Academic year: 2019–2022
Code of scientific discipline: GEO/07

Acknowledgements

I would like to express my deepest appreciation to my supervisors, Prof. Dr. Chiara Groppo, Dr. Frédéric Girault, Prof. Dr. Franco Rolfo and Prof. Dr. Frédéric Perrier, and for their invaluable advice, continuous support, guidance, and patience during my PhD study. Their immense knowledge and plentiful experience have encouraged me throughout the time of my PhD research. I am grateful to Prof. Dr. Chiara Groppo and Prof. Dr. Franco Rolfo, for their help during my PhD fieldwork as well. I really feel lucky to work with Prof. Dr. Frederic Perrier, and Dr. Frederic Girault during my master's degree, which helped to enhance my knowledge and undoubtedly work in the field of geology. I consider myself fortunate to be connected to the Italian–France research team and to gain knowledge in the field of metamorphic petrography. Also, my great thank to the jury members for their humble remarks and observations.

I greatly thank Dr. Kabi Raj Paudyal who supervised me during my Master thesis and always there to help in difficult circumstances. Without his motivation and constant support, it would not have been possible to gain this position.

A sincere thanks go to Mr. Sandeep Thapa who has helped me since my master's degree and mounting during difficult situations. I also thank him for deconstructing the gas flux and organizing the field works during my PhD. I also thank my flatmate here in Turin, Ms. Pratiksha Tripathi and Mr. Raj Krishna Shrestha for their humble encouragement, laughter and outings that made my PhD period fun. Also, thanks to my PhD colleagues here in the Department of Earth Sciences, Turin for their suggestions and support during my PhD.

A special thank goes to my family, who are the pillar of success in my life. Their encouragement, unconditional love, and believing me during my hard times is indelible moments of my life. Lastly, thanks and huge respect to all those who carry me to this position.

Abstract

The main aim of this work is to investigate the along–strike variation of the past metamorphic CO_2 degassing from the Nepal Himalaya and to compare the CO_2 fluxes of the past with the present–day CO_2 emissions. The Himalayan belt is the largest active orogen on Earth and hosts variable amounts of CO_2–source rocks at various structural levels; for these reasons it is the ideal natural laboratory for studying metamorphic CO_2–producing processes which occurred in the past and still occur in the present days. Previous studies have documented significant CO_2 production in the past from the Greater Himalayan Sequence lithologies, whereas nothing is known so far about the CO_2 productivity of the Lesser Himalayan Sequence (LHS), which is a thick sedimentary sequence of Paleo–to Meso– Proterozoic age, metamorphosed at low– to medium–grade conditions during the Himalayan orogeny. Important CO_2 emission sites have been identified in the last decades in central and western Nepal, whereas data on the present–day CO_2 outgassing from eastern and far–western Nepal Himalaya are lacking.

A comparison between past and present–day CO_2 emissions has so far only been attempted at a punctual level. The extrapolation of punctual petrologic data to the orogen scale led to estimate past CO_2 fluxes of the same order of magnitude as the present–days CO_2 fluxes from hot–springs, thus suggesting that CO_2–producing processes similar to those occurring in the past are still active in Nepal Himalaya. To correlate these data at a regional scale, it is necessary to additionally understand: (i) which is the CO_2–productivity of LHS lithologies and which was their contribution to the past CO_2 degassing, and (ii) whether CO_2 emission sites do occur in eastern and far–western Nepal. This project aims at answering these two questions, therefore focusing on the processes responsible for both past and present–days metamorphic CO_2 production in the Nepal Himalaya.

The P–T evolution of the upper–LHS has been constrained through the thermodynamic forward modelling approach applied on six aluminous phyllitic schists, containing porphyroblasts of garnet, staurolite and/or kyanite, overgrowing (at least in part) the main schistosity (i.e. they are post–kinematic minerals). The inferred P–T paths are characterized by prograde heating coupled with tectonic overload (peak–P conditions of 9.5–10.5 kbar, 580–590°C), followed by heating during exhumation (peak–T conditions of 8.2–8.9 kbar, 610–630 °C). The results of this study, which are preliminary to the modelling of the carbonate–bearing lithologies, strongly support those thermo–mechanical models that predict a period of slowdown (or quiescence) of the Main Central Thrust activity. In particular, the static growth of the main minerals defining the peak assemblages provides strong evidence that decompression coupled with heating occurred in the absence of deformation, i.e., in the time interval between two episodes of intense thrusting. The study also provides the opportunity for investigating which are the implications of garnet nucleation overstepping for the P–T evolution of a Barrovian metamorphic sequence. Comparison between the P–T conditions inferred for the growth of garnet core, the

assemblages predicted to be stable at these P–T conditions, and the modelled garnet–in reaction boundary, suggests that the studied samples have experienced different degrees of apparent thermal (ΔT) and/or baric (ΔP) overstepping of garnet nucleation. We find a strong correlation between the bulk–rock MnO content and the apparent ΔT overstepping of the garnet–in reaction. However, we also find that the apparent ΔT overstepping of garnet nucleation could reflect the attainment of the critical 0.5% threshold of garnet abundance, rather than representing a failure of garnet to nucleate at equilibrium conditions. The apparent ΔP overstepping of garnet nucleation could be instead related to the bulk–rock CaO content. Kinetic factors seem much less critical in controlling the growth of the garnet rim at peak P–T conditions.

Thermodynamic forward modelling has been applied to selected carbonate–bearing lithologies derived from protoliths characterized by different amounts of carbonate minerals. Two different series of rocks have been investigated, which are representative of the CO_2 source rocks exposed in the LHS: a dolomite series (ranging from dolomitic pelites, to dolomitic marls and dolostones), and a magnesite series (ranging from magnesite pelites to magnesitic marls and magnesite deposits). This approach allowed to understand the nature of the main decarbonation reactions, to constrain the P–T conditions at which these reactions occurred, and to estimate the amounts of carbonates consumed during metamorphism, with the corresponding amounts of CO_2 produced. The obtained results show that, for all the investigated samples, decarbonation occurs in one (or more) pulse through nearly discontinuous reactions, rather than being a continuous process occurring during most of the prograde evolution. However, the temperatures at which these decarbonation pulses occur, vary as a function of the rock composition: samples originally containing low amounts of carbonates (<10 vol%) release most of the CO_2 during the prograde stage, at T<600 °C, whereas samples containing higher amounts of carbonate in the protolith (10–30 vol%) produce CO_2 during the decompression stage, at peak P–T conditions. The carbonate content of the protolith also influences the final amount of CO_2 released by each lithology, but the relation between these two parameters is not linear. In both series, the maximum CO2 productivity is observed for samples originally containing a moderate amount of dolomite or magnesite (i.e. 15–30 vol%), whereas dolomitic/magnesitic pelites containing less than 10% of carbonates are less productive. Moreover, for original carbonate amounts higher than 40 vol%, the CO_2 productivity of the sample is negligible. Overall, the obtained results show that the amount of carbonates consumed during metamorphism varies in the range of 7–20 vol%, corresponding to 3–10 wt.% of CO_2 released. It emerges that the CO_2 productivity of dolomitic and magnesitic pelites and marls is significant and these lithologies could have been and could still be relevant sources of CO_2, thus contributing to the diffuse Himalayan CO_2 degassing observed at present.

Extrapolation of the petrological results to the orogen scale allows concluding that the minimum fluxes of metamorphic CO_2 in the past from the eastern, central and western segments of the Nepal Himalaya are: 0.06, 1.06 and 1.77 Mt/year, respectively. These estimates have been obtained by considering: (i) the type and distribution of the CO_2

source rocks in the different formations of the LHS, (ii) the volumes of the CO_2 source rock within each formation, (iii) the amounts of CO_2 produced by each lithology and, (iv) the timing of CO_2 production.

For the present–day CO_2 emissions, the direct flux was measured in the field with the accumulation chamber method. Based on new data obtained during this thesis in Eastern and Far Western Nepal and on the already available dataset in Central and Western Nepal, the amount of current CO_2 degassing was estimated using kriging and interpolation procedures. The results yield the following total amount of CO_2 degassing from known hydrothermal systems in the Nepal Himalaya of 14.6±2.8 mol/s, which is equivalent to $(2.03\pm0.4)\times10^4$ t/year. These first estimates of past CO_2 production and current CO_2 emission from the Nepal Himalaya suggest that more work is needed to draw a more exhaustive overview of the current CO_2 emission and open numerous perspectives on the carbon sink/source duality of large orogens and on the global carbon cycle.

Table of Contents

Chapter 1

Introduction

1.1 Background and problem statement

The exponential increase of anthropogenic CO_2 emissions, and their effects on global warming, are among the most debated topics of recent decades. In this context, it is becoming increasingly evident that a detailed knowledge of the geological processes through which our planet produces CO_2 and releases it into the atmosphere, and of how these processes are modulated over time, is of fundamental importance for predicting the short– and long–term consequences that anthropogenic CO_2 production has on the climate (Evans, 2011). This has encouraged the researchers of different disciplines to investigate what are the main CO_2 source(s) and sink(s) in our planet, what are the most important processes allowing CO_2 transfer from one reservoir to another, and to quantitatively estimate the amounts and the timing of the natural CO_2 release. Most emphasis has been given in previous decades to the short–time scale (<1000 years) variations in atmospheric CO_2 levels caused by the carbon cycle between biological, atmospheric and oceanic reservoirs (i.e., "short–term carbon cycle"). However, it is now widely accepted that this exogenic carbon cycle operates on top of a much longer deep Earth carbon cycle (i.e. "long–term carbon cycle"; Berner, 1999), which occurs over millions of years and involves the slow exchange of carbon between rocks and the surficial system (Lee et al., 2019). In this endogenic carbon cycle, CO_2 is released in the atmosphere through different processes, including volcanic degassing in different geodynamic contexts (arc volcanoes, mid–ocean ridges, intraplate volcanism; e.g. Marty & Tolstikhin, 1998; Burton et al., 2013), mantle degassing in extensional settings (continental rifts; e.g. Lee et al., 2016), and metamorphic degassing through decarbonation reactions in active orogenic systems (e.g. Bickle et al., 1996; Kerrick & Caldeira, 1998; Gaillardet & Galy, 2008). Estimating the metamorphic CO_2 degassing fluxes, particularly on a global scale, is challenging because metamorphic degassing is diffuse and spatially heterogeneous (Lee et al., 2019). Despite the increasing number of studies focusing on this issue in the last years, the net carbon budget of collisional orogens, which reflects the balance between carbon sources and sinks, remains difficult to be quantified (e.g. Galy & France–Lanord, 1999; Quade et al., 2003; France–Lanord et al., 2003; Märki et al., 2021).

The Himalayan belt is the largest active orogen on Earth, and hosts variable amounts of CO_2–source rocks at various structural levels (Rolfo et al., 2017); therefore, it is the ideal natural laboratory for studying metamorphic CO_2–producing processes what have occurred in the past and which still occur in the present days. Previous studies have demonstrated that, during the Himalayan prograde metamorphism (ca. 20–30 Ma ago), a remarkable amount of metamorphic CO_2 was produced (e.g. Evans, 2011; Groppo et al., 2017; Rapa et

al., 2017; Groppo et al., 2022) through decarbonation reactions that occurred in different lithologies (e.g. calcic metapelites, calc–silicate rocks and impure marbles, respectively derived from carbonate–rich pelites, marls and impure limestones) (e.g. Groppo et al., 2013, 2017, 2021, 2022; Rolfo et al., 2015, 2017; Rapa et al., 2017). Such investigations have been focused on the Greater Himalayan Sequence (GHS) lithologies, which mostly derive from Neoproterozoic sedimentary protoliths and experienced medium– to high–grade metamorphism during the Himalayan orogeny. Conversely, nothing is known so far about the CO_2 productivity of the Lesser Himalayan Sequence (LHS) lithologies, mostly derived from Paleo– to Meso–Proterozoic sedimentary protoliths and metamorphosed at low– to medium–grade metamorphic conditions.

Several investigations over the last decades have shown that metamorphic CO_2 outgassing is occurring along the active Himalayan orogen also in the present days. The widespread occurrence of CO_2–rich hot springs and gaseous CO_2 ground discharges, with CO_2 fluxes at places similar to diffusive fluxes from active volcanoes (Girault et al., 2014 a,b, 2018), is the clearest evidence of the present–day CO_2 degassing in the Nepal Himalaya. These CO_2–rich hot springs are located along the entire length of the Himalayan belt, from Pakistan (Chamberlain et al., 2002), to NW India (e.g. Tiwari et al., 2016), Nepal (e.g. Evans et al., 2004, 2008; Becker et al., 2008; Perrier et al., 2009; Girault et al., 2014a, b,2018), NE India (Evans et al., 2008) and Bhutan (Singh et al., 2004), where they are concentrated in the proximity of the major tectonic discontinuities. In Nepal, most of the important CO_2 emission sites have been identified so far in central and western regions, whereas data on the present–day CO_2 outgassing from eastern and far–western Nepal Himalaya are still lacking.

A comparison between past and present–day CO_2 emissions has so far only been attempted at a punctual level. The extrapolation of punctual petrologic data to the orogen scale led to an estimate of past CO_2 fluxes of the same order of magnitude as the present–day CO_2 fluxes from hot springs (Groppo et al., 2017; Rapa et al., 2017), thus suggesting that CO_2–producing processes similar to those occurring in the past are still active in Nepal Himalaya. However, in order to transform this “rough” extrapolation in a more reasoned correlation on a regional scale, it is at least necessary to additionally understand: (i) which is the CO_2–productivity of Lesser Himalayan Sequence (LHS) lithologies and which was their contribution to the past CO_2 degassing, and (ii) whether CO_2 emission sites do occur in eastern and far–western Nepal and which are the similarities/differences with respect to those already known in central–western Nepal Himalaya. This project aims at answering these two questions, therefore focusing on the processes responsible for both past and present–days metamorphic CO_2 production in the Nepal Himalaya.

1.2 Objectives

The main aim of this project is **to investigate the along–strike variation of the past metamorphic CO_2 degassing from the Nepal Himalaya and to compare the CO_2 fluxes of the past with the present–day CO_2 emissions**.

Specific objectives are:

(i) clarifying the volumes and types of CO_2 –source rocks in the Lesser Himalayan Sequence (LHS), and their lateral variations along a significant portion of the Himalayan chain;

(ii) understanding the types of the metamorphic CO_2 –producing reactions, with a special focus on lithologies that have not been investigated in previous studies (e.g. metamorphic rocks derived from dolomite– and/or magnesite–bearing protoliths);

(iii) estimating the P–T conditions at which the decarbonation reactions took place, the composition (XCO_2) of the fluids released through these reactions, and the amounts of CO_2 released per unit volume of reacting rocks;

(iv) investigating the along–strike variations of present–day CO_2 emissions by exploring possible new CO_2 emission sites in eastern and far–western Nepal.

Fieldwork activity within the Lesser Himalayan Sequence combined with a detailed petrographic and petrologic (i.e. thermodynamic modelling) study of the LHS lithologies is needed for achieving goals (i) to (iii). To achieve the goal (iv), the punctual measurement of the CO_2 degassing flux in the vicinity of the hot springs is required.

1.3 Dissertation format

This PhD thesis is organized into 8 chapters.

Chapter 1: Chapter 1 is a basic introduction to the PhD thesis, that summarizes the main challenges and queries to which the thesis aims to answer, about the highly debated topic of the contribution of orogenic settings to the Earth's deep carbon cycle. It also includes the main goal and the specific objectives of the PhD project.

Chapter 2: In this chapter, the general geological setting of the Nepal Himalaya is briefly introduced. The structural architecture, the lithostratigraphy and the metamorphic evolution of the Lesser Himalayan Sequence is then summarized, in order to introduce the reader to the main features of the metasedimentary sequence that has been investigated in detail in the framework of this project. The state–of–the–art about present–day CO_2 emissions in the Nepal Himalaya is also discussed briefly at the end of this chapter.

Chapter 3: This chapter describes the methods used to collect the data and the strategies followed to interpret them.

Chapter 4: This chapter presents field data collected along different cross sections in central and eastern Nepal, either during previous fieldwork campaigns or during fieldwork

related to this project. A comprehensive petrographic description of the main lithologies exposed in the LHS is provided, which is based on the careful petrographic investigation of hundreds of thin sections. In the end, a broad reconstruction of the pristine depositional environment for most of the LHS lithologies is presented. Data presented in this Chapter have been published as a chapter ***(Chapter 7) within the book entitled "Himalaya: dynamics of a giant" (eds. R. Cattin & J.L. Epard, ISTE editions)***, presently in press.

Chapter 5: This chapter presents a detailed petrographic, microstructural and mineral chemical study of six selected samples of aluminous metapelites from the Upper–LHS of central Nepal, whose assemblages are especially useful for thermobarometric purposes. The P–T evolution of the Upper–LHS is constrained through equilibrium thermodynamic modelling; these results are preliminary to the modelling of the carbonate–bearing lithologies (see Chapter 6). The study also provides the opportunity for investigating which are the implications of garnet nucleation overstepping for the P–T evolution of a Barrovian metamorphic sequence. Data and results presented in this chapter have been published in: ***Tamang et al. Implications of garnet nucleation overstepping for the P–T evolution of the Lesser Himalayan Sequence of central Nepal. Journal of Metamorphic Geology, accepted***.

Chapter 6: This chapter focuses on the types and the distribution of CO_2–source rocks in the Upper–LHS of central Nepal. Detailed petrographic, microstructural and mineral chemical data are discussed for samples derived either from dolomite–bearing protoliths or from magnesite–bearing protoliths (i.e. dolomite– and magnesite–series). The results of P/T–X(CO_2) pseudosection modelling applied on seven selected samples from both the dolomite– and the magnesite series are used to constrain their P–T–X(CO_2) evolution. Different metamorphic CO_2–producing processes are investigated, and the amount of CO_2 produced per unit volume of reacting rocks are estimated. A paper summarizing the data and results discussed in this chapter is in preparation.

Chapter 7: This chapter presents the result related to the study of the present–day CO_2 emissions in the Nepal Himalaya. The CO_2 fluxes from ground discharges have been directly measured in the field, in the eastern, central, and far–western regions of Nepal. The obtained field data are further processed, and the total CO_2 discharge is estimated using kriging and interpolation procedures.

Chapter 8: In this chapter, the overall results obtained are summarized and critically discussed. The past production of CO_2 through metamorphic decarbonation reactions is extrapolated from punctual data to a regional–scale estimation. A comparison of past and present CO_2 production from the Nepal Himalayas is tentatively proposed.

Chapter 2

Geological outline

2.1 Introduction to the geology of the Himalaya

Considered the archetype of collisional orogens, the Himalaya is the highest and the youngest mountain range in the world, defined as "the young and restless giant" (Valdiya, 1988) due to its age, extension and still active nature. Geographically, it is bounded by the Namche Barwa and the Nanga Parbat syntaxes to the east and the west respectively, by the Yarlung Tsangpo (Brahmaputra) and Indus rivers to the north and by the Indo–Gangetic plain to the south, extending for ca. 2400 km in length and 200–300 km in width (Wadia, 1933) between the Tibetan plateau (north) and the Indian craton (south). Tectonically, the Himalayan orogen is broadly bounded by four major tectonic structures, the Indus–Tsangpo suture to the north, the left–slip Chaman Fault to the west, the right–slip Sangiang Fault to the east and the Main Frontal Thrust to the south (Le Fort, 1975; Yin, 2006).

The Himalayan belt was formed as a consequence of the tectonic collision between the Indian Plate and the Asian plate (Le Fort, 1975), which started ca. 50 – 55 Ma ago (e.g. Najman et al., 2010). This complex orogenic system was developed because of the closure of the Tethys Ocean, interposed between two great continents since the Paleozoic: Laurasia in the north and Gondwana in the south (Hsu et al., 1995; Sengor & Natal'in, 1996; Yin & Harrison, 2000). After the break–up of Gondwana, at about 250 Ma, the Indian plate began to move toward the north in the Cretaceous, resulting in the northward subduction of the Tethyan Ocean below the southern margin of the Asian Plate. The final closure of the Neo–Tethys ocean, which occurred during the Early–Middle Cretaceous, at ca. 60 to 50 Ma (e.g. Tapponier et al., 1982, 1986; Patriat & Achache, 1984; Dewey et al., 1989; LePichon et al., 1992; Zhu et al., 2005, 2013; Leech et al. 2005; Hu et al., 2016), led to the India–Asia continental collision. The collision between these two continental plates occurred obliquely: the north–western part of the Kohistan–Ladakh first collided with the Eurasian plate at ca. 65–55 Ma (Jaeger et al., 1989; Klootwijk, 1984; Dhital, 2015); then, the Indian plate rotated anticlockwise, colliding with the Eurasian plate toward the east at ca. 50–45 Ma (Besse et al., 1984; Dewey et al., 1989). The convergence rate between India and Asia was not always uniform, significantly decreasing from ca. 150 – 40 mm/yr at about 50–35 Ma (e.g., Copley et al., 2010; Dhital, 2015) to 13 – 20 mm/yr since the Pliocene (Powers et al., 1998; DeCelles et al., 1998a, 2001; Lavé & Avouac, 2000), with a present–day mean value of 17 mm/yr in the central part of the belt (Bilham et al., 1997; Larson et al., 1999). The main cause of the slowdown of the convergence rate is attributed to the progressive crustal thickening, which ultimately led to the uplift of the Tibetan Plateau (Copley et al.,

2010). After the collision of the two plates along the Indus–Tsangpo Suture Zone (ITSZ) the tectonic activity was progressively transferred southward, resulting in the formation of a number of deep intracrustal tectonic discontinuities progressively younger toward the south (e.g. Gansser, 1977; Dhital, 2015). Consequently, the Himalayan orogen evolved through a stage of intense deformation related to the continental collision, leading to thrusting and folding accommodating the crustal shortening and thickening, followed by episodic exhumation, uplift, and erosion.

The collisional suture between the Indian and Asian plates is marked by the Indus–Tsangpo Suture Zone (ITSZ), which represents the northern tectonic boundary between the Himalaya s.s. (Indian Plate) and the Tibetan Plateau (Eurasian Plate). The ITSZ is represented by a ca. 2000 km long topographic depression along the Indus and Tsangpo (Brahmaputra) rivers, which flow in two opposite directions (Heim & Gansser, 1939). The ITSZ consists of the obducted remnants of Triassic–Cretaceous turbidites deposited on the Indian Plate (Frank et al., 1977; Burg & Chen, 1984; Ding et al., 2005), ophiolitic mélanges interpreted as relics of paleo–accretionary prisms (e.g. Corfield et al., 1999; Robertson, 2000; Ding et al., 2005; Guillot et al., 2008) and minor well–preserved ophiolites such as those of Spongtang in Ladakh (Hodges, 2000 and references therein). These ophiolites were metamorphosed at various conditions, ranging from very–low and low metamorphic grade to blueschist and rarely eclogite–facies conditions (Ghose & Singh, 1980; Honegger et al., 1989; Chatterjee & Ghose, 2010; Bhowmik & Ao, 2016; Groppo et al., 2016). The ITSZ has a complex geometry, dominated by nearly vertical, highly deformed, tectonic slices (Diener, 1895, 1898; von Krafft, 1902; Heim & Gansser, 1939).

The Himalaya s.s. is located south of the ITSZ; it mostly consists of thick sedimentary sequences originally deposited on the northern margin of the Indian plate and ranging in age from Paleoproterozoic to Eocene (Upreti & Yoshida, 2005), intensely deformed and variably metamorphosed during the Himalayan collision. The tectono–stratigraphic architecture of the Himalaya is quite uniform at the regional scale; in fact, the main units and tectonic discontinuities show a striking lateral continuity along the whole length of the orogen.

Four east–west trending litho–stratigraphic and tectono–metamorphic units, each one with remarkable lithological and metamorphic features (Gansser, 1946), are distinguished in the Himalayan orogen. All the four units are exposed along the Nepal Himalaya, which occupies a central position within the entire Himalayan belt. From south to north, and from the lowermost to the uppermost, these units are (Yin & Harrison, 2000; Kohn, 2014): the Siwaliks, the Lesser Himalayan Sequence (LHS), the Greater Himalayan Sequence (GHS) and the Tethyan Himalayan Sequence (THS) (Fig. 2.1). These units are bounded by four, regional–scale north–dipping, tectonic discontinuities: the Main Frontal Thrust (MFT), the Main Boundary Thrust (MBT), the Main Central Thrust (MCT) and the South Tibetan Detachment System (STDS) (Fig. 2.1). An additional regional–scale tectono–metamorphic

discontinuity (High Himalayan Discontinuity, HHD; Montomoli et al. 2013) separates the GHS into two portions with different tectono–metamorphic evolutions.

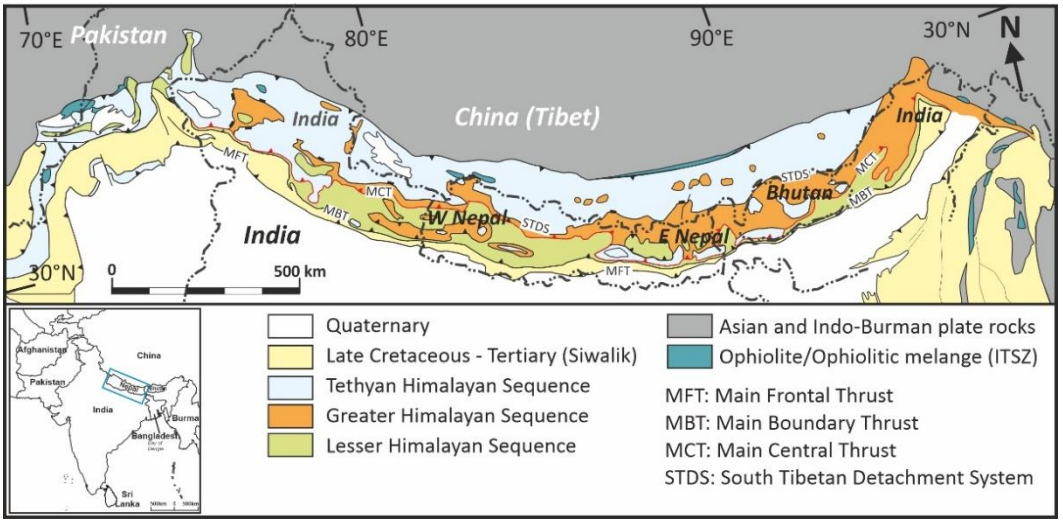

Figure 2.1: Simplified tectonic map of the Himalaya, showing the major tectono–metamorphic units, tectonic discontinuities and the locations of the major hot springs in Nepal Himalaya (modified after Joshi et al., 2003; Yin, 2006; He et al., 2015; and Wang et al., 2016).

The **Siwalik**, also known as Sub–Himalaya, consists of unmetamorphosed sediments of mid–Miocene–Pleistocene age, representing the Himalayan foreland basin deposits (DeCelles et al., 1998; Paudel & Arita, 2000; Upreti, 1999; Hodges, 2000). The Siwalik, extended from western to eastern Nepal Himalaya, mostly consists of mudstones, siltstones, sandstones, and fluvial deposit conglomerates (DeCelles, 1998; Upreti, 1999). A distinct variety of flora and fauna fossils are preserved in the Siwalik lithologies (West et al., 1978; West & Munthe, 1981; Munthe et al., 1983; Corvinus, 1988; Upreti, 1999). The Siwalik is further subdivided into three major sub–units: i) the Lower Siwalik, ii) the Middle Siwalik, and iii) the Upper Siwalik. These sub–units have their own specific lithology and sedimentary succession, but they define a coarsening–upward sequence as a whole, reflecting the uplift history of Himalaya (Gansser, 1964a; Dhital, 2015). The Siwalik unit is bounded by the Main Frontal Thrust (MCT) to the south and by the Main Boundary Thrust (MBT) to the North, over which the Lesser Himalaya Sequence is thrusted.

The **Lesser Himalaya Sequence** (LHS) is bounded by the Main Central Thrust (MCT) to the north and the Main Boundary Thrust (MBT) to the south, and mostly consists of low– to medium–grade meta–sedimentary rock units (DeCelles et al., 1998a; Upreti, 1999; Pearson & DeCelles, 2005; Webb et al., 2011). The LHS rocks are derived from the Paleo– to Meso–Proterozoic sedimentary sequences originally deposited on the northern margin of the Indian plate, known in the literature as the Nawakot Group (e.g., Gansser, 1964; Stöcklin, 1980; Parrish & Hodges, 1996; Upreti ,1999; Hodges, 2000; Pearson & DeCelles, 2005). The Nawakot Group (Stöcklin, 1980) is broadly divided into two units: the lower unit mostly

consists of pelitic rocks without carbonate–bearing lithologies, whereas the upper unit comprises pelites intercalated with carbonate–bearing lithologies. The Nawakot Group is locally unconformably overlain by Permian to Paleocene limestones and calcareous sandstones of the Tansen Group (Sakai, 1985; Valdiya, 1998). The LHS sedimentary units were intruded by different types of igneous lithologies, whose metamorphic products are represented by augen gneisses and amphibolites (e.g., Frank et al., 1995; DeCelles et al., 1998a; Upreti, 1999; Kohn et al., 2010). Within the LHS the metamorphic grade increases from the foreland (south) to the hinterland (north), and from the lower to the upper structural level (e.g. Paudel & Arita, 2000, 2006a,b and references therein).

The **Greater Himalayan Sequences** (GHS) is composed of several km thick pelitic, psammitic and calcareous paragneisses, granitic orthogneisses and migmatites, derived from Neoproterozoic to Cambrian protoliths and representing the core of the Himalaya (e.g. Colchen et al., 1980; Arita, 1983; Le Fort, 1975, Parrish & Hodges, 1996; Upreti, 1999; Hodges, 2000; DeCelles et al., 2000; Robinson et al., 2001). The metamorphic grade of the GHS gradually increases from the lower to the upper structural levels, ranging from medium–grade staurolite– and kyanite–bearing lithologies to high–grade, anatectic, sillimanite, K–feldspar and cordierite –bearing rocks. The GHS is bounded by the MCT to the south and by the STDS to the north and is internally divided in a Lower–GHS unit and an upper–GHS unit by the High Himalayan Discontinuity (Montomoli et al., 2013).

The GHS is overlaid by the sedimentary sequence of the **Tethyan Sedimentary Sequence** (TSS) through the South Tibetan Detachment System (STDS), which is a brittle–ductile normal fault system with top–to–the–NE sense of movement (e.g. Burg & Chen, 1984; Burchfield et al., 1992; Carosi et al., 1998; Kellet et al., 2010). The TSS consists of sedimentary rocks originally deposited on the northern edge of the Indian passive margin from Cambrian to Eocene (e.g. Gaetani & Garzanti, 1991; Garzanti, 1999), locally interbedded with Paleozoic and Mesozoic volcanic rocks (Yin, 2006). It mostly consists of unmetamorphosed sediments, but it is characterized by a low to medium–grade metamorphic overprint in its lower structural levels, close to the contact with the GHS (e.g. Lombardo et al., 1993; Upreti, 1999).

2.2 Lesser Himalayan Sequence

2.2.1 Structural architecture of the Lesser Himalayan Sequence

The Lesser Himalayan Sequence (LHS) is a thick, Paleo– to Meso–Proterozoic sedimentary sequence originally deposited on the northern margin of the Indian plate (e.g., Gansser, 1964; Parrish & Hodges, 1996; DeCelles et al., 2000; Martin et al., 2005), intruded by Proterozoic igneous lithologies (e.g., Kohn et al., 2010; Larson et al., 2017, 2019). During the Himalayan orogeny, this sedimentary sequence was variably deformed and metamorphosed developing a typical inverted metamorphism, with metamorphic grade increasing from south to north and from lower to upper structural levels (e.g. Pêcher, 1989;

Kohn, 2014). In Nepal, the LHS is mostly exposed in the midlands, at altitudes ranging from 300 to 3500 m a.s.l., and forms a belt up to 100 km wide. The current LHS exposure is due to the interplay between thrusting, folding and erosion. The structure of the LHS is dominated by a regional–scale structural culmination (i.e. the Lesser Himalayan Duplex DeCelles et al., 2001; Pearson & DeCelles, 2005; Long & Robinson, 2021), testified by the occurrence of a broad antiform developed longitudinally with respect to the Himalayan thrust–belt. The erosion was more intense towards the west (Dhital, 2015), resulting in a wider exposure of the LHS in western and central Nepal compared to eastern Nepal; there, the LHS crops out in large antiformal tectonic windows (in the Chautara–Okhaldhunga, Arun valley and Tamur valley regions) (Fig. 2.2).

The LHS fold–thrust belt is tectonically interposed between the underlying Siwalik group to the south and the overlying Greater Himalayan Sequence (GHS) to the north, from which it is separated by the Main Boundary Thrust (MBT) and the Main Central Thrust (MCT) respectively (Yin & Harrison 2000) (Fig. 2.1, 2.2). The precise location of the main tectonic discontinuity (i.e. the MCT) juxtaposing the GHS over the LHS is still debated due to the number of different criteria (structural, metamorphic, chronological, compositional; e.g. Searle et al., 2008 for a review) that have been used to define it. In this thesis, the definition proposed by Goscombe et al. (2006, 2018) is followed, namely: (i) the boundary between the LHS and the GHS is mostly a lithostratigraphic boundary (i.e. Himalayan Unconformity HU), separating two sequences with different and unique provenance; (ii) rather than being a discrete thrust, the MCT is a broad high strain zone (i.e. Main Central Thrust Zone: MCTZ) which affects both the upper structural levels of the LHS and the lower structural levels of the GHS; (iii) the lower boundary of the MCTZ is marked by two distinct tectonic discontinuities, recognized all along the Himalayan belt: the Main Central Thrust (or Basal Main Central Thrust according to Goscombe et al., 2018) at upper structural levels, mostly coincident with the HU and the Ramgarh Thrust (as defined in central–western Nepal by DeCelles et al., 2000 and Robinsion et al., 2001, 2006) or Munsiari Thrust (in Garhwal, NW India; Valdiya, 1980) at lower structural levels.

At the regional scale, two main domains are generally distinguished within the LHS (e.g. Dithal, 2015): a narrow outer (southern) domain consisting of predominantly non–metamorphosed sedimentary rocks, and a broad inner (northern) domain, recording a metamorphic overprint whose grade increases upward from the biotite to the garnet and the staurolite/kyanite first appearance (e.g. Kohn, 2014). This thesis focuses on the LHS metamorphic successions, therefore, the outer, non–metamorphic, LHS domain is not furtherly discussed in the following.

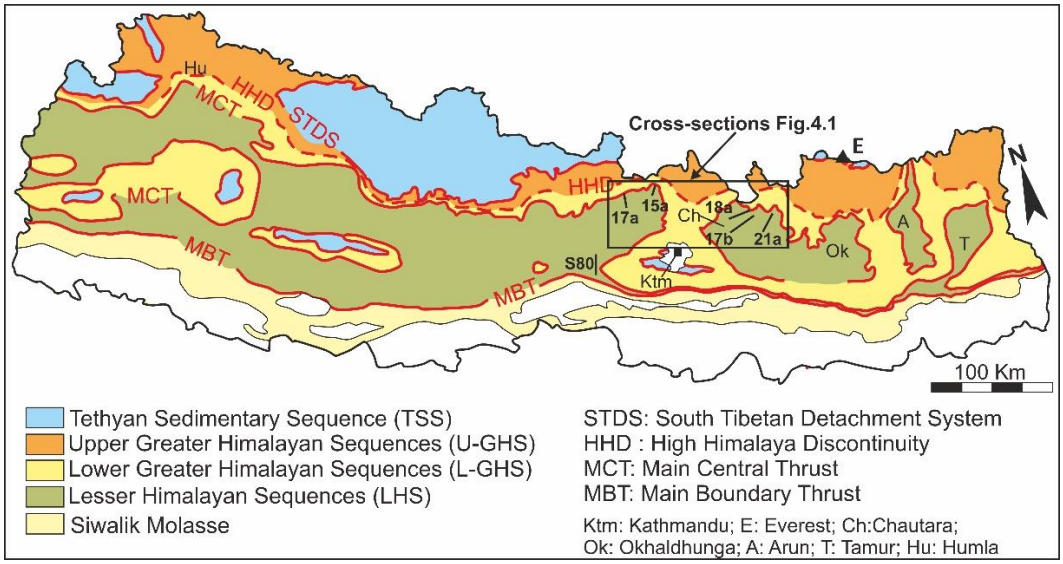

Figure 2.2: Geological sketch map of the Nepal Himalaya showing the major tectono–metamorphic units (modified from Dithal, 2015; He et al., 2015). The location of the High Himalayan Discontinuity (HHD) is based on: Groppo et al. (2009, 2010, 2012, 2013), Mosca et al. (2012) and Rapa et al. (2016, 2018) for central–eastern Nepal and on Montomoli et al. (2013) and Wang et al. (2016) for central–western Nepal. Cross sections indicated as (a), (b) etc. refer to Fig. 4.1; S80: reference section of Stöcklin (1980).

2.2.2 Lithostratigraphy of the Lesser Himalayan Sequence

The LHS in Nepal is conventionally divided into two complexes, characterized by distinct lithological associations: the Paleo–Proterozoic Lower–LHS (Lower Nawakot Unit of Stöcklin 1980), dominated by siliciclastic rocks, and the Meso–Proterozoic Upper–LHS (Upper Nawakot Unit of Stöcklin 1980) consisting of both carbonatic and siliciclastic rocks. The Nawakot Group rocks are locally overlain unconformably by Gondwana and post–Gondwana sediments collectively named as Tansen Group (Sakai, 1983), consisting of Permian to Paleocene shales, conglomerates, limestones, and calcareous sandstones. The LHS units are intruded by Proterozoic igneous rocks, now transformed mostly into granitic augen gneisses and amphibolites (e.g. Frank et al., 1995; DeCelles et al., 1998a; Upreti, 1999; Kohn et al., 2010).

<table>
<tr><th rowspan="2">Lesser Himalayan Sequence(LHS)</th><th>Eastern Nepal Schelling 1992</th><th>Central Nepal (Malekhu Section) Stöcklin 1980</th><th colspan="3">Western Nepal (Kali Gandaki & Tansen section) Sakai 1985</th><th>Western Nepal(northern Dang) Dhital & Kizaki 1987</th><th>Far-western Nepal (Karnali & Seti section) DeCelles 2001</th><th colspan="2">This Study</th><th>Geologic Age</th></tr>
<tr><td>Not exposed</td><td>Not exposed</td><td rowspan="11">Kali Gandaki Super group</td><td rowspan="2">Post-Gondwana Group</td><td>Dumri Formation</td><td rowspan="2">Dubring Formation</td><td>Dumri Formation</td><td rowspan="3"></td><td rowspan="2">Not exposed</td><td>Miocene</td></tr>
<tr><td rowspan="2">Tansen Group</td><td>Bhainskati Formation</td><td>Bhainskati Formation</td><td>Eocene</td></tr>
<tr><td rowspan="3">Gondwana Group</td><td rowspan="3">Not exposed</td><td rowspan="3">Gondwana Group</td><td>Amile Formation</td><td rowspan="3">Phalabang Formation</td><td rowspan="3">Gondwanas</td><td rowspan="3">Not exposed</td><td rowspan="3">Cretaceous-Permian</td></tr>
<tr><td>Taltung Formation</td></tr>
<tr><td>Sisne Formation</td><td>Sallyan Formation</td></tr>
<tr><td colspan="3">Unconformity</td><td colspan="3">Unconformity</td><td colspan="2"></td></tr>
<tr><td rowspan="9">The Ramechap-Tumlingtar-Taplejung Group (including Ulleri type Augen Gneiss)</td><td>Robang Formation</td><td>Kerabari Formation</td><td>Ranibas Formation</td><td rowspan="8">Lakaparta Group (including Benighat Slate)</td><td rowspan="8">Upper-LHS</td><td>Malekhu Limestone</td><td rowspan="2">Early Paleozoic</td></tr>
<tr><td>Malekhu Limestone</td><td rowspan="2">Ranihgat Formation</td><td rowspan="2">Sirchaur Formation</td><td rowspan="2">Benighat Slate</td></tr>
<tr><td>Benighat Slate</td><td rowspan="3">Dhadhing Dolomite</td><td rowspan="2">Saidi Khola Formation</td><td rowspan="3">Dhorbang Khola Formation</td><td rowspan="3">Dhading Dolomite</td><td rowspan="4">Early-Meso Proterozoic</td></tr>
<tr><td>Khoraidi Formation</td></tr>
<tr><td>Chappani Formation</td><td>Hapurkot Formation</td></tr>
<tr><td>Nourpul Formation</td><td>Virkot Formation</td><td>Khamari Formation</td><td>Syangia Formation</td><td>Nourpul Formation</td></tr>
<tr><td>Dandagaon Phyllite</td><td>Heklang Formation</td><td>Ranagaon Formation</td><td>Galyang Formation</td><td rowspan="4">Lower-LHS</td><td>Dandagaon Phyllite</td></tr>
<tr><td>Fagfog Quartzite</td><td>Naudanda Formation</td><td>Baile Quartzite</td><td>Sangram Formation</td><td>Fagfog Quartzite</td></tr>
<tr><td>Kuncha Formation</td><td>Kuncha Formation</td><td>Dangri Formation</td><td>Ranimata Formation (including Ulleri Augen Gneiss)</td><td>Kuncha Formation</td></tr>
<tr><td colspan="3"></td><td>Kushma Formation</td><td></td></tr>
</table>

Table 2.1: General stratigraphy of the Lesser Himalayan Sequence of Nepal Himalaya

2.2.2.1 Lower–LHS

The Lower–LHS mostly consists of metasedimentary rocks derived from pelitic and arenaceous protoliths. In central Nepal, the following formations have been defined by Stöcklin (1980): the Kuncha Formation, the Fagfog Quartzite Formation and the Dandagon Phyllite Formation. The ***Kuncha Formation*** consists of a thick and monotonous succession of greenish–grey phyllites and meta–sandstones mostly derived from pelitic sediments with intercalations of arenites, reaching a thickness of about 500–800 m. It is overlain by the fine– to medium–grained quartzites of the ***Fagfog Quartzite Formation***, which represent the metamorphic products of quartzitic sandstones. The ***Dandagaon Phyllite Formation*** consists of dark grey to greenish–grey phyllites alternated with thin quartzitic layers, whose protoliths are similar to those of the Kuncha Formation, although the quartzitic layers are less abundant.

2.2.2.2 Upper–LHS

The Upper–LHS sequence differs from the Lower–LHS for its lithological heterogeneity and the widespread occurrence of carbonate–bearing lithologies, whose thickness is significantly variable along strike. In central Nepal, the following formations have been defined by Stöcklin (1980); Nourpul Formation, Dhadhing Dolomite Formation, Benighat Slate Formation, Malekhu Limestone Formation and Robang Formation.

The ***Nourpul Formation*** is a lithologically heterogeneous succession mostly consisting of phyllites, black slates, carbonatic phyllites, calcschists and minor quartzites, alternated in metric to decametric layers. This formation can be correlated with the Virkot Formation of Sakai (1995), the Variegated Formation of Sharma et al. (1984), and the Nourpul Formation of Upreti (1996, and reference therein). This formation typically appears thickly banded and varied in colour, consisting of a thick intercalation of various types of metamorphic rocks derived from slate, sandstone and limestone protoliths. The amount of carbonatic lithologies generally increases upward, whereas quartzites are mostly concentrated in the lowermost portion of the formation.

The ***Dhading Dolomite Formation*** overlies the Nourpul Formation with a transitional contact marked by the progressive increase of the carbonatic lithologies counterbalanced by a decrease of the siliciclastic ones. It mostly consists of massive, bluish grey to dark grey, variably recrystallized limestones and dolostones, locally preserving stromatolitic structures. This formation is widely and continuously exposed from central to western Nepal, whereas it is absent in eastern Nepal (Upreti, 1996). The Dhading Dolomite Formation as defined by Stöcklin (1980) can be correlated with the Chappani–Khoraidi Formation and the lower part of Saidi Khola Formation of Sakai (1983, 1985) in the Tansen area. Similarly, the Dhading Dolomite Formation is described as Surtibang Dolomite in the Rukumkot and Thulo Bheri sections, and as Hatiya Formation west of the Kali Gandaki section by Sharma et al. (1984) and Upreti (1996). In the northern Dang of western Nepal,

Dhital & Kizaki (1987) described light grey to greenish grey, dolostones associated with green slates as Dhorbang Khola Formation, which can be also correlated with the Dhading Dolomite Formation of Stöcklin (1980)). Magnesite deposits are locally associated to the dolomitic rocks of the Dhading Dolomite Formation, interpreted as the syn–sedimentary diagenetic replacement of dolomite in an evaporitic environment developed behind biohermal barriers which inhibited water circulation (Valdiya, 1995; Joshi & Sharma, 2015).

The overlying **Benighat Slate Formation** is the thickest formation in the Upper–LHS, with a thickness ranging from 500 m to more than 3000 m. It is lithologically heterogeneous and dominated by dark phyllites, with frequent intercalations of graphitic schist and calcic metapelites and minor carbonatic lithologies and quartzites. Originally defined by Stöcklin (1980) in central Nepal, this formation can be correlated to other similar formations in other sectors of the Nepal Himalaya, such as the Ramdighat Formation and the lower part of the Kerabari Formation in the Tansen area (Sakai, 1985). Similarly, it can be correlated to the lower part of the Hatiya Formation of Sharma et al. (1984), and to the Sirchaur Formation of Dhital & Kizaki (1987b).

The Malekhu Limestone and the Robang Formation are the uppermost formations of the Upper–LHS sequences. According to Stöcklin (1980), the **Malekhu Limestone Formation** is mainly composed of dark grey limestones, dolostones and sandstones with occasional columnar stromatolites, and is distinctly different from the Dhadhing Dolomite Formation exposed at lower lithostratigraphic levels. It can be correlated with the upper part of the Kerabari Formation of Sakai (1985), the Ranibas Formation of Dhital & Kizaki (1987b) and Malekhu Limestone of Upreti (1996). The **Robang Phyllite Formation** is dominated by chlorite–rich phyllites, with abundant intercalations of quartzites and amphibolites, the latter being probably derived from basic dykes and/or tuff layers.

2.2.2.3 Tansen Group

The Tansen Group rocks have been firstly described in western Nepal (Sakai, 1983) along the Kali Gandaki section, where it overlies unconformably the much older LHS succession. It consists of sedimentary rocks from the Gondwana (Sakai, 1993) and Lower Tertiary or post–Gondwana sequences (Sakai, 1983; Upreti, 1996) (Table 2.1). The Gondwana sequence is divided into the Lower Gondwana and the upper Gondwana, depending on the fossil contents and other characteristics (Sakai, 1983; Upreti, 1996). The Lower Gondwana sequence, known as Sisne Formation (Sakai, 1983), mostly consists of fossiliferous shales/slates interbedded with sandstones and conglomerates. It is separated from the Upper Gondwana sequence by an unconformity. The Upper Gondwana in the Tansen area is highly fossiliferous and consists of different plants (Sakai, 1983; Upreti, 1996 and references therein) as well as animal fossils belonging to different species, aged between the upper Jurassic to Paleocene.

The Lower Tertiary sequence, which lies conformably (Upreti, 1996) over the youngest bed of the Gondwana sequences is further sub–divided into two units named Bhainskati Formation and Dumri Formation. The Bhainskati Formation, which is the oldest among these two formations, consists of a marine sedimentary succession composed of fossiliferous muddy carbonates (Sakai, 1983; Upreti, 1996). The overlying Dumri Formation consists of sandstones interbedded with shales of different colours and conglomerates.

The sedimentary sequences of the Tansen Group are widely reported all along the whole Himalayan range (Fuchs & Frank, 1970; Sakai, 1983; Sharma, et al. 1984; Dhital & Kizaki, 1987b), from western Nepal (Bashyal, 1980; Schelling, 1992), to eastern Nepal (Valdiya 1980) and India.

2.2.2.4 Meta–igneous rocks

The LHS sedimentary sequence of Nepal experienced several episodic magmatic intrusions over geologic time. Peculiar granitic augen orthogneisses are widespread within the LHS. These are mostly known as Ulleri–type Formation, although different names are extensively used in the literature, from the names of type localities where they crop out. These rocks and their equivalents were firstly described as intrusive within the Kuncha Formation of the LowerLHS Unit (Le Fort, 1975; Le Fort & Rai, 1999; DeCelles et al., 2001; Upreti et al., 2003; Larson et al., 2019 and references therein), which was deposited in the Paleoproterozoic (Parrish & Hodges, 1996; DeCelles et al., 2000; Martin et al., 2005). However, similar orthogneisses also occur at different structural levels in the LHS i.e., both within the Lower–LHS and the Upper–LHS sequences (Stöcklin, 1980). These two mica mylonitic orthogneisses often contain K–feldspar porphyroclats up to few centimetres in size and are characterized by a pervasive stretching lineation (Pêcher 1977, 1991).

The Ulleri–type gneisses have been interpreted either as derived from igneous protoliths formed in a continental rift setting (e.g., Sakai et al., 2013; Larson et al., 2018) or as the metamorphic products of an arc–related volcano–sedimentary sequence (Le Fort & Rai, 1999; Kohn et al., 2010). Despite theis controversial genetic interpretation, the results of various geochronological studies point to a Paleo–Proterozoic age for these gneisses (Kohn et al., 2017; Larson et al., 2017).

2.2.3 Metamorphism of the Lesser Himalayan Sequence

It is well known, since the pioneering works of Le Fort (1975), Pêcher (1975, 1989) and Stöcklin (1980) among others, that the LHS is characterized by a structurally upward increase of the metamorphic grade, which defines a typical Barrovian inverted metamorphic gradient. Petrographic observations clearly indicate that the metamorphic grade increases, with the progressive appearance of chlorite, biotite, garnet and staurolite/kyanite over a structural distance of a few kilometers. Most of the published studies aimed at constraining the peak pressure–temperature (P–T) conditions

experienced by the LHS are based on conventional and/or multi–equilibrium thermobarometry (e.g. Macfarlane, 1995; Rai et al., 1998; Catlos et al., 2001; Kohn et al., 2001; Goscombe et al., 2006, 2018; Kohn, 2008; Martin et al., 2010; Imayama et al., 2010; Corrie & Kohn, 2011; Mosca et al., 2012; Rapa et al., 2018); these studies typically constrain the peak metamorphic temperatures, but do not provide tight information on peak pressures. Raman Spectroscopy of Carbonaceous Material (RSCM) has been also used along several LHS cross–sections (Bollinger et al., 2004; Beyssac et al., 2004): this method also provides detailed information about the maximum temperature reached at the metamorphic peak, but not on pressure. For these reasons, most of the peak pressure values are widely scattered and hold large errors along most of the LHS sections studied so far. Comprehensive reviews of the variations in peak P–T conditions registered by the inverted metamorphic LHS sequence from the lower to the upper structural levels, and along–strike from western to eastern Nepal, are provided by Kohn (2014) and Goscombe et al. (2018).

2.2.3.1 Lower LHS

The metamorphic evolution of the Lower–LHS is characterized by maximum temperature experienced at maximum pressure, defining typical hairpin P–T paths (e.g. Catlos et al., 2001; Kohn et al., 2001; Groppo et al., 2009; Rolfo et al., 2015; Rapa et al., 2016; Iaccarino et al., 2017) (Fig. 2.3). Maximum temperatures of 570–600 °C and pressures of 7–8 kbar are registered in the uppermost structural levels of the Lower–LHS (i.e. Dandagaon Phyllite Formation) (Fig. 2.3); these P–T conditions are consistent with the appearance of small garnet grains in the Dandagaon Phyllite Formation and with the common occurrence of biotite, both in the main foliation and as late post–kinematic porphyroblasts.

2.2.3.2 Upper LHS

A number of studies both in central–western Nepal (Catlos et al., 2001, 2018; Kohn et al., 2001; Kohn, 2014) and in eastern Nepal (Groppo et al., 2009; Rolfo et al., 2015) suggest that the Upper–LHS lithologies experienced maximum temperature after maximum pressure. The overall shape of the Upper–LHS P–T paths is characterized by a prograde moderate increase in both P and T, up to peak–P conditions, followed by a heating decompression, up to peak–T conditions (Fig. 2.3). The results obtained in the framework of this project (Tamang et al., in press, and see Chapter 5) constrain peak–P conditions at 9.5–10.5 kbar, 580–590 °C and peak–T conditions at 620 ± 20 °C, 8.5 ± 0.2 kbar, consistent with the observed stability of staurolite and kyanite in many samples from the Nourpul and Benighat Formations. It is worth noting that the shape of the P–T paths constrained through the differential thermodynamic method is similar to that deduced using the P–T pseudosections approach (Fig. 2.3), although absolute P–T values are systematically lower for the first method. The tectonic implications of such P–T trajectories are discussed in Chapter 5.

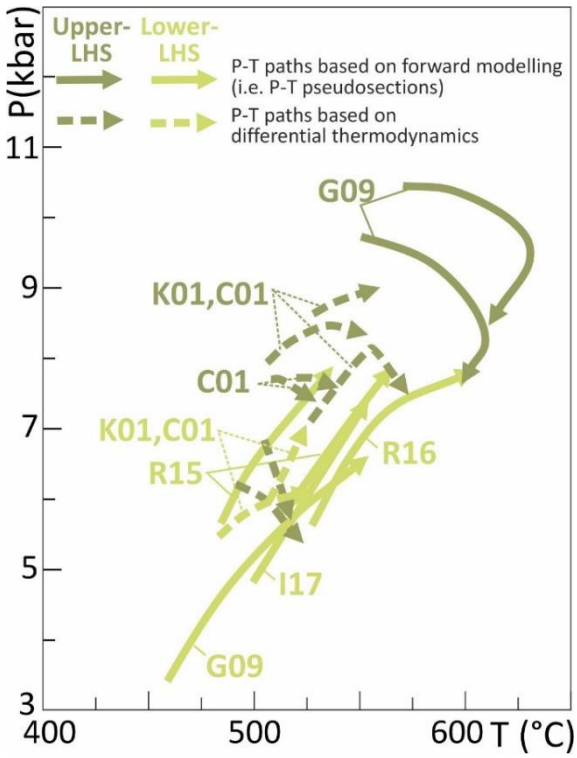

Figure 2.3: P–T paths constrained for the Lower–LHS and Upper–LHS units using the forward modelling approach (continuous curves) or differential thermodynamics (dashed curves). C01: Catlos et al., 2001; K01: Kohn et al., 2001; G09: Groppo et al., 2009; R15: Rolfo et al., 2015; R16: Rapa et al., 2016; I17: Iaccarino et al., 2017

2.3 Present–day CO_2 emissions in the Nepal Himalaya

The Himalaya is the largest tectonically active region in the globe, hosting a large number of CO_2–rich thermal springs, mostly located in the proximity of the MCT along the whole Himalayan belt (Bhattarai, 1980; Evans et al., 2008; Becker et al., 2008; Perrier et al., 2009; Girault et al., 2014a; Chamberlain et al., 2002; Rai et al., 2020; Giggenbach et al., 1983; Tiwari et al., 2016; Singh et al., 2004). The present–day CO_2 emission from these hot springs has been investigated either based on the chemical and/or isotopic compositions of the waters (Evans et al., 2008; Becker et al., 2008; Tiwari et al., 2016) or through the direct measurement of the outgassed gaseous CO_2 from the ground surface (Girault et al., 2014a; Girault et al., 2018).

The metamorphic nature of the CO_2 released from the hot springs of the Nepal Himalayas is testified by the high alkalinity of the waters that contributes, for example, to the total dissolved inorganic carbon (DIC) of the Narayani River (Evans et al., 2004). Moreover, the high values of $\delta^{13}C$ measured at hot springs also suggest a metamorphic origin for the CO_2 originated at depth (Evans et al., 2008; Becker et al., 2008; Tiwari et al., 2016). In central and western Nepal, ground discharges of CO_2 gas emissions were discovered in the vicinity of the main hot springs, and the systematic measurement of the gaseous CO_2 and radon 222 emissions (Perrier et al. 2009; Girault et al., 2014 a,b; Girault et al., 2018) led to estimate CO_2 fluxes similar to those of diffusive fluxes from the active volcanoes (Girault et al., 2014 a,b; Girault et al., 2018).

Chapter 3

Methods

3.1 Fieldwork

Fieldwork was conducted in the eastern, central and far–western parts of Nepal with the aim of: (i) investigating the lateral lithological variations and the main structural features within the LHS; (ii) measuring the CO_2 flux from the ground discharges in the vicinity of the observed hot springs.

Fieldwork finalized to the geological investigation of the LHS was conducted in the following areas: (1) Kharidhunga–Kalinchowk area in the Sindhupalchok and Dolakha districts of central Nepal, ca. 50 km NE from the Kathmandu valley and, (2) along the Jumla–Mugu–Humla section and the Karnali river in far–western Nepal. The fieldwork in central Nepal was conducted in April 2021 and it lasted for ca. 15 days. The Kharidhunga–Kalinchowk transect in central Nepal starts from Tekanpur village, located on the left bank of the Sunkoshi River, continues eastward up to the Kharidhunga mine and the Makaibari village. It then turns northward reaching the village of Kuri, the Kalinchowk temple and the Tingsang La pass. It finally turns westward towards the Gathi village, ending at the Last Resort along the Sunkoshi River, and overall making a loop along the Arniko Highway. Altitudes along this transect vary from a minimum of ca. 750 m a.s.l. to a maximum of ca. 3700 m a.s.l. The filedwork in far–western Nepal was performed in November 2021 for about 1 month. The Jumla–Mugu–Humla transect starts from Jumla, a small city in Far Western Nepal, located about 150 km north of the city of Nepalgunj. This transect runs from Jumla toward NNW to the Naurighat village in the Jumla district and reaches Rara Lake and Luma village in the Mugu district. The transect continues NNW up to Darma, then turns westward up to Sialtadi village and then follows the Humla Karnali river toward north, till Simikot in the Humla district. Altitudes along this transect vary from a minimum of ca. 1500 m a.s.l. to a maximum of ca. 3600 m a.s.l.

66 samples were collected during the fieldwork in central Nepal, and 69 samples were collected from the Jumla–Mugu–Humla section in far–western Nepal. Most of the samples are medium–grade metapelites and carbonate–bearing lithologies, with minor amounts of orthogneisses, amphibolites and quartzites. Samples collected from both the transects have been observed at the optical microscope in order to recognize their main mineral assemblages. The complete list of the collected samples and their locations are provided in Appendix 1.

Fieldwork finalized to the direct measurement of diffusive CO_2 flux was conducted in the eastern and the far–western parts of Nepal. In eastern Nepal, diffusive CO_2 gas flux was measured in two places: (i) at Nundhaki in the Sankhuwasabha district (ca. 60 km north of

the city of Dharan) and (ii) at Sekhathum in the Taplejung district. In far–western Nepal the field campaign was conducted in Simikot, Humla district. Geologically, all these locations lie in the GHS of the Nepal Himalaya. A total of 11 hot springs were observed in these localities and CO_2 flux was measured in the vicinity of these hot springs.

3.2 Samples location

A limited number of samples from the Upper–LHS have been studied in detail in order to: (i) constraining the P–T evolution of the Upper–LHS (see Chapter 5), and (ii) investigate the CO_2–producing processes and the amounts of CO_2 released through these processes (see Chapter 6). Aluminous metapelites have been selected to achieve the first target, whereas various lithologies derived from the metamorphism of carbonate–bearing protoliths have been selected to achieve the second goal. In the following, these last lithologies are referred to as carbonate–bearing lithologies, although carbonates are not always preserved in all samples. Except for sample 21a–22a, collected from the Kharidhunga–Kalinchowk transect, all the samples investigated in detail were collected by Chiara Groppo and Franco Rolfo during previous expeditions.

Specifically:

- the six metapelite samples investigated in detail were collected along two different sections in central Nepal, located ca. 50 km NNW of Kathmandu. The first section is located in the upper part of the Ankhu valley (samples 17a–), ca. 15 km NW of Dhunche, whereas the second section is located in the upper part of the Trisuli valley, (samples 15a–), ca. 8 km north of Dhunche (Fig. 3.1). Samples 17a–22 and 15a–15b belong to the Nourpul Formation (see Chapter 4), whereas samples 17a–34, 17a–33, 15a–28b and 17a–42 belong to the uppermost Benighat Slates (see Chapter 4).
- the eleven carbonate–bearing lithologies were collected from five different sections: two of these sections are the same already described for metapelites (i.e. samples 17a– and 15a–). The other three sections are all located in central Nepal, ca. 60 km eastward of Kathmandu. Specifically: (i) in the upper part of the Sunkhosi valley, along the Arniko Highway (samples 18a–); (ii) along the Barabise–Tinsang La Pass section (samples 17b–); (iii) along the Kharidhunga–Kalinchowk section (samples 21a–). Samples 15a–28a, 17a–29, 17a–35 and 17a–36b belong to the Benighat Slates Formation, whereas samples 17b–7d, 17b–10b, 17b–12, 17b–18, 18a–26, 18a–31 and 21a–22a all belong to the Dhading Dolomite Formation (see Chapter 4).

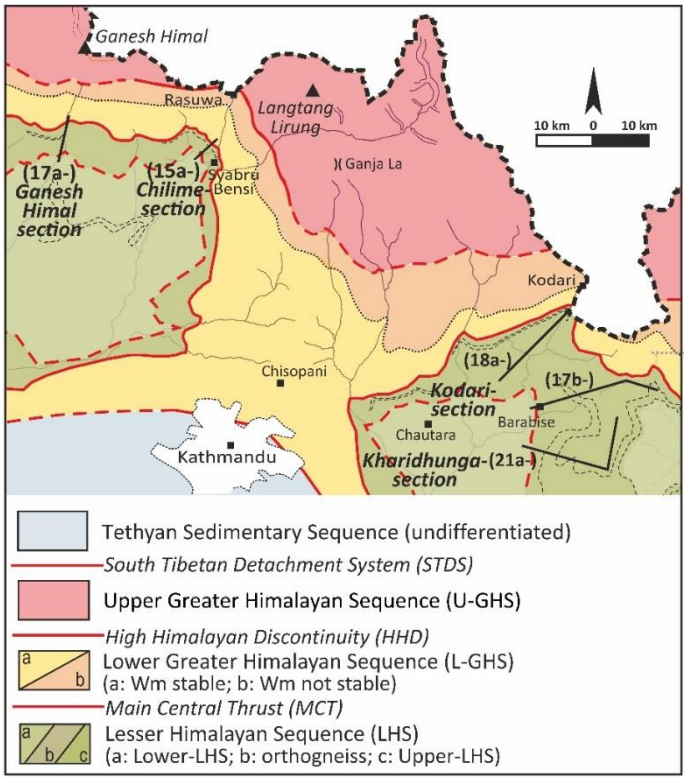

Figure 3.1: Geological sketch map of central Nepal Himalaya, showing the location of the five sections from which the samples studied in detail have been collected (black lines). Modified from Dhital (2015) and He et al. (2015) and based on our own data. The dashed black line is the Nepal–China border.

3.3 Microstructural and mineral chemistry study

For all samples, high–resolution multispectral maps were performed on the entire thin sections (ca. 3 × 1.5 cm) to obtain their modal compositions and to highlight their microstructures at the thin section scale. These X–ray maps were obtained using a JEOL IT300LV Scanning Electron Microscope (SEM) at the Department of Earth Sciences, University of Torino, Italy. The instrument is equipped with an energy dispersive spectrometry (EDS) Energy 200 system and an SDD X–Act3 detector (Oxford Inca Energy, UK). Operating conditions used for mapping are: 15 kV accelerating voltage, process time 1, 2.5 µm point step, 500 ms pixel dwell time. The raw data were processed using the MultiSpec© software (Purdue Research Foundation, USA) in order to obtain the modal compositions.

Some of the carbonate–bearing lithologies were additionally observed with the cathodoluminescence (CL) technique for detecting the possible occurrence of microstructures involving carbonate minerals not evident from the major elements X–ray maps (e.g. presence of zoning, the occurrence of different carbonate generations, etc.). CL images of the entire thin sections were obtained using Cathodyne optical cathodoluminescence (CATHODO SP02), at the Institut de Physique du Globe de Paris (IPGP), Paris, France. The Cathodyne software was used to analyse the samples, adjusting the current and voltage at 170 µA and 13 kV respectively with the long exposure time.

The rock–forming minerals were analysed with the same SEM–EDS instrument used for the high–resolution X–ray maps. Operating conditions are: 15 kV accelerating voltage, process time 2, 15 s counting time. SEM–EDS quantitative data were acquired and processed using the Microanalysis Suite Issue 12, INCA Suite version 4.01; natural mineral standards were used to calibrate the raw data; the ΦρZ correction (Pouchou & Pichoir, 1988) was applied. Fig. 5.2 and 6.9 in Chapters 5 and 6 and Datasets 1, 4 and 5, report the whole set of compositional data for all the minerals analysed in each sample. Most analyses were recalculated using the NORM computer software (Ulmer, 1986); structural formulae have been calculated based on 12 oxygens for garnet, 11 oxygens for muscovite and biotite, 48 oxygens for staurolite, 8 oxygens for plagioclase, 28 oxygens for chlorite, 6 oxygens for dolomite, 3 oxygens for calcite and magnesite and 12 oxygen for talc. Amphibole group minerals were normalized using the software WinAmphcal (Yavuz, 2007). Compositional profiles were systematically analysed each time garnet porphyroblasts occur in a sample. In metapelites, compositional profiles were carried out on two (samples 17a–22 and 15a–15b) or three (samples 17a–33 and 17a–42) garnet porphyroblasts, except for sample 15a–28b for which a single, cm–sized, garnet was analysed. In carbonate–bearing lithologies, compositional profiles were carried out on two garnet porphyroblasts (samples 17a–29, 17a–35 and 17b–12). In all samples, the analysed garnet porphyroblasts were selected among those showing the highest MnO content in the core, based on the MnO X–ray maps of the whole thin sections.

3.4 Estimation of bulk rock compositions

The bulk–rock compositions of each sample investigated in detail (i.e., measured bulk compositions: MBC; Table 5.2 and Table 6.1) have been calculated by combining the estimated mineral modes (Table 5.1 and Table 6.2) with mineral chemistry, and considering the molar volumes of each phase (details reported in the Datasets 2, 6 and 7). Additional bulk–rock compositions of both metapelites and carbonate–bearing lithologies from the LHS and the GHS were used to discuss the nature of the investigated samples (e.g. to recognise the existence of a dolomite series vs. a magnesite series; see Chapter 6, Fig. 6.1). These bulk–rock compositions refer to samples previously studied by Groppo et al. (2009, 2021) and Rapa et al. (2016) or to unpublished data. Most of them were acquired by inductively coupled plasma mass spectrometry (ICP–MS) analysis by ALS Chemex, Vancouver, Canada, except where explicitly indicated in the reference papers. Table S2 available in Appendix 2 reports the whole set of used bulk–rock compositions. Mineral abbreviations in the text, figures and tables are from Whitney & Evans (2010).

3.5 Reconstruction of the protoliths' assemblages

The protoliths of the investigated carbonate–bearing lithologies were reconstructed to identify the mineral assemblages of the protolith using the PCalc software of Godard (2009). More specifically, starting from the bulk–rock compositions, approximated

protolith's mineralogical compositions have been reconstructed according to the following assumptions: (a) CaO from silicate fraction (CaO* in Datasets 3, 8 and 9) is equivalent to Na_2O (e.g. Hofer et al., 2013; McLennan et al., 1993) and is incorporated in anorthite; the remaining CaO is incorporated in calcite; (b) chlorite is the only mafic mineral in the protolith and, (c) albite incorporates all the Na_2O. The modal proportions of the protolith's minerals have been obtained by applying the least square method (PCalc; Godard, 2009) and using end–member compositions and molar volumes for kaolinite, illite, clinochlore, daphnite, albite, anorthite, quartz, K–feldspar, calcite, dolomite and magnesite. The result is considered satisfactory if the residuals (i.e. molar bulk composition of the protolith's minerals—molar bulk–rock composition) is close to zero. The results obtained for each carbonate–bearing sample are shown in Datasets 3, 8 and 9 and are summarized in Table 6.1 (see Chapter 6).

3.6 Forward thermodynamic modelling

The forward thermodynamic modelling approach was applied on both metapelites and carbonate–bearing lithologies for two different purposes: (i) constraining the P–T evolution of the Upper–LHS, and (ii) investigating the CO_2–producing processes in terms of P–T conditions at which the main decarbonation reactions occurred and of the amounts of CO_2 released. All the isochemical phase diagrams (i.e. pseudosections) were calculated using Perplex (Connolly, 1990, 2009), versions 6.9.0 (for metapelites) and 6.9.1 (for carbonate–bearing lithologies). P–T isochemical phase diagrams were calculated for metapelites, whereas P/T–X(CO_2) pseudosections were calculated for carbonate–bearing lithologies.

3.6.1 P–T pseudosections for metapelites

The P–T isochemical phase diagrams were calculated for six metapelite samples using the internally consistent thermodynamic dataset of Holland & Powell (1998, update 2004) (ds55) and the following solution models: garnet, chloritoid, cordierite, staurolite and epidote (Holland & Powell, 1998), biotite (White et al., 2007), chlorite (Holland et al., 1998), feldspar (Fuhrman & Lindsley, 1988), white mica (Coggon & Holland, 2002; Auzanneau et al., 2010), ilmenite (White et al., 2014). Quartz, kyanite/sillimanite, and rutile were considered pure phases. All the P–T pseudosections were calculated in the system MnNKCFMASTOH ($MnO–Na_2O–K_2O–CaO–FeO–MgO–Al_2O_3–SiO_2–TiO_2–Fe_2O_3–H_2O$), except for sample 17a–34, for which the system NKFMASTH was used, due to the lack of Mn–, Ca– and Fe^{3+}– bearing minerals.

Most of the modelled samples are graphitic phyllites; the occurrence of graphite should require, in principle, the use of a C–buffered COH equation of state (EoS) for fluid. However, fluid has been treated here in the more traditional way, using the EoS of Holland & Powell (1998) and assuming it is a saturated pure phase ($aH_2O = 1$). This choice is justified by considering that the finely dispersed graphite in these samples derives from the metamorphic recrystallization of the carbonaceous matter originally present in the

sedimentary protoliths and it likely behaved as a passive phase during all the metamorphic evolution (i.e. neither it participated in fluid–rock interaction processes, nor it precipitated from the fluid). Tests conducted using the C–buffered COH EoS of Connolly & Cesare (1993) at X(O)=0.333 and αC = 1 (i.e. assuming an H_2O–dominated fluid in equilibrium with graphite) showed that the topology of the modelled phase diagrams does not change and that the shift of the phase assemblage boundaries is negligible ($\leq$ 10 °C toward lower temperatures).

Five of the studied samples contain strongly zoned garnet porphyroblasts: for these samples, two P–T pseudosections have been calculated considering the fractionation effects on the bulk composition due to the growth of the zoned garnets. The fractionated bulk compositions have been obtained by subtracting the garnet core and mantle compositions (i.e. the modal amount of garnet core + mantle, as derived from the modal analysis of the X–ray maps) from the measured bulk composition (MBC). The two pseudosections have been used to model: (i) the P–T conditions for the growth of garnet core and mantle (MBC, Table 5.2), and (ii) the P–T conditions for the growth of garnet rim in equilibrium with the matrix assemblage (MBC – garnet cores and mantles, Dataset 1). In both cases, P–T conditions have been inferred based on the intersection of compositional isopleths modelled for garnet (core: GrtC; mantle: GrtM; rim: GrtR), biotite, staurolite, chlorite and plagioclase. Specifically, the intersection of XMn, XMg, XCa and XFe isopleths has been used to constrain the P–T conditions of garnet growth, according to the following strategy: (i) the composition corresponding to the maximum XMn has been selected for GrtC; (ii) an average composition has been selected for GrtM; (iii) the composition corresponding to the maximum XMg has been considered for GrtR. The garnet isopleths intersection has been defined considering an uncertainty of ± 0.01 for all the isopleths (e.g. Lanari & Duesterhoef, 2019). For biotite, staurolite and chlorite the modelled XMg isopleths corresponding to the average measured XMg values have been used, with uncertainties covering their compositional interval from the minimum to the maximum XMg. The same approach has been applied to plagioclase, for which the XCa isopleths have been used.

3.6.2 P/T–X(CO_2) pseudosections for carbonate–bearing lithologies

The P/T–X(CO_2) isochemical phase diagrams were calculated for 7 carbonate–bearing samples (dolomite–bearing: samples 17b–12, 17a–29, 15a–28a, 18a–26 and 17b–10b; magnesite–bearing: samples 17a–36b, 17a–35, 17b–7d) using the internally consistent thermodynamic dataset of Holland & Powell (1998, update 2004) (ds55) and the following solution models: carbonate (i.e. Ca–Mg–Mn–Fe carbonate with calcite structure; Massonne, 2010), garnet, chloritoid, staurolite, cordierite, epidote, dolomite and clinopyroxene (Holland & Powell, 1998), biotite (White et al., 2007), chlorite (Holland et al., 1998), feldspar (Fuhrman & Lindsley, 1988), white mica (Coggon & Holland, 2002; Auzanneau et al., 2010), ilmenite (White et al., 2014), clino– and ortho– amphibole (Diener et al., 2007; Diener & Powell, 2012), talc (ideal model) and scapolite (Kuhn, 2005). Quartz,

titanite, zoisite, kyanite/sillimanite and rutile were considered as pure phases. The P/T gradient was defined based on the P–T evolution constrained from the associated metapelites, i.e., a prograde stage characterized by an increase in both P and T conditions up to peak–P conditions, and a decompression stage from peak–P to peak–T conditions. The P/T gradient for the prograde stage was defined as: P(bar) = 17*T(K) –5065, in the temperature interval 400–600 °C; the P/T gradient for the decompression stage was defined as: P(bar) = –63.8*T(K) +65473, in the temperature interval 600–700 °C. Each P/T–X(CO_2) pseudosection thus consists of two parts, with the junction located at 600°C, 9.8 kbar. The P/T–X(CO_2) pseudosections were calculated in the full MnO–Na_2O–K_2O–CaO–FeO–MgO–Al_2O_3–SiO_2–TiO_2– Fe_2O_3–H_2O–CO_2 (MnNKCFMASTO–H_2O–CO_2) system (sample 17b–12), or in the reduced NKCFMASTO–H_2O–CO_2 (sample 17a–36b), MnNKCFMAST–H_2O–CO_2 (samples 17a–29 and 17a–35), NKCFMAST– H_2O–CO_2 (samples 15a–28a and 18a–26) and CFMAS–HC (sample 17b–7d) systems, according to the observed mineral assemblages and compositions (e.g. MnO was included to model the garnet–bearing samples); Fe_2O_3 was considered for the modelling of samples containing white mica anomalously enriched in Fe^{3+}.

Fractionation effects on the bulk composition due to the growth of garnet porphyroblasts in samples 17b–12, 17a–29 and 17a–35 were not considered due to the complexity of the modelling. However, garnets are relatively poorly zoned compared to those of metapelites, or even unzoned (sample 17b–12). Minor discrepancies between the observed and the modelled mineral assemblages and compositions could be in any case related to this simplified approach.

The P–T–X(CO_2) evolution of the modelled carbonate–bearing lithologies was constrained according to the following strategy:

(i) the starting P–T–X(CO_2) conditions were fixed at T=400 °C (P=6.4 kbar) and at a X(CO_2) value such as the predicted mineral modes are as close as possible to the calculated protolith's mineral modes (with muscovite replacing illite ± K–feldspar, Al–rich minerals such as pyrophyllite or chloritoid replacing kaolinite, and paragonite replacing albite);

(ii) prograde P–T–X(CO_2) conditions were inferred based on the intersection of compositional isopleths (XMn, XMg and XCa) modelled for garnet core in those samples where garnet porphyroblasts are slightly zoned (samples 17a–29 and 17a–35);

(iii) peak P–T–X(CO_2) conditions were inferred based on the intersection of compositional isopleths modelled for biotite ± plagioclase ± hornblende ± ortho–amphibole ± garnet rim, depending on the observed peak assemblages. The XMg isopleths were used for biotite, hornblende, and ortho–amphibole, the XCa isopleths for plagioclase and the XMn, XMg and XCa isopleths for garnet rim. In all cases, two isopleths have been used for each compositional parameter, corresponding to the measured compositional range in each phase. The only exception is sample 17b–7d (magnesite + talc rock), for

which the peak P–T–X(CO_2) conditions were inferred based on the intersection of the modelled isomodes for magnesite, talc and chlorite, due to the almost pure composition of all the phases (approaching the Mg– end–members).

3.7 Accumulation Chamber method

The accumulation chamber method (Chiodini et al., 1998, Girault et.al., 2014) is considered a reliable technique to measure the CO_2 flux from the ground discharge. This is one of the effective methods to measure the fluxes of CO_2 as it can be effectively used even in remote locations and even during the monsoon. This technique aid in measuring the CO_2 fluxes over more than five orders of magnitude (Girault et.al. 2009 and 2016). Initially, the site around the hot springs is selected for the gaseous CO_2 measurement. Then the profile is selected along which the measurement is to be taken. Before the measurement, the atmospheric pressure and the surrounding temperature is recorded which will be helpful for the calculation later. Then the measurement is taken along the profile in the specific distance, here we take the distance between two measurements of 1 to 2 meters in eastern Nepal and for Far Western Nepal we took the distance of 5 meters. Then after, the ground (where the measurement is to be done) is made clean by removing the vegetation (Fig. 3.3a), and 3–5 cm (depth) of the soil is removed to make a relatively flat and homogeneous emplacement site for the chamber (Fig. 3.3a,c). The volume and the footprint area of the chamber used were 0.0085 m^3 and 0.092 m^2 respectively. Then the sensor probe (Fig. 3.3b) is placed inside the chamber and soil was plastered around the base of the chamber to seal it, and the sensor measures the CO_2 flux at the function of time. The graphical representation of the measurement of the CO_2 flux in ppm vs time is shown in Fig. 3.2.

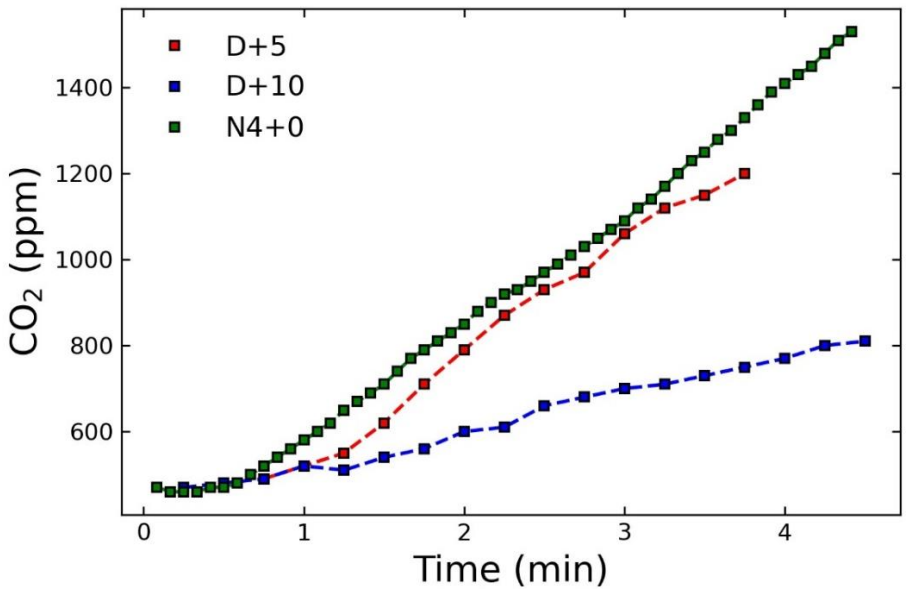

Fig. 3.2: Graphical representation of the CO_2 flux measured in the field vs time, the different colored diamond represents the profile in a different place.

The sensor used was the semiautomatic Vaisala™ sensor (Vaisala™ CARBOCAP® Hand–Held GM70, Finland), which is based on infrared absorption of gaseous CO_2 (Fig. 3.2b). The sensor used during the field was V1 and V3 for eastern Nepal and V2 for Far Western Nepal. The probe used was CF6 for eastern Nepal and CF4 for Far Western Nepal and measure up to 10000 ppm of gas flux. The CO_2 flux expressed in g m^{-2} d^{-1}, is directly related to the slope at the origin of the CO_2 accumulation curve ($dC/dt|t=0$) according to Chiodini et al. (1998). The total CO_2 discharge, expressed in mol s^{-1} (or ton d^{-1}) is estimated using the CO_2 flux dataset by kriging and interpolation procedures (Girault et. al., 2014) according to the following equation:

$$\Phi_{CO_2} = \frac{P_{atm} M_{CO_2}}{RT} \frac{V}{S} \frac{dC}{dt} \Bigg|_{t=0}$$

where C is the CO_2 concentration, P_{atm} is the mean atmospheric pressure, Mco_2 is the molar mass of CO_2, R is the ideal gas constant, T is the ambient temperature, and V and S are chamber volume and footprint area, respectively.

Fig. 3.3: Representative photographs for the measurement of CO_2 gas emission in the field (a) recording the CO_2 flux in the Nundhaki site along the profile shown by the white line in the (b) picture of the CO_2 measuring sensor and the bucket used to cover the sensor. (c) measuring CO_2 from the ground in the Far Western Nepal, Kermi site.

Chapter 4

Lithostratigraphy of the Lesser Himalayan Sequence

4.1 Lithostratigraphy and petrography

The stratigraphic reconstruction of the extremely thick (more than 15 km) LHS metasedimentary sequence along the approximately 850 km long stretch of LHS in Nepal is prevented by its complex structural setting (e.g. DeCelles et al., 2001; Pearson & DeCelles, 2005). Different stratigraphic units have been defined in different areas, whose correlation at the regional scale is not always straightforward. In western and central Nepal, the stratigraphic subdivisions of the LHS are mostly based on the detailed mapping by Stöcklin (1980), Sakai (1983), Colchen et al. (1986), DeCelles et al. (2001) and Robinson et al. (2001), whereas in eastern Nepal, the LHS stratigraphy remains poorly understood and mostly based on data from Schelling & Arita (1991) and Schelling (1992). In this chapter, the lithostratigraphic and petrographic features of the LHS are described in detail starting from the reference section defined by Stöcklin (1980) and Upreti (1999) in central Nepal (S80 in Fig. 2.2) and combining field and petrographic observations from several sections in central Nepal (Fig. 4.1), either related to previous fieldwork campaigns (Chiara Groppo, Franco Rolfo and Pietro Mosca) or to the Kharidhunga–Kalinchowk section investigated in the framework of this project. The main along–strike variations with respect to these reference sections are then discussed.

The LHS is conventionally divided into two complexes, characterized by distinct lithological associations: the Lower–LHS (Lower Nawakot Unit; Stöcklin, 1980), dominated by siliciclastic rocks, and the Upper–LHS (Upper Nawakot Unit; Stöcklin, 1980) consisting of both carbonatic and siliciclastic rocks. U–Pb dating of detrital zircons constrained the depositional age of the Lower–LHS to the Paleo–Proterozoic, with most ages converging in the interval 1900–1850 Ma (e.g. Parrish & Hodges, 1996; DeCelles et al., 2000; Martin et al., 2005, 2011; Sakai et al., 2013), whereas the depositional age of the Upper–LHS sequence is still poorly constrained, although a Paleo– to Meso–Proterozoic age is tentatively proposed in the literature (e.g. DeCelles et al., 2000; Martin et al., 2005; Gehrels et al., 2011).

4.1.1 Lower–LHS

The Lower–LHS sequence consists of a thick package of metasedimentary rocks mostly derived from pelitic and arenaceous protoliths. From the bottom to the top of the sequence, the following formations have been distinguished in the reference section of

Stöcklin (1980): Kuncha Formation, Fagfog Quartzite Formation and Dandagon Phyllite Formation.

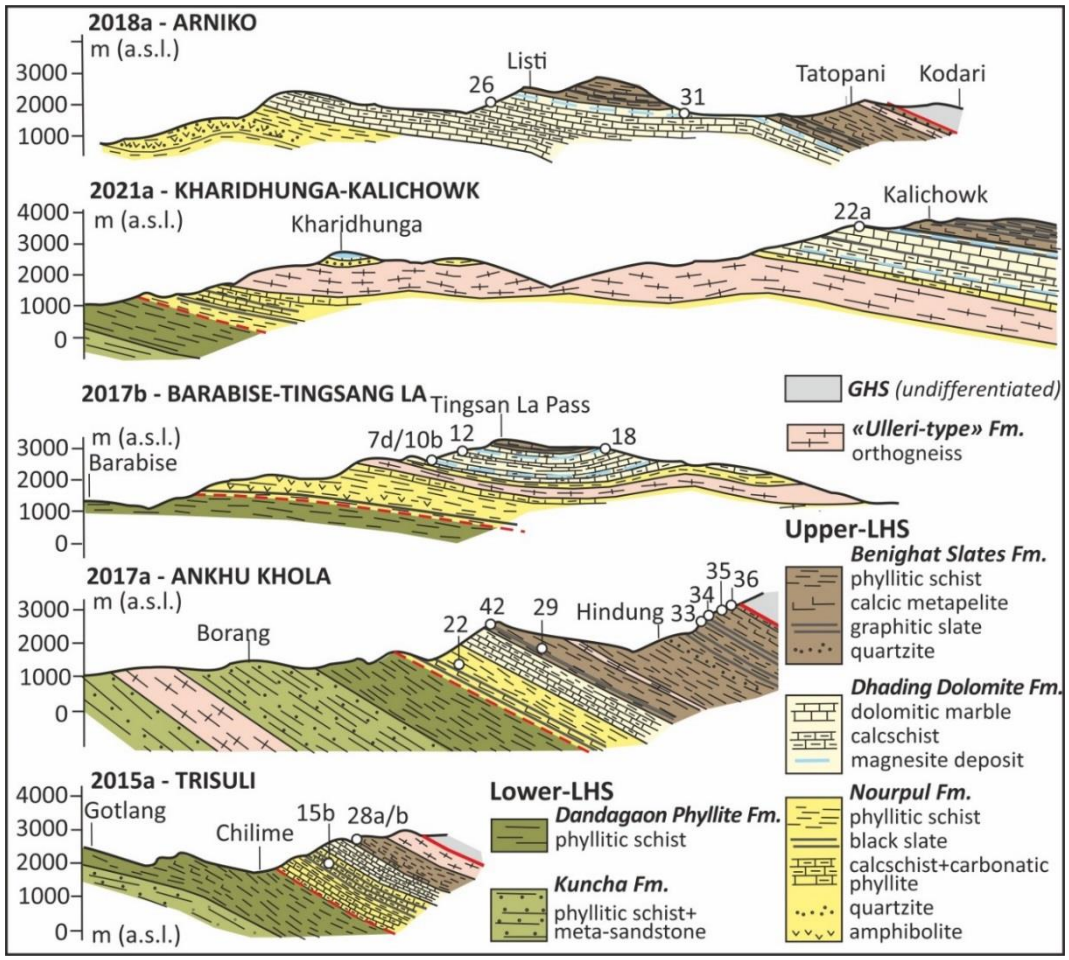

Figure 4.1: Representative cross–sections across the Lower– and Upper–LHS in central Nepal. Location of each cross–section is reported in Fig. 2.2 and 3.1. Most pictures reported in Fig. 4.2–4.11 refer to these cross–sections or to adjacent transects, except where explicitly indicated.

4.1.1.1. Kuncha Formation

The Kuncha Formation is a thick (more than 2500 m), monotonous succession of grey greenish phyllites, meta–sandstones and minor meta–conglomerates, alternating in layers of variable thickness (from decimetric to decametric) (Fig. 4.2a–c), derived from the metamorphism of original turbiditic flysch deposits.

In the fine–grained **phyllites**, the pervasive main foliation is defined by muscovite ± chlorite ± biotite, this last mostly confined to the quartz–richer domains. The main foliation derives from the transposition of an earlier foliation, still preserved in microlithons (Fig. 4.2d), and it is often pervasively crenulated, with the local development of an axial–plane foliation, defined by muscovite ± biotite. Small garnet grains (Fig. 4.2d) locally appear in the uppermost (northern) part of this formation.

The **meta–sandstones** show a well–preserved clastic structure, with abundant millimetre–sized clasts of quartz and minor feldspars and muscovite (Fig. 4.2e), already evident at the outcrop scale. The foliation is less pervasive than in the associated phyllites, resulting in a massive appearance at the outcrop scale (Fig 4.2c), and it is defined by the alignment of muscovite, biotite and chlorite. Chloritoid sporadically occurs in both the phyllites and the meta–sandstones; in the formers, it forms millimetre–sized porphyroblasts syn– to post–kinematic with respect to the main foliation, whereas in the latters, it forms fine–grained radial aggregates.

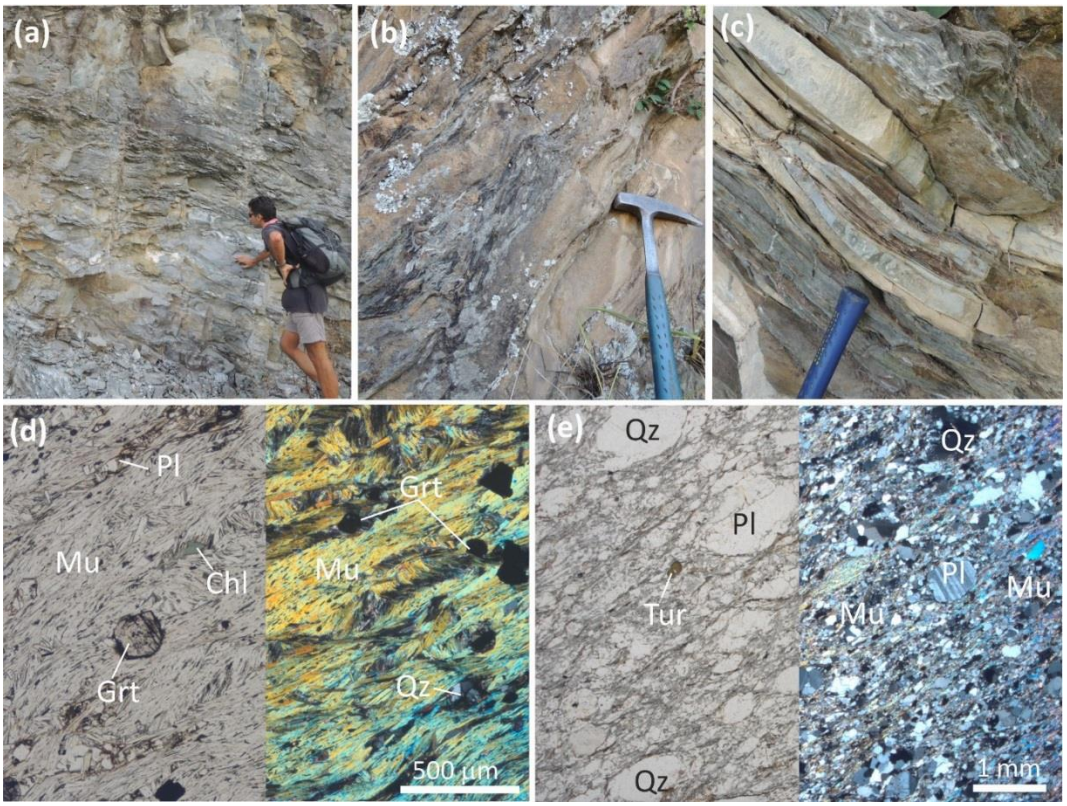

Figure 4.2: Kuncha Formation. (a-c) Meta–sandstone intercalations (whitish and massive) within grey–greenish, pervasively foliated, phyllites. (d) Garnet–bearing muscovite + chlorite phyllite (left: Plane Polarized Light, PPL; right: Crossed Polarized Light, XPL). (e) Meta–sandstone preserving the clastic structure of the protolith (PPL/XPL). (c) and (d) are from the Tamur and Arun sections in eastern Nepal (Fig..2.2).

4.1.1.2. Fagfog Quartzite formation

The Fagfog Quartzite Formation consists of fine– to medium–grained banded quartzite (Fig. 4.3b) with several phyllite intercalations. This formation reaches a maximum thickness of approximately 500–800 m, but it is not presented in some sections. Its stratigraphic position is controversial, having been placed either below (Stöcklin, 1980) or above (Shrestha et al., 1987) the Dandagaon Phyllites Formation. According to our own observations in the inner (northern) LHS domain in central Nepal, a thick quartzite layer often occurs stratigraphically above the Dandagaon Phyllite, but its attribution to the

Fagfog Quartzite Formation is ambiguous, and it is consequently not included as a stand–alone formation in Fig. 4.1.

The **quartzites** show a marked fissility and tend to separate in dm–thick plates (Fig. 4.3a), although the foliation, defined by muscovite and minor biotite, is not pervasive (Fig. 4.3c)

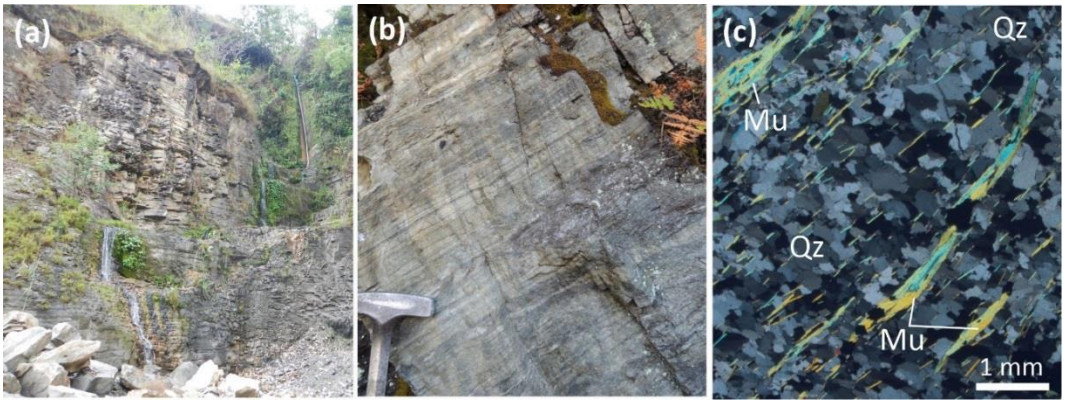

Figure 4.3: Fagfog Quartzite Formation. (a) and (b) Outcrop appearance of banded, highly fissile quartzite. (c) The main foliation in the quartzite is defined by muscovite (XPL).

4.1.1.3. Dandagaon Phyllite Formation

The Dandagaon Phyllite Formation is described as a succession dominated by dark and grey–green homogeneous phyllites, with sporadic thin layers of quartzites. Compared to the Kunchha Formation, the Dandagaon Phyllite Formation is almost free of meta–sandstone intercalations. Centimeter–thick quartz veins, deformed and stretched parallel to the main foliation, are locally quite abundant at this stratigraphic level (Fig. 4.4a,b). An additional common feature in this formation is the presence of a pronounced mineral stretching defined by biotite (Fig. 4.4c).

In the **phyllites**, the main foliation, defined by muscovite ± chlorite ± biotite, transposes an earlier foliation preserved in the microlithons (Fig. 4.4d,e) and it is often pervasively crenulated. Pre–kinematic garnet porphyroblasts (up to few millimeters in size) wrapped around by the main foliation are common (Fig. 4.4d), as well as late biotite porphyroblasts overgrowing the main foliation (Fig. 4.4f), which are not related to the mineral lineation described above.

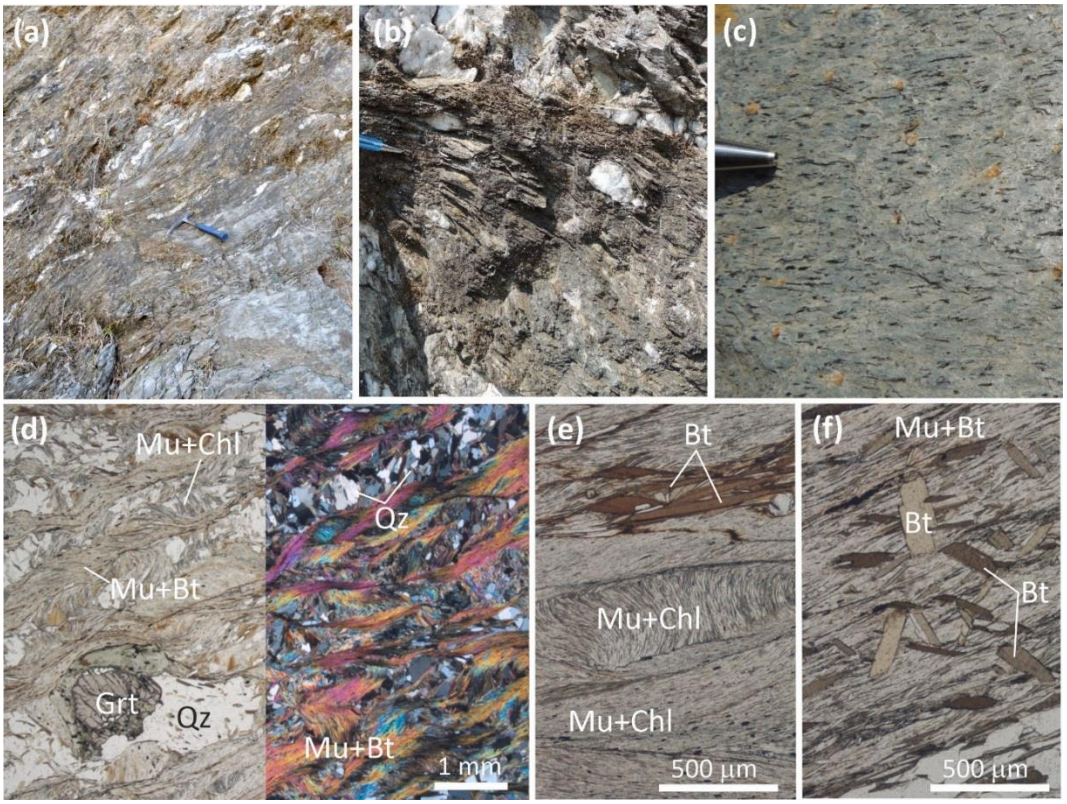

Figure 4.4: Dandagaon Phyllite Formation. (a) and (b) Quartz veins stretched parallel to the main foliation. (c) Mineral lineation defined by biotite in a garnet–bearing phyllite. (d) Pre–kinematic garnet porphyroblast wrapped around by a foliation defined by muscovite + chlorite + biotite (PPL/XPL). (e) The main foliation derives from transposition of an early foliation preserved in the microlithons (PPL). (f) Late biotite flakes statically overgrowing the main foliation (PPL).

4.1.2. Upper–LHS

The Upper–LHS sequence differs from the Lower–LHS for its marked lithological heterogeneity and for the occurrence of carbonate–bearing lithologies, whose abundance is, nevertheless, highly variable along strike. In the central Nepal reference section (Stöcklin 1980), the following formations have been distinguished from the bottom to the top of the sequence: Nourpul, Dhading Dolomite, Benighat Slate, Malekhu Limestone and Robang Phyllite Formations.

4.1.2.1 Nourpul Formation

The Nourpul Formation is a lithologically heterogeneous succession mostly consisting of phyllites, black slates, carbonatic phyllites, calcschists and minor quartzites, alternated in metric to decametric layers. At the outcrop scale, this formation typically appears thickly banded and varied in colour (Fig. 4.5a,b); the heterogeneity at the outcrop scale is the main feature that allows distinguishing this formation from the underlying Dandagaon Phyllite Formation. Protoliths of these lithologies are mostly represented by pelites variably

enriched in carbonaceous material, dolomitic pelites, dolomitic marls and quartzitic sandstones. The abundance of carbonate–bearing protoliths (dolomitic pelites and marls) varies from 1 to 25% of the whole sequence, depending on the considered cross–section. Quartzites are generally concentrated in the lowermost portion of the formation, whereas the amount of carbonatic lithologies increases upward. Thin layers and/or small lenticular bodies (up to few meters in thickness) of amphibolites, possibly derived from original basic dykes (Fig. 4.6c), occasionally occur in this formation.

In the **phyllites**, the main foliation is generally defined by abundant muscovite and minor biotite, more rarely also by chlorite. They typically contain syn– to post–kinematic garnet porphyroblasts, up to several millimetres in size (Fig. 4.5c,d); staurolite porphyroblasts are rarer and they generally overgrow the main foliation (Fig. 4.5e). **Black slates** (Fig. 4.6a) have a very simple assemblage consisting of abundant graphite, quartz, phlogopite and/or muscovite, the last two aligned to define the main foliation (Fig. 4.6d).

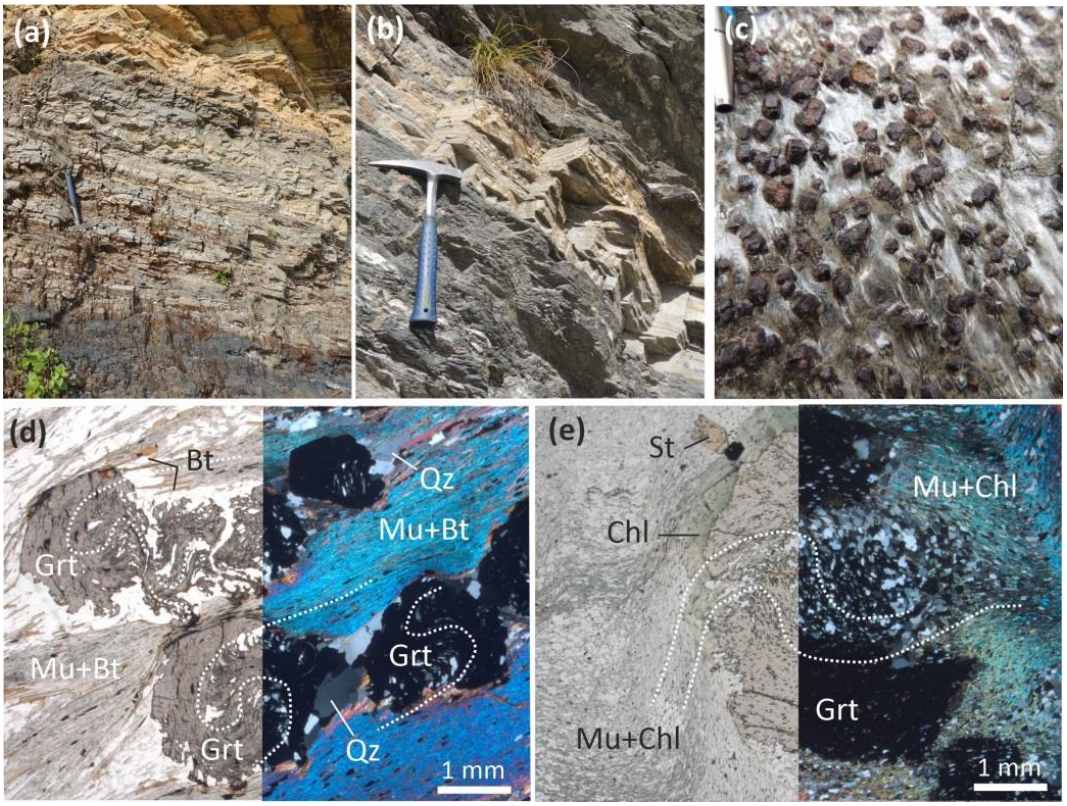

Figure 4.5: Nourpul Formation. (a,b) Banded appearance of the Nourpul Formation, with alternating layers consisting of different lithologies. From bottom to top: (a) graphitic phyllites, calcschists and impure marbles; (b) graphitic phyllites, quartzites and phyllites. (c) Mm–sized garnet porphyroblasts in a phyllite. (d,e) Syn–kinematic garnet porphyroblasts including a rotated internal foliation continuous with the external one, defined by muscovite + biotite (d) or by muscovite + chlorite ± biotite (e). Garnet rims overgrow the main foliation (PPL/XPL).

Calcschists and impure marbles are intimately associated and generally show a banded structure, with alternating layers characterized by different proportions of the silicatic and carbonatic fractions (Fig. 4.6b); the main foliation is defined by phlogopite and/or muscovite (Fig. 4.6e). **Amphibolites** are generally characterized by a relatively simple mineral assemblage, consisting of peciloblastic hornblende, quartz and plagioclase (Fig. 4.6f), and accessory ilmenite and/or titanite. Epidote and garnet only rarely occur within this lithology.

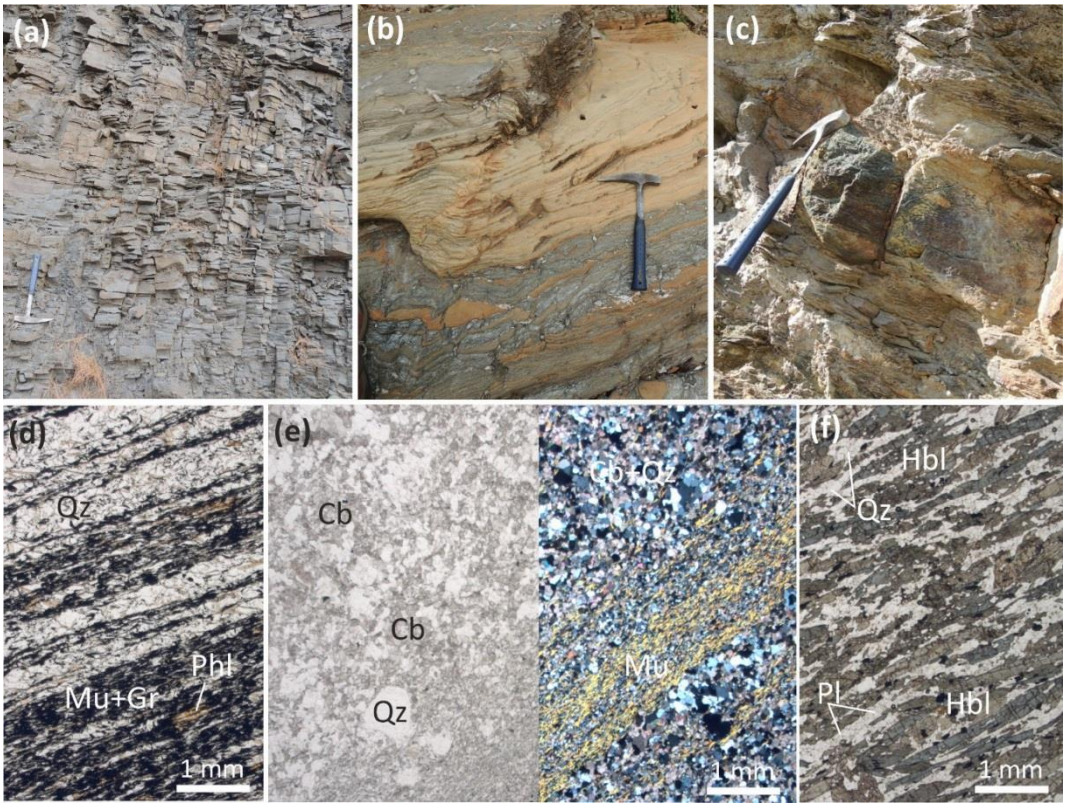

Figure 4.6: Nourpul Formation. (a) Black slates. (b) Banded calcschists. (c) Thin layer of amphibolites within phyllites. (d) Black slate: the foliation is defined by muscovite, graphite and phlogopite (PPL). (e) Calcschist: the foliation is defined by muscovite, concentrated in millimeter–thick layers (PPL/XPL). (f) Amphibolite: the foliation is defined by hornblende (PPL).

4.1.2.2. Dhading Dolomite Formation

The transition from the Nourpul Formation to the overlying Dhading Dolomite Formation is marked by a progressive increase of the carbonatic lithologies counterbalanced by a decrease of the siliciclastic ones. However, the transition is gradual and the distinction between the two formations is not always straightforward. The Dhading Dolomite Formation mostly consists of fine–grained phlogopite ± muscovite–bearing dolomitic marbles with intercalations of calcschists, carbonatic phyllites and minor graphitic schists, respectively, derived from the metamorphic transformation of original dolostones,

dolomitic marls, dolomitic pelites and pelites enriched in carbonceous material. Overall, carbonatic protoliths represent 70–90% of the whole Dhadhing Dolomite Formation.

Despite their metamorphic recrystallization, the light to dark grey **dolomitic marbles** generally preserve a finely laminated structure (Fig. 4.7a), possibly inherited from the dolostone protolith. Remnants of stromatolitic structures are widely reported from several localities in central and western Nepal (Fig. 4.7c). In the dolomitic marbles, the main foliation is defined by the preferred orientation of phlogopite and/or minor muscovite (Fig. 4.7d). Sulfide–rich layers are locally present (Fig. 4.7b,e), as well as radial aggregates of acicular tremolite developed at the expense of coarse–grained phlogopite.

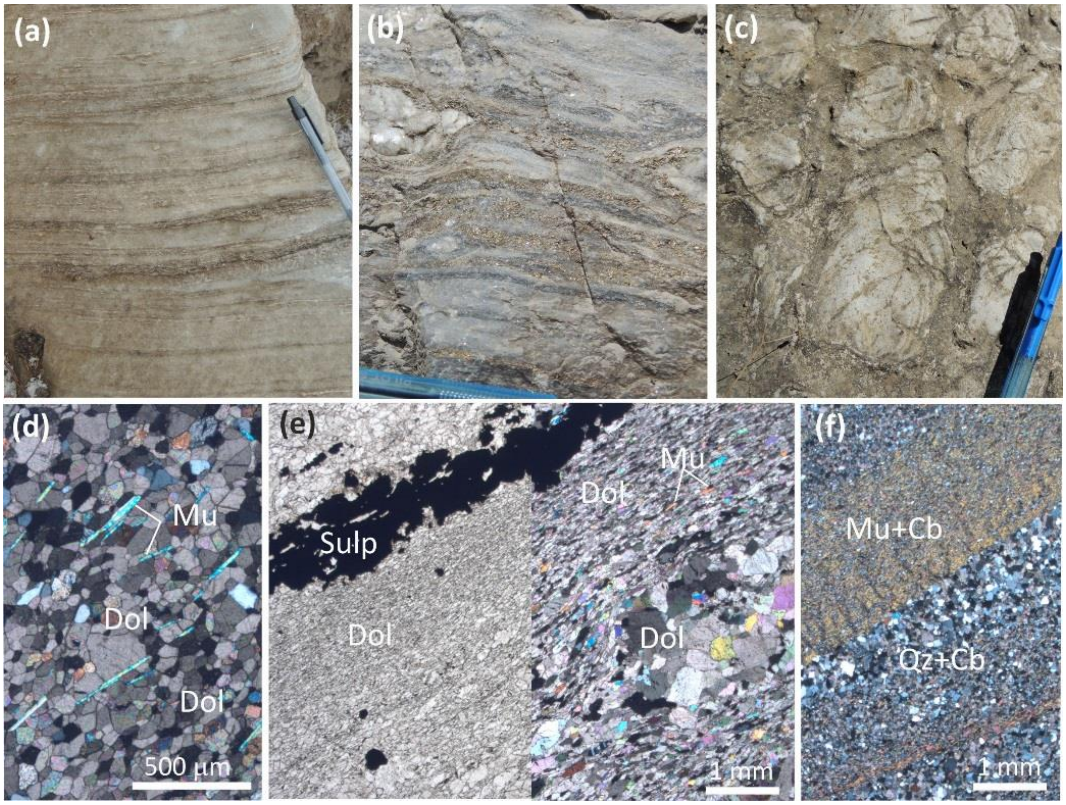

Figure 4.7. Dhading Dolomite Formation. (a–b) Laminated structure (a) and sulphide–rich layers (b) in dolomitic marbles. (c) Preserved stromatolitic structure (Humla section, western Nepal; Fig. 2.2). (d) Microstructure of a dolomitic marble, with a discontinuous foliation defined by muscovite (XPL). (e) Dolomitic marble with sulfide–rich layers (PPL/XPL). (f) Microstructure of a calcschist (XPL).

The mineral assemblage in the **calcschists** is similar to that of the marbles, but with a more abundant silicatic fraction; the main foliation is defined either by light orange phlogopite or by greenish biotite associated with minor muscovite (Fig. 4.7f). **Graphitic schists** are dominated by graphite and quartz, with phlogopite defining the main foliation.

Massive **magnesite + talc ores** occur as lenses and layers, from a few meters to tens of meters thick, associated with the dolomitic marbles and/or the graphitic schists (Fig. 4.8a). The largest magnesite + talc deposit is exposed in the Kharidhunga area of central Nepal

(Fig. 4.1) and has been exploited for many years. Magnesite occurs as coarse–grained centimetric crystals, locally with a columnar habit (Fig. 4.8d) or forming radial, rosette–type aggregates. Coarse–grained magnesite is partially replaced by finer–grained magnesite, talc and minor Mg–chlorite (Fig. 4.8e,f). Talc veins, from a few mm to a few cm thick (Fig. 4.8c) locally form a pervasive network (Fig. 4.8b). The origin of these sparry magnesite deposits has been attributed to the syn–sedimentary diagenetic replacement of dolomite by magnesite in an evaporitic environment developed behind biohermal barriers which inhibited water circulation (Valdiya, 1995; Joshi & Sharma, 2015). Talc and Mg–chlorite replaced magnesite through metamorphic hydration reactions.

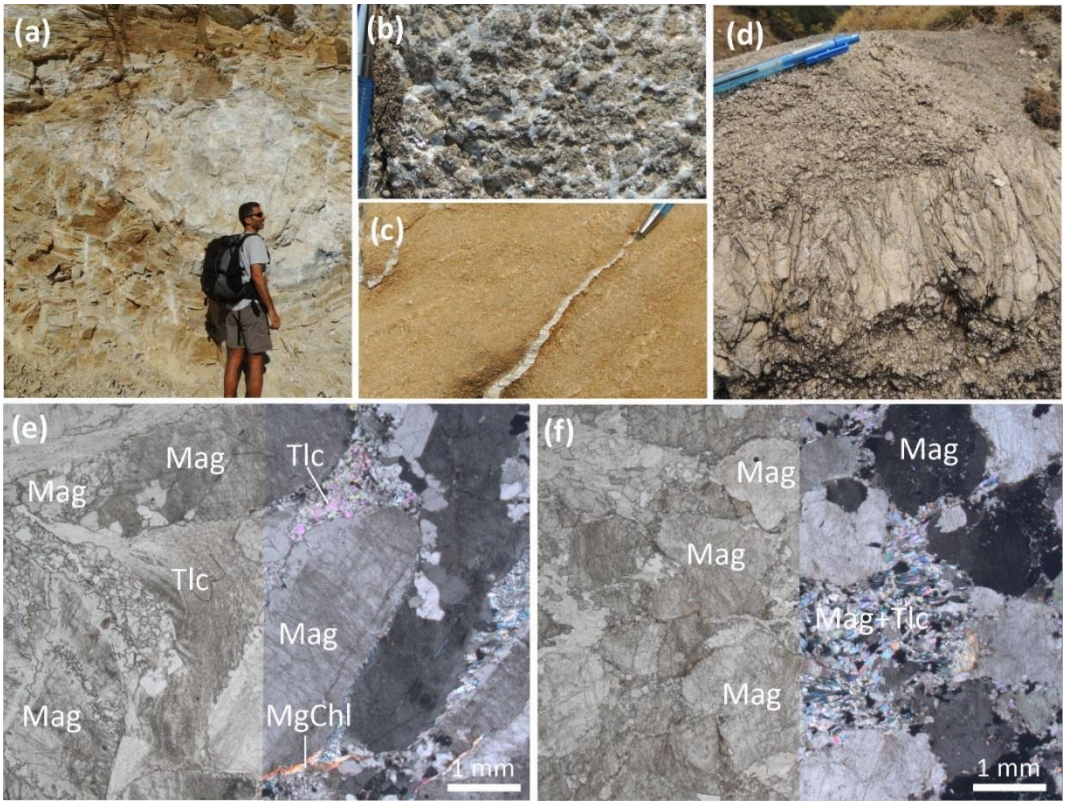

Figure 4.8: Dhading Dolomite Formation. (a) Magnesite + talc lens (white) embedded within dolomitic marbles (yellowish). (b) and (c) Talc veins forming a pervasive inter–granular network (b) or cross–cutting the magnesite rock (c). (d) Coarse–grained magnesite with a columnar habit. (e) and (f) Microstructure of the sparry magnesite deposits, with talc and minor Mg–chlorite replacing magnesite through a pervasive network of veins (PPL/XPL).

4.1.2.3 Benighat Slate Formation

The Benighat Slate Formation is the thickest formation of the Upper–LHS, ranging in thickness from 500 m to more than 3000 m. It is lithologically heterogeneous and dominated by dark phyllites, with frequent intercalations of graphitic schists (Fig. 4.9a,b) and calcic metapelites, and minor carbonatic lithologies (calcschists and impure marbles)

and quartzites (Fig. 4.10a–c). Protoliths of these lithologies are mostly represented by pelites enriched in carbonaceous material, dolomitic pelites and dolomitic marls, with minor dolostone and limestones. The abundance of carbonate–bearing protoliths in this formation varies between 15% and 35% of the whole sequence, depending on the considered cross–section.

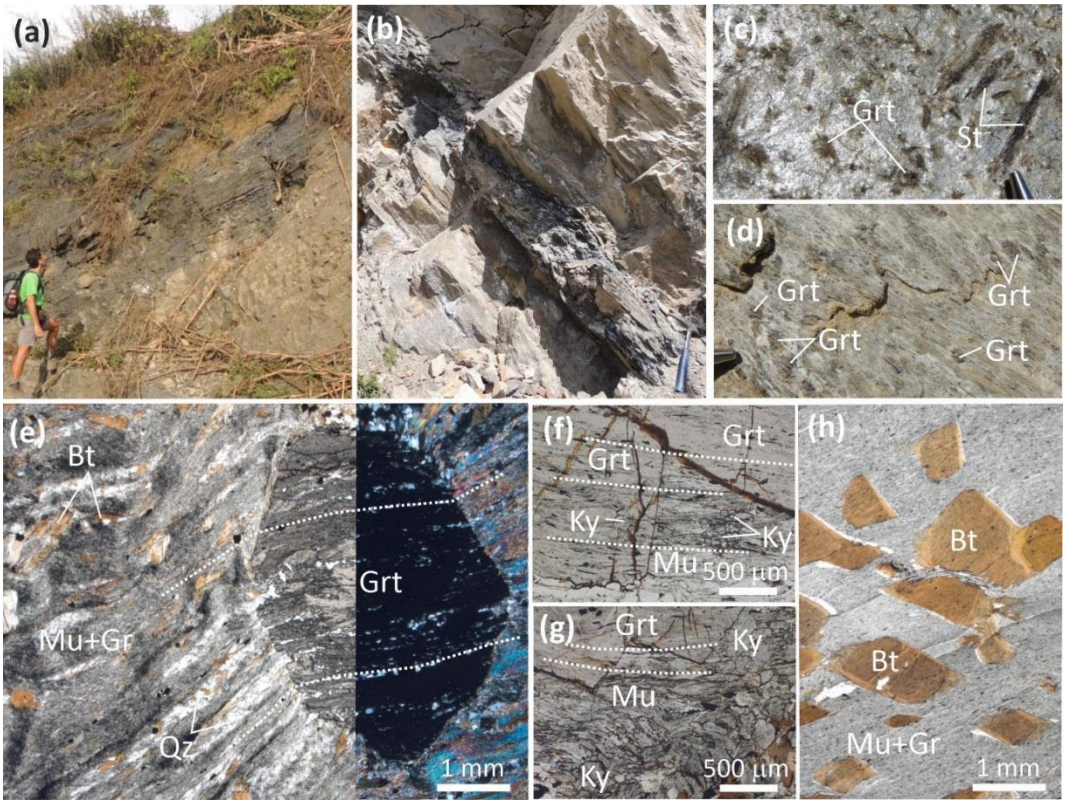

Figure 4.9: Benighat Slate Formation. (a) and (b) Graphitic schists (dark grey) within phyllites. (c) and (d) Pluri–mm garnet and staurolite porphyroblasts overgrowing the main foliation. (e) Post–kinematic garnet porphyroblast (PPL/XPL). (f) and (g) Details of garnet rim and kyanite overgrowing the main foliation (dotted lines) (PPL). (h) Post–kinematic biotite porphyroblasts in a graphitic phyllite (PPL).

The most common lithology is represented by two–micas, graphitic phyllites with porphyroblasts of aluminous minerals (garnet, staurolite and/or kyanite) (Fig. 4.9c,d). Garnet porphyroblasts are typically syn– to post–kinematic, and can reach several millimeters in size (Fig. 4.9e); they locally show large rim domains statically overgrowing the main foliation (Fig. 4.9f,g), sometimes already evident at the outcrop scale (Fig. 4.9d). Staurolite and kyanite are generally post–kinematic (Fig. 4.9f,g) and can be up to few centimeters long. Large porphyroblasts of biotite locally overgrow the main foliation (Fig. 4.9h).

Dark **graphitic schists** locally containing up to 30–40% of graphite form meter–thick layers embedded within the phyllites (Fig. 4.9a,b); they are generally characterized by a relatively simple assemblage (quartz + muscovite ± phlogopite), but sometimes also include

aluminous minerals (kyanite, staurolite and garnet; Fig. 4.10d). **Calcic metapelites** are one of the most peculiar lithologies in the Benighat Slate (Fig. 4.10a,b); these are mostly two–micas graphitic phyllites characterized by the systematic occurrence of Ca–bearing minerals (plagioclase and/or epidote) (Fig. 4.10e) and/or of carbonate relics (dolomite calcite) (Fig. 4.01f) (see also Groppo et al., 2021). Although not common, garnet, kyanite and/or staurolite porphyroblasts can also occur.

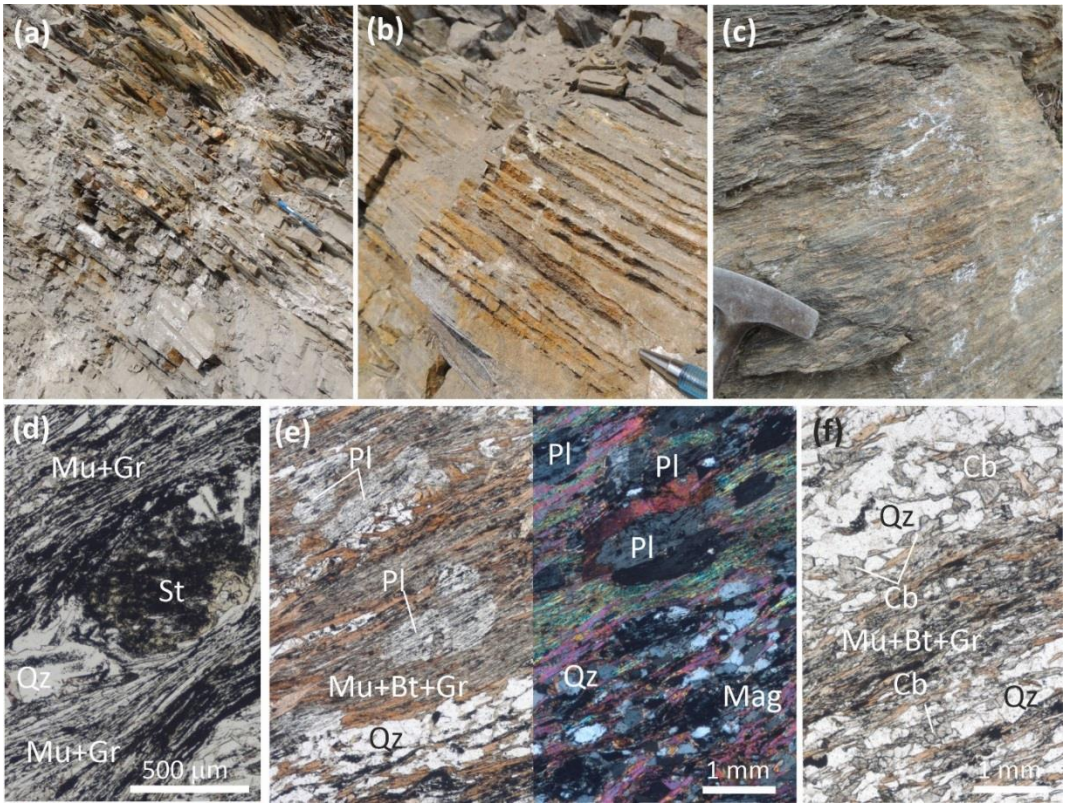

Figure 4.10: Benighat Slate Formation. (a)–(c) Outcrop appearance of calcic metapelites (a) and (b) and calcschists (c) intercalated with phyllites. (d) Staurolite porphyroblast in a graphitic schist (PPL). (e) Plagioclase porphyroblasts overgrowing the main foliation in a calcic metapelite (PPL/XPL). (f) Carbonate–bearing domains in a calcic metapelite (PPL).

Calcschists are less common than calcic metapelites, but easier to recognize in the field, due to their higher abundance of carbonates (Fig. 4.10c). They generally show a banded structure, with silicatic layers rich in quartz and micas alternated with carbonatic layers. The main foliation is defined by biotite/phlogopite ± muscovite; locally, amphibole porphyroblasts overgrow the main foliation. Thin layers of **impure dolomitic marbles** are rare and include both muscovite–bearing and phlogopite + tremolite–bearing varieties.

4.1.2.4 Malehu Limestone and Robang Phyllites Formations

The Malekhu Limestone and the Robang Phyllite Formations are the uppermost formations of the Upper–LHS sequence. They have been described in the central Nepal reference

section by Stöcklin (1980) (section S80 in Fig. 2.2), where the outer (southern) domain of the LHS is exposed. Our observations along numerous cross–sections in the LHS inner (northern) domain of central Nepal did not allow us to unambiguously recognize these two formations, which are therefore described following Stöcklin (1980) and Upreti (1999).

The Malekhu Limestone Formation is mainly composed of impure marbles mostly derived from a limestone protolith. The marbles appear foliated especially in their lower and upper parts, with the foliation defined by muscovite ± chlorite. According to Stöcklin (1980), this formation is distinctly different from the Dhadhing Dolomite Formation exposed at lower lithostratigraphic levels, and it can reach several hundred meters of thickness. We have observed thin layers of marbles, less than 100 m thick, in a similar lithostratigraphic position along few cross–sections in central Nepal, which could be correlated to this formation, but for the reasons discussed above, they are undifferentiated in Fig. 4.1.

The Robang Phyllite Formation is dominated by chlorite–rich phyllites, with abundant intercalations of quartzites and amphibolites, the latter being probably derived from basic dykes and/or tuff layers.

4.1.3 Meta–igneous rocks

4.1.3.1 Ulleri–type Formation

Peculiar augen orthogneisses, variably referred as Ulleri, Melung, Salleri, Phaplu or Num Formations from the names of the localities where they crop out (Le Fort and Rai 1999; Larson et al. 2019, and references therein), are extensively exposed within the LHS. In the literature, these gneisses are commonly associated with the phyllites of the Kuncha Formation; however, they occur variably at different structural levels, both within the Lower–LHS and the Upper–LHS sequences (Stöcklin, 1980 and our own data), where they form stratiform horizons of variable thickness. It is worth noting that these augen gneisses do not occur along the reference section of Stöcklin (1980). They are mylonitic two–micas augen gneisses, with K–feldspar porphyroclasts up to few centimeters in size (Fig. 4.11a–c), characterized by a pervasive stretching lineation and often showing a marked L–tectonite structure. The main foliation is defined by muscovite and biotite (Fig. 4.11c); in the strongly mylonitic varieties, both micas form coarse–grained mica–fish, wrapped around by the fine–grained schistosity. Zoned greenish tourmaline and small cloudy allanitic epidotes are typical accessory minerals.

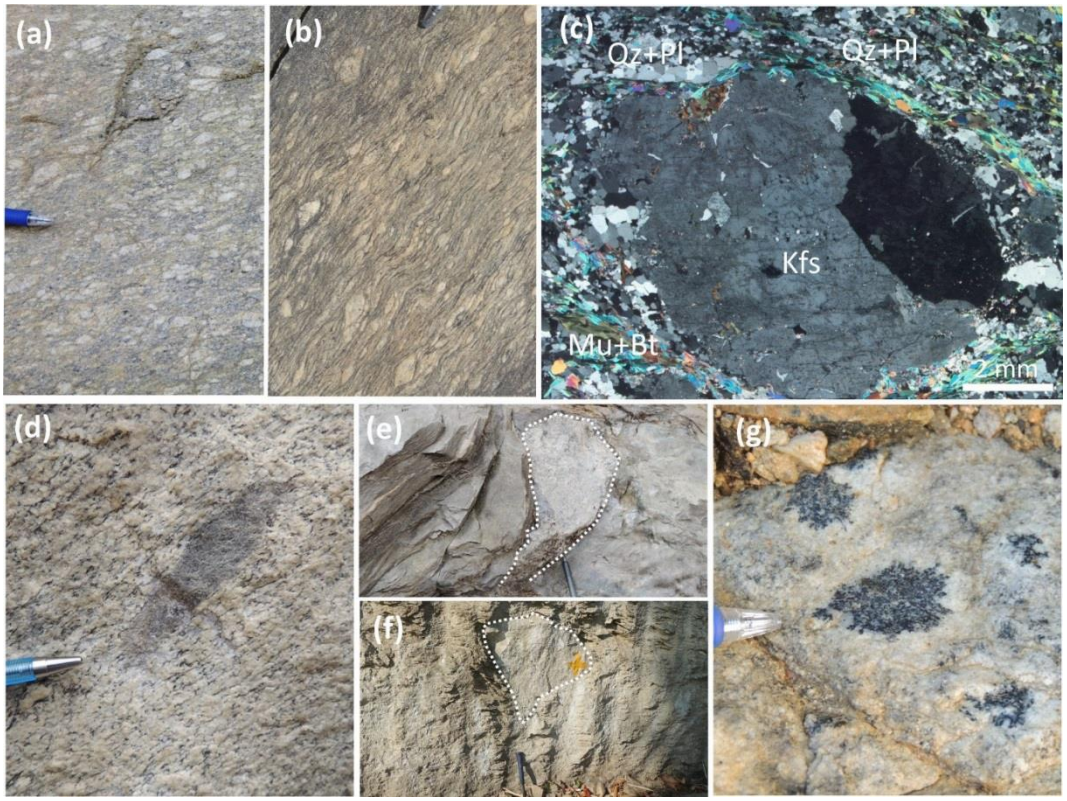

Figure 4.12: Ulleri–type Formation. (a,b) The structure varies from gneissic (a) to mylonitic (b) depending on the intensity of the deformation. (c) Centimeter–sized K–feldspar porphyroclast enveloped by the main foliation defined by muscovite and biotite (XPL). (d–g) Evidence supporting the intrusive nature of the augen gneisses: melanolite (d), granitic pods in the phyllites, close to the contact with the orthogneiss(e) and (f), and tourmaline nodules in a poorly deformed metagranite domain (g). (f) and (g) are from the Tamur and Arun sections in eastern Nepal (Fig. 2.2).

The Ulleri–type augen gneisses have been either interpreted as derived from igneous protoliths formed in a continental rift setting (e.g. Sakai et al., 2013; Larson et al., 2019) or as the metamorphic product of an arc–related volcano–sedimentary sequence (Le Fort & Rai, 1999; Kohn et al., 2010). Despite these different genetic interpretations, the results of different geochronological studies converge towards a Paleo–Proterozoic age for these gneisses, with most ages grouped in two clusters centred at approximately 1900 Ma (1880–1940 Ma; Kohn et al., 2010; Larson et al., 2016, 2019) and 1800 Ma (1780–1840 Ma; Kohn et al., 2010; Larson et al., 2017). Our observations in central and eastern Nepal strongly support an intrusive origin for these gneisses, in agreement with the interpretation of Sakai et al. (2013) and Larson et al. (2019). Petrographic evidences in favour of this interpretation are: (i) the common occurrence of small melanoliths within the (ortho)gneiss (Fig. 4.11d); (ii) the local occurrence of undeformed granitic pods within the hosting phyllites, in proximity of the contact between the orthogneiss and the country rocks (Fig. 4.11e); (iii) the rare occurrence of poorly deformed domains, still preserving the hypidiomorphic sequential structure of the granitic protolith and containing centimeter–sized tourmaline

nodules surrounded by a leucocratic halo (Fig. 4.11g). Similar tourmaline nodules in different geological contexts have been explained as the result of several processes (i.e. hydrothermal, magmatic–hydrothermal, magmatic: Perugini and Poli 2007, and references therein), all of them invariably related to an igneous environment.

4.1.3.2 Suri Dobhan orthogneiss and Taplejung metagranite

Minor bodies of granitic orthogneisses exposed in the core of the Chautara–Okhaldhunga (Tama Khosi valley) and Tamur antiformal tectonic windows (central and eastern Nepal; Fig. 2.2) are generally considered separately from the Ulleri–type Formation, and they are known as Suri Dobhan orthogneiss (e.g. Larson, 2012; Dithal, 2015) and Taplejung metagranites (e.g. Sakai et al., 2013), respectively. These orthogneisses bodies are embedded within the lowermost structural levels of the LHS (i.e. in the Lower–LHS; Fig. 4.1); in their central part, these rocks are relatively poorly deformed, but a strong mylonitic structure develops at contact with the adjacent phyllites. Their mineral assemblage is similar to that of the Ulleri–type orthogneiss. The igneous nature of these orthogneisses is testified by the locally preserved intrusive contacts at the outcrop scale, characterized by the occurrence of a network of aplitic dykes intruding the hosting phyllites, now transposed parallel to the main foliation.

4.2 Reconstruction of depositional environments

In spite of the significant metamorphic overprint (see Chapter 2), the original stratigraphic relationships among the different protoliths are mostly preserved, allowing a broad reconstruction of the pristine depositional environment for most of the LHS lithologies. The following depositional history proposed by Valdiya (1995) and Sakai et al. (2013) is substantially confirmed by our own data (Fig. 4.13):

- In the Lower–LHS, the lowermost Kuncha Formation represents a turbiditic sequence likely deposited by strong currents in a rapid subsiding basin in an extensional tectonic setting (i.e. continental rift setting). The Ulleri–type granitic rocks intruded in this sequence could represent the expression of acid magmatism related to the rifting stage.
- The overlying Dandagaon Phyllite Formation, characterized by minor supplies of clastic sediments with respect to the Kuncha Formation, could represent a tidal flat complex, whereas the Fagfog Quartzite Formation was probably deposited on a very shallow platform in the supratidal zone, in a coastal plain or fluvial environment.
- The Upper–LHS formations reflect the final stages of rifting and the progressive subsidence of the passive continental margin. The heterogeneous Nourpul Formation is often characterized by thick granitic intrusions and minor mafic horizons likely derived from original basic dykes, which could reflect a syn–sedimentary magmatism associated to the last stage of rifting.

- The overlying Dadhing Dolomite Formation is dominated by carbonatic lithologies, deposited on a very shallow carbonate platform. The occurrence of magnesite deposits associated to this formation has been interpreted as related to the local occurrence of evaporitic conditions, developed in basins closed by biohermal barriers which inhibited the water circulation.
- The thick Benighat Slate Formation is a thick argillo–calcareous sequence (pelites, dolomitic pelites, marls, and minor dolostones and limestones) locally dominated by euxinic facies and testifies the deepening of the depositional basin due to the progressive subsidence of the passive continental margin.

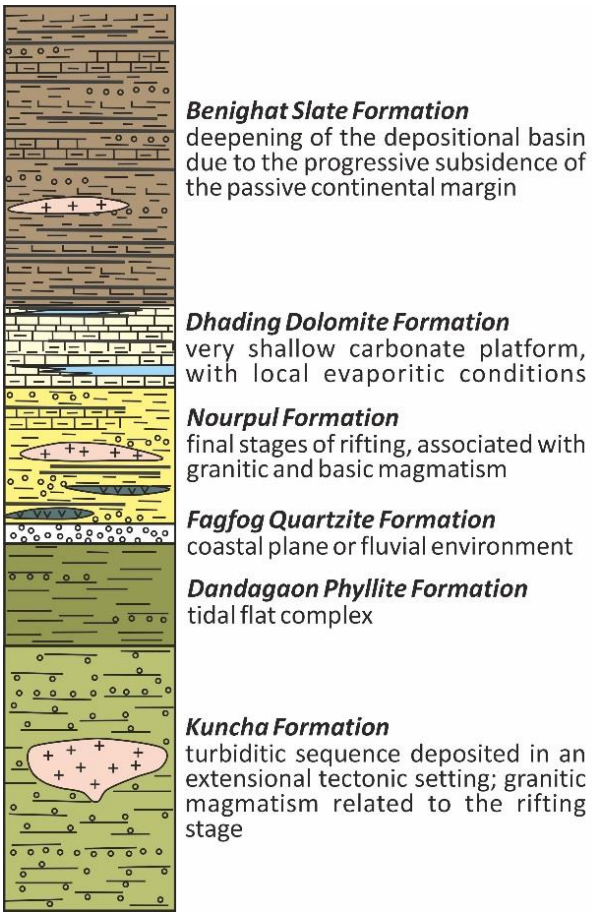

Fig. 4.13: Summary of the depositional environments reconstructed for the Lower–LHS and Upper–LHS sequences, based on the lithostratigraphic features observed in central–eastern Nepal. Symbols and colors as in Fig. 4.1.

Chapter 5

Implications of garnet nucleation overstepping for the P–T evolution of the Lesser Himalayan Sequence of central Nepal

5.1 Introduction and aims

5.1.1 Premise

This chapter presents the results of a detailed petrographic and petrologic investigation on six metapelite samples collected from different structural levels of the Upper–LHS. Initially, the primary purpose of this study was to constrain the P–T evolution of the Upper–LHS unit, which is preliminary to the investigation of the CO_2–producing processes in the associated carbonate–bearing lithologies (see Chapter 6). However, because the results of thermodynamic modelling suggested that the studied samples have experienced different degrees of overstepping of garnet nucleation, the focus of the study was also addressed on testing the influence of kinetics factors on garnet nucleation processes. This allowed us to make the study more interesting to a global audience (i.e. not strictly related to the community of Himalayan geologists). Data and results presented in this chapter have been published in: ***Tamang et al. Implications of garnet nucleation overstepping for the P–T evolution of the Lesser Himalayan Sequence of central Nepal. Journal of Metamorphic Geology, accepted***. This paper is substantially reproduced here, except for the Geological setting and the Methods sections, which are presented in detail in Chapter 2 and Chapter 3 (sections 3.3, 3.4 and 3.6.1).

5.1.2 Introduction

Barrovian–type metamorphic sequences are widespread in both ancient and modern collisional orogenic belts, being the result of crustal thickening induced by continent collision. The forward thermodynamic modelling approach, based on the principles of equilibrium thermodynamics, is currently routinely applied to constrain their P–T evolution, which is crucial for our understanding of the mountain–building processes. Aluminous metapelites from Barrovian garnet– and staurolite– zones are particularly suitable for this aim because they generally develop specific assemblages as a function of P–T conditions; moreover, application of isopleth thermobarometry to garnet–bearing aluminous metapelites is a powerful method for tightly constraining their P–T evolution, due to the relatively common preservation of prograde growth zoning within garnet porphyroblasts (e.g. Tinkham & Ghent, 2005). The reliability of thermobarometric methods based on equilibrium thermodynamics has been recently questioned by a number of

studies that demonstrate that garnet nucleation can be significantly influenced by kinetic factors, resulting in a delay of garnet appearance with respect to the equilibrium predictions. Initially discussed as a relevant process in contact metamorphic settings (e.g. Waters & Lovegrove, 2002; Pattison & Tinkham, 2009), the overstepping of garnet nucleation is being more and more frequently reported also in regional metamorphic terranes, including Barrovian metamorphic settings (e.g. Pattison et al., 2011; Spear et al., 2014; Carlson et al., 2015; Spear & Wolfe, 2019). Studies specifically focused on understanding the relative importance of equilibrium vs. kinetic–controlled garnet nucleation in Barrovian metamorphic terranes, show that the apparent degree of overstepping of garnet nucleation can be extremely variable, ranging from minimal (<10 °C and 0.5 kbar; e.g. Gaidies et al., 2008, 2015; Moynihan & Pattison, 2013; George & Gaidies, 2017; Gaidies & George, 2021), to moderate (<30 °C and 1 kbar; e.g. Spear et al., 2014) or pronounced (>30 °C and 2 kbar; e.g. Spear et al., 2014; Spear & Wolfe, 2019). The factors controlling such highly variable degrees of overstepping of garnet nucleation are still unclear (Nagurney et al., 2021).

This study focuses on garnet nucleation and growth in aluminous metapelites from central Nepal's Upper–LHS of the Ganesh Himal region. The LHS experienced Barrovian metamorphism during the Himalayan orogenic cycle, developing an inverted metamorphic gradient ranging from the chlorite to the biotite, garnet, staurolite and kyanite zones (e.g. Pêcher, 1989; Kohn, 2014; Goscombe et al., 2018; Waters et al., 2019). We focus our attention on the uppermost structural levels of the LHS (Upper–LHS), where studies have shown that peak metamorphic temperatures up to 630–650 °C have been reached, consistent with the sporadic occurrence of staurolite and/or kyanite–bearing lithologies (e.g. Macfarlane, 1995; Rai et al., 1998; Catlos et al., 2001; Khanal et al., 2020; Kohn et al., 2001; Goscombe et al., 2006, 2018; Kohn, 2008; Groppo et al., 2009; Martin et al., 2010; Imayama et al., 2010; Corrie & Kohn, 2011; Mosca et al., 2012; Rolfo et al., 2015; Rapa et al., 2016, 2018). Our aims are threefold: (i) to test the reliability of thermobarometric methods based on equilibrium thermodynamics applied on aluminous metapelites from the same metamorphic domain; (ii) to understand to what extent garnet nucleation in aluminous metapelites can be influenced by kinetic factors, and explore whether the difference in bulk rock composition might control the different degrees of apparent overstepping; and (iii) to constrain the P–T metamorphic evolution of the Upper–LHS in this key area and discuss the results in the framework of the existing thermo–mechanical models used to explain the inverted metamorphism in the LHS.

5.2 Petrography and mineral chemistry results

The studied samples, for which an overview at the thin section scale is provided in Fig. 5.1, can be classified as Al–rich metapelites, plotting above the garnet–chlorite tie line in the AFM diagram (Fig. 5.2e), with Mg/(Mg+Fe) values in the range 0.27–0.53. Three compositional groups have been identified, based on their bulk compositions: (1) samples

with A ≥ 50 in both the AFM and ACF diagrams projected from muscovite (A = $Al_2O_3 – 3K_2O$); (2) samples with A < 50 and very low MnO and CaO contents (MnO < 0.05 mol%; CaO < 1.0 mol%); (3) samples with A < 50 and higher amounts of MnO and CaO (MnO > 0.05 mol%; CaO > 1.0 mol%). Group 1 includes samples 17a–34 and 17a–33, which are almost devoid of CaO, and differ in the MnO content (null for 17a–34 and relatively high for 17a–33). Group 2 includes samples 17a–22 and 15a–15b, and Group 3 includes samples 15a–28b and 17a–42. Mineral chemical results for all the samples are summarized in Fig. 5.2, and representative microstructures are presented in Fig. 5.3 and Fig. 5.4.

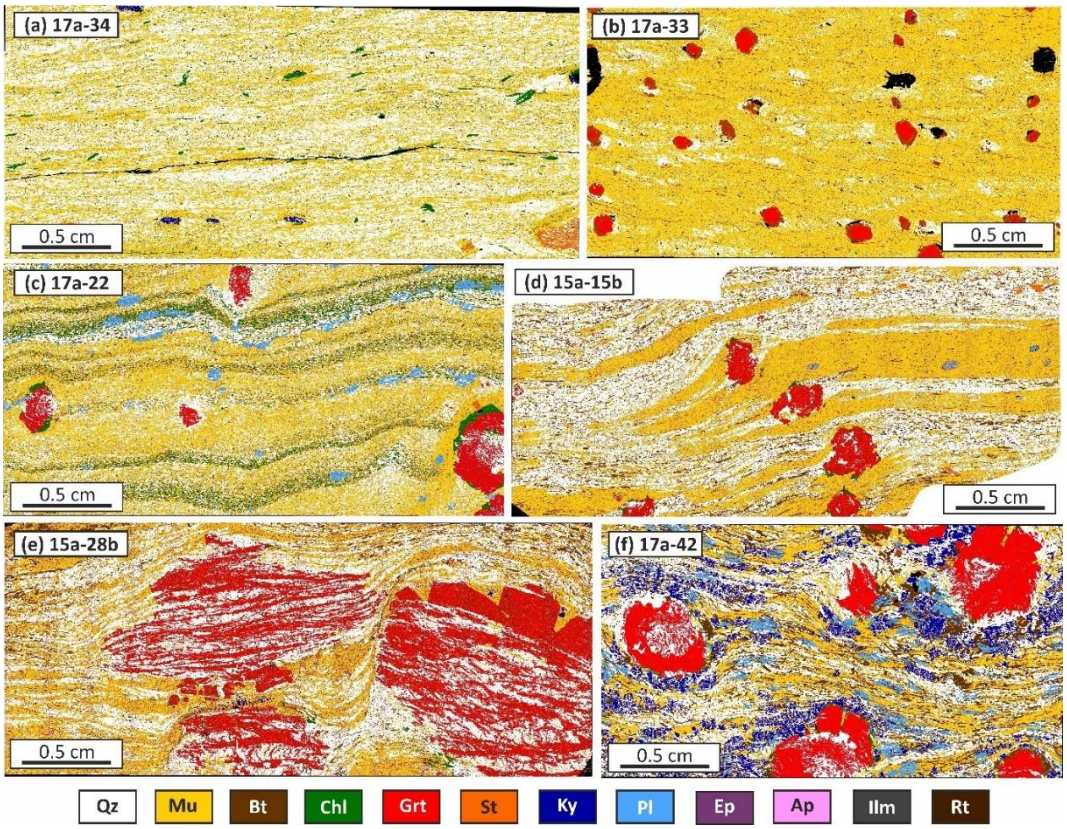

Fig. 5.1: Processed X–Ray maps of the studied samples: (a) 17a–34; (b) 17a–33; (c) 17a–22; (d) 15a–15b; (e) 15a–28b; and (f) 17a–42.

Most of the studied samples are garnet–bearing, two–micas ± chlorite phyllites; however, most Al–rich samples (Group 1: 17a–34 and 17a–33) are almost devoid of biotite. Besides phyllosilicates, all the studied samples contain one or more of the following aluminous minerals: garnet, staurolite and/or kyanite, showing variable microstructural relationships with the main foliation. Mineral assemblages and modes are summarized in Table 5.1 (see Chapter 3, section 3.3) for details on the method used for the modal estimates). Blastesis–deformation relations for all the samples are reported in Fig. 5.5. In most samples, the peak assemblage consists of minerals (including garnet rim) statically overgrowing the main foliation (S_m); the development of the S_m has been therefore ascribed to the prograde

metamorphic stages. Early prograde and late prograde assemblages comprise those minerals that are in equilibrium with the garnet core and mantle, respectively. Sample 17a–34 differs from the others for the lack of garnet and post–S_m minerals; the distinction between the late prograde and the peak assemblages is thus more uncertain.

Table 5.1 - Assemblages and modal compositions (vol%) of the modelled metapelites

Sample	Qz	Mu	Bt	Chl	GrtC+M	GrtR	St	Ky	Pl	Ilm	Rt
17a-34	54.8	36.8	-	4.5	-	-	2.3	1.6	-	-	<0.1
17a-33	13.0	80.4	4.0	0.0	1.0	0.7	0.0	0.0	0.0	0.9	0.0
17a-22	30.2	47.0	2.3	9.3	1.4	3.4	1.1	-	4.8	0.5	-
15a-15b	38.2	42.1	8.9	1.3	2.0	3.2	2.5	-	1.3	0.5	-
15a-28b	40.1	23.9	6.2	2.7	18.3	3.2	2.1	3.4	-	<0.1	-
17a-42	35.0	20.3	13.9	0.0	4.7	11.0	0.0	8.2	6.5	0.1	0.3

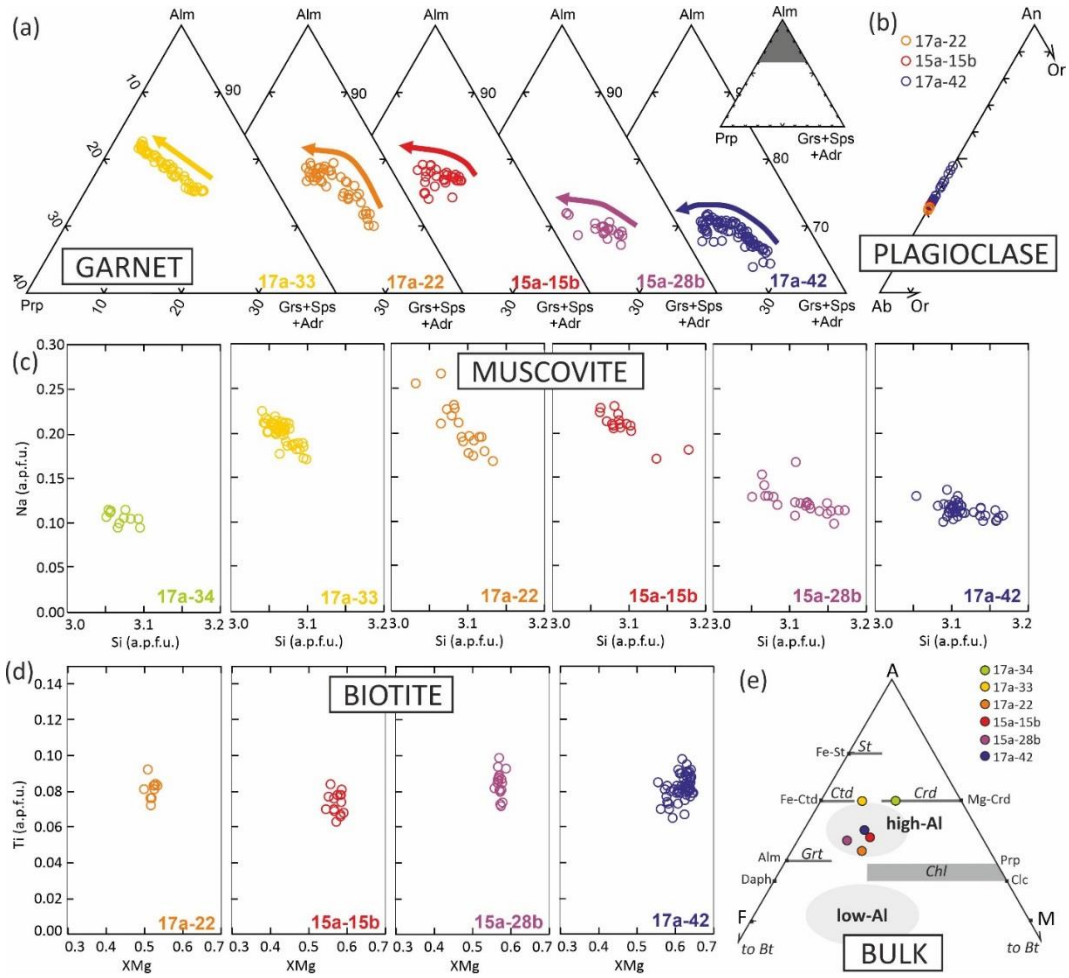

Fig. 5.2: Compositional diagrams for garnet (a; arrows show the zoning trend from garnet core to garnet rim), plagioclase (b), muscovite (c) and biotite (d), and bulk compositions of the studied samples (e) plotted in the AFM diagram projected from muscovite (quartz and H_2O in excess). The low–Al and high–Al metapelite fields in (e) are from Spear (1993).

5.2.1 Sample 17a–34

This kyanite + staurolite –bearing graphitic muscovitic schist consists of quartz (55%), muscovite (37%), chlorite (4%), kyanite (2%) and staurolite (2%), with accessory graphite and rutile. It shows a well–developed foliation (S_m) defined by the preferred orientation of muscovite, which is concentrated in mm–thick continuous layers alternated with discontinuous quartzitic layers of similar thickness. Staurolite and kyanite occur as pluri–mm–sized porphyroblasts wrapped around by the main foliation (i.e. pre–kinematic with respect to S_m) (Fig. 5.1a and 5.3a, b). They both include an internal foliation (S_{m-1}) mostly defined by quartz and graphite, and by minor chlorite and muscovite, discordant with respect to the external S_m (Fig. 5.3a,b). Staurolite is partially replaced at the rim by muscovite, and kyanite is locally overgrown by chlorite (Fig. 5.1a). Late fine–grained muscovite and medium–grained chlorite flakes overgrow statically the main foliation (i.e. they are post–kinematic with respect to the S_m). The composition of the different muscovite generations is relatively homogeneous, with Si=3.05–3.10 a.p.f.u. and Na=0.10–0.12 a.p.f.u. (Fig. 5.2c). Staurolite has XMg ranging from 0.18 to 0.19 and contains limited amounts of both Ti and Zn (Ti=0.14–0.16 a.p.f.u.; Zn=0.10–0.12 a.p.f.u.). Chlorite is homogeneous with XMg=0.58–0.59.

5.2.2 Sample 17a–33

This garnet–bearing graphitic muscovitic schist consists of muscovite (80%), quartz (13%), biotite (4%) and garnet (2%), with rare staurolite and accessory ilmenite and graphite (Fig.5.1b). The sample is characterized by a strong alteration, testified by the occurrence of abundant oxides and kaolinite. The main foliation S_m is defined by the preferred orientation of muscovite and it is crenulated, with the development of a pervasive axial plane schistosity (S_{m+1}) defined by muscovite (Fig. 5.3c). Biotite is rare and mostly occurs as fine–grained flakes statically overgrowing the S_m. The millimetric garnet porphyroblasts are wrapped around by the S_{m+1} and are likely in equilibrium with the S_m; they are almost free of inclusions and are strongly oxidised at the rim and along fractures, where they are replaced by brownish–red Fe–oxides (Fig. 5.3c). The S_m is overgrown by pluri–mm aggregates of fine–grained kaolinite + Fe–oxide, this last concentrated in the centre of the aggregates (Fig. 5.3d). These aggregates likely represent pseudomorphs after a former feldspar (e.g. plagioclase), post–kinematic with respect to the S_m. Staurolite is very rare (it has not been observed in the thin section used for mapping and mineral chemical analysis); it forms mm–sized porphyroblasts overgrowing the S_m, but pre–kinematic with respect to the S_{m+1} (Fig. 5.3d). Among the accessory phases, fine–grained ilmenite is widespread in the matrix, where it is aligned with the S_m.

The composition of muscovite is homogeneous for all generations, with Si=3.05–3.09 a.p.f.u. and Na=0.18–0.23 a.p.f.u. (Fig. 5.2c). Biotite is rare, strongly oxidized and partially replaced by chlorite; chemical analyses obtained on different flakes are therefore not reliable, being anomalously enriched in Fe and depleted in K.

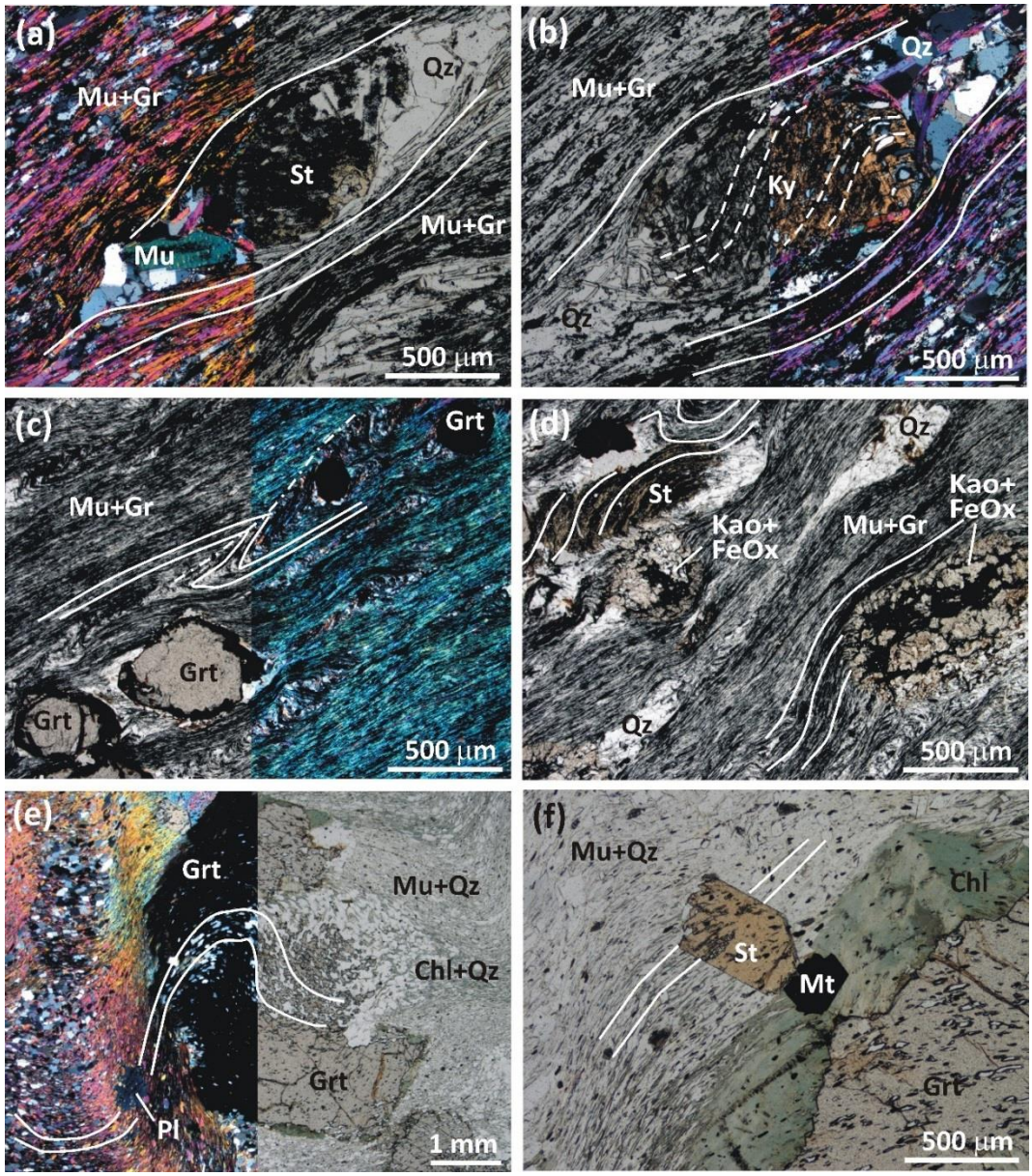

Fig. 5.3: Representative assemblages and microstructures of samples 17a–34, 17a–33 and 17a–22. White lines in all the pictures are: S_m = continuous; S_{m-1} = dashed; S_{m+1} = dotted–dashed. Sample 17a–34: (a) Staurolite porphyroblasts enveloped by the S_m defined by muscovite (XPL/PPL). (b) Kyanite porphyroblast wrapped around by the S_m and includes an internal rotated foliation defined by quartz and muscovite (PPL/XPL). Sample 17a–33: (c) Garnet porphyroblasts in equilibrium with S_m, but pre–kinematic with respect to S_{m+1}. Note the dark brown, oxidized rim of garnet (PPL/XPL). (d) Staurolite occurs as porphyroblasts overgrowing S_m and enveloped by S_{m+1}. Large aggregates of kaolinite+Fe–oxides overgrow the S_m and likely replace former plagioclase (PPL). Sample 17a–22: (e) Multi–mm garnet porphyroblast including a rotated internal foliation continuous with the external S_m (XPL/PPL). (f) Post–kinematic garnet rim is completely replaced by late chlorite. Staurolite porphyroblast overgrows S_m defined by muscovite and chlorite (PPL).

On the contrary, despite the strong oxidation at its rims, garnet preserves prograde zoning, with XMn and XCa decreasing and XMg and XFe increasing towards the rim (Fig.5.2a). The compositions of garnet core and rim are as follows: GrtC: XFe=0.75–0.78,

XCa=0.025–0.035, XMg=0.095–0.13, XMn=0.07–0.12; GrtR: XFe=0.81–0.82, XCa=0.01–0.02, XMg=0.13–0.15, XMn=0.025–0.035. Ilmenite is mostly pure with no geikelite component.

5.2.3 Sample 17a–22

This garnet + staurolite–bearing muscovitic–chloritic schist consists of muscovite (47%), quartz (30%), chlorite (9%), plagioclase (5%), garnet (5%), biotite (2%), staurolite (1%) and accessory epidote, ilmenite and apatite. The main foliation (S_m) is defined by cm–thick phyllosilicate–rich layers alternated with mm–thick discontinuous quartzitic layers (Fig. 5.1c). The S_m is crenulated in gently open folds (Fig. 5.1c and 5.3e), without the development of an axial planar foliation. Muscovite is the dominant phyllosilicate and it is aligned along the S_m; chlorite and minor biotite are mostly concentrated in pluri–millimetric continuous layers, in equilibrium with muscovite. Pluri–mm–sized garnet porphyroblasts are mostly syn–kinematic with respect to the S_m; they include a rotated internal foliation defined by inclusions of quartz, epidote and ilmenite, continuous with respect to the external S_m (Fig. 5.3e). Post–kinematic garnet rims, originally overgrowing the S_m, are completely replaced by a late generation of chlorite (Fig. 5.3f). Plagioclase and staurolite both occur as mm– to pluri–mm–sized porphyroblasts overgrowing the main foliation (post–S_m) (Fig. 5.3f). Among accessory phases, fine–grained epidote and ilmenite are included in garnet and dispersed in the matrix, where they are aligned with the main foliation.

Muscovite is relatively rich in Fe (Fe=0.13–0.16 a.p.f.u.), with Si=3.06–3.12 a.p.f.u. and Na=0.17–0.25 (Fig. 5.2c). Both the biotite defining S_m and the later biotite statically overgrowing S_m has a homogeneous composition with XMg=0.50–0.56 and Ti=0.07–0.09 a.p.f.u. (Fig. 5.2d). Chlorite in the S_m has slightly higher XMg compared to post–S_m chlorite, with XMg=0.51–0.55 and XMg=0.48–0.51, respectively. Garnet shows well–preserved prograde zoning with XMn and XCa decreasing and XMg increasing rimward, while XFe is relatively constant in all the domains (Fig. 5.2a). Garnet core and mantle compositions are as follow: GrtC: XFe=0.70–0.75, XCa=0.14–0.17, XMg=0.06–0.08, XMn=0.015–0.06 and GrtM: XFe=0.77–0.79, XCa=0.12–0.14, XMg=0.10–0.12, XMn=0.00. The composition of the garnet rim is unknown because it is completely replaced by chlorite. XMg of staurolite ranges between 0.17 and 0.19; its Ti content is low (Ti=0.07–0.12 a.p.f.u.), whereas Zn is quite abundant compared to the other samples (Zn=0.68–0.79 a.p.f.u.). Plagioclase is an andesine, with XAn=0.31–0.32 (Fig. 5.2b).

5.2.4 Sample 15a–15b

This two–micas, garnet + staurolite–bearing graphitic schist consists of muscovite (42%), quartz (38%), biotite (9%), garnet (5%), staurolite (2.5%), plagioclase (1%) and chlorite (1%), and accessory epidote, ilmenite, graphite and tourmaline. Its pervasive foliation (S_m) is defined by the preferred orientation of muscovite and minor biotite, concentrated in pluri–

mm continuous layers alternated with quartzitic layers of similar thickness (Fig. 5.1d and 5.4a). Muscovite occurs in two different generations: most of the fine–grained flakes are aligned parallel to the S_m (syn–S_m), but some flakes overgrowing the S_m are also observed (post–S_m). Also, biotite occurs in syn–S_m and post–S_m generations; it is mostly fine–grained, although few medium–grained porphyroblasts with a rotated internal foliation defined by graphite locally occur in the micaceous layers. Garnet porphyroblasts, up to several millimetres in size, are syn– to post–kinematic with respect to the S_m. The cores and mantles of garnet porphyroblasts, in fact, include a rotated internal foliation defined by the alignment of quartz and ilmenite inclusions (Fig. 5.4a), whereas their rims overgrow the S_m (Fig. 5.4b). Staurolite occurs as mm–sized porphyroblasts syn– to post–kinematic with respect to the S_m. They either include an undulated internal foliation defined by quartz (Fig. 5.4c), or overgrow the S_m (Fig. 5.4d). Plagioclase is scarce and forms mm–sized porphyroblasts statically overgrowing the S_m. Chlorite is a late phase, mostly replacing garnet at its rim and rarely forming fine–grained flakes statically overgrowing the S_m (Fig. 5.1d). Epidote, ilmenite and tourmaline are both scattered within the matrix and included in garnet, where they define the internal foliation.

Both muscovite and biotite are quite homogeneous, without significant compositional variations between different generations. Muscovite has Si and Na contents mostly in the range Si=3.06–3.10 a.p.f.u. and Na=0.17–0.23 a.p.f.u. (Fig. 5.2c), and biotite has XMg=0.54–0.59 and Ti=0.06–0.08 a.p.f.u (Fig. 5.2d). Garnet preserves a typical growth zoning, with XMn decreasing and XMg increasing from core to rim; XCa decreases from core to mantle and then increases from the mantle to rim, and XFe shows the opposite behaviour (Fig. 5.2a). Garnet core, mantle and rim compositions are as follows: GrtC: XFe=0.77–0.79, XCa=0.10–0.12, XMg=0.08–0.09, XMn=0.03–0.04; GrtM: XFe=0.78–0.80, XCa=0.10–0.12, XMg=0.11–0.13, XMn=0.010–0.015; GrtR: XFe=0.74–0.76, XCa=0.10–0.12, XMg=0.13–0.14, XMn=0.00. Staurolite has XMg=0.19–0.21 and contains low amounts of Ti (Ti=0.10–0.14 a.p.f.u) and Zn (Zn=0.00–0.15 a.p.f.u.). Chlorite has XMg=0.53–0.54; plagioclase is an andesine (XAn=0.32) (Fig. 5.2b). Ilmenite is almost pure, with very low amounts of geikelite component (<2%).

5.2.5 Sample 15a–28b

This two–micas, garnet + staurolite + kyanite –bearing schist consists of quartz (40%), muscovite (24%), garnet (21%), biotite (6%), chlorite (3%), kyanite (3%) and staurolite (2%), with accessory ilmenite and epidote. The main foliation (S_m) is marked by the preferred orientation of muscovite, biotite and minor chlorite, which define mm–thick continuous layers alternated with discontinuous quartzitic layers, and it is locally crenulated, with the development of open folds. The axial foliation (S_{m+1}) of these crenulation folds is developed just locally and it is mostly defined by muscovite and minor chlorite. The sample grain size is strongly heterogeneous for the presence of large garnet porphyroblasts, up to a few cm in size (Fig. 5.1e). The cores of these garnet porphyroblasts are skeletal (Fig. 5.4e) and overgrow a S_{m-1} foliation, testified by the preserved shape of the microlithons and by the

rare occurrence of muscovite and chlorite included in garnet. Garnet rims are idioblastic and statically overgrow the S_m (i.e. post–S_m) (Fig. 5.4f,g), but they grew earlier than the development of the crenulation. Muscovite in the S_{m-1} is rarely preserved within garnet cores. In the matrix, muscovite occurs in two different generations: most of the fine–grained flakes define the S_m; a later generation statically overgrows the S_m and defines the S_{m+1}. Biotite and chlorite are less abundant than muscovite and mostly aligned with S_m; locally, few biotite flakes overgrowing the S_m also occur, and minor chlorite is aligned along the S_{m+1}. Both staurolite and kyanite form mm–sized porphyroblasts post–kinematic with respect to the main foliation (Fig. 5.4f,g); they occur both as inclusion in the garnet rim and in the matrix, where they statically overgrow the S_m. Epidote is rare and occurs as small idioblasts within the matrix and is included in the garnet core and mantle.
Muscovite is relatively rich in Fe, with Si=3.06–3.17 a.p.f.u. and Na=0.10–0.15; muscovite flakes defining the S_{m-1} have slightly higher Si contents with respect to the flakes defining the S_m, whereas there are no significant compositional variations between the syn–S_m and the post–S_m muscovite generations. Biotite and chlorite defining the S_m are quite homogeneous in composition, with XMg=0.56–0.59 and XMg=0.55–0.58, respectively; chlorite included in garnet (S_{m-1}) is richer in Fe, with XMg=0.47–0.49. Garnet porphyroblasts are characterized by a well–preserved growth zoning, with XMn and XCa decreasing and XMg and XFe increasing rimward (Fig. 5.2a). Garnet core, mantle and rim compositions are as follows, GrtC: XFe=0.68–0.70, XCa=0.18–0.19, XMg=0.08–0.11, XMn=0.03–0.04; GrtM: XFe=0.70–0.71, XCa=0.17–0.18, XMg=0.11–0.14, XMn=0.02–0.03; GrtR: XFe=0.71–0.72, XCa=0.14–0.15, XMg=0.13–0.14, XMn=0.00. Staurolite has XMg ranging between 0.17 and 0.20; its Ti content is low (Ti=0.09–0.15 a.p.f.u.) and Zn is below the detection limit.

5.2.6 Sample 17a–42

This two–micas, garnet + kyanite –bearing graphitic schist consists of quartz (35%), muscovite (20%), garnet (16%), biotite (14%), kyanite (8%), plagioclase (6%) and minor chlorite with accessory ilmenite, apatite, epidote and rutile. The well–developed foliation (S_m) is defined by the preferred orientation of muscovite and biotite, which form pluri–mm thick continuous layers alternated with mm–thick, discontinuous quartzitic layers (Fig. 5.1f). Both muscovite and biotite also occur as post–kinematic flakes, statically overgrowing the main foliation. Garnet occurs as pluri–mm porphyroblasts characterized by two distinct growth zones. The cores and mantles of these porphyroblasts include a rotated internal foliation (S_{m-1}) (Fig. 5.4h) mostly defined by quartz, epidote, ilmenite (in the core) and ilmenite + rutile (in the mantle); garnet cores and mantles are interpreted as syn–S_{m-1}. They are surrounded by a thick rim statically overgrowing the main foliation and therefore interpreted as post–S_m (Fig. 5.4h,i); garnet rim includes quartz and rutile and is partially replaced by late chlorite. Pluri–mm–sized kyanite and plagioclase porphyroblasts are both post–kinematic with respect to the S_m, statically overgrowing it (Fig. 5.4i,j). Rutile is widespread in the matrix, where it is partially replaced by ilmenite.

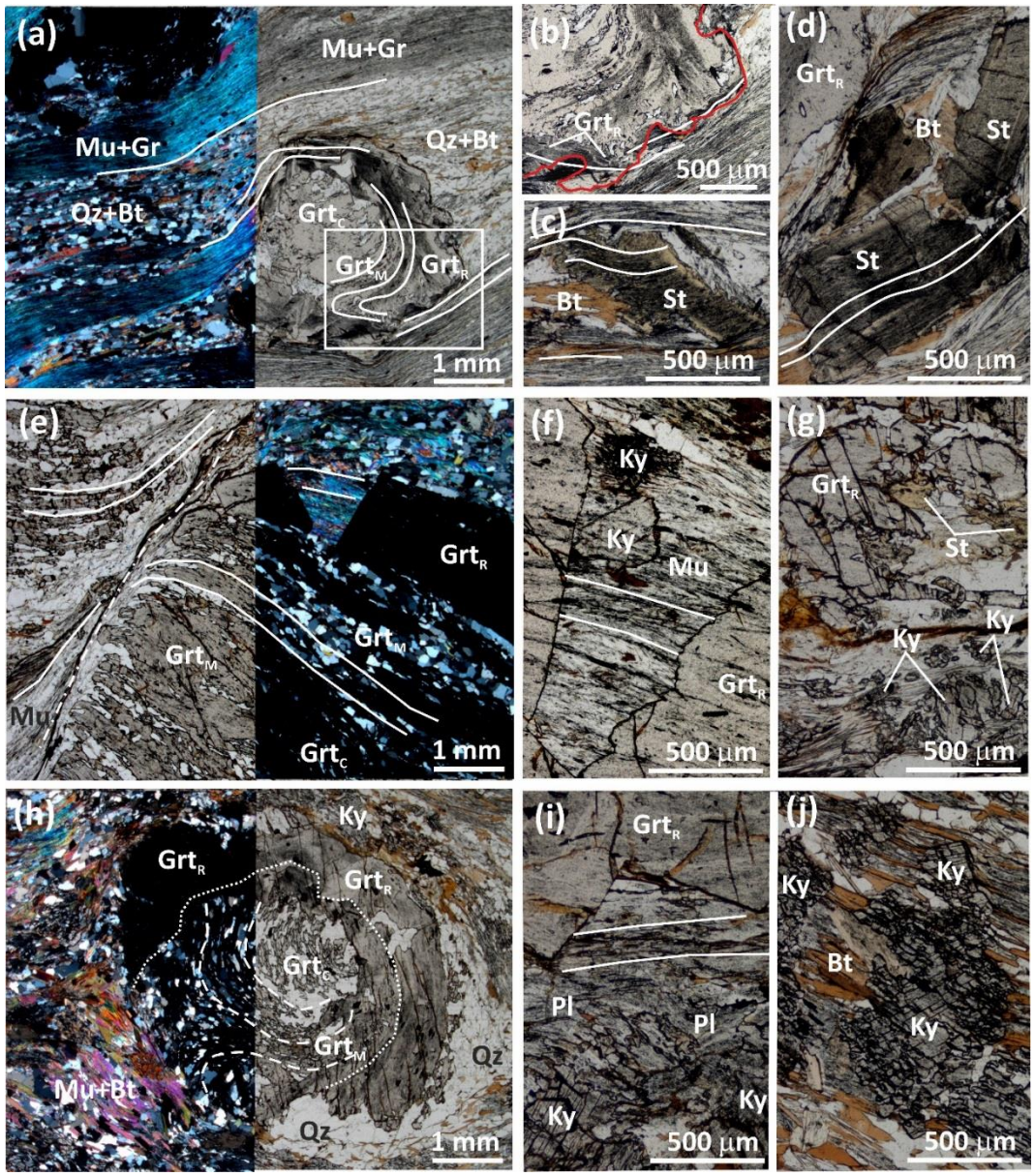

Fig. 5.4: Representative assemblages and microstructures of samples 15a–15b, 15a–28b and 17a–42. White lines are defined as in Fig. 5.3. Sample 15a–15b: (a) Garnet porphyroblasts including a rotated internal foliation continuous with the external S_m. GrtC and GrtM are syn–kinematic with respect to S_m, whereas GrtR statically overgrows it. The inset refers to detail reported in (b) (XPL/PPL). (b) Detail highlighting the post–kinematic relations of GrtR with respect to the S_m (PPL). The red line marks the garnet border. (c) Syn–kinematic staurolite porphyroblasts including an internal foliation defined by graphite, continuous with the external S_m (PPL). (d) Post–kinematic staurolite porphyroblasts statically overgrowing the S_m (PPL). Sample 15a–28b: (e) Centimetric garnet porphyroblast with a skeletal core and a post–kinematic rim overgrowing the S_m (PPL/XPL). (f) Detail of the garnet rim overgrowing the S_m; kyanite porphyroblasts are also post–kinematic (PPL). (g) Post–kinematic staurolite and kyanite developed close to garnet rim (PPL). Sample 17a–42: (h) Garnet porphyroblast characterised by two distinct domains: a pre–kinematic Grt_C + Grt_M, including a rotated internal foliation (S_{m-1}) discontinuous with respect to the external S_m, and a post–kinematic Grt_R, statically overgrowing the S_m (XPL/PPL). (i) Detail of garnet rim, plagioclase and kyanite statically overgrowing the S_m (PPL). (j) Kyanite porphyroblasts overgrow the S_m defined by biotite and muscovite (PPL).

Muscovite and biotite do not show significant compositional variations among different generations (i.e. syn–S_m and post–S_m). Muscovite has Si=3.09–3.16 a.p.f.u. and Na=0.10–0.13 a.p.f.u. (Fig. 5.2c). Biotite is relatively rich in Mg, with XMg=0.56–0.64 and Ti=0.07–0.10 a.p.f.u. (Fig. 5.2d). Garnet porphyroblasts are strongly zoned, with XMn and XCa decreasing and XMg and XFe increasing towards the rim (Fig. 5.2a). The garnet core, mantle and rim compositions are as follows: GrtC: XFe=0.66–0.69, XCa=0.18–0.21, XMg=0.07–0.10, XMn=0.02–0.06; GrtM: XFe=0.69–0.70, XCa=0.18–0.19, XMg=0.11–0.13, XMn=0.015–0.02; GrtR: XFe=0.69–0.71, XCa=0.16–0.18, XMg=0.13–0.15, XMn=0.00. Plagioclase is slightly zoned, with the X_{An} values increasing toward the rim from XAn=0.34 to XAn=0.47 (Fig. 5.2b). Ilmenite is almost pure with no geikelite component.

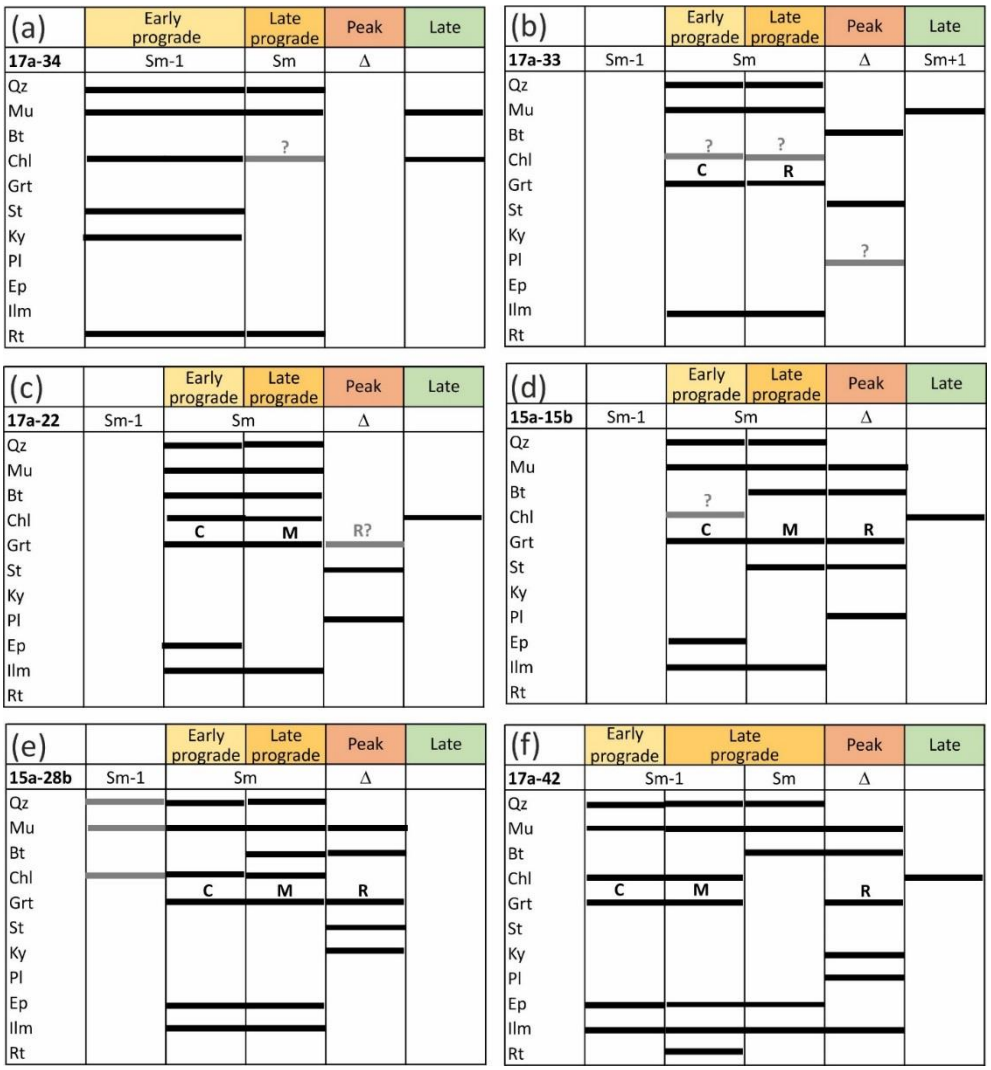

Fig. 5.5: Blastesis–deformation diagrams for the studied metapelites. Black lines clearly represent stable phases; grey lines represent phases presumed to be stable on the basis of microstructural observations and/or completely replaced by late phases. S_m is the main foliation; S_{m-1} and S_{m+1} developed earlier and later than S_m, respectively. ? refers to the static growth of the peak mineral assemblage.

5.3 Thermodynamic modelling results

The isochemical phase diagram (Fig. 5.6–5.8) approach has been applied to all six metapelites to constrain their peak P–T conditions and to reconstruct their metamorphic evolution. The effective bulk compositions used for the thermodynamic modelling are reported in Table 5.2 (see Chapter 3, section 3.4 for details on the methods used to calculate them). Figs. S3–S8 in Appendix 6 show the complete unfractionated and fractionated P–T pseudosections calculated for each sample, whereas composite phase diagrams are presented in Fig. 5.6–5.8. The compositional isopleths with corresponding uncertainties are reported in Appendix 7, Figs. S9–S13; In the following, the results of the thermodynamic modelling are presented, highlighting the consistency (or inconsistency) between the observed vs. modelled mineral assemblages and compositions.

Table 5.2 - Effective bulk compositions (mol%) of the modelled metapelites

	17a-34	17a-33		17a-22		15a-15b		15a-28b		17a-42	
	MBC	MBC	MBC-(GrtC + GrtM)	MBC	MBC-(GrtC + GrtM)	MBC	MBC-(GrtC + GrtM)	MBC	MBC-(GrtC + GrtM)	MBC	MBC-(GrtC + GrtM)
SiO_2	81.54	64.32	64.67	68.21	68.73	72.27	73.14	68.23	76.20	67.33	68.97
TiO_2	0.19	1.25	1.27	0.49	0.50	0.62	0.64	0.15	0.19	0.68	0.73
Al_2O_3	11.52	22.15	22.28	14.52	14.53	13.91	13.90	12.83	12.38	14.23	14.23
Fe_2O_3	0.00	0.17	0.15	0.19	0.17	0.13	0.11	0.26	0.11	0.21	0.17
FeO	1.80	3.30	2.85	7.29	6.83	5.28	4.49	10.26	4.43	8.21	6.84
MnO	0.00	0.09	0.01	0.04	0.00	0.04	0.00	0.31	0.00	0.11	0.00
MgO	2.03	1.42	1.36	4.04	4.07	3.37	3.35	3.76	3.59	4.43	4.50
CaO	0.00	0.02	0.00	0.76	0.63	0.43	0.30	2.10	0.33	2.03	1.62
Na_2O	0.36	1.53	1.55	1.19	1.22	0.88	0.91	0.24	0.32	0.65	0.69
K_2O	2.56	5.76	5.85	3.26	3.33	3.07	3.16	1.86	2.45	2.11	2.25
Total	100.00	100.00	100.00	100.00	100.00	100.00	100.00	100.00	100.00	100.00	100.00

5.3.1 Sample 17a–34

Prograde evolution and development of S_m

The calculated P–T pseudosection shows that muscovite is stable over the whole P–T range of interest; chlorite is stable up to 560–610 °C at 5–12 kbar, and it is replaced by biotite at higher T. Kyanite is predicted over almost all the P–T range of interest, either in equilibrium with chloritoid (at T<520–580 °C) or with staurolite (at higher T). The garnet–in curve is located at P>11 kbar and T>630 °C (Fig. 5.6a). Microstructural observations show that both staurolite and kyanite porphyroblasts are pre–kinematic with respect to the main foliation (Fig. 5.5a): thus, they provide information about the prograde evolution of the sample. Compositional isopleths modelled for staurolite (XMg=0.18 ± 0.01) constrain its growth at 575–590 °C, P>8 kbar, in the Qz + Mu + Chl + St + Ky + Rt field (Fig. 5.6b,c and Appendix 7, Fig. S9a), consistent with the observed prograde assemblage. The development of S_m should have occurred at higher T with respect to the growth of staurolite and kyanite, i.e. in the biotite stability field, according to the modelled pseudosection (Fig. 5.6a). Biotite is modelled in low amounts (<7 vol%); its absence in the sample could be justified by its replacement by chlorite during retrogression. This conclusion is supported by the

observation that staurolite, and to a minor extent kyanite, are partially replaced by muscovite, thus confirming that the sample suffered a slight retrogression. The estimate of peak P–T conditions is hampered by the absence of preserved minerals post–kinematic with respect to the S_m (Fig. 5.5a).

5.3.2 Sample 17a–33

Prograde evolution and development of S_m

The pseudosection calculated for the unfractionated bulk composition (Fig. 5.6d and Appendix 6, Fig. S4) shows that muscovite is stable over the entire P–T range of interest, in equilibrium with chlorite at T<560–600 °C, depending on pressure. The biotite–in curve has a positive slope, limiting its stability at T<560 °C for P<6.5 kbar and at T>580 °C for P>8.5 kbar. Garnet is predicted at T>510°C for P<9.5 kbar; however, its modal amount exceeds 0.5 vol% only at T>550 °C, i.e. at a temperature which is 40 °C higher than the garnet–in curve (Fig. 5.6f). Chloritoid is predicted at T<590 °C and P>6.5 kbar and is replaced by staurolite with increasing temperature. Staurolite is predicted to be stable up to 620–650 °C; at higher T, it is replaced by kyanite. Plagioclase is limited to P<7.0–8.0 kbar.

The compositional isopleths modelled for garnet core (GrtC: XMg=0.095, XCa=0.035, XMn=0.12, XFe=0.75; all with ± 0.01 uncertainties) are nearly parallel to each other (Fig. 5.6e and Appendix 7, Fig. S9b), constraining its growth at T=550–570 °C and P>8.5 kbar, in the Qz + Mu + Chl + Grt + Ctd + Ilm field (Fig. 5.6f). The modelled amounts of chlorite and chloritoid at these P–T conditions are lower than 3 vol% and 2 vol%, respectively; thus, their absence from the observed prograde assemblage could be likely due to their complete consumption during prograde metamorphism.

The garnet porphyroblasts in their entirety (i.e. both GrtC and GrtR) are syn–kinematic with respect to the main foliation, i.e. they grew earlier than the metamorphic peak (Fig. 5.5b). The growth of the garnet rim is constrained using the P–T pseudosection calculated for the fractionated bulk composition. The effects of fractionation are minimal; the most significant variation concerns the position of the garnet–in curve, which is shifted up–T and up–P of about 50 °C and 2 kbar, respectively, and the stability field of plagioclase, which is now enlarged toward higher P (Appendix 6, Fig. S4). Compositional isopleths modelled for the garnet rim (GrtR: XMg=0.15, XCa=0.01, XMn=0.03, XFe=0.82; all with ± 0.01 uncertainties) converge at 585–595 °C, 9.5–11.0 kbar (Fig. 5.6e,f and Appendix 7, Fig. S9c). The absence of biotite in the main foliation constrains the development of the S_m at T<580–590°C, in equilibrium with garnet rim.

Peak P–T conditions

Peak P–T conditions are difficult to constrain, because the post–kinematic minerals overgrowing the main foliation are either completely altered (e.g. plagioclase is completely replaced by kaolinite, biotite is strongly oxidized) or very rare (e.g. staurolite), and were not found in the polished thin section used for compositional analysis. Both biotite and staurolite are predicted to be stable at temperatures higher than those estimated for the

growth of GrtR, and plagioclase is modelled at P<8.0 kbar (Fig. 5.6d). Both these observations are consistent with a heating–decompression path, but peak metamorphic conditions cannot be more precisely constrained.

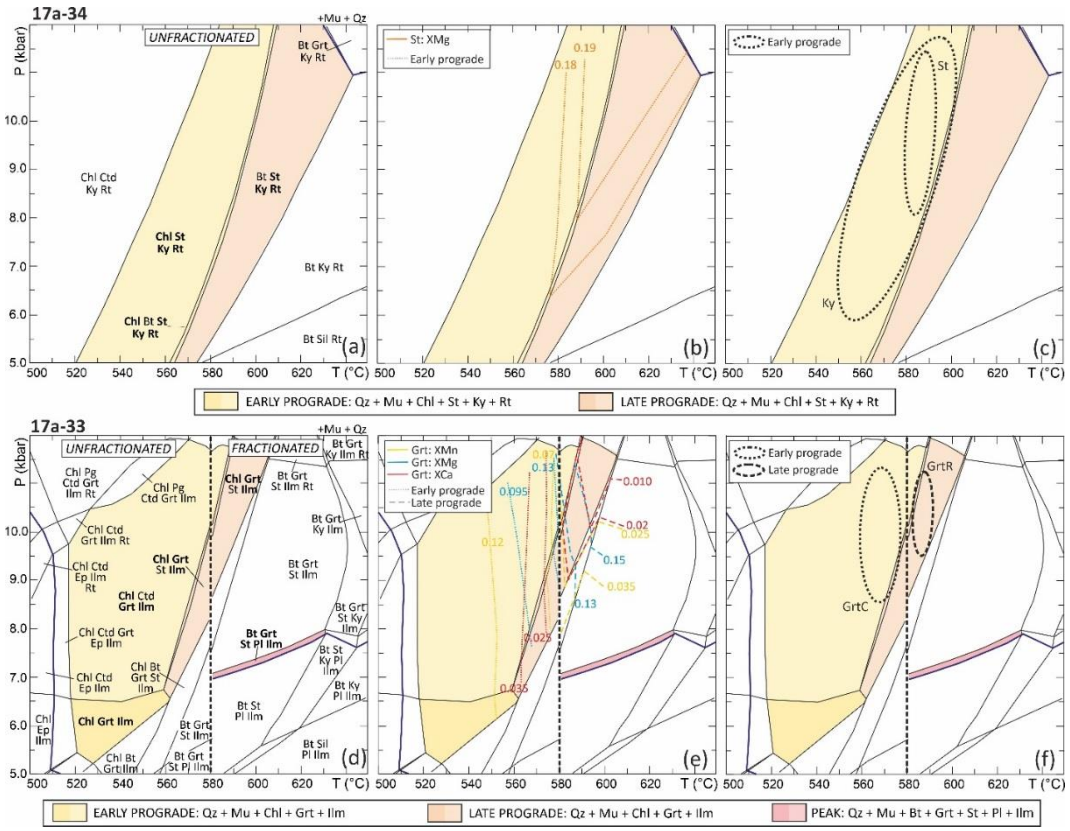

Fig. 5.6: P–T isochemical phase diagrams modelled for sample 17a–34 (a–c) and 17a–33 (d–f) using the measured bulk–compositions (unfractionated: on the left in d–f), and the effective bulk compositions after fractionation of garnet core + mantle (fractionated: on the right in d–f). The variance of the fields varies from two (i.e. 7 phases) to four (i.e. 5 phases) for sample 17a–34 (a), and from three (i.e. 9 phases) to seven (i.e. 5 phases) for sample 17a–33 (d). Early prograde, late prograde and peak assemblages corresponding to those reported in Fig. 5.5 are indicated in yellow, orange and red, respectively, with darker tones highlighting the best fit between the observed and the modelled assemblages (for each modelled assemblage, the observed minerals are reported in bold). The modelled compositional isopleths are reported in (b) and (e); the correspondent uncertainties are reported in Appendix 7, Fig. S9. Dotted and dashed isopleths refer to composition of early prograde and late prograde phases. The black ellipses in (c) and (f) summarize the P–T conditions constrained for the growth of each mineral, based on the intersection, or overlap of the correspondent compositional isopleths (see also Appendix 7, Fig. S9) reported in (b) and (e). The different line styles of the ellipses refer to early prograde and late prograde phases, as indicated in the legends. The thick continuous blue lines in (c) and (f) are the Grt–in boundary curves; dotted blue lines in (f) refer to 0.5% and 1.0% garnet isomodes.

5.3.3 Sample 17a–22

Prograde evolution and development of S_m

The P–T pseudosection calculated for the unfractionated bulk composition (Fig. 5.7a and Appendix 6, Fig. S5) shows that muscovite and biotite are stable in the whole P–T region of interest, whereas chlorite is stable at T<560–610 °C. The garnet–in curve is located at

500–530 °C, and the 0.5 vol% garnet isomode is shifted up–T of 10 °C (Fig. 5.7c); staurolite is modelled in the T interval of 560–640 °C, and the staurolite–out curve mostly coincides with the kyanite–in curve. Na–bearing phases are paragonite and plagioclase, which are stable at low–T/high–P and high–T/low–P, respectively. The compositional isopleths modelled for garnet core (GrtC: XMg=0.06, XCa=0.17, XMn=0.06, XFe=0.72; all with ± 0.01 uncertainties) constrain its growth at 535–550 °C and 5.5–6.0 kbar, in the Qz + Mu + Bt + Chl + Grt + Pl + Ilm ± Mt fields (Fig. 5.7b,c and Appendix 7, Fig. S10). The modelled assemblage in equilibrium with the arnet core is not consistent with the observed one; specifically, epidote is found as inclusion within GrtC, instead of plagioclase. This discrepancy will be discussed in section 5.4.2.

Both garnet core and garnet mantle are syn–kinematic with respect to the main foliation (Fig. 5.5c). Although the modelled XFe isopleths do not match perfectly with the observed GrtM composition (XFe=0.78 ± 0.01), the other compositional isopleths (GrtM: XMg=0.12, XCa=0.11, XMn=0.01; all with ± 0.01 uncertainties) converge at about 570–590 °C and P>8.0 kbar, in the Qz + Mu + Bt + Chl ± Pg + Grt + Ilm fields (Fig. 5.7b,c and Appendix 7, Fig. S10). With the exception of paragonite, whose amount is lower than 5 vol%, the modelled assemblage in equilibrium with GrtM is consistent with the observed one. Compositional isopleths of the syn–kinematic chlorite and biotite (Chl: XMg=0.53 ± 0.02; Bt: XMg=0.53 ± 0.03) constrain their growth at 560–580 °C and 575–590 °C, respectively, i.e. at conditions roughly overlapping with those estimated for garnet mantle (Fig. 5.7b,c). This implies that the S_m developed in the temperature interval of 570–590 °C.

Peak P–T conditions

The P–T pseudosection calculated for the fractionated bulk composition shows that the effects of fractionation are minimal, and mostly reflected by a significant reduction of the garnet stability field, which is now limited at T>530–560 °C (Appendix 6, Fig. S5). As garnet rims are completely replaced by late chlorite, peak P–T conditions were constrained by the other post–kinematic minerals overgrowing the main foliation, i.e. staurolite and plagioclase. Compositional isopleths modelled for these phases (St: XMg=0.18 ± 0.01; Pl: XCa=0.31 ± 0.01) converge at 600–620 °C and 8.0–9.0 kbar, constraining peak P–T conditions in the Qz + Mu + Bt + Grt + St + Pl + Ilm field, consistently with the observed peak assemblage (Fig. 5.7b,c and Appendix 7, Fig. S10).

5.3.4 Sample 15a–15b

Prograde evolution and development of S_m

The P–T isochemical diagram calculated for the unfractionated bulk composition (Fig. 5.7d and Appendix 6, Fig. S6) shows that muscovite is stable in the whole P–T range of interest, whereas chlorite is modelled at T<550–600 °C and is replaced by biotite at higher T. The garnet–in curve is located at ca. 510–530 °C, and the 0.5 vol% garnet isomode is shifted up–T of ca. 15–20 °C (Fig. 5.7f). Chloritoid is stable at T<550–580 °C and is replaced by staurolite at higher temperatures; kyanite is modelled at T>600 °C. The plagioclase–in curve

has a positive slope, constraining its stability at relatively low–P and high–T conditions. The intersection of the garnet core compositional isopleths (GrtC: XMg= 0.08, XCa= 0.11, XMn= 0.04, XFe=0.75; all with ± 0.01 uncertainties) points to T = 550–565 °C and P = 5.5–6.3 kbar for the growth of GrtC (in the Qz + Chl + Mu + Bt + Grt + St + Pl + Ilm field) (Fig. 5.7e and Appendix 7, Fig. S11). For the garnet mantle, the modelled XFe isopleths do not match perfectly with the observed GrtM composition (XFe=0.77 ± 0.01); however, the other compositional isopleths (GrtM: XMg= 0.12, XCa= 0.11, XMn= 0.01; all with ± 0.01 uncertainties) converge at T=580–600 °C and P=8.5–11.0 kbar (in the Qz + Chl + Mu ± Bt + Grt + St + Pl + Ilm fields) (Fig. 5.7f and Appendix 7, Fig. S11).

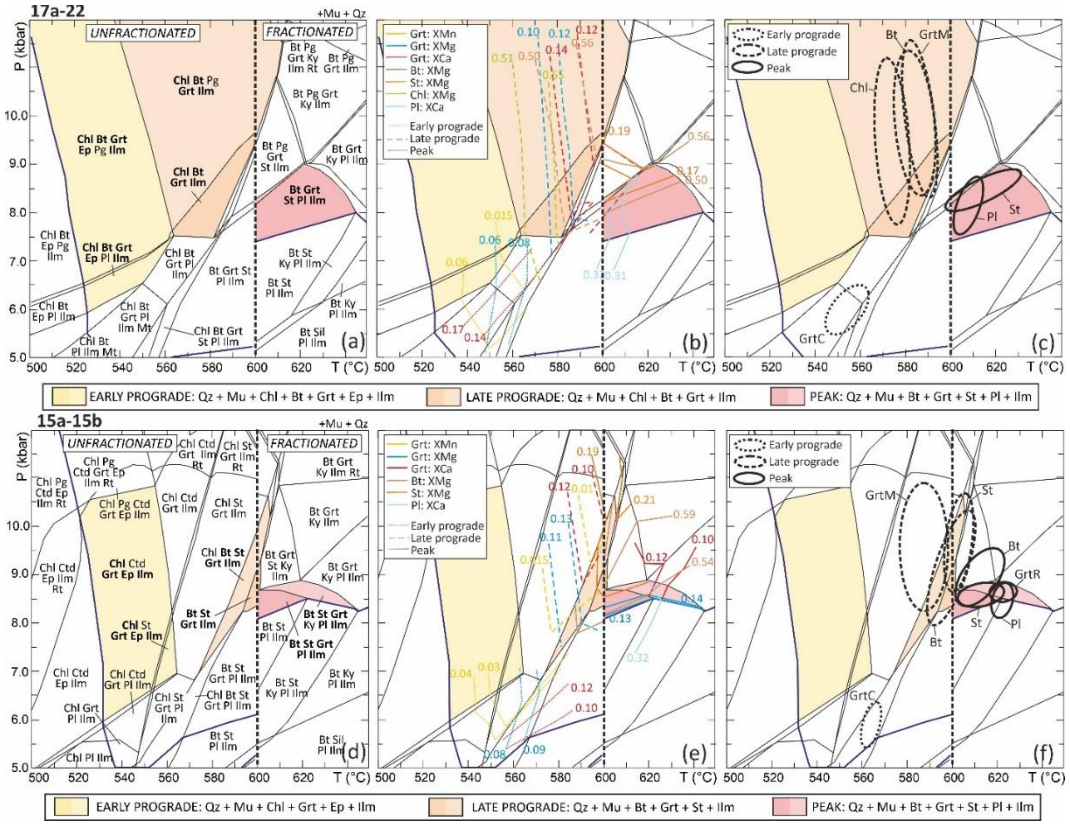

Fig. 5.7: P–T isochemical phase diagrams modelled for ssamples17a–22 (a–c) and 15a–15b (d–f) using the measured bulk–compositions (unfractionated: on the left in all the diagrams), and the effective bulk compositions after fractionation of garnet core + mantle (fractionated: on the right in all the diagrams). The variance of the fields varies from three (i.e. 9 phases) to six (i.e. 6 phases) for sample 17a–22 (a), and from three (i.e. 9 phases) to seven (i.e. 5 phases) for sample 15a–15b (d). Colours and lines as in Fig. 5.6 with the addition of continuous isopleth lines in (b) and (e) referring to compositions of peak phases and of continuous ellipses in (c) and (f), referring to the P–T conditions constrained for the growth of peak assemblage. Uncertainties for compositional isopleths of each phase are reported in Appendix 7, Figs. S10S11.

The observed mineral assemblage in equilibrium with GrtM (Qz + Mu ± Bt + Grt + St + Ilm) matches the field assemblages modelled for the growth of GrtM; on the opposite, the observed mineral assemblage in equilibrium with GrtC (Qz + Chl + Mu + Grt + Ep + Ilm) is not consistent with the plagioclase-bearing field modelled for the growth of GrtC (Fig. 5.7f).

This discrepancy will be discussed in Chapter 6, section 6.1. Syn–kinematic biotite (Bt: XMg=0.57 ± 0.03) is predicted to form at the expenses of chlorite in the narrow T interval of 590–600 °C, partially overlapping the P–T conditions predicted for the growth of GrtM (Fig. 5.7e,f and Appendix 7, Fig. S11). This is in agreement with microstructural observations suggesting that GrtM is syn–kinematic with respect to the main foliation (Fig. 5.5d), and constrains the development of S_m at T<600 °C.

5.3.5 Sample 15a–28b

Prograde evolution and development of S_m

The P–T pseudosection calculated for the unfractionated bulk–composition (Fig. 5.8a and Appendix 6, Fig. S7) shows that muscovite is stable in most of the P–T range of interest, in equilibrium with chlorite at T<530–600 °C and with biotite at higher T. Garnet is stable over the whole P–T range of interest, the garnet–in curve is located at 440–470 °C (i.e. outside the investigated P–T range; Fig. 5.8c), with the 0.5 vol% isomode shifted up–T of 15–20 °C. Chloritoid is modelled up to 540–580 °C, and at higher T it is replaced by staurolite. Kyanite is stable at T>580 °C, and the kyanite–in curve mostly coincides with the staurolite–out curve. The compositional isopleths modelled for garnet apparent core ("GrtC": XMg=0.08, XCa=0.185, XMn=0.04, XFe=0.69; all with ± 0.01 uncertainties) mutually intersect at 550–570 °C and >8.5 kbar, in the Qz + Mu + Chl + Grt + Ctd + Ep + Ilm field (Fig. 5.8b and Appendix 7, Fig. S12); this is consistent with the observed prograde assemblage, except for chloritoid which is predicted to occur in low amounts (<7 vol%) and could have been completely consumed during prograde metamorphism. The modelled isopleths for garnet mantle (GrtM: XMg=0.12, XCa=0.17, XMn=0.02, XFe=0.69; all with ± 0.01 uncertainties) constrain its growth at 570–590 °C and 8.0–11.0 kbar, in the Qz + Mu + Chl + Grt + St ± Ep + Ilm fields (Fig. 5.8c and Appendix 7, Fig. S12), in agreement with the occurrence of quartz, muscovite, chlorite, epidote and ilmenite inclusions in GrtM. The amount of staurolite predicted at these P–T conditions is lower than 3 vol%, and its absence as inclusion in GrtM is therefore justifiable. Both GrtC and GrtM are syn–kinematic with respect to the main foliation (Fig. 5.5e), defined by muscovite, chlorite and biotite. The modelled compositional isopleths for chlorite and biotite (Chl: XMg=0.57 ± 0.02; Bt: XMg=0.57 ± 0.02) suggest that chlorite grew at 565–575 °C, and biotite appeared at slightly higher temperatures (T=590–600 °C) (Fig. 5.8b,c and Appendix 7, Fig. S12), thus constraining the development of S_m at 570–600 °C.

Peak P–T conditions

The P–T pseudosection calculated for the fractionated bulk composition is used to constrain the growth of the garnet rim, in equilibrium with the other post–kinematic phases (i.e. biotite, staurolite and kyanite). The fractionation effects are significant (Appendix 6, Fig. S7); the garnet–in curve is now located at T>560 °C, and the staurolite and kyanite stability fields are enlarged toward higher P and lower T, respectively. Compositional isopleths modelled for the garnet rim (GrtR: XMg=0.14, XCa=0.15, XMn=0,

XFe=0.72; all with ± 0.01 uncertainties) constrain its growth at T=615–625 °C and P=7.8–8.5 kbar, in the Qz + Mu + Bt + Grt + Ky + St + Pl + Ilm ± Mt fields (Fig. 5.8b,c and Appendix 7, Fig. S12), in agreement with the observed peak metamorphic assemblage (plagioclase is predicted in very low amounts, <1 vol%). Compositional isopleths of staurolite (St: XMg=0.19 ± 0.02) suggest that this phase grew at 600–620 °C (Fig. 5.8b,c and Appendix 7, Fig. S12), consistent with the occurrence of post–kinematic staurolite in equilibrium with garnet rim.

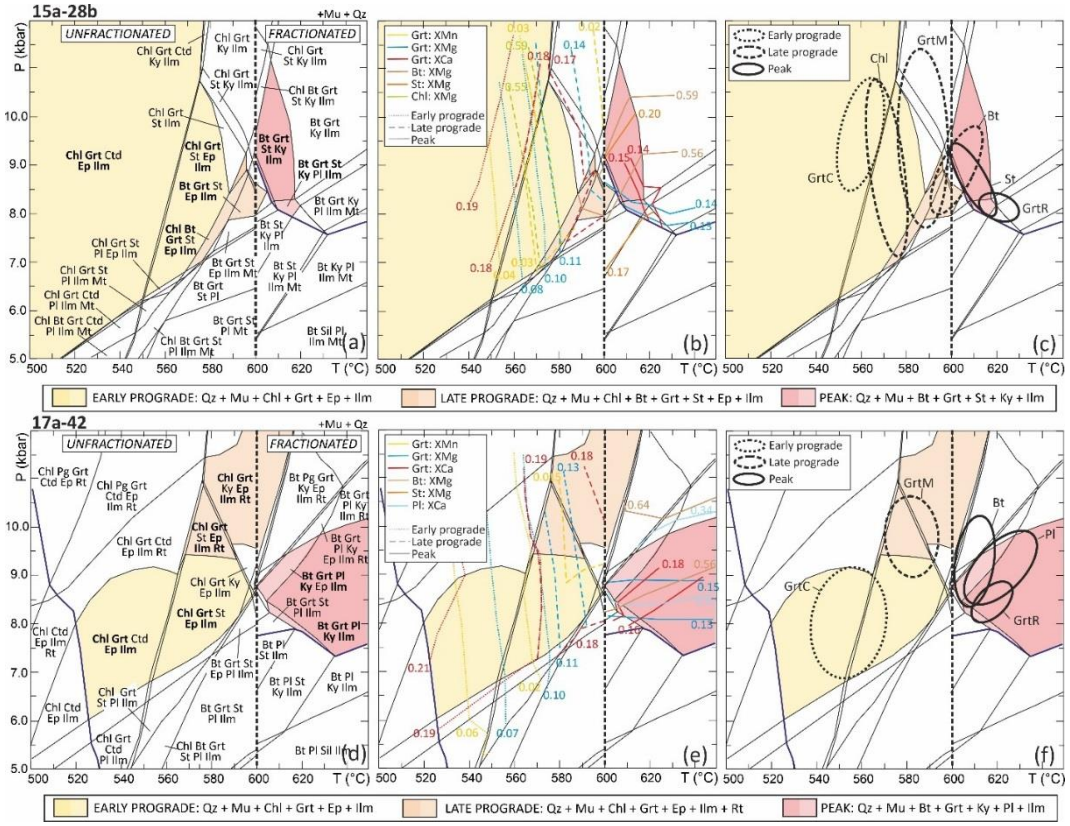

Fig. 5.8: P–T isochemical phase diagrams modelled for sample 15a–28b (a–c) and 17a–42 (d–f) using the measured bulk–compositions (unfractionated: on the left in all the diagrams), and the effective bulk compositions after fractionation of garnet core + mantle (fractionated: on the right in all the diagrams). The variance of the fields varies from three (i.e. 9 phases) to six (i.e. 6 phases) for both samples 15a–28b (a) and 15a–15b (d). Colours and lines as in Figs. 5.6–5.7. Uncertainties for compositional isopleths of each phase are reported in Appendix 7, Figs. S12–S13.

5.3.6 Sample 17a–42

Prograde evolution and development of S_m

The pseudosection calculated for the unfractionated bulk–composition (Fig. 5.8d and Appendix 6, Fig. S8) shows that muscovite is stable in almost all the P–T range of interest, either in equilibrium with chlorite (at T<560–610 °C)) or with biotite (at higher T). The garnet–in curve is located at T<530 °C, and the 0.5 vol% garnet isomode is shifted up–T of 10–15 °C (Fig. 5.8f); chloritoid is modelled up to 550–580 °C and is replaced by staurolite at

higher T, and kyanite is stable at T>580 °C for P>11 kbar, and at T>600 °C for P<8 kbar. The plagioclase–in curve has a positive slope, constraining its stability at relatively low–P and high–T conditions. The compositional isopleths modelled for the garnet core (GrtC: XMg=0.07, XCa=0.21, XMn=0.06, XFe=0.67; all with ± 0.01 uncertainties) converge at 535–555 °C and 7.0–9.2 kbar, in the Qz + Mu + Chl + Grt + Ctd + Ep + Ilm fields (Fig. 5.8e,f and Appendix 7, Fig. S13). Except for chloritoid, which is nevertheless a minor phase (<3 vol%), the modelled assemblage is consistent with the observed inclusions in GrtC (e.g. epidote and ilmenite). Compositional isopleths modelled for the garnet mantle (GrtM: XMg=0.12, XCa=0.18, XMn=0.015, XFe=0.69; all with ± 0.01 uncertainties) converge at 570–590 °C and 9.0–11.0 kbar, in the Qz + Mu + Chl + Grt + St + Ep + Ilm + Rt field (Fig. 5.8e,f and Appendix 7, Fig. S13); the coexistence of ilmenite and rutile in this field is in good agreement with microstructural observations (i.e. inclusions of both ilmenite and rutile in GrtM; Fig. 5.5f). The isopleths modelled for the syn–kinematic biotite (XMg=0.60 ± 0.04) allow constraining the development of the S_m at about 600–620 °C, i.e. at higher T with respect to the growth of GrtM, consistently with the pre–kinematic (pre–S_m) nature of GrtC and GrtM.

Peak P–T conditions

The peak assemblage, represented by the post–kinematic garnet rim, kyanite, plagioclase, biotite and muscovite, is modelled by the pseudosection calculated using the fractionated bulk composition. The most significant effects of fractionation are represented by the shift of garnet–in curve up–T of about 40 °C, and by the enlargement of the staurolite and kyanite stability fields toward higher P and lower T, respectively (Appendix Fig. SM12). Compositional isopleths modelled for garnet rim (GrtR: XMg= 0.14, XCa= 0.17, XMn= 0.00, XFe=0.70; all with ± 0.01 uncertainties) constrain its growth at 610–625 °C and 8.0–8.6 kbar, in the Qz + Mu + Bt + Grt + Ky + Pl + Ilm field (Fig. 5.8e,f and Appendix 7, Fig. S13), which is consistent with the observed peak assemblage. Compositional isopleths modelled for plagioclase (XCa= 0.40 ± 0.06) are partially overlapped with those of GrtR, thus defining peak P–T conditions of 600–635 °C and 8.4–9.5 kbar (Fig. 5.8e,f and Appendix 7, Fig. S13).

5.4. Discussion

5.4.1 P–T evolution of the Upper–LHS: regional implications and methodological considerations

In all the samples, the compositional isopleths used to constrain the prograde P–T conditions are mostly T–dependent and parallel to each other, providing tight constraints on temperature, but poor constraints on pressure. Peak P–T conditions are, instead, well–constrained for most of the samples because they are defined based on low–variant assemblages. Despite the relatively large uncertainties on the estimated prograde pressures, all the reconstructed P–T paths show a common shape, characterized by a prograde moderate increase in both P and T, up to peak–P conditions, followed by a heating

decompression, up to peak–T conditions (Fig. 5.9). Peak–P conditions are invariably reached at T=580–590 °C in all the samples, spanning 8.5–11 kbar. Considering that all the samples belong to the Upper–LHS unit and should therefore have experienced the same P–T evolution, this range can be reduced to 9.5–10.5 kbar by overlapping all the trajectories. Peak–T conditions are tightly constrained at 610–630 °C and 8.2–8.9 kbar, and are consistent among the samples (Fig. 5.9). The development of the main foliation is constrained at 580–600 °C, earlier than the static growth of minerals defining the peak assemblage (Fig. 5.9).

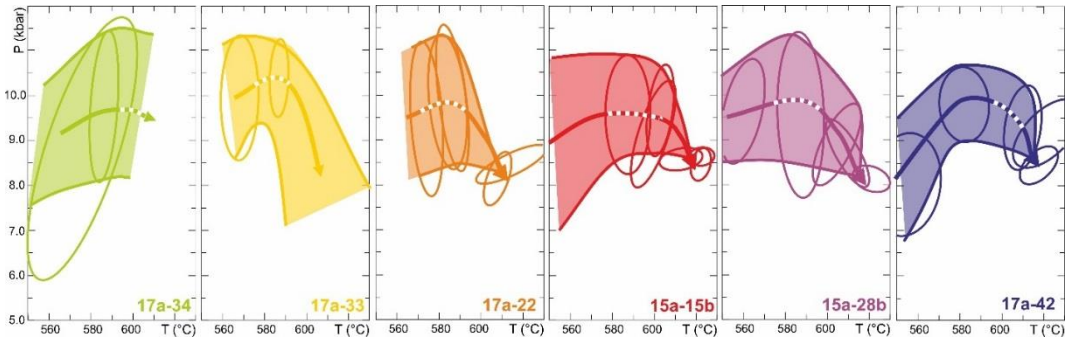

Fig. 5.9: P–T grids summarizing the P–T paths reconstructed for the studied metapelites. The ellipses are the same as reported in Figs. 5.6–5.8 (panels (c) and (f)). The large, coloured paths envelop the ellipses; the thin arrows are traced in the middle of each envelope. The dashed white portion of the arrows constrains the development of the main foliation S_m in each sample. Note that, despite the relatively large uncertainties on the estimated prograde pressures, all the reconstructed P–T paths show a common shape.

These results show that, in the study area, the Upper–LHS experienced the temperature peak after the pressure peak, in agreement with the P–T paths reported westward by Catlos et al., (2001) and Kohn et al., (2001) (Margsyandi and Daraundi sections, central Nepal; their Domain 3) (see also Kohn, 2014 and Catlos et al., 2018), and eastward by Groppo et al., (2009), Mosca et al. (2012) and Rolfo et al., (2015) (Arun and Tamor sections, eastern Nepal; their Lower MCTZ or Lower IMS units). This type of P–T trajectory is significantly different from the hairpin P–T path generally described for the Lower–LHS unit (see Chapter 2, section 2.2.3), which is characterized by maximum temperature experienced at maximum pressure (e.g. Catlos et al., 2001; Kohn et al., 2001; Groppo et al., 2009; Imayama et al., 2010; Mosca et al., 2012; Rolfo et al., 2015; Rapa et al., 2016, 2018). The occurrence of P–T paths with different shapes in the Lower– and Upper– LHS units has been explained by previous authors (Catlos et al., 2001, 2018; Kohn et al., 2001) as the result of the accretion of different LHS tectonic slices to the MCT hanging wall, through a progressive southward (and downward) propagation of the thrust activity. According to this model, during the evolution of the MCT in early Miocene, the Upper–LHS rocks in the footwall experienced an increase in both P and T during tectonic loading. The successive slowdown (or quiescence) of the movement along the MCT allowed isotherms to relax and temperature to increase in the Upper–LHS unit, at slightly decreasing pressure and in the absence of significant deformation. The reactivation of strain occurred through the

downward propagation of the thrust, which allowed the contemporaneous exhumation of the Upper–LHS unit and the burial of the Lower–LHS unit. Our results strongly support this model; in particular, the static growth of the main minerals defining the peak assemblages documented in this study provides strong evidence that decompression coupled with heating occurred in the absence of deformation, i.e., in the time interval between two episodes of intense thrusting.

One may wonder why this type of P–T trajectory has rarely been reported so far from the Upper–LHS in Nepal Himalaya. In our opinion, this may be due to:

(i) the substantial lack of studies based on forward petrological modelling. Most studies focusing on the LHS metamorphic evolution are based on inverse thermodynamic modelling approaches, i.e. conventional and/or multi–equilibrium thermobarometry (e.g. Macfarlane, 1995; Rai et al., 1998; Catlos et al., 2001; Kohn et al., 2001; Goscombe et al., 2006, 2018; Kohn, 2008; Groppo et al., 2009; Martin et al., 2010; Imayama et al., 2010; Corrie & Kohn, 2011; Mosca et al., 2012; Rolfo et al., 2015; Rapa et al., 2016, 2018; Khanal et al., 2020). These methods require precise knowledge of the composition of minerals supposed to be in equilibrium at a certain metamorphic stage (e.g. garnet–biotite pair for the Grt–Bt thermometer; all the minerals defining a specific assemblage for Average P–T etc.). While the peak assemblage in common metapelites is typically well preserved and often consists of several minerals (i.e. it is a low–variant assemblage), the prograde assemblages are more difficult to be defined, because some minerals stable during the prograde stages may have been consumed or may have changed their composition during the prograde evolution. For this reason, the inverse modelling approaches have been mostly applied to the peak assemblages, but not to the prograde assemblages, thus hampering the reconstruction of the whole P–T paths. Forward modelling approaches, i.e. isochemical phase diagrams combined with isopleth thermobarometry, allow this issue to be overcome; with this method, in fact, prograde P–T conditions can be constrained based on the composition even of a single mineral (typically garnet), combined with the predicted stability field of the inferred prograde assemblages.

(ii) the relatively rare occurrence, in the LHS, of appropriate lithologies for documenting the static growth of the low–variant peak metamorphic assemblage, and especially of the garnet rim. It is well known that deformation enhances metamorphic reactions (e.g. Terry & Heidelbach, 2006); in the absence of deformation, however, mineral growth is mostly controlled by diffusion, and metamorphic reactions are dependent on the bulk composition (Carlson, 1989; Ketcham & Carlson, 2012). It is therefore expected that significant growth (i.e. growth in amounts which can be easily detectable under the microscope) of aluminous minerals such as garnet, staurolite and kyanite (i.e. minerals commonly used as thermobarometers) is favoured by high–Al bulk compositions. Al–rich metapelites, whose composition

plots above the garnet–chlorite tie line in the AFM diagram, are, therefore, the most suitable candidates for recording the peak metamorphic stage. Conversely, the heating decompression stage might remain elusive and/or difficult to be constrained in low–Al metapelites.

(iii) the still controversial definition of the MCT. The consequent uncertainties in the exact location of the MCT (see Chapter 2, section 2.2.1) lead to ambiguities in what is to be considered as Upper–LHS and what is instead Lower–GHS, so that the same litho–stratigraphic unit can have been placed alternatively in the Upper–LHS or in the Lower–GHS depending on the criteria adopted by different authors (see Searle et al., 2008 for further discussion).

Following these considerations, we suggest that the ideal approach for a detailed reconstruction of the whole P–T evolution of the Upper–LHS is to apply the thermodynamic forward modelling approach on Al–rich metapelites (see also Catlos et al., 2018, 2020 for a similar strategy), especially looking for those samples that show microstructural evidence of static growth of the main peak mineral phases. However, recognizing the evidence of overstepping garnet nucleation is important for the definition of the correct prograde path (see below). The application of this method on a suite of samples from the same unit (rather than on a single sample) can be helpful in this sense.

5.4.2 Equilibrium vs. kinetic –controlled growth of garnet core

The isochemical phase diagram approach is based on the principles of equilibrium thermodynamics, i.e. on the assumption that each mineral grew in equilibrium with its surroundings, and thus its composition reflects the predicted P–T conditions (e.g. Guiraud et al., 2001; Powell et al., 2005; Powell & Holland, 2008). However, this assumption is not always valid for garnet porphyroblasts, which often nucleate and grow only after significant overstepping of the garnet–in curve, i.e. at higher T and/or P conditions with respect to those predicted by equilibrium thermodynamics (Hollister, 1969; Waters & Lovegrove, 2002; Pattison & Tinkham, 2009; Spear et al., 2014; Carlson et al., 2015; Castro & Spear, 2016; Wolfe & Spear, 2018; Spear & Wolfe, 2018; Nagurney et al., 2021).

The results of thermodynamic modelling show that, for all the garnet–bearing samples, the P–T conditions inferred for garnet nucleation do not match the garnet–in reaction modelled by the pseudosections but lie at higher temperatures with respect to the garnet–in curve. We interpret this as evidence of temperature–overstepping of garnet nucleation, with a degree of overstepping varying from 10–15 °C for samples 17a–22 and 15a–15b, to 20 °C for sample 17a–42, 40 °C for sample 17a–33, and more than 50 °C for sample 15a–28b (Fig. 5.10c–g). Our results also show that, with the exception of sample 15a–28b, the modelled GrtC compositional isopleths systematically define P–T conditions lying on (or close to) the modelled 0.5% isomodes (Fig. 5.10c,e–g). Sample 15a–28b differs from the others because, at the P–T conditions defined by the “GrtC” isopleths intersection, the predicted garnet abundance is significantly higher (14%) than in the other samples. This is

likely due to our failure in sectioning the centimetric–sized porphyroblasts through the real core (i.e., the measured composition of "GrtC" does not reflect the composition of the first garnet nucleus).

Comparing the P–T conditions constrained for the growth of GrtC with the assemblages predicted to be stable at the same conditions, we note:

(i) for two samples (17a–22 and 15a–15b), the P–T conditions constrained for the growth of GrtC lie in fields which are not consistent with the observed assemblages in equilibrium with GrtC. Specifically, in both samples, the estimated P–T conditions are located at pressures which are lower than those predicted for the early prograde assemblages (Fig. 5.7c,f). Also, the prograde P–T paths defined for these two samples based on the P–T conditions estimated for GrtC and GrtM suggest nearly isothermal loading (<10 °C $kbar^{-1}$), which is anomalous in the context of Barrovian terranes (e.g. Gaidies et al., 2015). The discrepancy between the modelled and the observed early prograde assemblages, as well as the anomalous sub–vertical prograde paths suggest that garnet nucleation probably occurred after a significant pressure–overstepping, i.e. at pressures at least 2–3 kbar higher than those predicted by the pseudosections;

(ii) for the other three garnet–bearing samples (17a–33, 15a–28b and 17a–42), the growth of GrtC is predicted to occur in fields which are consistent with the observed early prograde mineral assemblages (Figs. 5.6f and 5.8c,f). Their prograde P–T paths calculated in the same way as in the previous samples display heating associated with a moderate loading (>25 °C $kbar^{-1}$), i.e. a typical scenario in Barrovian terranes (e.g. Gaidies et al., 2015). This suggests that, in these samples, the degree of pressure–overstepping (if any) was minimal.

Overall, these results support the conclusions of previous studies (e.g. Carlson et al., 2015; Spear & Wolfe, 2019 and references therein), confirming that garnet nucleation can be influenced by kinetic factors. To explore which parameters may be responsible for the delay in garnet appearance with respect to the equilibrium predictions, we considered the difference in bulk composition among the samples, with specific emphasis on MnO and CaO:

(i) bulk–rock MnO: previous studies demonstrated that samples with higher bulk–rock MnO content generally display more pronounced apparent overstepping of the garnet–in reaction (Nagurney et al., 2021). Our results confirm this conclusion, i.e. the samples with higher MnO content normalized to FeO+MgO+MnO (samples from Groups 1 and 3: 17a–33, 17a–42 and 15a–28b) are those for which garnet nucleation was apparently more overstepped toward higher temperatures (Fig. 5.10a). However, the apparent delay in garnet nucleation coincides with the temperature difference between the modelled garnet–in curve and the 0.5% isomode (Fig. 5.10c–f). This suggests that the T–overstepping of the garnet–in

reaction could have been negligible for all the samples and that the apparently delayed garnet nucleation could reflect the attainment of the critical 0.5% threshold of garnet abundance, below which garnet is not readily detected in thin section (see also Nagurney et al., 2021 for a similar conclusion).

(ii) bulk–rock CaO: we note that, in the two samples showing discrepancies between calculated and observed assemblages in equilibrium with GrtC (samples 17a–22 and 15a–15b), the main cause of the discrepancy is related to the location of the grossular isopleths (Fig. 5.7b,e). This observation is in line with the conclusions of Spear & Wolfe (2019), who demonstrated that the net transfer equilibrium controlling the grossular content in garnet is the one which is more influenced in case of overstepping. Although we recognise that the number of investigated samples is small, the two samples with lower bulk–rock CaO content (samples from Group 2: 17a–22 and 15a–15b) are those displaying the largest evidence of P–overstepping (sample 17a–33 is not considered here because it can be fundamentally described in a CaO–free system) (Fig. 5.10b,f,g).

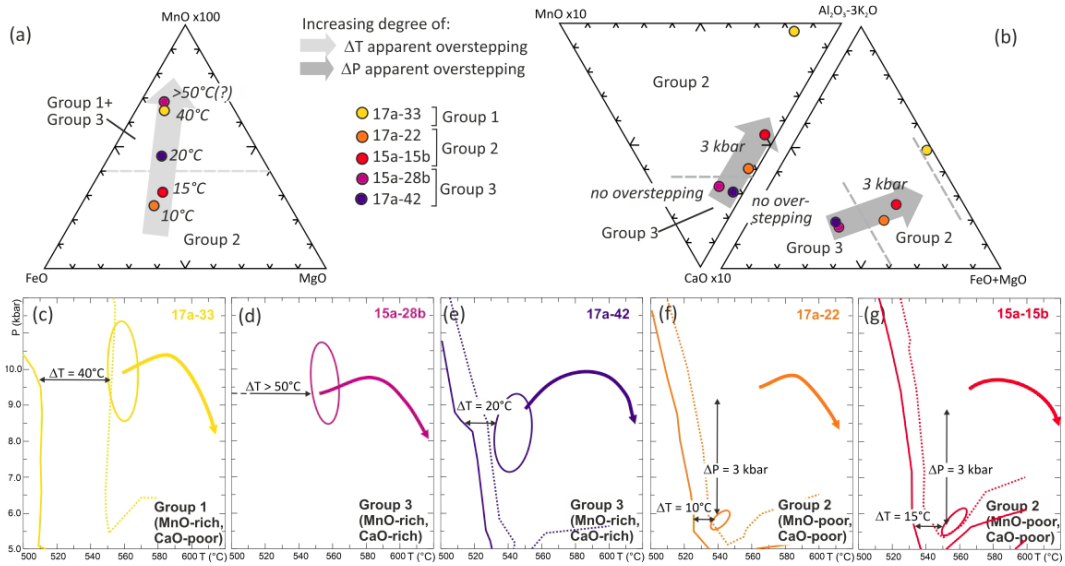

Fig. 5.10: (a–c) Bulk compositions of the studied samples plotted in ternary diagrams. This representation emphasizes the main differences between the three compositional groups. The bulk MnO content appears strongly correlated with the apparent ΔT overstepping of garnet nucleation (light grey arrow in a). The bulk CaO content seems correlated with the apparent ΔP overstepping of garnet nucleation (dark grey arrows in b and c). (c–g) Summary of the early prograde P–T conditions inferred for the growth of garnet core (ellipses) and apparent ΔT and ΔP overstepping of garnet nucleation. Continuous and dotted lines are the garnet–in curves and the 0.5% garnet isomodes. The coloured arrows represent the P–T paths reconstructed for each sample (see Fig. 5.9).

We, therefore, suggest that the T–overstepping of garnet nucleation was likely mostly influenced by the bulk–rock MnO content, i.e. the higher the bulk–rock MnO content, the more pronounced the apparent ΔT overstepping (Fig. 5.10a), whereas the P–overstepping of the garnet–in reaction was likely influenced by the bulk–rock CaO, i.e. the lower the bulk–rock CaO content, the more pronounced the ΔP overstepping (Fig. 5.10b). Based on

the results of forward thermodynamic modelling, overstepping nucleation of garnet should be presumed if the P–T conditions defined by garnet core lie at temperatures higher than the modelled garnet–in reaction, and if: (i) there are incongruities between the assemblage predicted to be stable at these P–T conditions and the assemblage observed in equilibrium with garnet core (see also Carlson et al., 2015 and references therein), and (ii) an anomalous nearly isothermal loading path is inferred. In such a case, the prograde P–T conditions inferred from garnet core composition should be considered with suspicion, because significant P–overstepping (rather than T–overstepping) of garnet nucleation could have occurred.

Kinetic factors seem instead much less critical in controlling the growth of the garnet rim at peak P–T conditions, as previously demonstrated by Spear & Wolfe (2019). For all the investigated samples, in fact, the modelled peak assemblages and mineral compositions are in good agreement with the observed ones and point to peak P–T conditions which are consistent among the samples. This confirms that the assumption of the garnet rim growing in equilibrium with the surrounding matrix is reasonable, and that peak metamorphic conditions constrained through equilibrium approaches based on the composition of the garnet rim and of the matrix assemblage can be considered reliable.

Chapter 6

CO_2 production in the Upper Lesser Himalayan Sequence of central Nepal

6.1 Introduction and aims

6.1.1 Premise

This chapter presents the results of a detailed petrographic and petrologic investigation of a selected number of carbonate–bearing samples from the Upper–LHS of central Nepal. The aim of the study is threefold: (i) characterizing the main assemblages and microstructures of various types of CO_2 source rocks within the LHS, derived from protoliths characterized by different amounts of carbonate minerals; (ii) investigating the most relevant metamorphic CO_2–producing reactions for each of them; (iii) estimating the P–T conditions at which the decarbonation reactions took place, the composition of the fluids released through these reactions, and the amounts of CO_2 released per unit volume of reacting rocks. This chapter represents the core of the thesis, because it provides the crucial information needed to evaluate the possible contribution of the LHS lithologies to the past CO_2 production during the Himalayan orogeny (see Chapter 8).

6.1.2 Dolomite vs magnesite series

Field data from several cross–sections in central and eastern Nepal (see Chapter 4), investigated either during previous fieldwork campaigns or during fieldwork related to this project, combined with petrographic and bulk–rock chemical analyses, allowed understanding that the CO_2 source rocks in the LHS mostly include metamorphic rocks derived from dolomite and magnesite–bearing protoliths, whereas calcite–bearing protoliths are much rarer. These lithologies are mostly concentrated in the Upper–LHS, especially within the Dhading Dolomite Formation and the Benighat Slate Formation, and in minor amounts also in the Nourpul Formation (see Chapter 4). Based on the most abundant carbonate mineral originally present in the protoliths (see Chapter 3, section 3.5 for the details on how the protoliths' assemblages have been reconstructed), the CO_2 source rocks have been classified into two groups:

- ***Dolomite series***: metamorphic rocks derived from dolomite–bearing protoliths;
- ***Magnesite series***: metamorphic rocks derived from magnesite–bearing protoliths;

Each series includes rocks derived from protoliths originally containing different amounts of carbonate minerals, ranging from less than 10% to more than 80% in volume, and classified as dolomitic pelites (dolomite <15%), dolomitic marls (dolomite 15–75%) and dolostones (dolomite >75%) for the dolomite series, and as magnesitic pelites (magnesite

<15%), magnesitic marls (magnesite 15–75%) and magnesite ores (magnesite >75%) for the magnesite series (Table 6.1). The two dolomite– and magnesite–series are clearly identifiable in the CAF diagram of Fig. 6.1, which shows the distribution of all the samples available in our dataset (including those studied here; bulk compositions reported in Appendix 2).

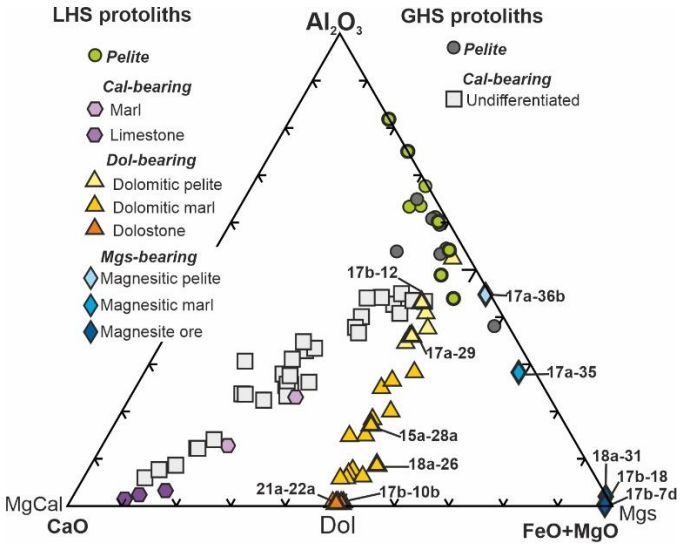

Fig. 6.1: Compositional variation of different types of carbonate–bearing lithologies from the LHS (coloured symbols) and the GHS (grey symbols), plotted in the CaO–$Al_2O_{3–}$(FeO+MgO) diagram. Samples belonging to the dolomite and magnesite series are aligned along two different trends, respectively defined by symbols from orange to yellow (dolomite series), and from dark blue to light blue (magnesite series). Note that all the analysed samples from the GHS belong to a calcite series.

Table 6.1 - Bulk compositions (mol%) and protoliths' assemblages (vol%) for the modelled carbonate-bearing lithologies

	Dolomite series						Magnesite series				
	Dolomitic pelites		Dolomitic marl		Dolostone		Magnesitic pelite	Magnesitic marl	Magnesite ores		
Sample	17b-12	17a-29	15a-28a	18a-26	17b-10b	21a-22a	17a-36b	17a-35	17b-7d	18a-31	17b-18
SiO_2	68.14	65.17	54.57	59.26	23.24	5.05	79.20	61.50	14.56	13.89	12.10
TiO_2	11.83	11.51	7.32	3.40	0.41	0.04	7.76	10.53	1.72	0.32	0.14
Al_2O_3	0.39	0.24	0.29	0.04	0.02	1.51	0.28	0.16	0.00	0.00	0.00
FeO	5.94	6.14	3.41	1.26	0.78	0.01	1.37	7.31	1.14	1.16	1.28
MnO	0.05	0.32	0.03	0.00	0.38	0.46	0.00	0.01	0.00	0.00	0.00
MgO	6.03	8.36	16.77	19.52	37.31	46.33	8.06	18.26	82.42	83.61	85.35
CaO	3.70	6.04	15.27	15.39	37.69	46.05	0.15	1.13	0.16	1.02	1.13
Na_2O	1.00	0.50	0.38	0.53	0.00	0.03	0.33	0.20	0.00	0.00	0.00
K_2O	2.91	1.73	1.95	0.59	0.17	0.52	2.85	0.90	0.00	0.00	0.00
Kao	0	11	0	0	0	0	0	21	5	0.3	0
Ill	29	24	20	3	0	4	25	12	0	0	0
FeChl	8	10	6	2	1	0	2	12	2	2	2
MgChl	5	5	3	0	0	0	0	0	0	0	0
Qz	33	31	28	47	16	1	50	32	9	11	10
Ab	8	4	3	5	0	0.2	3	2	0	0	0
Kfs	7	0	4	0	1	1	10	0	0	0	0
An	4	2	1	2	0	0	1	1	0	0	0
Dol	6	14	36	41	80	94	0	2	0.4	2	3
Mgs	0	0	0	0	0	0.3	9	18	84	85	86
Cal	0	0	0	0	0.5	0	0	0	0	0	0

6.2 Petrography and mineral chemistry results

Samples investigated in detail in this study were collected from the carbonate–rich lithologies of the Upper–LHS, i.e. the Dhading Dolomite Formation (17b–7d, 17b–10b, 17b–12, 17b–18, 18a–26, 18a–31, 21a–22a) and the Benighat Slate Formation (15a–28a, 17a–29, 17a–35, 17a–36b). The samples have been selected such that they are representative of protoliths characterized by low, medium, and high carbonate contents (i.e. dolomitic/magnesitic pelites, dolomitic/magnesitic marls and dolostone/magnesite ores). Eleven samples were considered for the petrographic and microstructural analyses, and the thermodynamic modelling approach was applied on seven of them: two dolomitic pelites (17b–12, 17a–29), two dolomitic marls (15a–28a, 18a–26), one magnesitic pelite (17a–36b), one magnesitic marl (17a–35) and one magnesite ore (17b–7d) (Fig. 6.1 and Table 6.1). The dolostone samples (17b–10b and 21a–22a) were not modelled, because the comparison between the calculated amounts of dolomite in the protoliths and the observed amounts of dolomite in the samples (see Appendix 3) suggests that dolomite was not consumed during metamorphism (i.e., decarbonation reactions didn't occur).
An overview of the thin section scale of the samples from the dolomite series is provided in Fig. 6.2 (see also Appendix 8), whereas representative microstructures are presented in Fig. 6.3, 6.4 and 6.5. Similarly, Fig. 6.6 and Appendix 9 show an overview of the thin section scale of the samples from the magnesite series, and the corresponding microstructures are illustrated in Fig. 6.7, 6.8. Assemblages and modal compositions of all the samples are reported in Table 6.2. Mineral chemical results for all the samples (both dolomite and magnesite series) are summarized in Fig. 5.9.

Table 6.2 - Assemblages and modal compositions (vol%) for the modelled carbonate-bearing lithologies

	Dolomite series						Magnesite series				
	Dolomitic pelites		Dolomitic marl		Dolostone		Magnesitic pelite	Magnesitic marl	Magnesite ores		
Sample	17b-12	17a-29	15a-28a	18a-26	17b-10b	21a-22a	17a-36b	17a-35	17b-7d	18a-31	17b-18
Cal	-	3	14	-	-	-	-	-	-	-	-
Dol	-	1	7	37	81	93.5	-	-	-	1	2
Mgs	-	-	-	-	-	-	-	-	74	78	82
Qz	37	36	26	42	16	1	54	27	-	-	-
Bt/Phl	23	18	32	8	2	1	21	20	-	-	-
Mu	17	8	-	-	-	5	24	-	-	-	-
Chl	-	6	-	4	-	-	-	-	14	4	1
Pl	21	18	10	8	-	-	2	-	-	-	-
Zo/Ep	<1		-	-	-	-	<1	-	-	-	-
Grt	2	7	-	-	-	-	-	3	-	-	-
Crd	-	-	-	-	-	-	-	5	-	-	-
Hbl	-	-	11	-	-	-	-	6	-	-	-
Oamp	-	-	-	-	-	-	-	29	-	-	-
Ky	-	2	-	1	-	-	-	10	-	-	-
St	-	1	-	-	-	-	-	-	-	-	-
Tlc	-	-	-	-	-	-	-	-	12	17	15

6.2.1 Dolomite series

6.2.1.1 Sample 17b–12

This two–mica, plagioclase + garnet–bearing graphitic schist consists of quartz (37%), biotite (23%), muscovite (17%), plagioclase (21%), garnet (2%) and epidote (<1%) with

minor K–feldspar and accessory graphite, Fe–sulphides and apatite. The well–developed foliation (S_m) is defined by the preferred orientation of muscovite and biotite, which are concentrated in pluri–mm continuous layers alternated with mm–thick layers of quartz (Fig. 6.2a). Muscovite is fine–grained and mostly aligned with the main foliation (Fig. 6.3c). The brown–red biotite occurs in two different generations: the first generation is represented by fine–grained flakes, syn–kinematic with respect to the S_m, whereas the second–generation forms coarse–grained flakes overgrowing statically and discordantly the S_m (Fig. 6.3c). Plagioclase is highly zoned, with a Na–richer core and a Ca–richer rim and is post–kinematic with respect to the S_m, statically overgrowing the micaceous layers (Fig. 6.3b,c). The pluri–mm–sized garnet porphyroblasts have a skeletal habit and are post–kinematic with respect to the S_m (Fig. 6.2a, 6.3a). Epidote is fine–grained and widespread in the matrix; it is highly zoned, with an allanitic core and a clinozoisite rim.

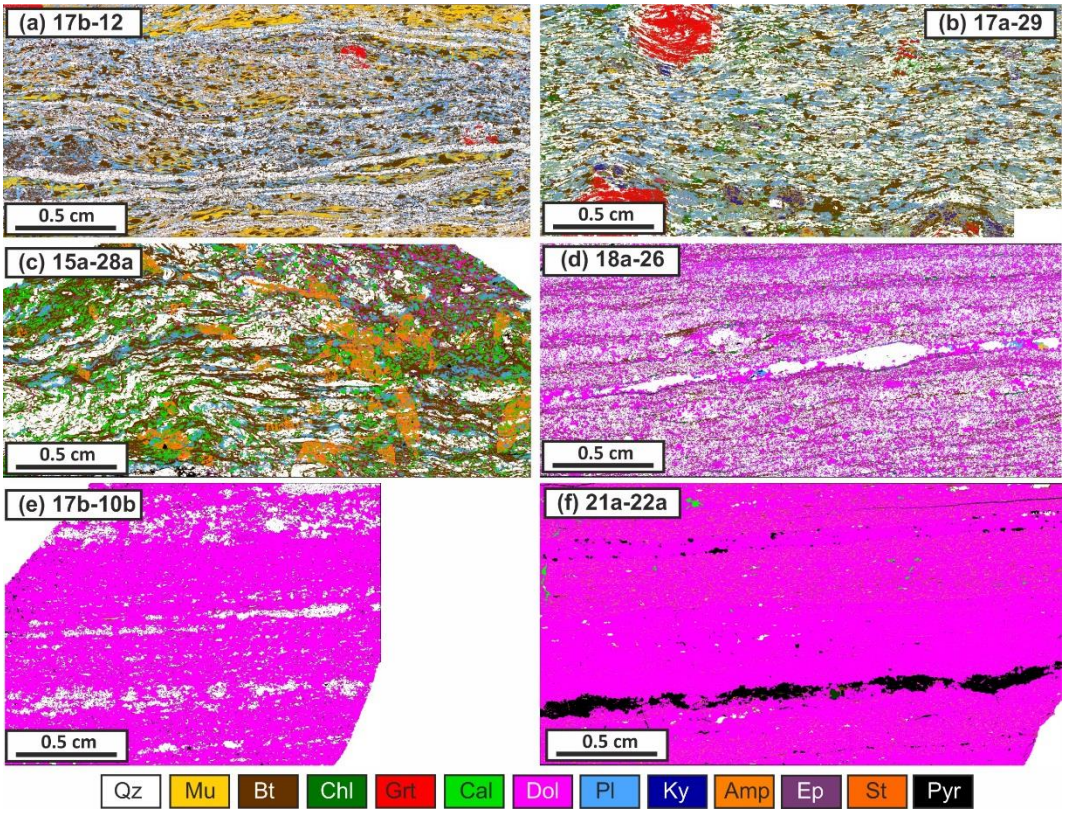

Fig. 6.2: Processed X–Ray maps of the studied carbonate–bearing lithologies from the dolomite series: (a) 17b–12; (b) 17a–29; (c) 15a–28a; (d) 18a–26; (e) 17b–10b; (f) 21a–22a

The fine–grained muscovite defining the S_m has relatively high Si contents in the range Si=3.10–3.27 a.p.f.u. (Fig. 6.9c), corresponding to values of ($Mg+Fe_{tot}$)=0.15–0.30 a.p.f.u. Muscovite compositions plot systematically above the line of ideal celadonitic substitution in the Si vs. ($Mg+Fe_{tot}$) diagram, suggesting that Fe is mostly in the trivalent state. The Na content is low, in the range Na=0.05–0.06 a.p.f.u. No significant compositional variations

have been observed between different generations of muscovite. Biotite from different generations is homogeneous in composition having XMg=0.53–0.57 and Ti=0.06–0.10 a.p.f.u. (Fig. 6.9d). The Na–rich plagioclase cores are mostly andesine, with XCa=0.28–0.49, whereas the Ca–rich plagioclase rim have XCa=0.60–0.81 (labradorite–bytownite) (Fig. 6.9b). Garnet is unzoned and has an average composition of $Alm_{65–67}Grs_{19–21}Prp_{10–11}Sps_{3–4}$ (Fig. 6.9a). Epidote has an allanitic core surrounded by a thin clinozoisite rim with XZo=0.63–0.64.

6.2.1.2 Sample 17a–29

This garnet + plagioclase + kyanite + staurolite –bearing biotitic schist consists of quartz (36%), biotite (18%), plagioclase (18%), garnet (6.5%), kyanite (2%), staurolite (1%), calcite (3%) and dolomite (1%), with late muscovite (8%) and chlorite (7%) and accessory graphite, epidote and tourmaline. The main foliation (S_m) is defined by the preferred orientation of biotite, which forms mm–thick discontinuous layers alternated with mm–thick quartzitic layers; the schistosity is not pervasive, because it is partially obliterated by the static overgrowth of abundant plagioclase (Fig. 6.2b, 6.3f). Biotite occurs in two different generations: a syn–S_m generation, aligned to define the main foliation (Fig. 6.3d), and a post–S_m generation, occurring as large flakes overgrowing discordantly the S_m. Garnet porphyroblasts are pluri–mm (Fig. 6.3b), syn– to post–kinematic with respect to the S_m. They include an internal foliation defined by quartz, carbonate, and graphite inclusions, which is continuous with the external main foliation but more widely spaced (Fig. 6.3d).
Plagioclase forms mm–sized porphyroblasts overgrowing the S_m schistosity (Fig. 6.3e,f) and locally partially replaced by very fine–grained muscovite. The pluri–mm to mm–sized kyanite and staurolite porphyroblasts are post–kinematic with respect to the S_m (Fig. 6.3e,f); they are pervasively replaced by fine–grained muscovite at the rim, which partially obliterates their microstructural relationships. Carbonates (dolomite and calcite) are finely dispersed in the matrix and locally form pluri–mm aggregates together with quartz. The occurrence of skeletal garnet adjacent to these carbonate–rich aggregates and of carbonate inclusions within large garnet porphyroblasts, suggests that carbonates are involved in the garnet–forming reaction. Among the carbonates, dolomite systematically occurs as rounded inclusion within calcite, thus suggesting that calcite is a late phase. Chlorite is a retrograde mineral, mostly developed at the expense of biotite.

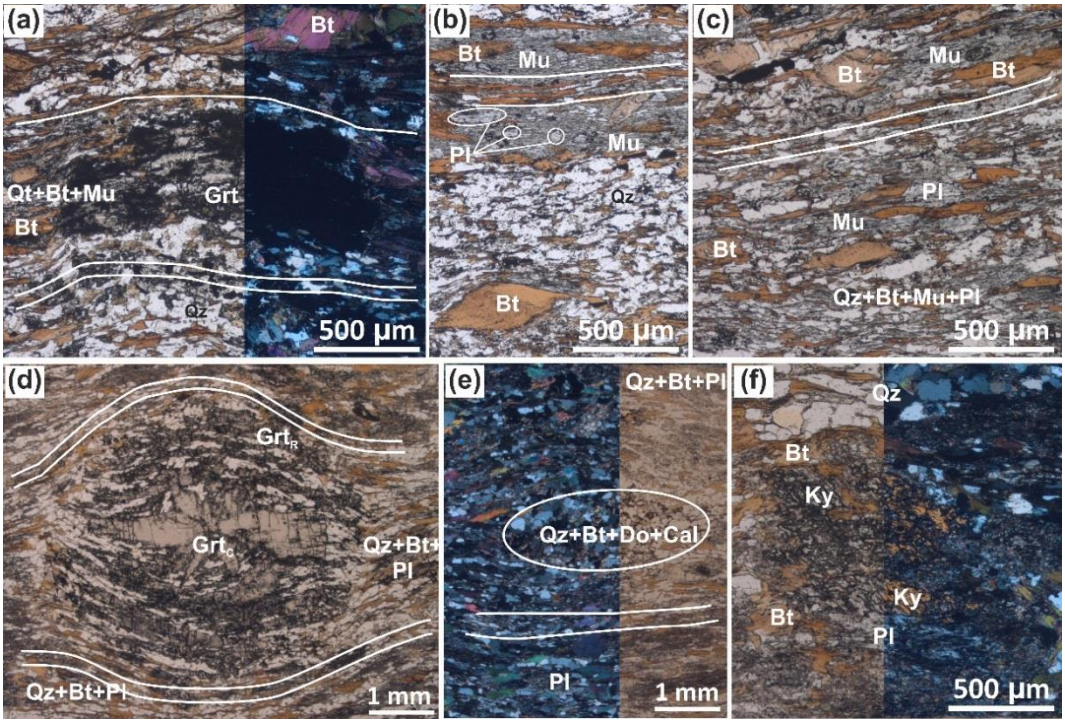

Fig. 6.3: Mineral assemblages and microstructures of samples 17b–12 (a–c) and 17a–29 (d–f). White lines in all the photographs represent the main foliation S_m. **Sample 17b–12** (two–micas, Pl+Grt –bearing graphitic schist): (a) Skeletal garnet porphyroblast overgrowing the S_m (PPL/XPL); (b) post–kinematic strongly zoned plagioclase (Na–rich core and Ca–rich rim) (PPL) (c) Late biotite overgrowing the S_m (PPL). **Sample 17a–29** (Grt+Pl+Ky+St –bearing biotitic schist): (d) Centimetric garnet porphyroblast with two distinct domains: a syn–kinematic core (GrtC) and a post–kinematic rim (GrtR) (PPL); (e) Skeletal garnet porphyroblast including dolomite (XPL/PPL); (f) Kyanite and plagioclase overgrowing the S_m (PPL/XPL).

Biotite defining the syn–S_m and the post–S_m generations are quite similar in composition, with XMg=0.67–0.71 and Ti=0.05–0.10 a.p.f.u. (Fig. 6.9d). Plagioclase in the matrix is mostly a bytownite, with XCa=0.72–0.84; few labradorite compositions are preserved in the core, with XCa=0.55–0.61 (Fig. 6.9b). Garnet porphyroblasts have well–preserved prograde zoning, with XMg and XFe increasing from core to rim, whereas XCa and XMn show opposite behaviour, i.e., they decrease rimward (Fig. 6.9a). The garnet core and rim compositions are in the range: GrtC: $Alm_{58–59}Grs_{20–22}Prp_{10–12}Sps_{8–11}$; GrtR: $Alm_{58–61}Grs_{18–20}Prp_{15–17}Sps_{5–6}$. Staurolite has XMg=0.27–0.31. Chlorite and muscovite are mostly retrograde phases: muscovite has Si = 3.00–3.11 a.p.f.u. and very low Na contents in the range Na = 0.00–0.05 a.p.f.u. (Fig. 6.9c), and chlorite is Mg–rich, with XMg = 0.64–0.70. Carbonates have compositions close to the calcite and dolomite end–members, respectively. Calcite has limited amounts of magnesite, siderite and rhodochrosite components ($Cal_{91–99}Mgs_{0–4}Sd_{0–2}Rds_{0–3}$), and dolomite is characterized by higher amounts of Fe (ankerite) and Mn (Mn–dolomite) components, in the range $Dol_{73-79}Ank_{18-26}MnDol_{1-2}$.

6.2.1.3 Sample 15a–28a

This amphibole + plagioclase –bearing carbonatic–phlogopitic schist consists of phlogopite (32%), quartz (26%), calcite (14%), amphibole (11%), plagioclase (10%) and dolomite (7%), with accessory titanite. The main foliation (S_m) is marked by the preferred orientation of the pale brown phlogopite, which defines mm–thick continuous layers alternated with pluri–mm thick quartzitic layers (Fig. 6.2c, 6.4a). The S_m is crenulated, with the development of asymmetric open folds (Fig. 6.4a); an axial planar foliation (S_{m+1}) locally occurs, which is defined by phlogopite. Carbonate minerals (calcite and dolomite) are quite abundant and dispersed in the main foliation (Fig. 6.4b). The occurrence of rounded inclusions of dolomite within calcite suggests that at least some calcite developed at the expenses of dolomite. Plagioclase forms mm–sized porphyroblasts overgrowing both the S_m and the S_{m+1} (i.e. post–S_m and post–S_{m+1}) (Fig. 6.4a). Colourless amphibole occurs as pluri–mm sized porphyroblasts statically overgrowing both the S_m and the crenulation folds, i.e., post–kinematic with respect to both the S_m and the S_{m+1} (Fig. 6.4b,c). Amphibole porphyroblasts are poikiloblastic, with abundant inclusions of quartz, dolomite and calcite.

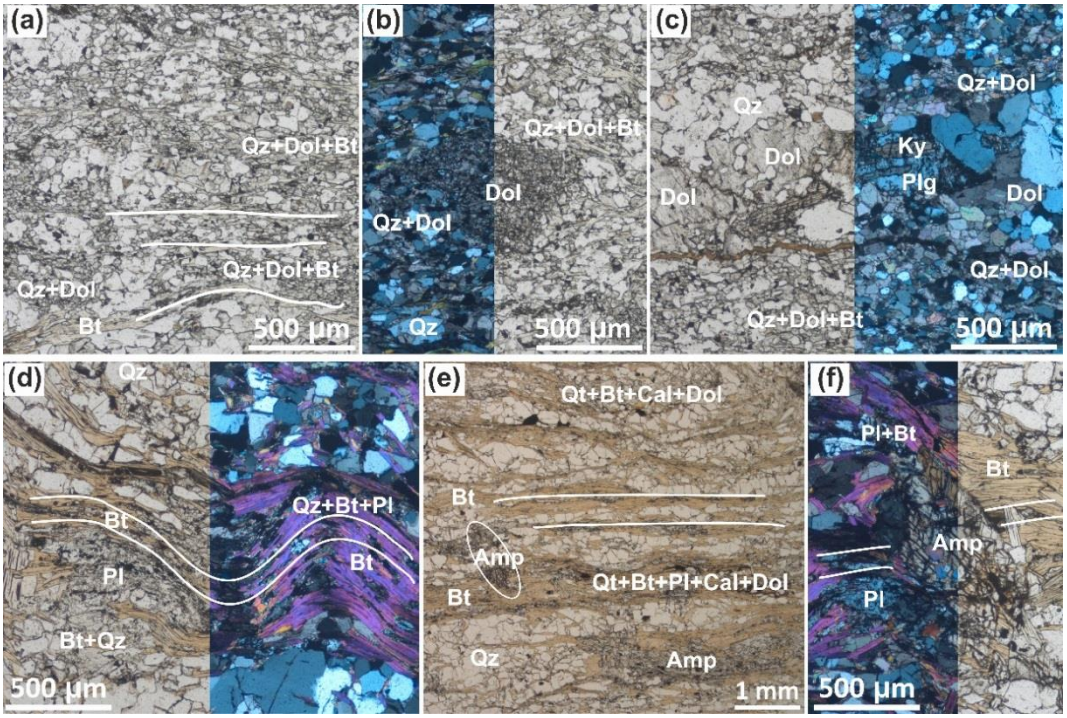

Fig. 6.4: Mineral assemblages and microstructures of samples 15a–28a (a–c) and 18a–26 (d–f). **Sample 15a–28a** (Hbl+Pl –bearing carbonatic–phlogopitic schist: (a) crenulated S_m defined by phlogopite (PPL/XPL); (b,c) Hornblende porphyroblasts overgrowing the S_m (PPL and XPL/PPL). **Sample 18a–26** (phlogopitic dolomitic calcschist): (d) fine–grained phlogopite defining the S_m and alternated with pluri–mm–thick layers dominated by fine –grained dolomite and quartz (PPL); (e) fine–grained aggregates of dolomite with inclusions of chlorite enveloped by the main foliation (XPL/PPL); (f) thin layer rich in fine–grained kyanite, aligned with the S_m (PPL/XPL).

Biotite is rich in magnesium and does not show significant compositional differences between the various generations, with XMg=0.81–0.83 and Ti=0.04–0.07 a.p.f.u. (Fig. 6.9d). Plagioclase is a bytownite and it is slightly zoned, with XAn decreasing rimward (Fig. 6.9b). Overall, the XCa in plagioclase is in the range XCa=0.76–0.90. Carbonates are compositionally closed to the calcite and dolomite end–members; average compositions of calcite and dolomite are $Cal_{93-95}Mgs_{4-6}Sd_{1-2}Rds_{0}$ and $Dol_{85-87}Ank_{10-14}MnDol_{0-1}$, respectively. Porphyroblastic amphibole is a magnesio–hornblende with a homogeneous composition, showing XMg mostly in the range XMg=0.85–0.90.

6.2.1.4 Sample 18a–26

This phlogopitic dolomitic calcschist consists of dolomite (37%), quartz (42%), phlogopite (8%), plagioclase (8%), chlorite (4%) and a minor amount of kyanite (1%) and late muscovite. The main foliation S_m is defined by the preferred orientation of fine–grained phlogopite concentrated in thin and discontinuous layers, alternated with pluri–mm –thick layers dominated by fine–grained dolomite and quartz (Fig. 6.2d). A mm–thick vein occurs parallel to the main foliation, and it is mostly filled by quartz and dolomite, which are coarser–grained with respect to the matrix (Fig. 6.2d). Phlogopite shows a weak pleochroism from very pale brown to colourless. Dolomite is mostly fine–grained and dispersed in the matrix; it also forms pluri–mm sized, fine–grained aggregates enveloped by the main foliation, locally including minor chlorite flakes (Fig. 6.4b). Dolomite appears homogeneous under CL, showing a dark red luminescence colour, without systematic variation related to its microstructural position (Appendix 10, Fig. S14a). Plagioclase is mostly concentrated within the quartz–rich vein, but also occurs as fine–grained randomly dispersed blasts in the matrix. The sub–mm sized kyanite is concentrated in thin layers aligned with the main foliation, particularly evident under CL for their bright luminescence (Appendix 10, Fig. S14a). Muscovite is generally a late phase, locally replacing plagioclase. Also, chlorite is mostly a retrograde mineral, developed at the expense of biotite, except for the few flakes locally included in the fine–grained aggregates of dolomite, which could be interpreted as prograde relics.

Phlogopite defining the S_m shows very low Fe contents, with XMg=0.94–0.95 and Ti=0.02–0.04 a.p.f.u. (Fig. 6.9d). Dolomite is almost pure, with low amounts of ankerite component ($Dol_{94-96}Ank_{3-5}$); no compositional differences are observed between the fine–grained dolomite in the matrix and that occurring in the pluri–mm aggregates enveloped by the main foliation. Plagioclase in the matrix is mostly andesine–labradorite, with quite scattered XCa values ranging from XCa=0.45–0.48 to XCa=0.56–0.69 (Fig.6.9b), whereas the plagioclase within the quartz + dolomite vein is an oligoclase with XAn=0.12–0.28. The retrograde chlorite and muscovite are homogeneous with XMg=0.93–0.94 and Si=3.11–3.14 a.p.f.u., Na=0.07–0.10 a.p.f.u., respectively.

6.2.1.5 Sample 17b–10b

This impure phlogopitic dolomitic marble consists of dolomite (81%), quartz (16%), phlogopite (2%) and minor amounts of muscovite and K–feldspar. It has a banded structure, defined by mm– to pluri–mm thick silicate layers alternated with cm–thick carbonatic layers (Fig. 6.2e). Dolomite is granoblastic and shows a quite homogenous fine–grained size, with few coarse–grained blasts concentrated in the silicate–rich layers (Fig. 6.5a,b). Under CL, dolomite mostly shows a homogeneous dark red luminescence colour, with few exceptions: (i) some fine–grained interstitial grains appear bright yellow and zoned (Appendix 10, Fig. S14b), and (ii) the coarse–grained blasts associated to the silicate layers are slightly zoned, with very dark red cores and dark red rims (Fig. 6.5c and Appendix 10, Fig. S14b). The main foliation S_m is defined by the orientation of the fine–grained, very pale brown phlogopite (Fig. 6.5b), and minor muscovite. This last also occurs as a late phase locally replacing K–feldspar. A minor amount of fine–grained K–feldspar is randomly distributed within the dolomite matrix.

Dolomite is almost pure, with composition in the range $Dol_{97–98}$ $Ank_{1–2}$. Phlogopite has a very low Fe content, with XMg=0.96–0.97 and Ti=0.04–0.06 a.p.f.u. Muscovite is anomalously enriched in the celadonitic component, with Si values in the range Si=3.25–3.44 a.p.f.u., counterbalanced by Mg contents of 0.28–0.39 a.p.f.u., whereas no Fe has been detected. The K–feldspar in the matrix is orthoclase with XOr=0.93–0.95 and XAb=0.05–0.07 and systematically contains low amounts of Ba up to 0.02–0.03 a.p.f.u.

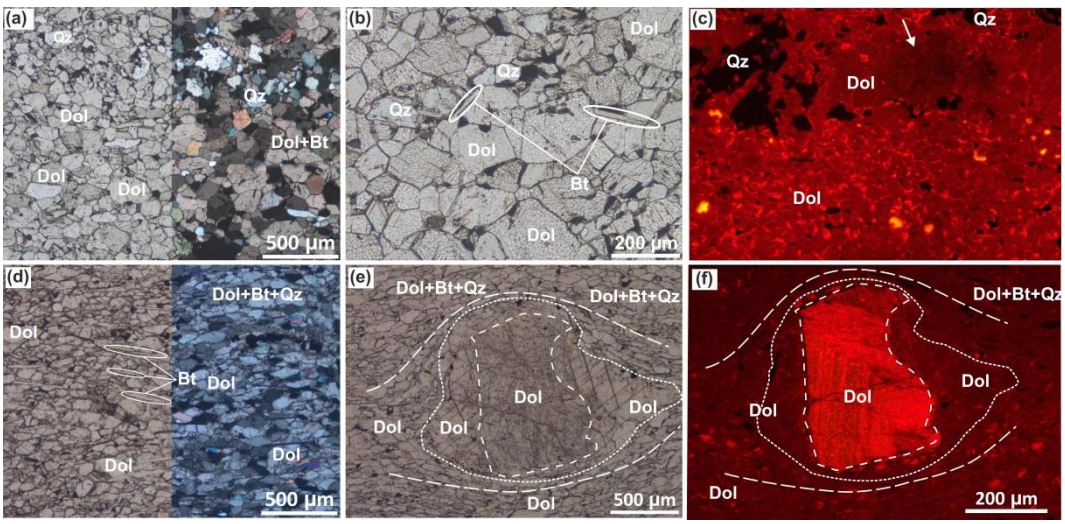

Fig. 6.5: Mineral assemblages and microstructures of samples 17b–10b (a-c) and 21a–22a (d-f). **Sample 17b–10b** (phlogopitic dolomitic marble): (a) granoblastic and homogeneous fine–grained dolomite alternated with mm–thick discontinuous silicatic layers (PPL/XPL); (b) granoblastic dolomite and interstitial phlogopite (PPL); (c) CL image showing most of the dolomite with homogeneous dark red luminescence colour, except for a coarse–grained blast slightly zoned, with very dark red cores and dark red rims and fine–grained (white arrow), and few interstitial blasts characterized by a bright yellow luminescence (CL). **Sample 21a–22b** (phlogopitic dolomitic marble): (d) fine-grained granoblastic dolomite alternated with discontinuous silicate layers (PPL/XPL); (e) cm–sized dolomite clast surrounded by the S_m (dotted lines) defined by granoblastic dolomite (PPL); (f) CL image of the same dolomite clast of (e) characterized by sharp zoning (CL).

6.2.1.6 Sample 21a–22a

This impure phlogopitic–muscovitic dolomitic marble consists of dolomite (93%), quartz (1%), phlogopite (1%), muscovite (5%) and sulphide minerals. The main foliation S_m is defined by the preferred orientation of fine–grained phlogopite and muscovite concentrated in discontinuous layers alternated with fine–grained dolomite (Fig. 6.5d; see also Fig. 4.7e). Dolomite is granoblastic and shows a homogeneous fine–grain size, with a few larger clasts enveloped by the S_m (Fig. 6.5e). Under CL, the fine–grained dolomite in the matrix shows homogeneous dark red luminescence colour, whereas two different types of coarse–grained dolomite clasts can be distinguished based on their contrasting luminescence: (i) abundant bright orange–yellow clasts, which appear also zoned (Fig. 6.5f and Appendix 10, Fig. S14c) and are concentrated in millimetre–thick layers with a brecciated structure, and (ii) less abundant very dark red clasts, isolated in the matrix (Appendix 10, Fig. S14c). A minor amount of calcite is also present in the form of veins.
Dolomite is almost pure, with a homogeneous composition in the range $Dol_{96–99}Ank_{2–4}$; no significant compositional variations have been observed among the fine–grained dolomite in the matrix and the different types of clastic dolomite, at least concerning the major elements detected at SEM–EDS. Phlogopite has a very low Fe content, with XMg=0.97–0.99 and Ti=0.02–0.04 a.p.f.u. Muscovite is very fine–grained, with Si values in the range Si=3.1–3.2 a.p.f.u and a XMg content of 0.21–0.30 a.p.f.u.

6.2.2 Magnesite series

6.2.2.1 Sample 17a–36b

This sample is a muscovitic schist with phlogopite, plagioclase, epidote ± kyanite porphyroblasts; it consists of quartz (54%), muscovite (24%), phlogopite (21%), plagioclase (2%), a minor amount of epidote (<1%) and accessory apatite. Although not present in the thin section used for the SEM–EDS analyses and map, kyanite has additionally been observed in a thin section obtained from the same sample. The main foliation (S_m) is marked by the preferred orientation of the fine–grained muscovite which defines thin layers pervasively alternating with quartz–rich layers (Fig. 6.6a and 6.7a,b). Phlogopite, plagioclase, epidote and kyanite porphyroblasts are all post–kinematic with respect to the main foliation, statically overgrowing it (Fig. 6.7a,b). Phlogopite forms pluri–mm sized post–S_m porphyroblasts, but also occurs as finer–grained flakes aligned with the S_m (Fig. 6.7a). Plagioclase porphyroblasts are millimetric in size and have a skeletal habit, and epidote is strongly zoned, with an allanitic core and a clinozoisite rim (Fig. 6.7a,b).
The fine–grained muscovite defining the S_m is characterized by a significant enrichment in celadonitic component, with Si = 3.10–3.25 a.p.f.u. (Fig. 6.9c), counterbalanced by $(Mg+Fe_{tot})$=0.29–0.41. Muscovite compositions plot systematically above the line of ideal celadonitic substitution in the Si vs. $(Mg+Fe_{tot})$ diagram (Fig. 6.9c), suggesting that all Fe is

in the trivalent state. Na contents are in the range Na=0.06–0.08 a.p.f.u. Phlogopite is almost pure, with XMg=0.91–0.93 and Ti=0.05–0.06 (Fig. 6.9d). Plagioclase is andesine, with XCa mostly in the range XCa=0.32–0.37 and sporadic values up to XCa=0.42 (Fig. 6.9b). Epidote has an allanitic core and a clinozoisite rim with XZo=0.31–0.39.

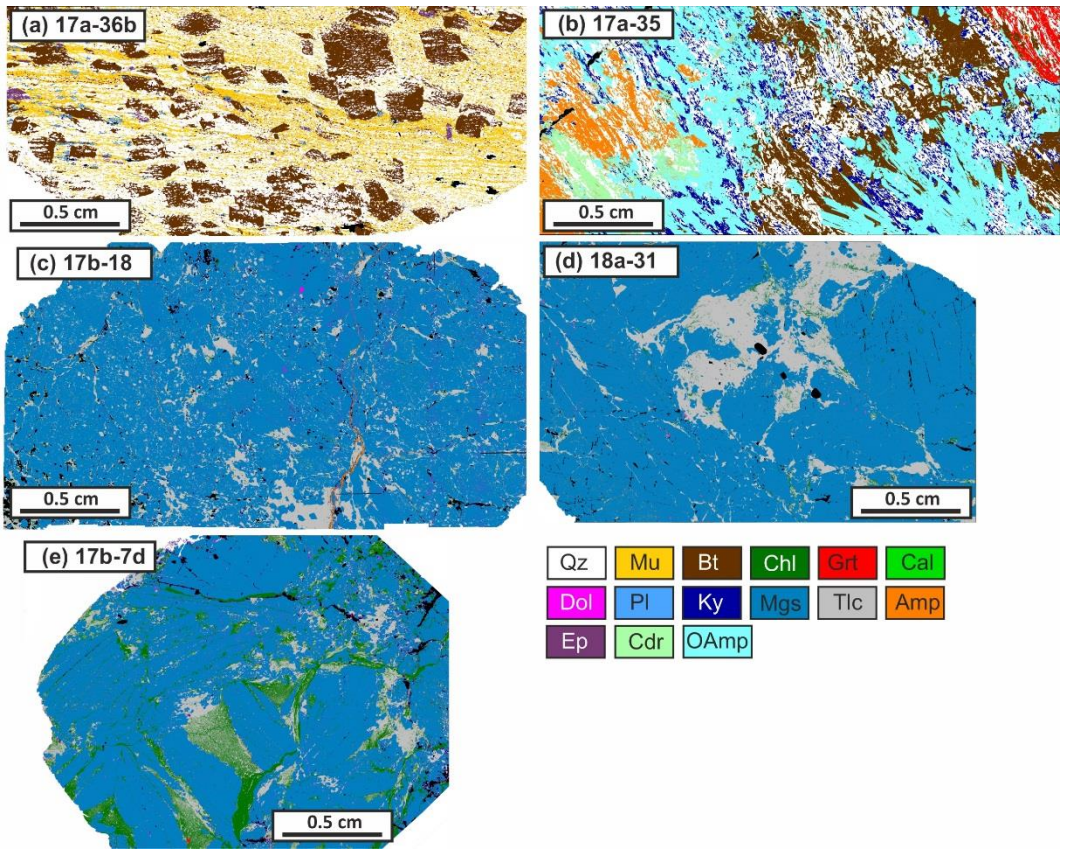

Fig. 6.6: Processed X–Ray maps of the studied carbonate–bearing lithologies belonging to the magnesite series: (a) 17a–36b, (b) 17a–35, (c) 17b–18, (d) 18a–31, (e) 17b–7d.

6.2.2.2 Sample 17a–35

This amphibole + kyanite + garnet + cordierite –bearing, phlogopitic schist consists of quartz (27%), orthoamphibole (29%), phlogopite (20%), kyanite (10%), green Ca–amphibole (6%), garnet (3%) and cordierite (5%). The sample has a banded structure (Fig. 6.6b), with alternated pluri-cm domains either phlogopite-rich (phlogopite + kyanite + orthoamphibole + garnet), or amphibole–rich (Ca–amphibole + orthoamphibole + cordierite). The main foliation (S_m) is defined by the preferred orientation of the pale brown phlogopite in the phlogopite–rich domains, and by the preferred orientation of orthoamphibole in the amphibole–rich domains (Fig. 6.7c,d). The S_m is not pervasive, because it is almost completely obliterated by the static overgrowth of pluri–mm to cm–sized porphyroblasts of orthoamphibole, garnet, kyanite, Ca–amphibole and/or cordierite (Fig. 6.6b). In the phlogopite–rich domains, the porphyroblastic phases overgrowing the S_m are: (i) cm–sized garnet, including an internal foliation defined by quartz, continuous with the S_m (Fig. 6.6b);

(ii) pluri–mm skeletal kyanite, partially intergrown with (iii) pluri–mm colourless orthoamphibole (Fig. 6.7c). In the amphibole–rich domains, the porphyroblastic phases are: (i) pluri–mm green Ca–amphibole, partially replaced by orthoamphibole, and (ii) pluri–mm cordierite elongated along the main foliation and overgrowing it (Fig. 6.7d).

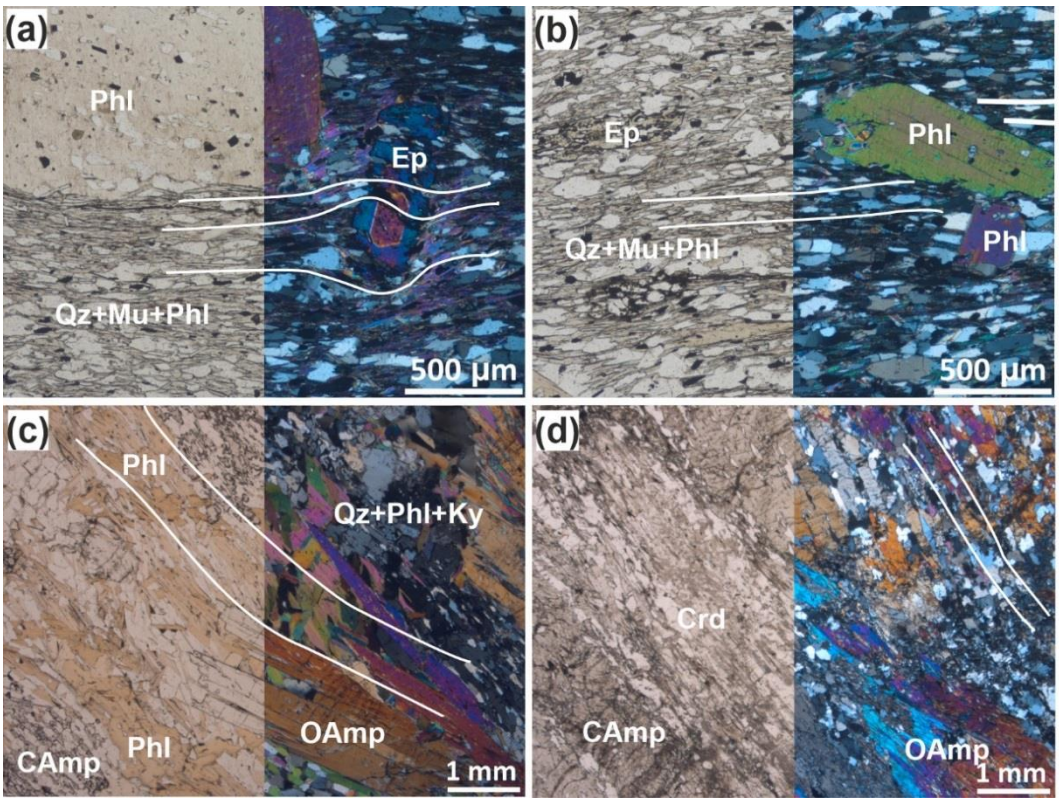

Fig. 6.7: Representative assemblages and microstructures of samples 17a–36b (a,b) and 17a–35 (c,d). **Sample 17a–36b** (muscovitic schist with phlogopite, plagioclase, epidote ± kyanite porphyroblasts): (a,b) Phlogopite porphyroblasts overgrowing the S_m defined by muscobite and minor fine–grained phlogopite; post–kinematic plagioclase and epidote porphyroblasts also occur (PPL/XPL). **Sample 17a–35** (Amp+Ky+Grt+Crd–bearing, phlogopitic schist): (c) post–kinematic ortho–amphibole, Ca–amphibole and kyanite (PPL/XPL); (d) post–kinematic cordierite, Ca–amphibole, kyanite and ortho–amphibole overgrowing the S_m defined by phlogopite (PPL/XPL).

Phlogopite contains relatively low amounts of Fe, with XMg values mostly in the range XMg=0.79–0.82, and a few values slightly enriched in Fe, with XMg=0.72–0.78. Ti content ranges between 0.03 and 0.06 a.p.f.u. (Fig. 6.9d). Ortho–amphibole is an anthophyllite, with XMg mostly in the range 0.67–0.73, and very low amounts of Ca (Ca=0.30–0.50 a.p.f.u.). The green Ca–amphibole is an aluminous–tschermackite, with XMg=0.80–0.85 and Si=6.29–6.48 a.p.f.u. It contains low amounts of Na, up to Na=0.28–0.32 a.p.f.u. Garnet porphyroblasts are slightly zoned with XMg increasing toward the rim, whereas XCa, XFe and XMn decrease toward the rim (Fig. 6.9a). The garnet core and rim compositions are in the range: GrtC: $Alm_{62–65}Grs_{14–16}Prp_{20–23}Sps_{1}$; GrtR: $Alm_{57–62}$ $Grs_{10–14}Prp_{25–32}Sps_{0–0.5}$. Cordierite has XMg=0.52–0.83.

6.2.2.3 Samples 17b–7d, 17b–18, 18a–31

Samples 17b–7d, 17b–18 and 18a–31 are magnesite + talc rocks consisting of magnesite (75%–80%), talc (12%–17%), chlorite (1%–14%) (Fig. 6.2g) and minor amounts of dolomite and accessory apatite. Magnesite is medium–to coarse–grained, with a strong heterogeneous grain size (Fig. 6.8 a,b).

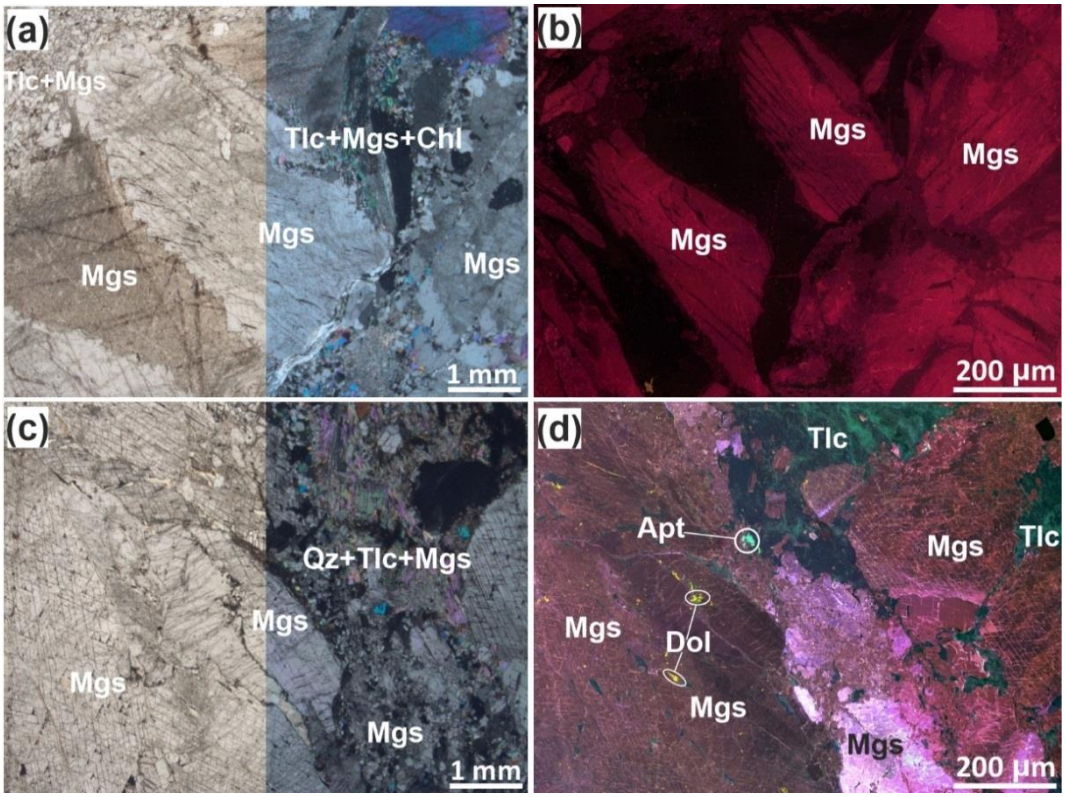

Fig. 6.8: Representative assemblages and microstructures of samples 17b–7d (a, b) and 18a–31 (c, d). **Sample 17b–7d** (Mgs+Tlc rock): (a) coarse–grained magnesite partially replaced by the second generation of magnestie associated with talc and Mg–chlorite. Note that the coarse–grained magnesite has a large cloudy core surrounded by a thin clear rim (PPL/XPL). (b) CL image of coarse–grained magnesite crystals with large cores showing a red luminescence, in contrast with the very dark red luminescence colour of the rims (CL). **Sample 18a–31** (Mgs+Tlc rock): (c) coarse–grained magnesite partially replaced by a second generation of magnesite associated with talc (PPL/XPL); (d) CL image of coarse–grained magnesite crystals with large cores showing a red luminescence, in contrast with the very dark red luminescence colour of the rims. Note the small rounded inclusions of dolomite and apatite in the core of the large magnesite crystals (CL).

Most of the magnesite crystals in all the samples are pluri–mm to cm–sized and often show an elongated habit. The coarse–grained magnesite crystals generally have a cloudy appearance, because they are crowded of fluid and solid inclusions, whereas the thin rims at contact with the surrounding talc ± chlorite are clear and transparent (Fig. 6.8a). The very fine–grained solid inclusions are especially abundant in the cores of the pluri–cm sized magnesite and mostly consist of rounded inclusions of dolomite and apatite (Fig. 6.8d). The microstructural zoning observed in the coarse–grained magnesite crystals is also evident

under CL, with the large magnesite cores showing a red luminescence which contrasts with the very dark red luminescence colour of the rims (Fig. 6.8b and Appendix 10, Fig. S13d). The coarse–grained magnesite is partially replaced at the rim and along fractures by medium–grained talc and variably abundant fine–grained Mg–chlorite, associated with the second generation of fine–grained magnesite, granoblastic and with a clear appearance (Fig. 6.8a.c). This second generation of magnesite shows the same very dark red luminescence colours as the rims of the coarse–grained magnesite (Fig. 6.8b,d and Appendix 10, Fig. S13d).

Both magnesite and dolomite in all the samples are very close to the pure end–members, with very low amounts of the siderite and ankerite components, respectively (magnesite: $Mag_{93–99}Sd_{1–2}$; dolomite: $Dol_{98–99}Ank_{0–1}$). Talc and Mg–chlorite contain very low amounts of Fe, with XMg systematically in the range of 0.98–1.00.

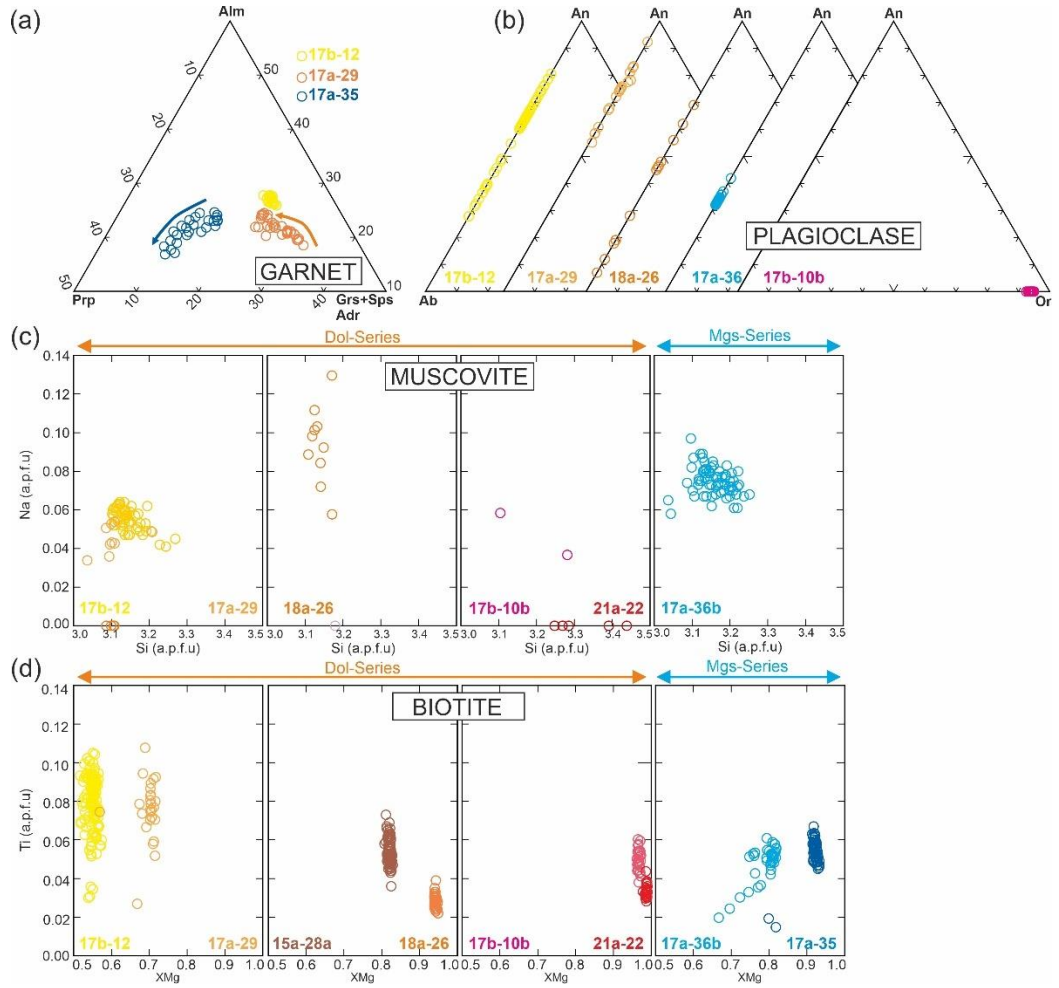

Fig. 6.9: Compositional diagrams for (a) garnet (arrows show the zoning trend from core to rim), (b) plagioclase, (c) muscovite, and (d) biotite in the samples investigated through thermodynamic modelling.

6.3 Thermodynamic modelling results

The goal of this modelling is to understand the nature of the main decarbonation reactions and to constrain the P–T conditions at which these reactions occurred. Therefore, P/T–$X(CO_2)$ pseudosections were calculated for the seven carbonate–bearing lithologies selected according to the strategy discussed in section 6.2: four samples from the dolomite series (17b–12, 17a–29, 15a–28a and 18a–26) and three from the magnesite series (17a–36b, 17a–35 and 17b–7d). The P/T–$X(CO_2)$ isochemical phase diagrams were calculated along a P/T gradient defined based on the P–T evolution constrained from the associated metapelites (see Chapter 5, section 5.4.1), as discussed in the Methods section (section 3.5.2) (i.e. a prograde stage characterized by an increase in both P and T conditions up to peak–P conditions, and a decompression stage from peak–P to peak–T conditions). In the interpretation of the phase diagrams presented in this chapter, it is therefore important to remember that, while temperature regularly increases along the vertical axes, pressure increases up to 600 °C, but decreases from T > 600 °C.

6.3.1 Dolomite series

6.3.1.1 Sample 17b–12

The P/T–$X(CO_2)$ isochemical phase diagram modelled for sample 17b–12 in the MnNKCFMASTO–H_2O–CO_2 system (Fig. 6.10a), is dominated by 4–, 5, and 6– variant fields (i.e. fields containing 8, 7, and 6 phases, respectively). Quartz and a Ti–bearing accessory mineral (either titanite, or rutile, or ilmenite) are stable in the entire P/T–$X(CO_2)$ range of interest. The chlorite stability field is located at relatively low P–T–$X(CO_2)$ conditions, for T>600 °C and $X(CO_2)$<0.2. Muscovite is predicted to be stable along most of the prograde and decompression evolution, up to 660–680 °C, independently from the $X(CO_2)$ values. During the prograde stage, biotite stability is limited to $X(CO_2)$<0.35, whereas it becomes the dominant phyllosilicate during the decompression stage, at every $X(CO_2)$ value. Dolomite and magnesite (i.e. Ca–Mg–Fe–Mn carbonate enriched in Mg) are modelled up to temperatures slightly higher than 600 °C. The Dol–out and Mgs–out curves are concave downward and mostly coincide with the garnet– and/or epidote–in boundaries. Garnet and epidote stability fields are therefore limited to relatively low $X(CO_2)$ values during the prograde stage, whereas during decompression (i.e. at T>600 °C), their stability is no more influenced by $X(CO_2)$. Epidote is stable up to 620 °C, whereas garnet is predicted up to 690 °C. Plagioclase and aluminosilicate are predicted to develop mostly at T>600 °C. The stability fields of the main phases are reported in Appendix 11, Fig. S15.

The ***protolith assemblage***, consisting of illite (29%), K–feldspar (7%), quartz (33%), chlorite (13%), dolomite (6%) and plagioclase (Ab8%, An4%), is reproduced at 400°C, $X(CO_2)$=0.02 by a modelled assemblage consisting of muscovite (35%), quartz (35%), chlorite (9%), dolomite (8%) and albite + paragonite (6%) (Fig. 6.10a,b). These conditions are therefore assumed as the starting point of the P/T–$X(CO_2)$ evolution.

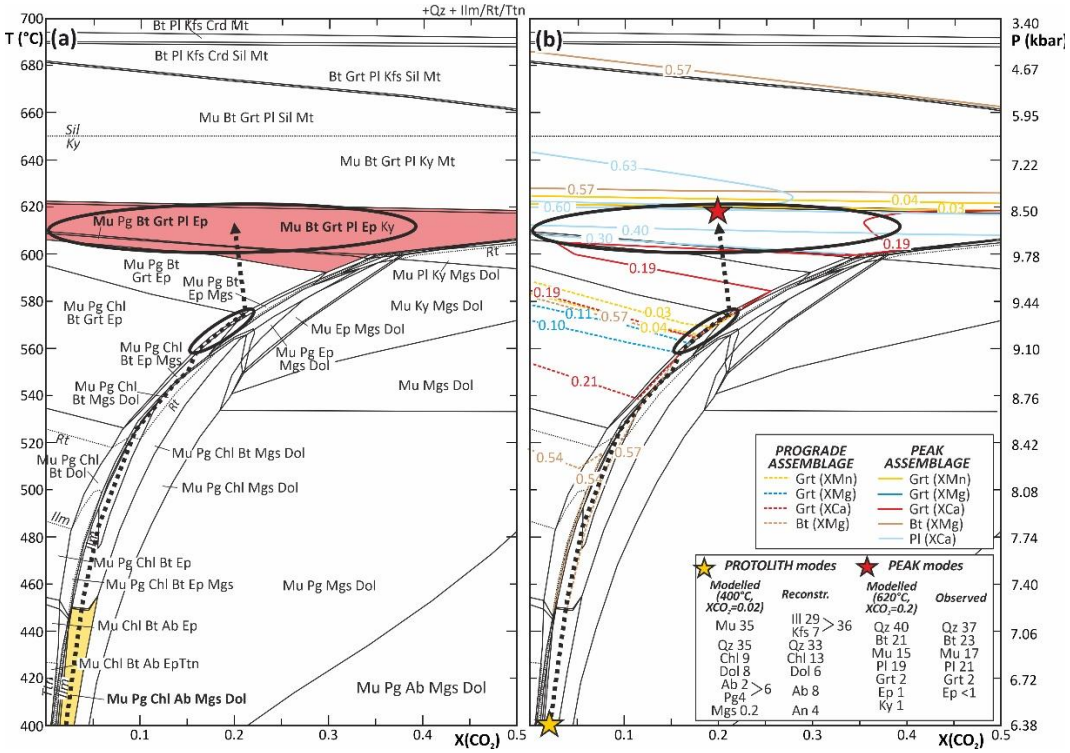

Fig. 6.10: (a) P/T–X(CO_2) isochemical phase diagram modelled for sample 17b–12 in the MnNKCFMASTO–H_2O–CO_2 system. The variance of the fields varies from two (i.e. 10 phases) to seven (i.e. 5 phases). Dotted lines delimit the stability fields of the Ti–bearing accessory minerals (titanite, rutile, ilmenite). The yellow field is the modelled stability field of the protolith's assemblage; the red fields correspond to the stability fields of the peak assemblage (for each modelled assemblage, the observed minerals are reported in bold). (b) Same P/T–X(CO_2) isochemical phase diagram as (a), contoured with the compositional isopleths for both prograde (dashed lines) and peak (continuous lines) phases. Yellow and red stars refer to the P–T–X(CO_2) conditions representing the best fit between the modelled and measured modal amounts of minerals in the protolith (yellow) and in the peak (red) assemblages. The black ellipses in both (a) and (b) summarize the prograde and peak P–T–X(CO_2) conditions. The dashed black arrows in both the diagrams represent the P–T–X(CO_2) evolution inferred for sample 17b–12 and discussed in Section 6.4.

The compositional isopleths modelled for garnet (Grt: XMg=0.10–0.11, XCa=0.19–0.21, XMn=0.03–0.04) converge in the very narrow 3–variant field Qz+Mu+Pg+Bt+Chl+Ep +Mgs+Grt+Ilm, constraining garnet nucleation at T=560–580 °C, P=9.1–9.4 kbar, X(CO_2)≈0.2 (Fig. 6.10b), and suggesting that garnet appearance is related to the breakdown of carbonate minerals, even if carbonates are no more preserved in the sample. The observed ***peak assemblage*** (Qz+Mu+Bt+Grt+Pl+Ep) is modelled by a large 4–variant field at T=600–620 °C, extended over the whole X(CO_2) interval (Fig. 6.10b). Kyanite is modelled in this field, but it is not observed in the sample. This is, however, a minor discrepancy, because the predicted amount of kyanite is very low (<1.5%). Garnet is mostly unzoned in this sample; this is in agreement with the modelled compositional isopleths, which do not predict significant changes in garnet composition from the prograde to the peak stage (Fig. 6.10b). Furthermore, the inferred peak P–T–X(CO_2) conditions are further confirmed by the

XMg and XCa isopleths modelled for biotite and plagioclase, which match well the measured compositions (biotite: XMg=0.53–0.57; plagioclase core: XCa=0.28–0.49; plagioclase rim: XCa=0.60–0.81) (Fig. 6.10b).

6.3.1.2 Sample 17a–29

The P/T–X(CO_2) pseudosection, calculated in the MnNKCFMAST–H_2O–CO_2 system (Fig. 6.11a), is dominated by 3–, 4–, and 5– variant fields (i.e. fields containing 8, 7, and 6 phases, respectively). Quartz is stable in the entire P/T–X(CO_2) range of interest, together with a Ti–bearing accessory mineral, represented by titanite, rutile or ilmenite depending on the P–T–X(CO_2) conditions. Among phyllosilicates, the chlorite stability field is limited to X(CO_2)<0.3 and T<640 °C, muscovite is predicted to be stable at T<615 °C over the entire range of X(CO_2), whereas biotite replaces chlorite at T>640 °C for X(CO_2)<0.3 and is predicted to be always stable along the modelled decompression path, independently from the X(CO_2) values. Calcite is stable at T<610 °C and the calcite–in boundary is concave downward; it coexists with dolomite in most fields, except for those located at X(CO_2)<0.02, in which dolomite is absent. The garnet stability field is complementary to that of calcite, being the garnet–in boundary mostly coincident with the Cal–out curve. Plagioclase stability is mostly limited to the decompression part of the P–T evolution (i.e. at T>600 °C), whereas at lower temperatures, the stable Ca–rich silicate is zoisite. Kyanite is modelled at X(CO_2)>0.1 along the prograde path, but becomes stable over the whole range of X(CO_2) at T>600 °C. The stability fields of the main phases are reported in Appendix 11, Fig. S16.

The ***protolith assemblage***, consisting of illite (24%), kaolinite (11%), quartz (31%), chlorite (15%), dolomite (14%) and plagioclase (Ab4%, An2%), is quite well reproduced at 400°C, X(CO_2)=0.02, where the modelled assemblage consists of muscovite (25%), chloritoid (10%), quartz (40%), chlorite (10%), dolomite (14%) and calcite (1%) (Fig. 6.11a,b). These conditions are therefore assumed as the starting point of the P–T–X(CO_2) evolution.

The compositional isopleths modelled for garnet core (GrtC: XMg=0.10–0.12, XCa=0.20–0.22, XMn=0.08–0.11) constrain its growth during the ***prograde stage***, at T=550–570 °C, P=8.8–9.2 kbar (in the Mu+Chl+Grt+Ky+Cal+Dol field) (Fig. 6.11b). The observed ***peak assemblage*** (Qz+Bt+GrtR+Ky+Pl+St+Dol, ±Mu±Cal) is modelled by a number of narrow 3– and 4–variant fields located at T=600–615 °C, P=8.8–9.8 kbar, X(CO_2)>0.3 (Fig. 6.11a). Calcite and dolomite, in fact, are predicted to be stable at T<610 °C and T<615 °C, respectively, whereas biotite and plagioclase only appear at T>600 °C for X(CO_2)>0.3 values. This implies that most of the minerals in sample 17a–29 grew during the decompression stage. Further constrain on the peak P–T–X(CO_2) conditions are given by the modelled compositional isopleths of the post–kinematic garnet rim (GrtR: XMg=0.15–0.17, XCa=0.18–0.20, XMn=0.05–0.06), combined with those of biotite (XMg=0.68–0.71) and plagioclase (XCa=0.72–0.84, and few cores analysis with XCa=0.55–0.61), which all converge at the P–T–X(CO_2) conditions constrained based on the modelled peak

assemblage field (Fig. 6.11b). Staurolite, occurring in low modal amounts in the same microstructural position as kyanite (i.e., post–kinematic phase) is not predicted at the inferred peak P–T conditions. This discrepancy could be related to the simplification of not considering the possible effects of chemical fractionation on the bulk composition due to the growth of garnet; however, the good match between the prediction of the modelling and the observed and measured assemblages and compositions makes the results of the modelling quite reliable.

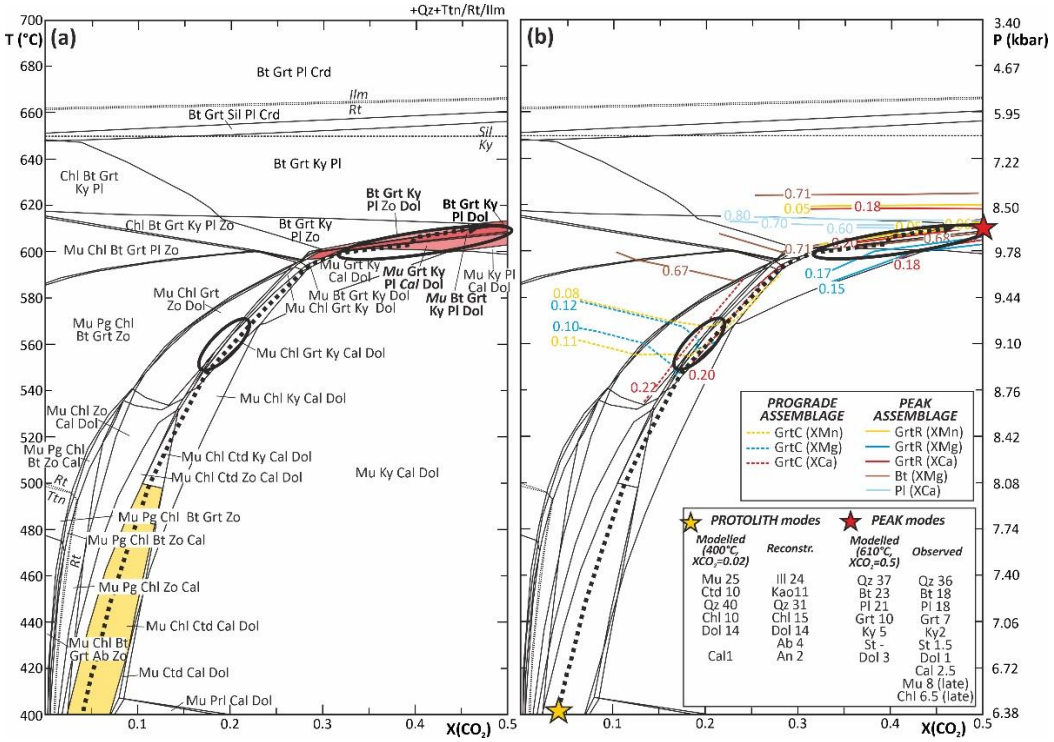

Fig. 6.11: (a) P/T–X(CO_2) isochemical phase diagram modelled for sample 17a–29 in the MnNKCFMAST–H_2O–CO_2 system. The variance of the fields varies from two (i.e., 9 phases) to five (i.e. 6 phases). Dotted lines delimit the stability fields of the Ti–bearing accessory minerals (titanite, rutile, ilmenite). The yellow field is the modelled stability field of the protolith's assemblage; the red fields correspond to the stability fields of the peak assemblage, with darker tones highlighting the best fit between the observed and the modelled assemblages (for each modelled assemblage, the observed minerals are reported in bold). (b) Same P/T–X(CO_2) isochemical phase diagram as (a), contoured with the compositional isopleths for both prograde (dashed lines) and peak (continuous lines) phases. Yellow and red stars refer to the P–T–X(CO_2) conditions representing the best fit between the modelled and measured modal amounts of minerals in the protolith (yellow) and in the peak (red) assemblages. The black ellipses in both (a) and (b) summarize the prograde and peak P–T–X(CO_2) conditions. The dashed black arrows in both diagrams represent the P–T–X(CO_2) evolution inferred for sample 17a–29 and discussed in Section 6.4.

6.3.1.3 Sample 15a–28a

The P/T–X(CO_2) pseudosection, calculated in the NKCFMAST–H_2O–CO_2 system (Fig. 6.12a) consists of 4– and 5– variant fields (i.e., fields containing 6 and 5 phases, respectively). Quartz is stable in the entire P/T–X (CO_2) range of interest, whereas Ti–bearing accessory

minerals are limited to T<560 °C (titanite) or 610 °C (rutile). Chlorite is stable in a relatively narrow P–T–X(CO_2) range, at T<590 °C, X(CO_2)<0.3. Along the prograde P–T path, muscovite and biotite show complementary stability fields: muscovite is stable at higher X(CO_2) values and lower temperatures, whereas biotite is stable at lower X(CO_2) and higher temperatures. Biotite is, instead, the only mica stable along most of the decompression evolution, being muscovite breakdown predicted at T< 610 °C. Dolomite is predicted to be stable at T<600 °C over a wide range of X(CO_2), being the Dol–out boundary concave downward; calcite is also predicted to be stable in low amounts at T<630 °C for relatively high X(CO_2) values, whereas higher amounts of calcite are predicted in a narrow X(CO_2) interval at X(CO_2)=0.00–0.02. Ca–rich silicates are represented by amphibole, clinopyroxene, zoisite and plagioclase, and their stability fields are mostly complementary to those of carbonates. Amphibole is stable at relatively low temperatures and for X(CO_2) <0.3 during the prograde evolution, whereas its stability is significantly enlarged over a wide range of X(CO_2) values during the decompression stage. Zoisite mostly coexists with amphibole along the prograde P/T gradient, but its stability is limited to T<620 °C during decompression. Plagioclase stability field is confined to T>490 °C and X(CO_2) <0.3 in the prograde stage, whereas at T>600 °C it of always stable, independently from the X(CO_2) values. The stability fields of the main phases are reported in Appendix 11, Fig. S17.

The ***protolith assemblage***, consisting of illite (16%), K–feldspar (8%), quartz (29%), chlorite (12%), dolomite (31%) and plagioclase (Ab3%), is reproduced at 400°C, X(CO_2)=0.02 (Fig. 6.12a,b), where the modelled assemblage consists of muscovite (23%), quartz (32%), chlorite (11%), dolomite (32%) and albite (2%). These conditions are therefore assumed as the starting point of the P–T–X(CO_2) evolution.

The observed ***peak assemblage*** (Qz+Bt+Hbl+Pl+Dol+Cal) is modelled by a 5–variant field located at T=610–620 °C, P=8.5–9.1 kbar, X(CO_2)>0.45 (Fig. 6.12a); dolomite is predicted as the only carbonate mineral at these conditions, but the predicted modal amount of dolomite (22%) is close to the observed amount of dolomite + calcite (21%). The XMg and XCa isopleths modelled for biotite/hornblende and for plagioclase, respectively, and corresponding to their measured compositions (biotite: XMg=0.81–0.83; hornblende: XMg=0.85–0.90; plagioclase: XCa=0.76–0.90), converge at the inferred peak P–T conditions (Fig. 6.12b). The good match between modelled and measured mineral compositions further confirms the reliability of the P–T–X(CO_2) estimates.

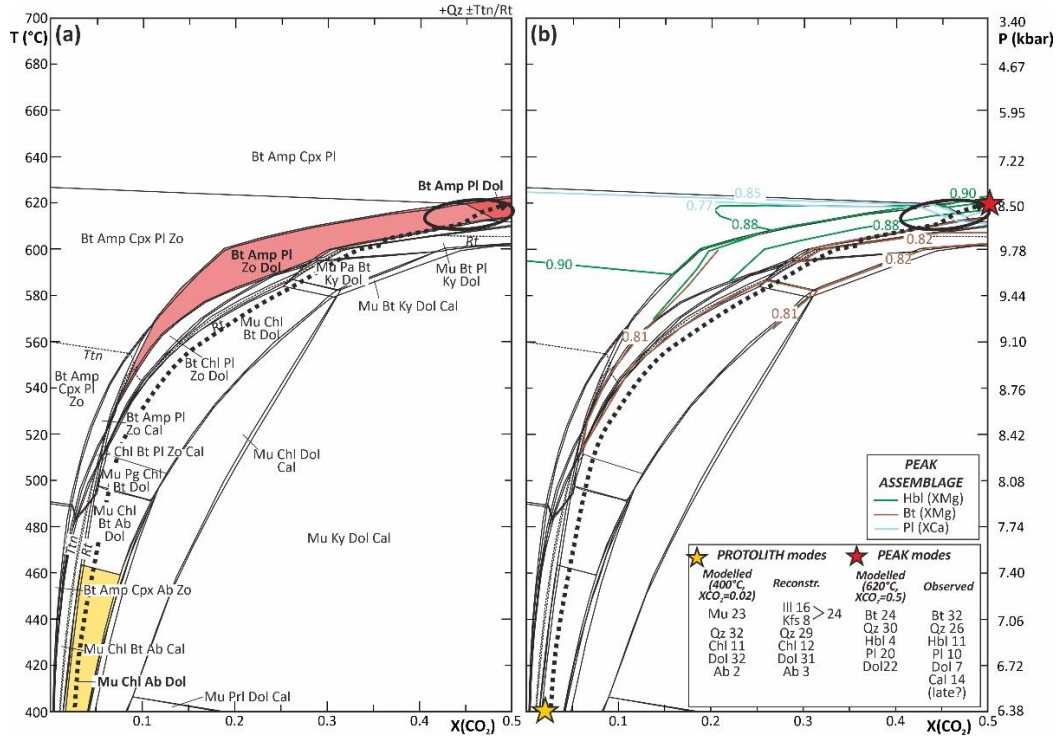

Fig. 6.12: (a) P/T–X(CO_2) isochemical phase diagram modelled for sample 15a–28a in the NKCFMAST–H_2O–CO_2 system. The variance of the fields varies from two (i.e. 8 phases) to five (i.e. 5 phases). Dotted lines delimit the stability fields of the Ti–bearing accessory minerals (titanite, rutile). The yellow field is the modelled stability field of the protolith's assemblage; the red fields correspond to the stability fields of the peak assemblage, with darker tones highlighting the best fit between the observed and the modelled assemblages (for each modelled assemblage, the observed minerals are reported in bold). (b) Same P/T–X(CO_2) isochemical phase diagram as (a), contoured with the compositional isopleths for peak phases. Yellow and red stars refer to the P–T–X(CO_2) conditions representing the best fit between the modelled and measured modal amounts of minerals in the protolith (yellow) and in the peak (red) assemblages. The black ellipses in both (a) and (b) summarize the P–T–X(CO_2) peak conditions. The dashed black arrows in both diagrams represent the P–T–X(CO_2) evolution inferred for sample 15a–28a and discussed in Section 6.4.

6.3.1.4 Sample 18a–26

The P/T–X(CO_2) pseudosection modelled for sample 18a–26 in the NKCFMAST–H_2O–CO_2 system (Fig. 6.13a) mostly consists of 3–, 4– and 5– variant fields (i.e., fields containing 7, 6, and 5 phases, respectively). Quartz is stable over the entire range of modelled P–T–X(CO_2) conditions; a Ti–bearing accessory mineral (either titanite or rutile) is present at T<610 °C for a relatively large range of X(CO_2) values but does not occur during most of the decompression stage. Chlorite is predicted to be stable only during the prograde evolution, for T<600 °C and X(CO_2)<0.35. The other two phyllosilicates, muscovite and biotite, show complementary stability fields, with muscovite stable at lower temperatures and higher X(CO_2) values, and biotite stable at higher temperatures and lower X(CO_2) values. The muscovite–out curve limits the muscovite field at T<610 °C, whereas biotite is the dominant mica during the decompression stage. Carbonate minerals are stable over a large P–T–X(CO_2) range, with dolomite predicted in higher amounts with respect to

Ca–Mg–Fe–Mn carbonate. This last is mostly magnesite for $X(CO_2)>0.05$, whereas it is calcite in the elongated and narrow fields predicted for the lowermost $X(CO_2)$ values. Ca–rich silicates mostly include zoisite, plagioclase, scapolite, amphibole and clinopyroxene; all these minerals are predicted to be stable at P–T–$X(CO_2)$ conditions complementary with respect to those at which carbonate minerals are stable and coexist in several fields. During the prograde evolution, kyanite is predicted only in trace amounts and for $X(CO_2)$ >0.1; it becomes more relevant in the decompression stage, where it is limited to T<615 °C, $X(CO_2)>0.35$. The stability fields of the main phases are reported in Appendix 11, Fig. S18.

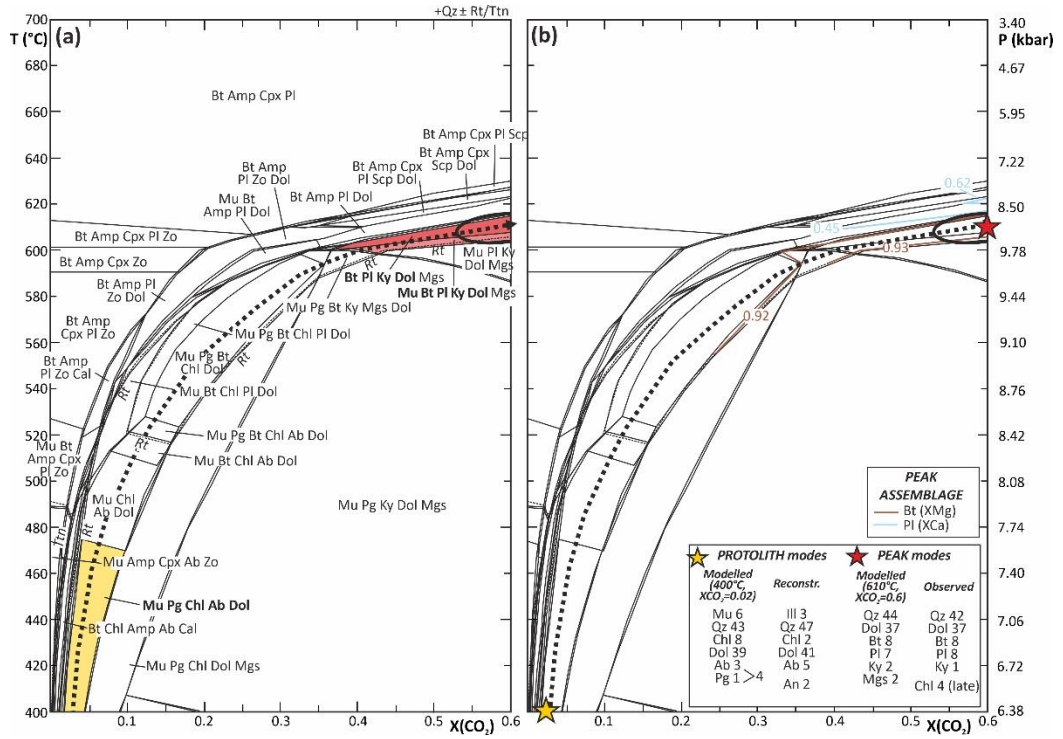

Fig. 6.13: (a) P/T–$X(CO_2)$ isochemical phase diagram modelled for sample 18a–26 in the NKCFMAST–H_2O–CO_2 system. The variance of the fields varies from two (i.e. 8 phases) to five (i.e. 5 phases). Dotted lines delimit the stability fields of the Ti–bearing accessory minerals (titanite, rutile). The yellow field is the modelled stability field of the protolith's assemblage; the red fields correspond to the stability fields of the peak assemblage, with darker tones highlighting the best fit between the observed and the modelled assemblages (for each modelled assemblage, the observed minerals are reported in bold). (b) Same P/T–$X(CO_2)$ isochemical phase diagram as (a), contoured with the compositional isopleths for peak phases. Yellow and red stars refer to the P–T–$X(CO_2)$ conditions representing the best fit between the modelled and measured modal amounts of minerals in the protolith (yellow) and in the peak (red) assemblages. The black ellipses in both (a) and (b) summarize the P–T–$X(CO_2)$ peak conditions. The dashed black arrows in both diagrams represent the P–T–$X(CO_2)$ evolution inferred for sample 18a–26 and discussed in Section 6.4.

The ***protolith assemblage***, consisting of illite (3%), quartz (47%), chlorite (2%), dolomite (41%) and plagioclase (Ab5%, An2%), matches with the assemblage modeled at 400 °C, $X(CO_2)=0.02$ (Fig. 6.13a,b), which consists of muscovite (6%), quartz (43%), chlorite (8%),

dolomite (38%) and albite + paragonite (4%). These conditions are therefore assumed as the starting point of the P–T–X(CO_2) evolution.

The observed ***peak assemblage*** (Qz+Dol+Bt+Pl+Ky) is modelled by a 4–variant field located at T=600–615 °C, P=9.8–8.8 kbar, X(CO_2)>0.40 (Fig. 6.13a). A minor amount of magnesite (<3%) is predicted in this field, although not observed in the sample. The XMg and XCa compositional isopleths modelled for biotite and plagioclase, respectively, and corresponding to their measured compositions (biotite: XMg=0.94–0.95; plagioclase: XCa=0.45–0.69) converge at the inferred peak P–T–X(CO_2) conditions (Fig. 6.13b).

6.3.2 Magnesite series

6.3.2.1 Sample 17a–36b

The P/T–X(CO_2) pseudosection modelled in the NKCFMASTO–H_2O–CO_2 system (Fig. 6.14a) is dominated by 3–, 4– and 5– variant fields (i.e. fields containing 8, 7, and 6 phases, respectively). Quartz and ilmenite are predicted over the whole range of P–T–X(CO_2) conditions; an additional Ti–bearing accessory mineral (titanite or rutile) is always present at T<590 °C. Among phyllosilicates, chlorite is predicted at T<620 °C, for X(CO_2)<0.35, and muscovite is predicted to be stable independently from the X(CO_2) values up to temperatures of 660–680 °C; biotite occurs at low temperatures (T<500 °C) only for low X(CO_2) values (X(CO_2)<0.2), whereas for T>550 °C its stability field is enlarged over the whole X(CO_2) range of interest. Although stable over a relatively large P–T–X(CO_2) range, dolomite is predicted to occur in negligible amounts (<0.5%); instead, the main carbonate mineral potentially stable for this bulk composition is magnesite, whose stability field is limited to X(CO_2)>0.04 and T<610 °C. Due to the very low amount of CaO in this system, Ca–rich silicates are modelled in low amounts; nevertheless, epidote occurs at relatively low X(CO_2) values and up to 620 °C, whereas plagioclase is mostly stable during the decompression stage, for T>600–620 °C. Low amounts of kyanite are also predicted to occur at T>580 °C. The stability fields of the main phases are reported in Appendix 11, Fig. S19.

The ***protolith assemblage***, consisting of illite (25%), K–feldspar (10%), quartz (50%), chlorite (2%), magnesite (9%) and plagioclase (Ab3%, An1%), matches with the assemblage modeled at 400 °C, X(CO_2)=0.04 (Fig. 6.14a,b), which consists of muscovite (34%), quartz (54%), chlorite (3%), magnesite (6%), albite (2%) and dolomite (0.4%). These conditions are therefore assumed as the starting point of the P–T–X(CO_2) evolution.

The observed ***peak assemblage*** (Qz+Bt+Mu+Pl+Ep±Ky) is modelled by a 4–variant field located at T=600–620 °C, P=9.8–8.5 kbar, X(CO_2)>0.05 (Fig. 6.14a). In this field, the predicted amount of kyanite and epidote is low (<1%), in agreement with the observed assemblage. The XMg and XCa compositional isopleths modelled for biotite and plagioclase, respectively, and corresponding to their measured compositions (biotite:

XMg=0.91–0.93; plagioclase: XCa=0.32–0.42) are coherent with these peak P–T–X(CO_2) conditions (Fig. 6.14b).

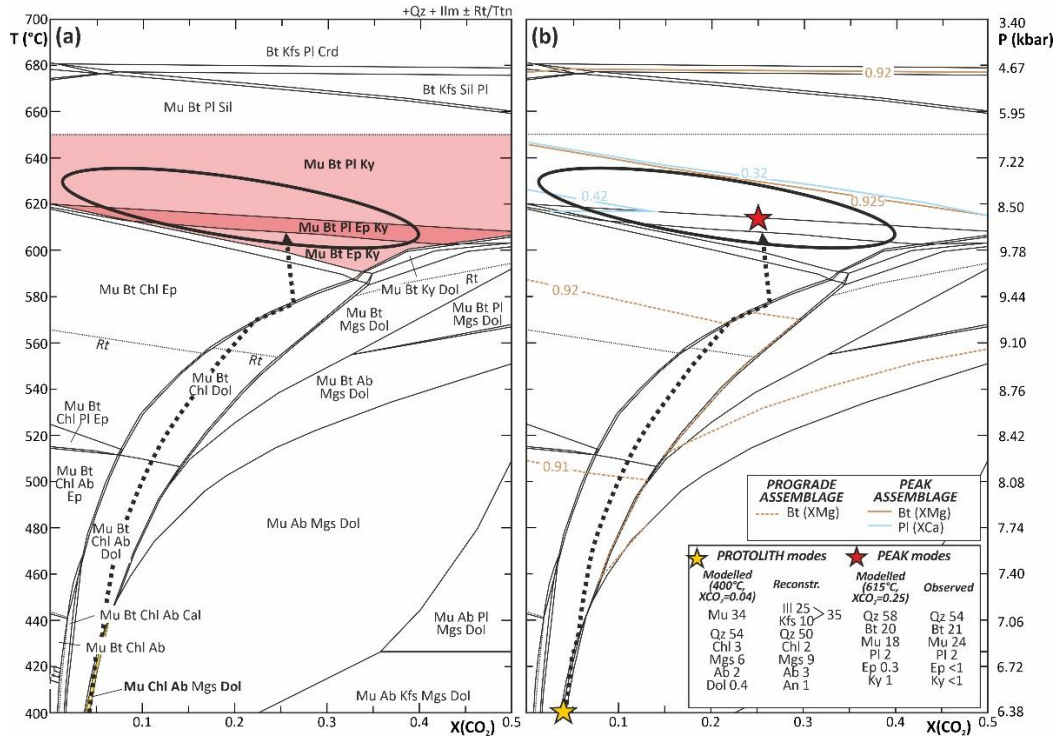

Fig. 6.14: (a) P/T–X(CO_2) isochemical phase diagram modelled for sample 17a–36b in the NKCFMASTO–H_2O–CO_2 system. The variance of the fields varies from two (i.e. 9 phases) to five (i.e. 6 phases). Dotted lines delimit the stability fields of the Ti–bearing accessory minerals (titanite, rutile). The yellow field is the modelled stability field of the protolith's assemblage; the red fields correspond to the stability fields of the peak assemblage, with darker tones highlighting the best fit between the observed and the modelled assemblages (for each modelled assemblage, the observed minerals are reported in bold). (b) Same P/T–X(CO_2) isochemical phase diagram as (a), contoured with the compositional isopleths for peak phases. Yellow and red stars refer to the P–T–X(CO_2) conditions representing the best fit between the modelled and measured modal amounts of minerals in the protolith (yellow) and in the peak (red) assemblages. The black ellipses in both (a) and (b) summarize the P–T–X(CO_2) peak conditions. The dashed black arrows in both diagrams represent the P–T–X(CO_2) evolution inferred for sample 17a–36b and discussed in Section 6.4.

6.3.2.2 Sample 17a–35

The P/T–X(CO_2) pseudosection modelled in the MnNKCFMAST–H_2O–CO_2 system (Fig. 6.15a) has a relatively simple topology dominated by 4–, 5– and 6– variant fields (i.e. fields containing 7, 6, and 5 phases, respectively), with quartz ± rutile as excess phases. Among phyllosilicates, chlorite is stable at T<600 °C for X(CO_2)<0.4; instead, muscovite and biotite are stable over the entire range of X(CO_2) values, with muscovite mostly limited to T<600 °C and biotite to T>590 °C. Dolomite and magnesite are stable at T<615 °C within a wide range of X(CO_2); of the two carbonates, magnesite is by far the most abundant (up to 29%). Two Ca–bearing silicates are predicted mostly in the carbonate–absent fields: zoisite at T<620 °C and X(CO_2) <0.25, and plagioclase at T>600 °C, over the entire range

of X(CO_2) values. Garnet appears at T>580 °C along the prograde evolution, but is mostly stable during the decompression stage, in the temperature interval 600–660 °C; at higher temperatures (i.e., T>650 °C), it is replaced by cordierite, whose stability field is independent of the X(CO_2). Kyanite is predicted in almost the entire P–T–X(CO_2) range of interest, except at low T and X(CO_2) values (i.e., T=400–480 °C and X(CO_2)<0.2) and at T>650 °C. Two types of amphibole are predicted at different P–T–X(CO_2) conditions: a Ca–amphibole (hornblende), at 600–630 °C, X(CO_2)>0.1, and a Mg–Fe orthoamphibole (anthophyllite) at T> 620 °C, over the whole range of X(CO_2) values. The coexistence of the two amphiboles is thus limited to the narrow temperature interval of 620–630 °C. Talc is additionally predicted in a narrow field at 620–640 °C, for X(CO_2)>0.25. The stability fields of the main phases are reported in Appendix 11, Fig. S20.

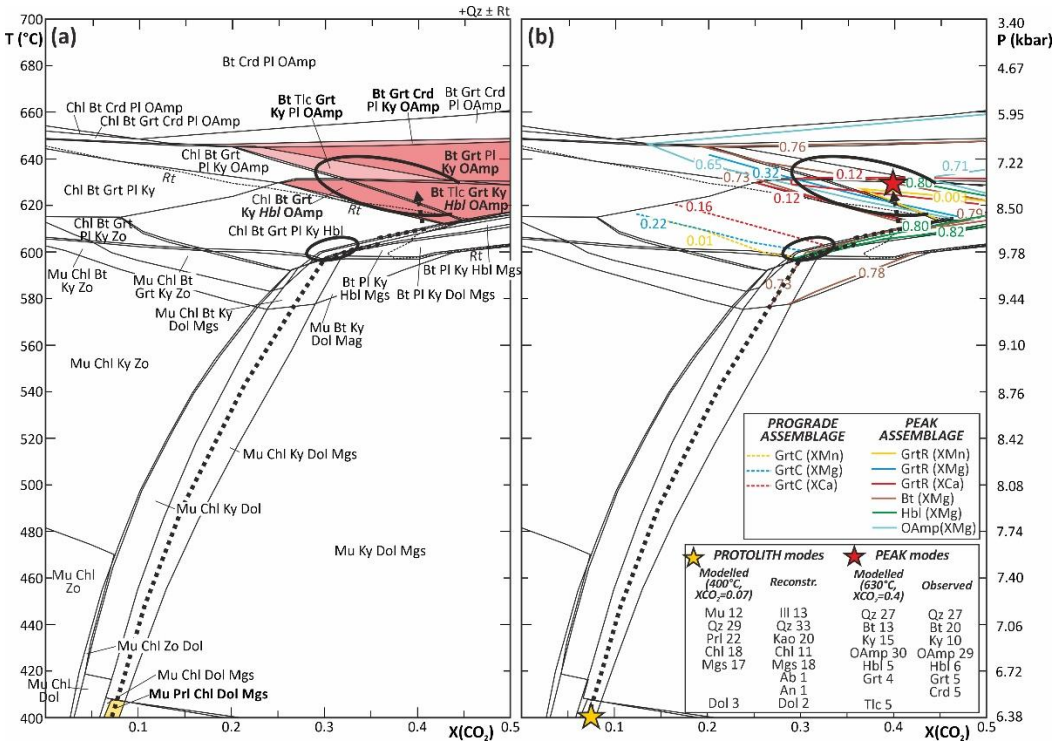

Fig. 6.15: (a) P/T–X(CO_2) isochemical phase diagram modelled for sample 17a–35 in the MnNKCFMAST–H_2O–CO_2 system. The variance of the fields varies from two (i.e. 9 phases) to five (i.e. 6 phases). Dotted lines delimit the stability fields of rutile. The yellow field is the modelled stability field of the protolith's assemblage; the red fields correspond to the stability fields of the peak assemblage, with darker tones highlighting the best fit between the observed and the modelled assemblages (for each modelled assemblage, the observed minerals are reported in bold, whereas relict phases are reported in italic). (b) Same P/T–X(CO_2) isochemical phase diagram as (a), contoured with the compositional isopleths for both prograde (dashed lines) and peak (continuous lines) phases. Yellow and red stars refer to the P–T–X(CO_2) conditions representing the best fit between the modelled and measured modal amounts of minerals in the protolith (yellow) and in the peak (red) assemblages. The black ellipses in both (a) and (b) summarize the prograde and peak P–T–X(CO_2) conditions. The dashed black arrows in both diagrams represent the P–T–X(CO_2) evolution inferred for sample 17a–35 and discussed in Section 6.4.

The ***protolith assemblage***, consisting of illite (13%), kaolinite (20%), quartz (33%), chlorite (11%), magnesite (18%), dolomite (2%) and plagioclase (Ab1%, An1%), matches with the assemblage modeled at 400 °C, $X(CO_2)$=0.07 (Fig. 6.15a,b), which consists of muscovite (12%), pyrophyllite (22%), quartz (29%), chlorite (18%), magnesite (17%) and dolomite (3%). These conditions are therefore assumed as the starting point of the P–T–$X(CO_2)$ evolution.

The compositional isopleths modelled for garnet core corresponding to its measured composition (GrtC: XMg=0.22, XCa=0.16, XMn=0.01), converge in the narrow 2–variant field Qz+Chl+Bt+Grt+Pl+Ky+Hbl+Rt+Mgs (Fig. 6.15b), constraining garnet nucleation in the ***prograde stage*** at T=595–615 °C, P=9–9.6 kbar, and suggesting that garnet appearance is related to the breakdown of magnesite, even if carbonates are no more preserved.

The observed ***peak assemblage*** (Qz+Bt+Ky+Grt+Oamp+Hbl±Crd) is approximated by different fields located at T=615–645 °C, P=8.6–7.2 kbar, $X(CO_2)$>0.3 (Fig. 6.15a). None of these fields matches perfectly the observed assemblage, because they include phases which are absent in the sample (i.e. chlorite, talc or plagioclase). However, the 4– variant field Qz+Bt+Grt+Ky+OAmp+Hbl+Tlc is the most similar to the observed peak assemblage, being able to reproduce the coexistence of hornblende and ortho–amphibole, as well as the correct proportions of kyanite and biotite. According to these results, cordierite is a later phase, anyway compatible with a decompression evolution (Fig. 6.15a). The compositional isopleths modelled for the post–kinematic garnet rim (GrtR: XMg=0.32, XCa=0.12, XMn=0.003) further constrain its growth at T=615–640 °C, P=8.5–7.2 kbar (Fig. 6.15b). The compositional isopleths of the other post–kinematic phases in equilibrium with a garnet rim, i.e. biotite, hornblende and orthoamphibole (Bt: XMg=0.73–0.78; Hbl: XMg=0.8–0.82; OAmp: XMg=0.65–0.71), intersect themselves in the same P–T interval (Fig. 6.15b), confirming that the peak assemblage developed during the decompression stage.

6.3.2.3 Sample 17b–7d

The P/T–$X(CO_2)$ pseudosection modelled in the CFMAS–H_2O–CO_2 system shows a simple topology (Fig. 6.16a), dominated by relatively large 3– and 4– variant fields (i.e. fields containing 4 and 3 phases, respectively), delimited by very narrow 2– and 3– variant fields which mark discontinuous reactions. Magnesite is stable in almost the entire P–T–$X(CO_2)$ range of interest, except for very low $X(CO_2)$ values at high temperatures. The dolomite stability field is, instead, limited to T<500 °C. Quartz requires $X(CO_2)$>0.1 for being stable at 400°C, and progressively higher $X(CO_2)$ values at increasing temperatures. Three main phyllosilicates are predicted to occur at different P–T–$X(CO_2)$ conditions: chlorite is stable at $X(CO_2)$<0.6 and up to temperatures of 660 °C, talc is stable at almost the same P–T conditions but over a more restricted $X(CO_2)$ range and antigorite occurs only for very low $X(CO_2)$ values. Other Mg– and/or Al– rich silicates occur at high temperatures

(T>640 °C), such as brucite, olivine, orthopyroxene, corundum, sapphirine and spinel. The stability fields of the main phases are reported in Appendix 11, Fig. S21.

The ***protolith assemblage***, consisting of kaolinite (5%), chlorite (2%), quartz (9%), magnesite (84%) and dolomite (0.4%), matches the assemblage modeled at 400°C, $X(CO_2)$=0.1 (Fig. 6.16a,b), consisting of pyrophyllite (9%), quartz (6%), magnesite (85%). These conditions are therefore assumed as the starting point of the P–T–$X(CO_2)$ evolution.

The observed ***peak assemblage*** (Mgs+Tlc+Chl) is modeled by a large 4–variant field, extending from the prograde stage (T>500 °C, $X(CO_2)$<0.1) to the decompression stage (T<650 °C, $X(CO_2)$<0.6) (Fig. 6.16a). Compositional isopleths of peak phases do not help in further constraining the peak P–T–$X(CO_2)$ conditions, because all the phases are close to the pure end–member compositions. Instead, the isomodes modeled for magnesite, talc and chlorite corresponding to the measured modal amount of each phase (Mgs74%, Tlc12%, Chl14%) constrain the peak P–T–$X(CO_2)$ conditions at ca. 630 °C, 8.0 kbar, $X(CO_2)$=0.5 (Fig. 6.16b).

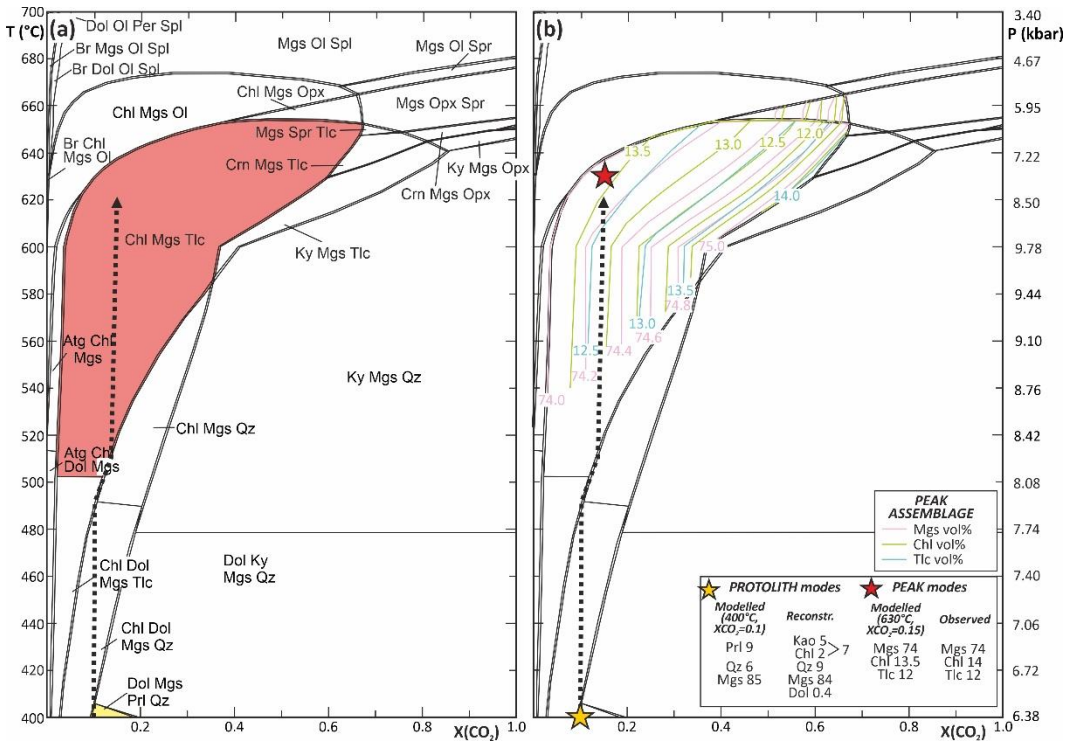

Fig. 6.16: (a) P/T–$X(CO_2)$ isochemical phase diagram modelled for sample 17b–7d in the CFMAT–H_2O–CO_2 system. The variance of the fields varies from two (i.e.5 phases) to four (i.e. 3 phases). The yellow field is the modelled stability field of the protolith's assemblage; the red field corresponds to the stability field of the peak assemblage. (b) Same P/T–$X(CO_2)$ isochemical phase diagram as (a), contoured with isomodes modelled for the peak phases. Yellow and red stars refer to the P–T–$X(CO_2)$ conditions representing the best fit between the modelled and measured modal amounts of minerals in the protolith (yellow) and in the peak (red) assemblages. The dashed black arrows in both diagrams represent the P–T–$X(CO_2)$ evolution inferred for sample 17b–7d and discussed in Section 6.4.

6.4 Discussion

6.4.1 P–T–X(CO_2) evolution and decarbonation processes

The approximate P–T–X(CO_2) evolution for the seven investigated samples has been reconstructed by connecting the "starting point" inferred based on the modelled protolith's assemblages, with the peak (± prograde) conditions inferred based on the modelled peak (± prograde) assemblages and compositions (see Chapter 3, section 3.6.2 and section 6.3). For most samples, the results of phase diagram modelling strongly suggest that the equilibrium mineral assemblages buffered the composition of the pore fluid during most of the metamorphic evolution. Most of the observed prograde and peak mineral assemblages, in fact, are modelled in equilibrium with a fluid characterized by a X(CO_2) value systematically higher than that of the fluid in equilibrium with the protolith's assemblage. The systematic nature of this observation makes it unlikely that this is due to the infiltration of external fluids rich in CO_2. An internally buffered behaviour is common during prograde metamorphism of silicate–carbonate rocks (Greenwood, 1975; Baker et al., 1991), as confirmed by several independent petrographic evidence (e.g. Connolly & Trommsdorff, 1991; Eberhard & Pettke, 2021; Groppo et al., 2017, 2021; Rapa et al., 2017). Such behaviour is assumed as the base for most of the following discussion. The exception is represented by sample 17b–7d (magnesite + talc rock), for which the peak conditions are inferred at a X(CO_2) value very similar to that of the fluid in equilibrium with the protolith's assemblage. This suggests an externally buffered evolution for this sample, controlled by the infiltration of externally derived fluids.

It has been demonstrated that, as long as a system remains internally buffered, the sudden and volumetrically significant appearance of new phases and the simultaneous disappearance of previously abundant phases occur at the isobaric/isothermal invariant points, whereas modal changes are only minor along the univariant curves (e.g. Greenwood, 1975; Groppo et al., 2017). In contrast, univariant reactions lead to the volumetrically significant appearance of new phases when the buffering ability of the system ceases due to the complete consumption of one or more reactants. These points become especially relevant if interested to investigate the main CO_2–producing processes because these correspond to significant episodes of carbonates consumption.

The following discussion describes the P–T–X(CO_2) evolution reconstructed for each sample, with emphasis on the main decarbonation reactions experienced during the prograde and/or decompression stages. The amount (wt%) of CO_2 released from each sample is estimated based on the amount of carbonates consumed along the inferred P–T–X(CO_2) evolution, calculated as the difference between the carbonates originally present in the protolith (see Chapter 3, section 3.5) and those still preserved at peak P–T conditions. The following reasoning is applied to convert carbonates modal amounts (vol%) in CO_2 amounts (wt%):

- 1 vol% of dolomite corresponds to 1 cm^3 of dolomite within 100 cm^3 of rock; dolomite has a density of 2.86 g/cm^3, whereas an average density of 2.7 g/cm^3 is assumed for the hosting rock. This means that 1 vol% of dolomite equals to 2.86 g/270 g = 1.06 wt% of dolomite. 1 mole of dolomite ($CaMg(CO_3)_2$) weights 184 g (CaO + MgO + $2CO_2$ = 56 + 40.3 + 2×44 g/mol). This implies that 1 g of dolomite contains 0.48 g of CO_2. To obtain the amount of CO_2 released by 1 vol% of dolomite, we thus need to multiply 1.06 × 0.48 = 0.51 wt% of CO_2.
- 1 vol% of magnesite corresponds to 1 cm^3 of magnesite within 100 cm^3 of rock; magnesite has a density of 2.96 g/cm^3, whereas an average density of 2.7 g/cm^3 is assumed for the hosting rock. This means that 1 vol% of magnesite equals to 2.96 g/270 g = 1.10 wt% of magnesite. 1 mole of magnesite ($MgCO_3$) weights 84 g (MgO + CO_2 = 40.3 + 44 g/mol). This implies that 1 g of magnesite contains 0.52 g of CO_2. To obtain the amount of CO_2 released by 1 vol% of magnesite, we thus need to multiply 1.10 × 0.52 = 0.57 wt% of CO_2.

6.4.1.1 Dolomite series

Sample 17b–12

At the inferred starting P–T–X(CO_2) conditions (400 °C, 6.4 kbar, X(CO_2)=0.02), the modelled assemblage consists of quartz, muscovite, chlorite, albite, paragonite, ilmenite, rutile, dolomite and magnesite (Fig. 6.17a); an amount of dolomite equal to 8 vol% is modelled at these conditions, whereas magnesite occurs in very low amounts (0.2 vol%). Assuming an internally buffered evolution for this sample, low amounts of biotite are predicted to appear at ca. 450 °C (i.e. once the system enters the Qz+Mu+Pg+Chl+Bt+Mgs+Dol +Ilm+Rt field). With the further T and P increase, the system reaches the discontinuous reaction Chl+Dol+Mu+Qz = Bt+Ep (reaction 3 in Fig. 6.17b), which represents the first significant decarbonation reaction experienced by the sample. The system then evolves along this reaction until dolomite is completely consumed and the system enters the Qz+Mu+Pg+Chl+Bt+Ep+Mgs+Ilm field. The amount of magnesite modelled in this field is very low (< 1 vol%). With increasing T and P, the decarbonation reaction Mgs+Mu = Bt+Grt (reaction 4 in Fig. 6.17b) is eventually reached, which is responsible for the nucleation of garnet (i.e. prograde stage at T=560–580 °C, P=9.1–9.4 kbar, X(CO_2)=0.2: Fig– 6.17a). It is likely that, due to the low amounts of magnesite at these conditions, the buffering ability of the system is low; once that magnesite is completely consumed, the system enters the carbonate–absent Qz+Mu+Pg+Chl+Bt+Grt+Ep+Ilm field. From this point onward, continuous reactions occurring in large 4– and 5–variant fields release low amounts of H_2O but no more CO_2, thus implying that the X(CO_2) of the fluid does no more increase up to the peak P–T–X(CO_2) conditions, inferred at 620 °C, 8.5 kbar, X(CO_2)=0.20 (Fig. 6.17a,b). It is to be noted that, although garnet nucleation is related to carbonate consumption through reaction 4, volumetrically significant growth of garnet mostly occurs during the decompression stage, through biotite and epidote–consuming continuous reactions.

The reconstructed P–T–X(CO_2) evolution implies that:

- the most significant decarbonation reaction occurs during the prograde evolution (reactions 3 in Fig. 6.17b), in the temperature interval 450–560 °C, and it is responsible for the final consumption of dolomite. A further decarbonation reaction is predicted at higher temperatures (540–580 °C), which leads to the consumption of a very low amount of magnesite (0.2 vol%), and it is therefore irrelevant for the overall estimate of the CO_2 budget;
- the fluid produced through the main decarbonation reaction has X(CO_2) = 0.1–0.2 (Fig. 6.17b);
- a total amount of dolomite of 6–8 vol% (depending on whether the modelled vs. reconstructed protolith's mode is used) is consumed through this process, which corresponds to an amount of CO_2 produced of 3.1–4.1 wt%.

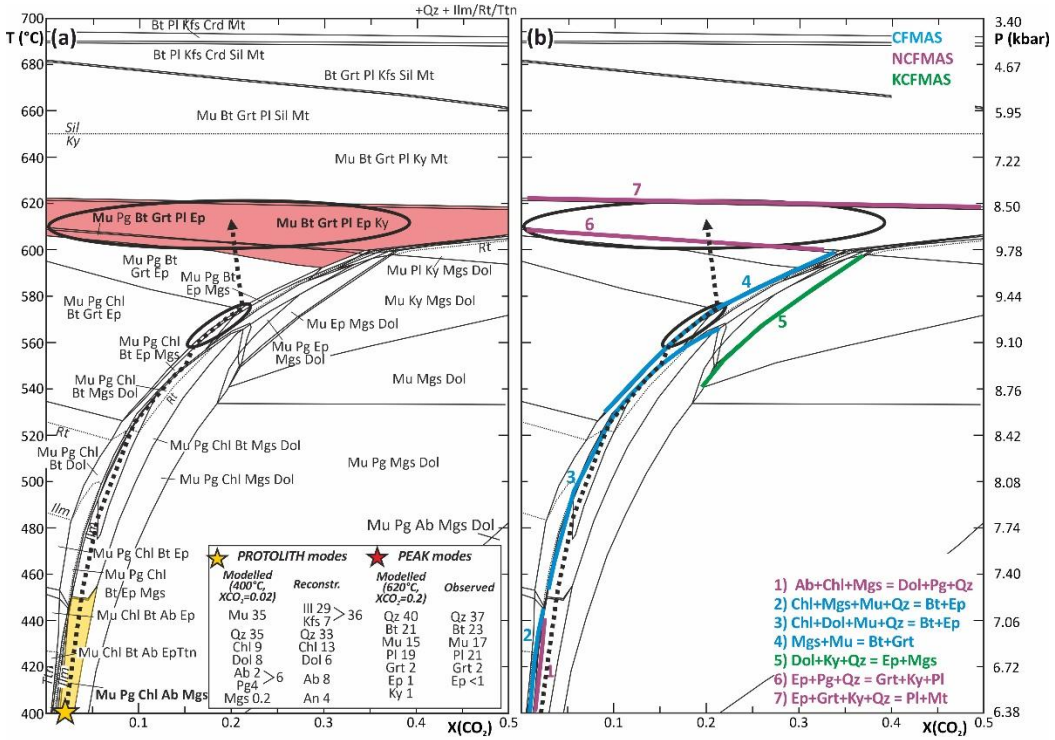

Fig. 6.17: (a) Same P/T–X(CO_2) isochemical phase diagram modelled for sample 17b–12 as in Fig. 6.10. The yellow and red fields correspond to the modelled stability fields of the protolith's and peak assemblages, respectively. Yellow and red stars refer to the "starting point" and peak P–T–X(CO_2) conditions as discussed in Section 6.3. The black ellipses summarize the prograde and peak P–T–X(CO_2) conditions. (b) Same diagram as (a), highlighting the isothermal/isobaric univariant equilibria relevant to this sample (different colours refer to different chemical systems). It should be noted that the univariant curves overlap the narrow low–variant fields of the pseudosection. Reactions are written such as the products are on the high–T side of the equilibrium curves. The dashed black arrows approximate the P–T–X(CO_2) evolution inferred for sample 17b–12 as discussed in the text.

Sample 17a–29

At the starting P–T–X(CO_2) conditions (400 °C, 6.4 kbar, X(CO_2)=0.02) the predicted assemblage consists of quartz, muscovite, chlorite, rutile, dolomite and calcite, with

chloritoid and muscovite likely derived from the kaolinite and illite fractions originally present in the protolith (Fig. 6.18a). The modelled amounts of dolomite and calcite at these conditions are 14 vol% and 1 vol%, respectively. The P–T–X(CO_2) evolution reconstructed by connecting this "starting point" with the inferred prograde conditions (550–570 °C, 8.8–9.2 kbar, X(CO_2)=0.20–0.22) is consistent with an internally buffered behaviour (Fig. 6.18a). Garnet nucleation at these prograde conditions occurs through the reaction Cal+Dol+Ky+Qz = Chl+Grt (reaction 7 in Fig. 6.18b), which marks the first decarbonation episode for this sample. At these P–T conditions, the amount of calcite is very low; therefore, it is likely that calcite is completely consumed, and the buffering ability of the system ceases, soon after this reaction is reached. Once that calcite is consumed, the system enters the small Qz+Mu+Chl+Grt+Ky+Dol+Rt field, eventually reaching the discontinuous reaction Chl+Mu = Bt+Ky+Qz (reaction 11 in Fig. 6.18b) at about 590 °C, which marks the first appearance of biotite. At the onset of the decompression evolution, decarbonation proceeds through the reaction Dol+Mu+Ky+Qz = Bt+Grt+Pl+Zo (reactions 13 in Fig. 6.18b); with the final consumption of muscovite, the buffering ability of the system ceases and it eventually reaches the Qz+Bt+Grt+Ky+Pl+Dol+Rt field at the inferred peak P–T–X(CO_2) conditions of 600–615 °C, 8.8–9.8 kbar, X(CO_2)>0.5 (Fig. 6.18b).

The following points can be inferred based on the reconstructed P–T–X(CO_2) evolution:

- most of the decarbonation occurs during the decompression stage, at T>610 °C, through a nearly discontinuous reaction (reaction 13, Fig. 6.18b) which is responsible for the consumption of a relatively high amount of dolomite (11 vol%). This decarbonation event is preceded by a further episode of carbonates consumption (reaction 7, Fig. 6.18b), which occurs during the prograde evolution at 550–570 °C; this reaction is responsible for the breakdown of a minor amount of calcite (<1 vol%) and it is, therefore, irrelevant for the overall estimate of the CO_2 budget;
- the fluid produced through the main decarbonation reaction is enriched in CO_2, with X(CO_2) ≥ 0.5 Fig. 6.18b;
- at the end of the modelled P–T–X(CO_2) evolution, a total amount of dolomite of about 11 vol% is consumed through this process, which corresponds to an amount of CO_2 produced of 5.6 wt%.

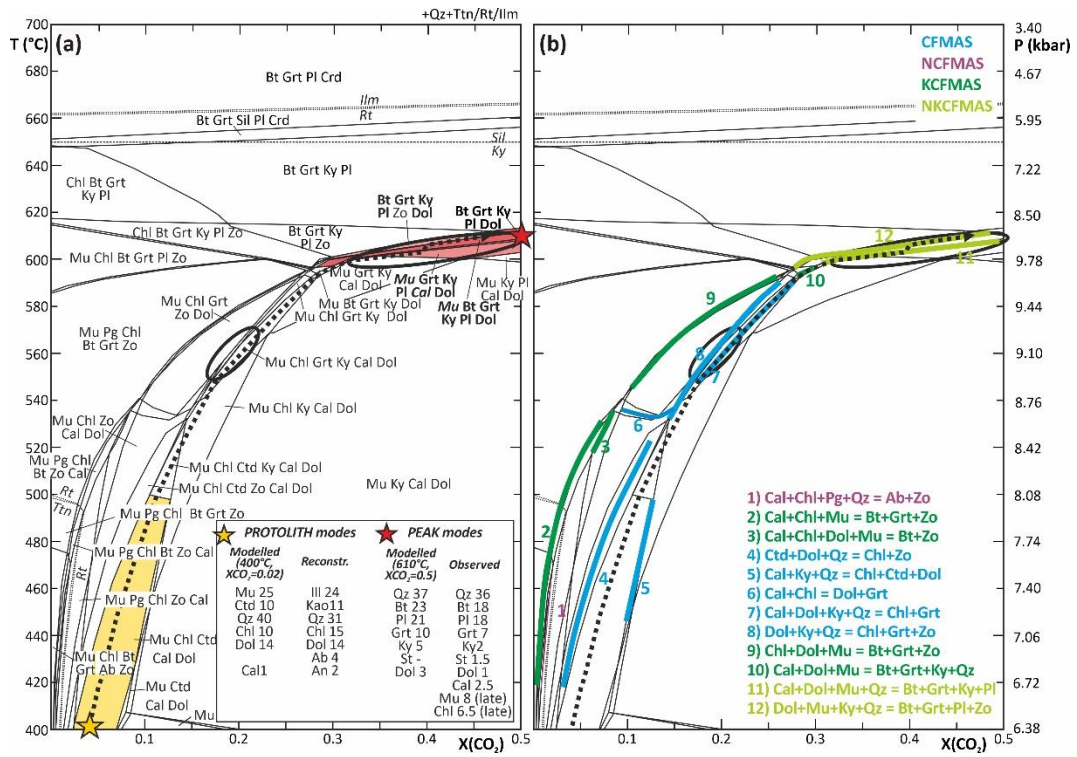

Fig. 6.18: (a) Same P/T–X(CO_2) isochemical phase diagram modelled for sample 17a–29 as in Fig. 6.11. The yellow and red fields correspond to the modelled stability fields of the protolith's and peak assemblages, respectively. Yellow and red stars refer to the "starting point" and peak P–T–X(CO_2) conditions as discussed in Section 6.3. The black ellipses summarize the prograde and peak P–T–X(CO_2) conditions. (b) Same diagram as (a), highlighting the isothermal/isobaric univariant equilibria relevant to the sample (different colours refer to different chemical systems). It should be noted that the univariant curves overlap the narrow low–variant fields of the pseudosection. Reactions are written such as the products are on the high–T side of the equilibrium curves. The dashed black arrows in both diagrams approximate the P–T–X(CO_2) evolution inferred for sample 17a–29 as discussed in the text.

Sample 15a–28a

The modelled assemblage at the starting P–T–X(CO_2) conditions (400 °C, 6.4 kbar, X(CO_2)=0.02) consists of quartz, muscovite, chlorite, albite, rutile and dolomite, and the modelled amount of dolomite is 32 vol% (Fig. 6.19a). Different P–T–X(CO_2) internally buffered paths can be, in principle, obtained by connecting this "starting point" with the inferred peak conditions at T=610–620 °C, P=8.5–9.1 kbar, X(CO_2)>0.45. The observed post–kinematic nature of hornblende porphyroblasts suggests that hornblende growth occurred during the decompression stage, thus implying that the hornblende–in reaction has been crossed at T>610 °C. This allows excluding reactions 7, 4 and 14 (Fig. 6.19b) as hornblende–in reactions, and strongly constrains the first appearance of hornblende to the reaction Dol+Ky+Pl+Qz = Bt+Hbl+Zo (reaction 18 in Fig. 6.19b). Any P–T–X(CO_2) internally buffered paths respecting the constraints previously discussed are equally possible, but these should all reach reaction 18, which corresponds to the most significant decarbonation event experienced by this sample. It is likely that, due to the low amounts

of kyanite modelled at these conditions, the buffering ability of the system along reaction 18 is low. The complete consumption of kyanite also coincides with a volumetrically significant decrease of dolomite; the system then enters the Qz+Bt+Amp+Pl+Dol±Zo fields, eventually reaching the inferred peak conditions (Fig. 6.19b).

Based on the reconstructed P–T–X(CO_2) evolution it emerges that:

- most decarbonation occurs through a single step–like reaction during the decompression stage, at T>610 °C (Fig. 6.19b), which consumes about one–third of the dolomite initially present in the protolith;
- the fluid released through this decarbonation reaction has X(CO_2) >0.5 (Fig. 6.19b);
- the amount of dolomite consumed through this process is about 10 vol%, which corresponds to an amount of CO_2 produced of 5.1 wt%.

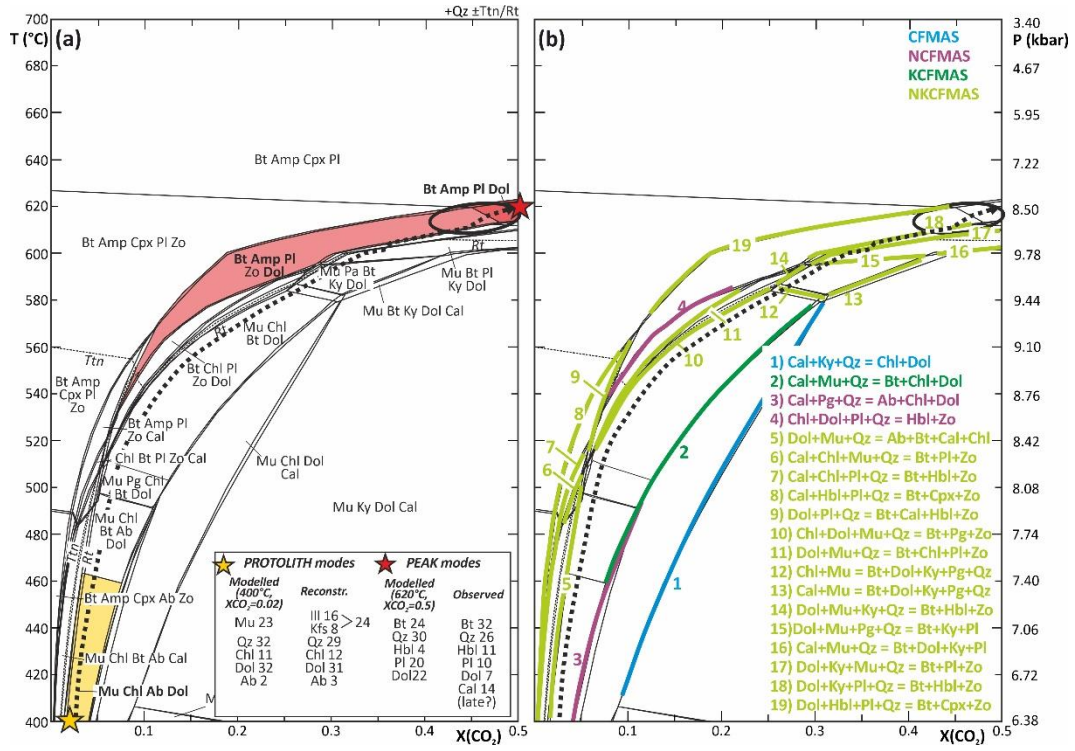

Fig. 6.19: (a) Same P/T–X(CO_2) isochemical phase diagram modelled for sample 15a–28a as in Fig. 6.12. The yellow and red fields correspond to the modelled stability fields of the protolith's and peak assemblages, respectively. Yellow and red stars refer to the "starting point" and peak P–T–X(CO_2) conditions as discussed in Section 6.3. The black ellipse summarizes the peak P–T–X(CO_2) conditions. (b) Same P/T–X(CO_2) isochemical phase diagram as (a), highlighting the isothermal/isobaric univariant equilibria relevant to this sample (different colours refer to different chemical systems). It should be noted that the univariant curves overlap the narrow low–variant fields of the pseudosection. Reactions are written such as the products are on the high–T side of the equilibrium curves. The dashed black arrows approximate the P–T–X(CO_2) evolution inferred for sample 15a–28a as discussed in the text.

Sample 18a–26

At the starting P–T–X(CO_2) conditions (400 °C, 6.4 kbar, X(CO_2)=0.02), the modelled assemblage consists of quartz, muscovite, paragonite, chlorite, albite, rutile and dolomite, with a predicted amount of dolomite equal to 38 vol% (Fig. 6.20a). A number of P–T–X(CO_2) internally buffered paths can be defined by connecting this "starting point" with the inferred peak conditions at T=600–615 °C, P=9.8–8.8 kbar, X(CO_2)>0.40; however, the lack of amphibole in the sample imposes a strong constraint to the location of the P–T–X(CO_2) path, which should remain below the Amp–in reactions (i.e. reactions 4, 8, 9, 11, 12 and 14 in Fig. 6.20b). This suggests that, during the prograde stage, the system mostly evolves through large high–variant fields, rather than crossing discontinuous reactions.

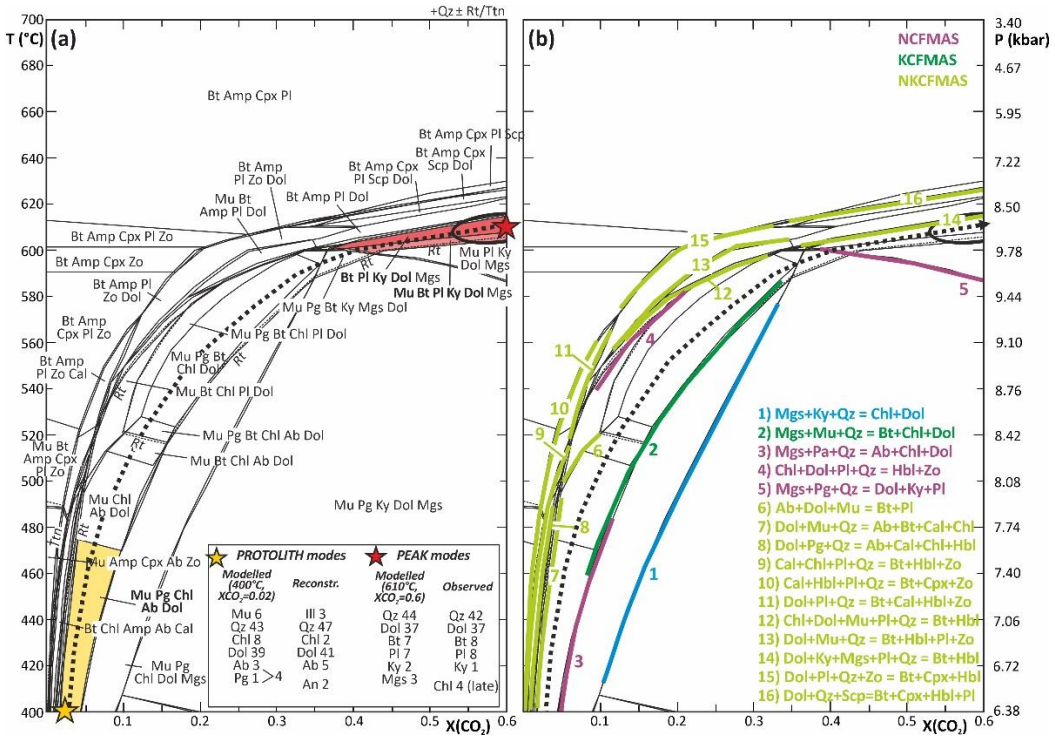

Fig. 6.20: (a) Same P/T–X(CO_2) isochemical phase diagram modelled for sample 18a–26 as in Fig. 6.13. The yellow and red fields correspond to the modelled stability fields of the protolith's and peak assemblages, respectively. Yellow and red stars refer to the "starting point" and peak P–T–X(CO_2) conditions as discussed in Section 6.3. The black ellipse summarizes the peak P–T–X(CO_2) conditions. (b) Same P/T–X(CO_2) isochemical phase diagram as (a), highlighting the isothermal/isobaric univariant equilibria relevant to this sample (different colours refer to different chemical systems). It should be noted that the univariant curves overlap the narrow low–variant fields of the pseudosection. Reactions are written such as the products are on the high–T side of the equilibrium curves. The dashed black arrows approximate the P–T–X(CO_2) evolution inferred for sample 18a–26 as discussed in the text.

At the onset of the decompression stage, the system likely intersects the reaction Chl+Dol = Mgs+Ky+Qz (reaction 1 in Fig. 6.20b), which is responsible for the appearance of small amounts of kyanite and magnesite. Because the consumption of dolomite is counterbalanced by the growth of magnesite, this reaction does not correspond to a

significant decarbonation episode. During decompression, the system evolves within the 4–variant Qz+Bt+Pl+Ky+Dol+Mgs field, eventually reaching the inferred peak conditions (Fig. 6.20b).

The reconstructed P–T–X(CO_2) evolution shows that:

- in this sample decarbonation processes are much less significant than in the other samples from the dolomite series, and occur through continuous reactions which operate over large P–T–X(CO_2) intervals rather than through discontinuous reactions;
- the fluid in equilibrium with the peak assemblage has X(CO_2) >0.6;
- according to the results of the modelling, 2 vol% of dolomite is consumed along this P–T–X(CO_2) path, but 2 vol% of magnesite is produced, therefore the overall budget of CO_2 is maintained. Even in the case magnesite is not produced (as suggested by the observed peak assemblage), the amount of CO_2 produced is very low (1.0 wt%).

6.4.1.2 Magnesite series

Sample 17a–36b

The predicted assemblage at the starting P–T–X(CO_2) conditions (400 °C, 6.4 kbar, X(CO_2)=0.04) consists of quartz, muscovite, chlorite, albite, ilmenite, rutile, magnesite and dolomite, in which magnesite modal amount is in the range 6–9 vol% (depending on whether the modelled vs. reconstructed protolith's mode is used), and dolomite is predicted in very low amounts (0.4 vol%) (Fig. 6.21a). This assemblage is modelled in a very narrow field; with the P–T increasing along the prograde path, the system reaches the discontinuous reaction Mgs+Mu+Qz = Bt+Chl+Dol (reaction 1 in Fig. 6.21b), in the temperature interval T=410–430 °C. This represents the most significant decarbonation reaction for this sample, which consumes all the magnesite initially present in the protolith to produce biotite, chlorite and a very low amount of dolomite (<0.5 vol%). The exact P–T conditions at which magnesite is completely consumed (and therefore most of the CO_2 is produced) are difficult to be predicted; however, being the initial amount of magnesite quite relevant, it is likely that the system is able to buffer the composition of the fluid over a relatively large P–T interval. Once that magnesite is completely consumed, the system evolves within the Qz+Mu+Bt+Chl+Dol+Ilm+Rt 4–variant field in which dolomite is substantially unreactive, until it reaches the discontinuous reaction Dol+Mu = Bt+Ep (reaction 4 in Fig. 6.21b), which marks the final breakdown of dolomite. The system thus enters the carbonate–absent Qz+Mu+Chl+Ep+Ilm field, and further evolves with increasing temperature toward the inferred peak P–T–X(CO_2) condition in the Qz+Mu+Bt+Pl+Ep+Ky+Ilm field (Fig. 6.21b). In this last part of the evolution, low amounts of H_2O–rich fluids are produced through continuous de–hydration reactions involving the breakdown of chlorite and muscovite (counterbalanced by the growth of biotite), whereas CO_2 is no more produced, as testified by the changing trend of the inferred P–T–X(CO_2) path (Fig. 6.21b).

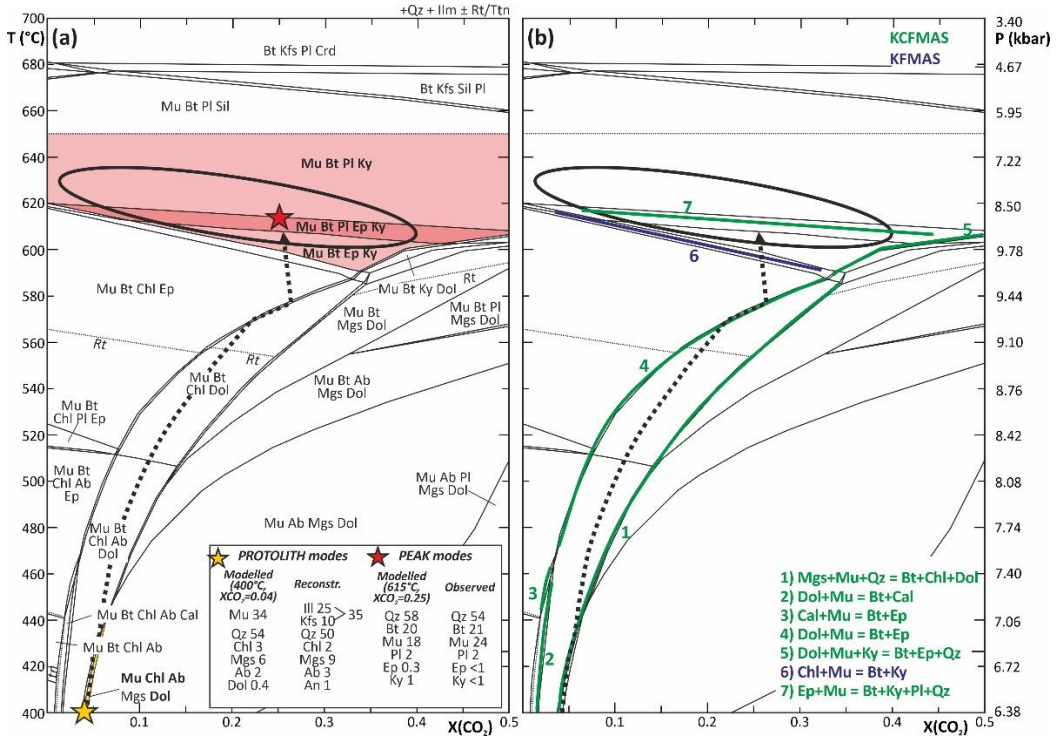

Fig. 6.21: (a) Same P/T–X(CO_2) isochemical phase diagram modelled for sample 17a–36b as in Fig. 6.14. The yellow and red fields correspond to the modelled stability fields of the protolith's and peak assemblages, respectively. Yellow and red stars refer to the "starting point" and peak P–T–X(CO_2) conditions as discussed in Section 6.3. The black ellipse summarizes the peak P–T–X(CO_2) conditions. (b) Same P/T–X(CO_2) isochemical phase diagram as (a), highlighting the isothermal/isobaric univariant equilibria relevant to this sample (different colours refer to different chemical systems). It should be noted that the univariant curves overlap the narrow low–variant fields of the pseudosection. Reactions are written such as the products are on the high–T side of the equilibrium curves. The dashed black arrows approximate the P–T–X(CO_2) evolution inferred for sample 17a–36b as discussed in the text.

The P–T–X(CO_2) evolution reconstructed for sample 17a–36b implies that:

- most decarbonation occurs through a single, step–like reaction responsible for the complete consumption of all the magnesite originally present in the protolith (reaction 1 in Fig. 6.21b). Although difficult to be precisely constrained, this main episode of CO_2 production occurs during the prograde stage (T=520–550 °C). A further decarbonation reaction is predicted at slightly higher temperatures (560–580 °C), which leads to the consumption of a very low amount of dolomite (<0.5 vol%), and it is therefore irrelevant for the overall estimate of the CO_2 budget;
- the fluid produced through the main decarbonation reaction has X(CO_2) = 0.1–0.2 (Fig. 6.21b);

- the amount of magnesite which is consumed through this process ranges between 6–9 vol% (depending on whether the modelled vs. reconstructed protolith's mode is used), which corresponds to an amount of CO_2 produced of 3.4–5.1 wt%.

Sample 17a–35

At the starting P–T–X(CO_2) conditions (400 °C, 6.4 kbar, X(CO_2)=0.07) the modelled assemblage consists of quartz, muscovite, pyrophyllite, chlorite, magnesite and dolomite; the predicted amounts of magnesite and dolomite are 17 vol% and 3 vol%, respectively (Fig. 6.22a). At T>410 °C, pyrophyllite is no more stable and it is replaced by kyanite + quartz; the system thus enters the Qz+Mu+Chl+Ky+Dol+Mgs+Rt field. With the increasing P–T conditions, the system likely evolves within this relatively large 4–variant field without crossing any significant discontinuous reaction, as suggested by the lack of relict zoisite, whose occurrence is otherwise expected if the system crosses the zoisite–in reaction 1 (Fig. 6.22b). Biotite is predicted to appear at T>580 °C through a continuous reaction. At the onset of the decompression evolution, the first significant decarbonation reaction is reached, which is responsible for the first appearance of hornblende and the final consumption of dolomite (Dol+Ky+Mgs+Pl = Hbl+Qz; reaction 6 in Fig. 6.22b). The reaction Mu+Hbl = Bt+Grt+Pl (reaction 4 in Fig. 6.22b) is crossed a few degrees up–temperature, which leads to the appearance of plagioclase counterbalanced by the disappearance of muscovite and to the first significant growth of garnet. The following temperature increase of a few degrees is sufficient for the system for reaching the discontinuous reaction Mgs+Ky+Qz = Chl+Grt (reaction 2 in Fig. 6.22b), which marks the final breakdown of magnesite. From this point onward, the system evolves across different carbonate–absent fields, crossing at least two discontinuous reactions, responsible for the growth of ortho–amphibole (Chl+Pl+Qz = Hbl+Ky+OAmp; reaction 8 in Fig. 6.22b) and, possibly, of low amounts of talc (Chl+Pl+Qz = Ky+OAmp+Tlc; reaction 9 in Fig. 6.22b), up to the inferred peak P–T–X(CO_2) conditions.

The following points emerge from the reconstructed P–T–X(CO_2) evolution:

- two main decarbonation reactions occur during the decompression stage at T=600–610 °C, which are responsible for the final consumption of all the dolomite and magnesite initially present in the protolith (reactions 6 and 2 in Fig. 6.22b). The magnesite–consuming reaction 2 is the most relevant in terms of CO_2 production because it leads to the consumption of 17–18 vol% of magnesite, vs. 2–3 vol% of dolomite consumed through reaction 6;
- the fluid produced through these decarbonation reactions is quite enriched in CO_2, with X(CO_2) values ranging between X(CO_2)=0.3 and X(CO_2)=0.4 (Fig. 6.22b);
- the amount of CO_2 produced through the breakdown of 2–3 vol% of dolomite and of 17–18 vol% of magnesite is equal to 1.0–1.5 wt% and 9.7–10.3 wt%, respectively.

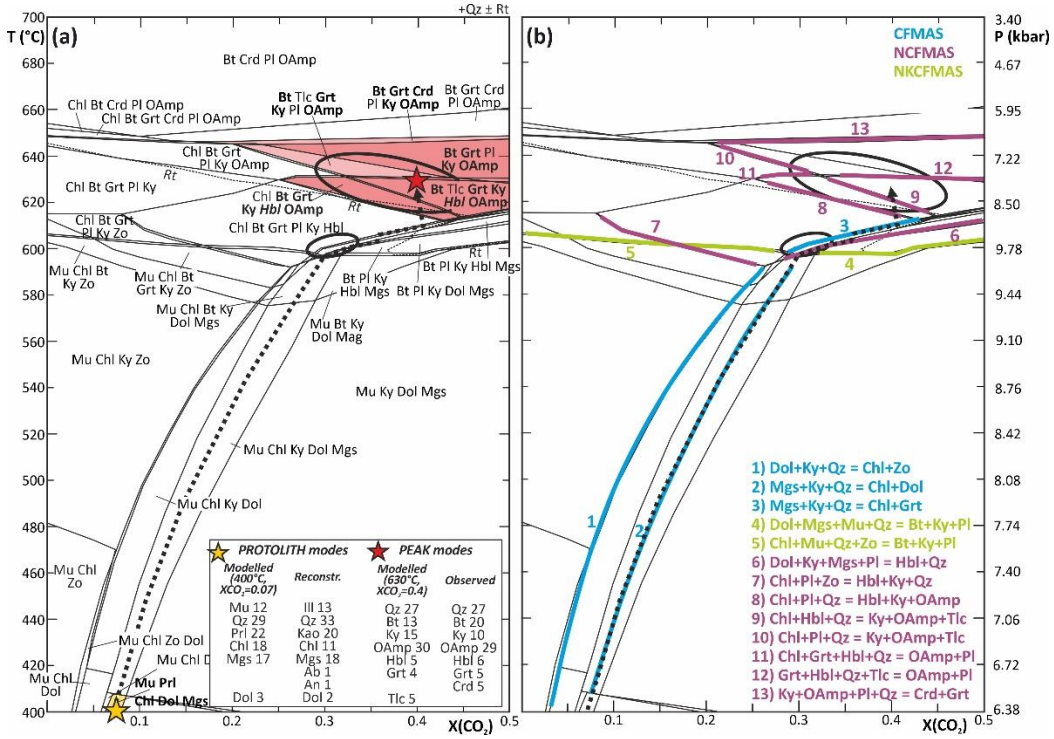

Fig. 6.22: (a) Same P/T–X(CO_2) isochemical phase diagram modelled for sample 17a–35 as in Fig. 6.15. The yellow and red fields correspond to the modelled stability fields of the protolith's and peak assemblages, respectively. Yellow and red stars refer to the "starting point" and peak P–T–X(CO_2) conditions as discussed in Section 6.3. The black ellipses summarize the prograde and peak P–T–X(CO_2) conditions. (b) Same P/T–X(CO_2) isochemical phase diagram as (a), highlighting the isothermal/isobaric univariant equilibria relevant to this sample (different colours refer to different chemical systems). It should be noted that the univariant curves overlap the narrow low–variant fields of the pseudosection. Reactions are written such as the products are on the high–T side of the equilibrium curves. The dashed black arrows approximate the P–T–X(CO_2) evolution inferred for sample 17a–35 as discussed in the text.

Sample 17b–7d

This sample differs from the others discussed so far, because the X(CO_2) of the fluid predicted in equilibrium with the peak assemblage is very similar to that of the fluid modelled at the "starting" P–T–X(CO_2) conditions (Fig. 6.23a). This implies that the sample has followed a nearly vertical P–T–X(CO_2) evolution, which is typical of externally buffered systems in which the composition of the fluid is controlled by the infiltration of external fluids rather than by the system itself.

The assemblage modelled at the starting P–T–X(CO_2) conditions (400 °C, 6.4 kbar, X(CO_2)=0.10) consists of pyrophyllite, quartz and magnesite, with magnesite being by far the most abundant phase (85 vol%) (Fig. 6.23a). A temperature increase of a few degrees is sufficient for the system for reaching the first decarbonation reaction (Mgs+Prl = Chl+Qz; reaction 1 in Fig. 6.23b), which is responsible for the production of chlorite and the consumption of about 5 vol% of magnesite at T=405–410 °C. Assuming that the system evolves following an externally buffered path, it then reaches a further important decarbonation reaction at about 480–500 °C, which marks the final consumption of quartz

and the appearance of talc (Mgs+Qz = Tlc; reaction 3 in Fig. 6.23b). This reaction consumes an additional 6 vol% of magnesite. Once entered within the Chl+Mgs+Tlc field, the system does not experience any other significant reaction, up to the estimated peak conditions at 630°C, 8.0 kbar, $X(CO_2)$=0.10–0.15 (Fig. 6.23b).

According to these results, the following points are worth to be mentioned:

- the sample experiences two main decarbonation events during the prograde stage (reactions 1 and 3 in Fig. 6.23b), each one responsible for the consumption of 5–6 vol% of magnesite. These decarbonation reactions are modelled at about 405–410 °C, and 480–500 °C, respectively and appear to be triggered by the influx of H_2O–rich external fluids, likely deriving from the metapelites hosting the lens–like bodies of magnesite–rich ores (see Chapter 4, section 4.1.2.1);
- the fluid produced through these decarbonation reactions has low $X(CO_2)$ values;
- the amount of CO_2 produced through the breakdown of 5–6 vol% of magnesite is equal to 2.8–3.4 wt% for each of the two CO_2–producing pulses, for a total CO_2 production of 6.2 wt%.

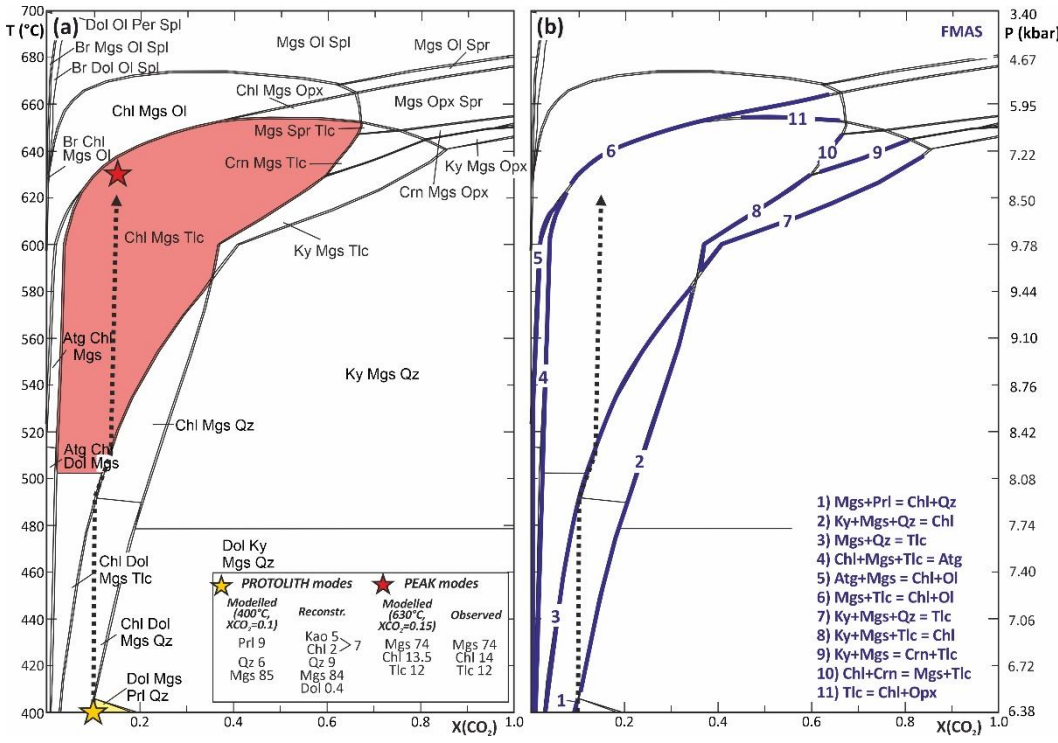

Fig. 6.23: (a) Same P/T–$X(CO_2)$ isochemical phase diagram modelled for sample 17b–7d as in Fig. 6.16. The yellow and red fields correspond to the modelled stability fields of the protolith's and peak assemblages, respectively. Yellow and red stars refer to the "starting point" and peak P–T–$X(CO_2)$ conditions as discussed in Section 6.3. (b) Same P/T–$X(CO_2)$ isochemical phase diagram as (a), highlighting the isothermal/isobaric univariant equilibria relevant to this sample. It should be noted that the univariant curves overlap the narrow low–variant fields of the pseudosection. Reactions are written such as the products are on the high–T side of the equilibrium curves. The dashed black arrows approximate the P–T–$X(CO_2)$ evolution inferred for sample 17b–7d as discussed in the text.

6.4.2 CO_2 productivity of the different lithologies

The results of thermodynamic modelling discussed in section 6.4.1 show that, for all the investigated samples, decarbonation occurs in one (or more) pulse through nearly discontinuous reactions operating in relatively narrow temperature intervals, rather than being a continuous process occurring during most of the prograde evolution. However, the temperatures at which these decarbonation pulses occur, vary as a function of the rock composition, and especially of the amount of carbonate (dolomite or magnesite) originally contained in the protolith (Table 6.3). Samples originally containing low amounts of carbonates (<10 vol%) release most of the CO_2 during the prograde stage, at T<600 °C, whereas samples containing higher amounts of carbonate in the protolith (10–30 vol%) produce CO_2 during the decompression stage, at peak P–T conditions. This implies that **the most significant episode of decarbonation in each sample occurs at a progressively higher temperature for increasing amounts of carbonate originally present in the protolith**.

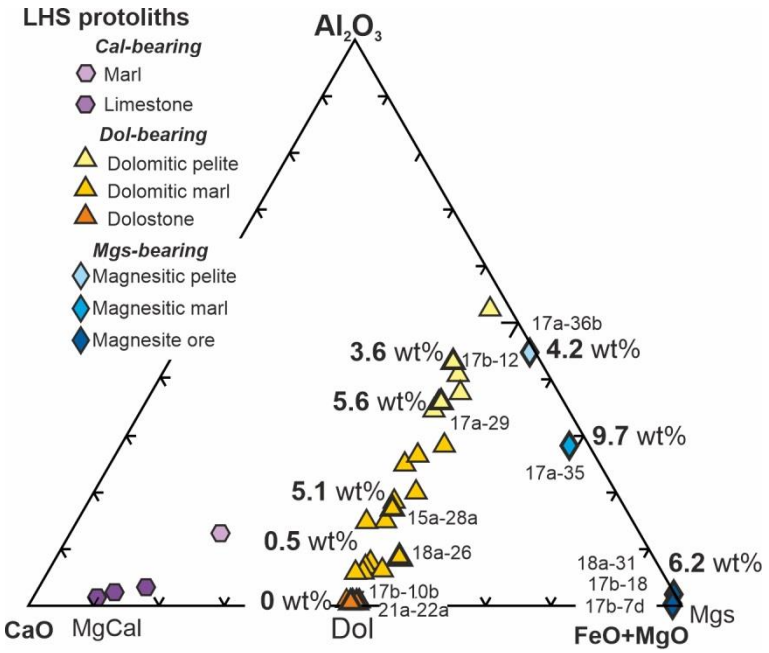

Fig.6.24: Dolomite and magnesite series plotted in the CAF diagram (same as Fig. 6.1); the amount of CO_2 produced by each sample is highlighted. Note that the maximum amounts of CO_2 are realized by samples containing the intermediate amount of carbonates in both the series.

The carbonate content of the protolith also influences the final amount of CO_2 released by each lithology, but the relation between these two parameters is not linear (Figs. 6.24 and 6.25). For the dolomite–series, the results of the modelling show that samples derived from protoliths originally containing 14–30% of dolomite (dolomitic marls and dolomitic pelites with Dol>10%; samples 17a–29 and 15a–28a) produce the largest amounts of CO_2, i.e. 5–6 wt% of CO_2 (Table 6.3, Fig. 6.24), whereas dolomitic pelites originally containing less than 10% of dolomite are less productive (3.6 wt% of CO_2). The sample derived from dolomitic marl originally containing more than 30% of dolomite (40%; sample 18b–26) is

substantially unreactive, and the same is for the dolomitic marbles derived from impure dolostones (samples 17b–10b and 21a–22a).

Table 6.3. Amounts of CO_2 produced by different lithologies

Dolomite series				
	vol% Dol in the protolith	vol% Dol consumed	T (°C) of the main decarbonation reaction	wt% CO_2 produced
17b–12	7	7	550–580	3.6
17a–29	14	11	> 610	5.6
15a–28a	31	10	> 610	5.1
18a–26	40	1	400–700	0.5
17b–10b	80	0		0
21a–22a	84	0.5		0
Magnesite series				
	vol% Mgs in the protolith	vol% Mgs consumed	T (°C) of the main decarbonation reaction	wt% CO_2 produced
17a–36b	7.5	7.5	520–550	4.2
17a–35	17	17	> 600	9.7
17b–7d	84	11	<500	6.2

Similarly, for the magnesite series, the sample derived from magnesitic marl with more than 17% of magnesite (sample 17a–35) is the most productive (9.7 wt% of CO_2) whereas the magnesitic pelite (sample 17a–36b) originally containing less than 10% of magnesite releases lower amounts of CO_2 (Table 6.3 and Fig. 6.24).

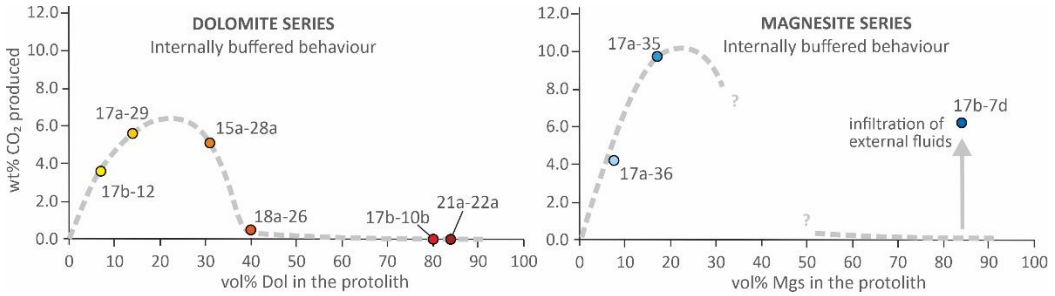

Fig: 6.25: Diagrams representing the amount of CO_2 released as a function of the initial amount of carbonates originally present in the protolith. Note that the most productive lithologies in terms of CO_2 released are dolomitic pelites and marls containing 15–30% of dolomite and magnesitic marls containing more than 10% of magnesite.

Samples derived from protoliths dominated by magnesite (i.e. magnesite ores) apparently have an opposite behaviour with respect to impure dolostones, being reactive during the prograde stage and releasing quite significant amounts of CO_2. However, this behaviour is strictly related to the availability of external H_2O–rich fluids which infiltrated the magnesite ores (Fig. 6.25). Field observations suggest that where the influx of external fluids was null

or negligible, little or no talc developed at the expenses of magnesite, and the magnesitic body remained substantially unreactive. On the opposite, where the infiltration of external fluids was pervasive (e.g. in the case of thin, metric layers of magnesitic rocks embedded within metapelites), most of the original magnesite was replaced by talc and the rock is transformed in a talc schist. Consequently, the amounts of CO_2 potentially released by magnesite ores vary dramatically from zero (in the case of no infiltration) to extremely high values in the case most of the magnesite is converted to talc. According to our field data, both these two extremes are uncommon; sample 17b–7d is, instead, quite representative, and the calculated amount of CO_2 released is therefore taken as an average value for this lithology.

Chapter 7

Present–day CO_2 emissions

7.1 Premise

Evidence of CO_2 release is widespread in the MCT zone of the Nepal Himalaya, either through the dissolved carbon in the hot springs' water or through direct degassing at the surface in the vicinity of the hot springs (Perrier et al., 2009). Several thermal springs, which are often famous pilgrimage sites for the local population, were first reported in Central and Western Nepal in the vicinity of the MCT and MFT (Le Fort, 1975; Bhattarai, 1980; Grabczak and Kotarba, 1985; Bhattarai, 1986; Kotarba, 1986; Sharma 1995; Perrier et al., 2002a). These thermal springs have high alkalinity, which contributes to the total dissolved inorganic carbon (DIC) of the Narayani watershed (Evans et al., 2004). The high carbon isotopic compositions ($\delta^{13}C$) of these thermal springs suggested a metamorphic decarbonation source and a massive CO_2 degassing near the water table in the Trisuli and Marsyandi valleys (Becker, 2005; Becker et al., 2008; Evans et al., 2008). CO_2 was not only observed in the water, but it was also reported as gaseous emissions from the ground, initially in the Trisuli valley at the Syabru–Bensi hydrothermal system (Perrier et al. 2009). This CO_2–rich gas is characterised by radiogenic helium, high radon–222 content (radioactive gas of 3.82–day half–life) and $\delta^{13}C$ values, suggesting metamorphic CO_2 production at more than 5 km depth (Perrier et al., 2009).

These seminal studies have stimulated intensive field research aimed at characterising the chemical features of thermal springs and quantifying the CO_2 emissions, not only in the Trisuli valley (Girault et al., 2014a; Girault et al., 2016b) but also in other regions of Western, Mid–Western and Central Nepal (Girault et al., 2014b; Girault et al., 2016b; Ghezzi et al., 2017 ; Ghezzi et al., 2019). Extensive work has been done, so far, in the central and western parts of Nepal Himalayas regarding the direct measurements of gaseous CO_2 and the CO_2 from the thermal springs (Perrier et al., 2009, Girault et al., 2014a,b, 2016b, 2018). At the beginning of this project, however, data from eastern Nepal and Far Western Nepal were lacking. Exploration of thermal springs in eastern and Far Western regions of the Nepal Himalaya was then performed in the framework of this project, with the aim of better understanding and quantifying the overall CO_2 release from the whole Nepal Himalaya. This chapter presents the data collected during the field exploration and the results obtained from each of the investigated sites. The present–day CO_2 emissions from eastern and Far Western Nepal are then summarized.

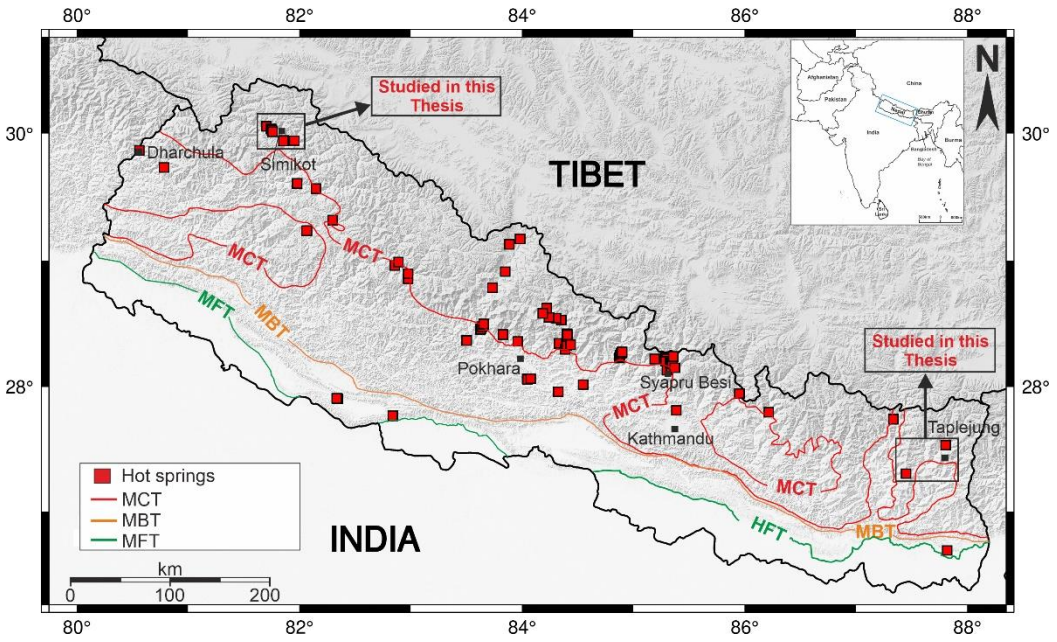

Fig. 7.1: Map of Nepal showing the location of the hot springs in relation to the main tectonic discontinuities (MFT, MBT, MCT).

7.2 Exploration in Eastern Nepal

In eastern Nepal, two places (Nundhaki and Sekhathum) have been explored for the hot springs and the CO_2 degassing measurements. The first hot spring is located in the Nundhaki village of Sankhuwasabha district and the second one is located in the Sekhathum village of Taplejung district (Fig. 7.1).

7.2.1 The Nundhaki hot spring (NUN)

7.2.1.1 Geological context and description of the site

The Nundhaki site is located at about 25 km southeast of Khandbari (Fig. 7.1) in the remote village of Nundhaki. To reach the site, it takes a total of 10–12 hours, 8 hours by public bus from Dharan to Chainpur Bazar, and about 2–4 hours from Chainpur Bazar to the Nundhaki village by local jeep. The roads from Chainpur Bazar to Nundhaki are off–road and the local jeep to Nundhaki is occasional, but one can reserve the vehicle to reach Nundhaki. The NUN hot spring lies at an altitude of 1405 m a.s.l. and seems to be a part of the stream, as the main outsource of the hot spring is not visible. The hot spring is located on the hillslope, on the southern bank of the Piluwa River, and it is channelized between cemented walls (Fig. 7.2a).

Geologically, the Nundhaki hot spring (NUN) is located within the GHS, here represented by fine– to medium–grained quartzo–feldspathic biotitic gneisses (Milke Gneiss Formation in Dhital, 2015). This unit also consists of two–mica paragneisses with abundant garnet

porphyroblasts, kyanite and sillimanite, thin layers of hornblende–bearing gneisses and quartzites, and is also frequently intruded by small bodies of tourmaline granites and pegmatites. The MCT lies a few km towards SW from the hot spring.

7.2.1.2 Results obtained at Nundhaki

The temperature measured at Nundhaki is 18.26 ± 0.03 °C. The CO_2 flux has been measured at the periphery of the observed hot spring using the accumulation chamber method (see Chapter 3). The CO_2 gaseous emission is not significant, and it is compatible with the background value (Fig. 7.4a–c). The average value and the geometric mean of the flux are 29.1±4.7 and 23.5±1.2 g m^{-2} s^{-1}.

7.2.2 The Sekhathum hot spring (SEK)

7.2.1.1 Geological context and description of the site

The SEK hot spring is located in the Sekhathum village of Taplejung district, ca. 35 km north–east of Taplejung, on the alluvium terrace on the right bank of the Ghunsa River, about 1 km upstream from the confluence of Tamor Nadi and Ghunsa Khola. The site can be accessed by public jeep, it takes about five to six hours to reach the Sekhathum village from Taplejung. The roads are mostly rough without blacktopped. At present, we cannot see the hot spring as it is covered by debris related to the road construction (Fig. 7.2b). According to the local people living nearby the Sekhathum hot spring, there was one hot spring just on the bank of the Ghunsa River, which is now no more accessible.
Geologically, the Sekhathum hot spring (SEK) lies in the GHS of the Nepal Himalaya (Shrestha et al., 1984; Dhital, 2015). The lithology around the hot spring mostly consists of homogeneous banded gneisses with mm–sized garnet.
CO_2 measurements were not performed because the periphery of the hot spring is not accessible (Fig.7.2b).

7.2.3 Present–day CO_2 emission in Eastern Nepal

Based on the field–data measurements, for the moment no large gaseous CO_2 emission is recorded near the vicinity of the observed hot springs. The measured CO_2 emission is compatible with the background value. The overall data set from eastern Nepal gives the arithmetic and geometric averages of 29.1±4.7 and 23.5±1.2 g m^{-2} d^{-1} and mean surface CO_2 flux (n= 21) ranges from 7.6–64.4 g m^{-2} d^{-1}. Considering all the data, the overall CO_2 discharge from eastern Nepal (Hatiya, Nundhaki and Sekhathum) is 0.8±0.2 mmol s^{-1}.

7.3 Exploration in Far–Western Nepal

In Far–Western Nepal, six main sites have been explored, all located in the periphery of Simikot in the Humla district. The main hot springs from each site are briefly discussed below.

Fig. 7.2: Representative images of the hot–springs sites from Eastern (a and b) and Far–Western Nepal (c to l).

7.3.1 The Kermi hot springs (KER1, KER2, KER3)

7.3.1.1 Geological context and description of the sites

There are three main hot springs in Kermi and other small hot springs are additionally present in the vicinity of the main hot springs. These are located in the Kermi village, which is about 14.5 km northwest of Simikot, on the banks of a small stream that ultimately joins the Humla Karnali River. The hot spring is accessed only by foot from Simikot, no public vehicles (bus or jeep) can reach the site because the road is still under construction. The sporadic (reserved) jeeps can only arrive halfway, as the last part of the road is under construction. The roads are not blacked topped, and they are off–road. It takes about 8 hours to reach Kermi on foot from Simikot. All these three hot springs are in almost natural conditions, although local people have channelized some water to make a few hot water bathing spots nearby the main springs by making a cemented tap.

Geologically, these hot springs are located within the GHS of the Nepal Himalaya (Murphy and Copeland, 2005; Robinson et al., 2006), here consisting of anatectic two–mica gneiss es and banded gneisses. The hot springs lie on a terrace formed by alluvium deposits brought by the stream.

7.3.1.2 Results obtained at Kermi

The temperature of the hot springs in Kermi is above 50 °C and the hot spring KER2 has the highest temperature of 76.9±0.5 °C evered measured in Nepal. The KER2 hot spring is also characterized by intense bubbling, with the release of H_2S gas as well, whereas there was no evidence of such bubbling and the presence of H_2S gas from the other hot springs. The CO_2 flux was measured in the vicinity of all the hot springs, but the values were consistent with the background value. So, no significant CO_2 degassing is observed from the ground in the Kermi site.

7.3.2 The Ghadapori, Chhahara and Kholsi hot springs (DAD, CHA and KHO)

7.3.2.1 Geological context and description of the site

The Ghadapori, Chahhara and Kholsi hot springs are located about 7–10 km northwest of Simikot and are distant about 1 km from each other. The hot springs are only accessible by foot or using reserved vehicles like jeeps (no public transportation available here); it takes about 2 hours to reach the site using a reserved vehicle, and about 4 hours by foot. All these hot springs are located on the western bank of the Humla–Karnali River. The hot springs in Ghadapori and Kholsi are located at the river level, while the Chhahara site is on the hill slope, just above the river. The hot springs are in an almost natural state with slight modifications by the locals, using the water for hot spring bathing.
The Ghadapori, Chahhara and Kholsi hot springs all lie in the GHS lithologies (Robinson et al., 2006), consisting of anatectic gneisses and medium to coarse–grained banded gneisses.

7.3.2.2 Results obtained at Ghadapori, Chahhara and Kholsi hot spring

The temperatures of Ghadapori, Chhahara and Kholsi hot springs are 65.8±0.2, 46.9±0.5 °C and 67.7±0.2 °C, respectively (Table 7.1). The flow rate measured in the Chhahara site is 0.27±0.03 L s^{-1}, whereas the flow rate of the other springs was not measured because they are at the ground level and it was difficult to measure the actual flow rate.

7.3.3 The Dojam hot spring (DOJ)

7.3.3.1 Geological context and description of the site

The Dojam site is located at ca. 3 km southeast of Dojam village, on the northern bank of the Dojam River, which is a tributary of the Humla Karnali River. The hot spring is only accessible by foot, and it takes about 3 hours to reach the hot spring from the Dojam village, which is in turn accessible by foot in 4 hours from Simikot (i.e. total of 7 hours from Simikot). This hot spring is located on the hill slope, and it is in a natural state. The water and the sediments brought by this spring are red in colour and have a strong smell of iron. Geologically, the Dojam hot spring lies in the GHS lithologies (Robinson et al. 2006), which consist of fine– to medium–grained two–mica gneisses with mm–sized garnet.

7.3.3.2 Results obtained at Dojam

The Dojam hot spring has a temperature of 15.17±0.01 °C and no bubbling is observed. Gaseous CO_2 emission was measured in the vicinity of the spring, butCO_2 flux values are compatible with the background value. The overall data set from Dojam sites gives the arithmetic and geometric averages of 24.4±4.06 and 21.6±0.7 g m^{-2} s^{-1} and the mean surface CO_2 flux (n= 9) ranges to 8.7–45.1 g m^{-2} d^{-1}. The plot for the flux in each point is shown in Fig. 7.4 (d and e).

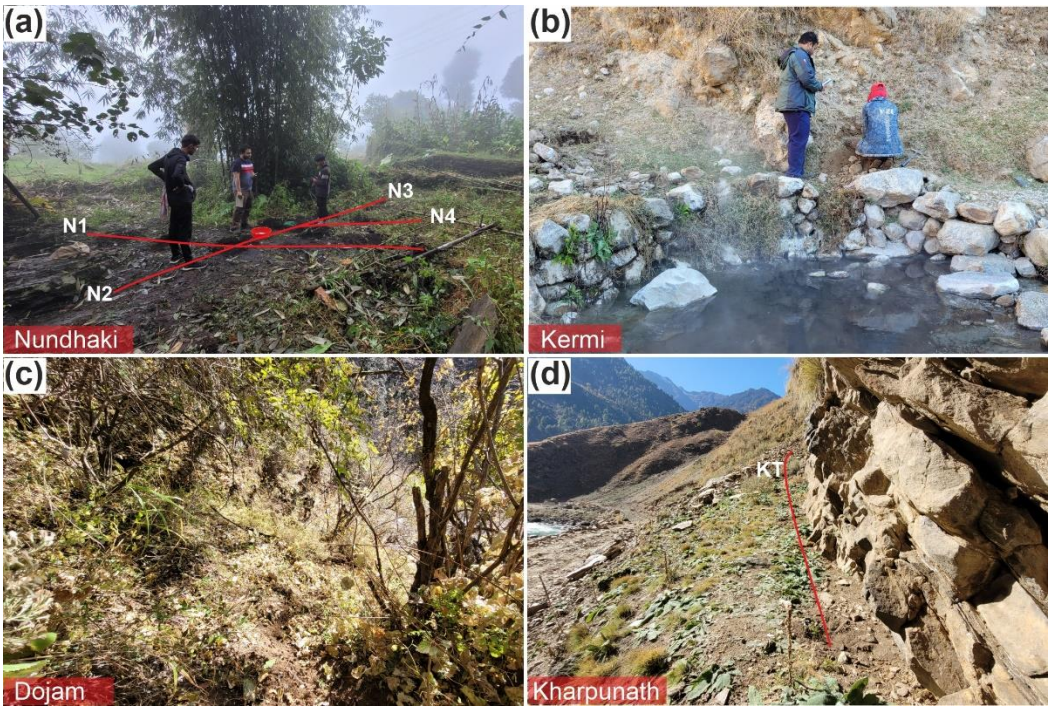

Fig. 7.3: Representative photographs of the direct measurement of the CO_2 flux in the field, the red lines are the profiles along which the measurements have been done. (a) Nundhaki site (b) Kermi site (c) Dojam site, and (d) Kharpunath site.

Table 7.1: Summary of the hot spring studied in eastern and Far–western Nepal with their detailed measured parameters. n.m.: not measure

S.N.	Spring	Location	Coordinates (longitude, latitude in °)	pH	Conductivity (µS/cm)	Temperature (°C)	Presence of Bubbles	Presence of H_2S	High content of CO_2
1	KER1	Humla–Karnali valley	81.703, 30.055	6.5±0.05	0.49±0.04	52.4±0.03	no	no	no
2	KER2	Humla–Karnali valley	81.702, 30.056	6.4±0.03	0.79±0.02	76.9±0.5	yes	yes	no
3	KER3	Humla–Karnali valley	81.702, 30.055	6.4±0.03	0.72±0.01	72.3±0.008	no	no	no
4	DAD	Humla–Karnali valley	81.752, 30.025	6.6±0.05	0.96±0.04	65.7±0.03	no	no	no
5	CHA	Humla–Karnali valley	81.744, 30.035	6.4±0.03	1.81±0.02	46.4±0.3	no	no	no
6	KHO	Humla–Karnali valley	81.757, 30.012	6.8±0.05	2.21±0.11	67.6±0.03	no	no	no
7	DOJ	Dojam valley	81.953, 29.942	5.9±0.03	1.10±0.00	15.2±0.007	no	no	no
8	KHA1	Humla–Karnali valley	81.857, 29.944	6.2±0.03	1.49±0.00	48.3±0.04	no	no	no
9	KHA2	Humla–Karnali valley	81.856, 29.940	6.0±0.03	1.90±0.00	63.6±0.001	no	yes	no
10	KHA3	Humla–Karnali valley	81.855, 29.940	5.9±0.03	1.81±0.00	52.5±0.02	no	yes	no
11	NUN	Nundaki, Chainpur	87.448, 27.306	5.9±0.07	0.06±0.00	15.2±0.005	no	no	no
12	SEK	Sekhathum, Taplejung	87.806, 27.535	n.m	n.m	n.m	n.m	n.m	n.m

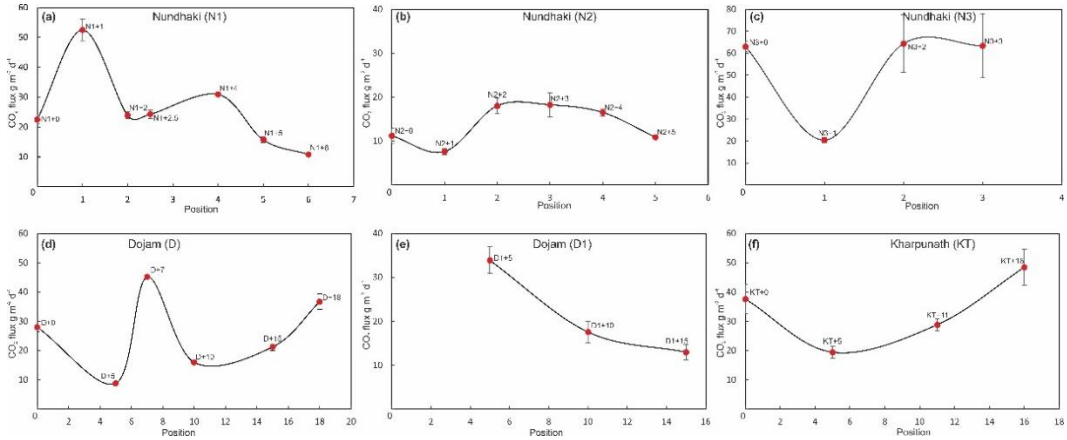

Fig.7.4: Graphical representation of the CO_2 flux in each position along the analysed profiles.

7.3.4 The Kharpunath hot springs (KHA1, KHA2 and KHA3)

7.3.4.1 Geological context and description of the site

The Kharpunath hot springs are located ca. 5 km southeast of Simikot, near the confluence of the Dojam River and Humla Karnali River. The Kharpunath site can be accessed by public jeep or by foot from Simikot. It takes about one and a half hours by jeep, and about 3–4 hours by foot to reach Kharpunath from Simikot. There are numerous hot springs on the bank of the Humla Karnali River near the Kharpunath area, and they are mostly near the river level or some below the river level. Among them, three springs have been studied; one of them is cemented and a pond for bathing was made by local people, whereas the other two are in the natural state. Nearby the hot springs, there is a famous Hindu temple of Shiva, close to the confluence of the Dojam River and Humla Karnali River.

The Kharpunath hot spring geologically lies in the GHS (Murphy and Copeland, 2005; Robinson et al., 2006) lithologies, consisting of two mica gneisses.

7.3.4.2 Results obtained at Kharpunath

The warmest spring (KHA2) in Kharpunath has a temperature of 63.72±0.02 °C, and the other two springs KHA1 and KHA3 have a temperature of 48.3±0.04 °C and 52.5±0.02 °C, respectively. A strong pervasive smell of H_2S was detected above each cemented basin. The CO_2 emissions were measured near the KHA1, but the value is similar to the background value (Girault 2011) and there was no evidence of bubbling as well. The CO_2 flux dataset from Kahrpunath site gives the arithmetic and geometric averages of 33.6±7.1 and 31.8±4.1 g m^{-2} d^{-1}, respectively and the mean surface CO_2 flux (n= 4) ranges from 19.42 to 48.48 g m^{-2} d^{-1}. The plot for the flux in each point is shown in Fig. 7.4(f).

7.3.5 Present–day CO_2 emission in Far–Western Nepal

A total of two sites and three profiles have been studied so far for the gaseous emissions in Far Western Nepal. There was no significant CO_2 gaseous emission from the sites. Based on the dataset from Far Western Nepal the overall arithmetic and geometric averages for CO_2 flux are 29.0±3.5 and 26.2±1.0 g m^{-2} d^{-1}, respectively. These values are compatible with the background value.

Table 7.2: Summary of CO_2 flux measured in the studied sites (three) in Eastern and Far–Western Nepal.

Site	Profile	Points	Coordinates	Flux	Uncertainties	Arithmetic Mean	Geometric Mean	Minimum	Maximum
Eastern Nepal									
Nundhaki	N1	N1+0		22.4	1.3	29.1±4.7	23.5±1.2	7.6	64.4
		N1+1	27.30127, 87.4543, 1798 m	52.5	3.7				
		N1+2		23.9	1.2				
		N1+2.5		24.3	1.5				
		N1+4		30.9	0.4				
		N1+5	27.30122, 87.4543, 1796m	15.7	0.9				
		N1+6		10.8	0.5				
	N2	N2+0	27.30122, 87.45427, 1796 m	11.22	1.68				
		N2+1		7.62	0.70				
		N2+2		18.02	1.81				
		N2+3		18.25	2.77				
		N2+4		16.52	0.84				
		N2+5	27.30125, 87.454306, 1798 m	10.88	0.36				
	N3	N3+0	27.301306, 87.454306, 1804 m	63.1	2.3				
		N3+1		20.4	1.2				
		N3+2		64.4	13.0				
		N3+3		63.4	14.6				
	N4	N4+0		50.1	1.0				
Far Western Nepal									
Dojam	D	D+7(below)	29.9425, 81.95361, 2788 m	45.13	4.39	24.4±4	21.6±0.7	8.76	45.13
		D+0	29.9424, 81.95367, 2794 m	28.03	1.53				
		D+5		8.76	0.64				
		D+10		15.96	0.39				
		D+15	29.9425, 81.95361, 2791 m	21.22	1.20				
		D+18	29.94258, 81.95364, 2807 m	36.67	2.66				
	D1	D1+5		33.89	3.02				
		D1+10		17.57	2.46				
		D1+15		12.96	1.74				
Kharpunath	KT	KT+0	29.94461, 81.95786, 2122 m	37.60	5.04	33.6±7.2	31.8±4.1	19.42	48.48
		KT+5		19.42	2.12				
		KT+11		28.81	2.09				
		KT+16	29.9445, 81.95778, 2128 m	48.48	6.15				

7.4 Conclusions

Hot springs are widespread along the whole Himalayan belt, not only in the MCT zone, but also above and below the MCT. The hot springs from eastern Nepal investigated in this study Nundhaki site (NUN) and Sekhathum site (SEK) are located within the GHS, and the measured CO_2 is similar to the background value, with the geometric mean of 23.5±1.2 and minimum and maximum flux of 7.62 g m^{-2} d^{-1} and 64.4 g m^{-2} d^{-1}. Also in Far Western Nepal, most of the analysed hot springs are located in the high–grade gneisses of GHS; among them, the hot spring KER2 has a temperature of 76.9±0.5 °C, which is the highest temperature measured so far in Nepal. The gaseous CO_2 emission in far–western Nepal is also negligible, as the value is compatible with the background value, with the average and geometric mean of 29.02±3.5 and 26.2±1.04 respectively and the minimum and maximum flux of 8.76 and 48.48 respectively.

Chapter 8

Discussion

8.1 CO_2 production in the past: from punctual data to a regional–scale estimate

The overall results presented in Chapters 4, 5 and 6 are summarized and critically discussed in this chapter. The aim is to extrapolate punctual data obtained from single samples to the regional scale and ultimately, to estimate the past production of metamorphic CO_2 at the scale of the whole LHS of Nepal Himalaya. Minimum, maximum and average values are provided for all the parameters involved in these estimates; this allows to give a reliable estimate of the uncertainties associated to the extrapolation.

8.1.1 CO_2–producing lithologies in the LHS

8.1.1.1 Types and distribution of CO_2–producing lithologies

The results presented in Chapter 4 show that, in the Upper–LHS, CO_2–producing lithologies are mostly represented by rocks derived from dolomite– and magnesite–bearing protoliths rather than from calcite–bearing protoliths. This is the main difference with respect to GHS, in which CO_2–source rock mostly derive from calcite–bearing protoliths (e.g. Rolfo et al., 2017; Groppo et al., 2017, 2021; Rapa et al., 2017); the potential paleo–geographic and stratigraphic implications of this observation are beyond the aim of this study. Among these CO_2–producing lithologies, the most productive in terms of CO_2 are those derived from protoliths originally containing <30 vol% of carbonates (i.e. dolomitic and magnesitic pelites, dolomitic and magnesitic marls) (see section 6.4.2).

Dolomite and magnesite–bearing lithologies are limited to the Upper–LHS, whereas they do not occur in the Lower–LHS. Within the Upper–LHS, dolomite– and magnesite–bearing lithologies occur in the Nourpul Formation, Dhading Dolomite Formation and Benighat Slate Formation. The carbonate–bearing protoliths of these formations were deposited: (1) during the final stages of rifting (Nourpul Fm.), (2) during the development of a shallow water carbonate platform locally characterized by evaporitic conditions (Dhading Dolomite Fm.) and, (3) during the drowning of the platform due to the progressive subsidence of the passive continental margin (Benighat Slates Fm.) (see section 4.2). The ***type and the abundance of carbonate–bearing protoliths*** deposited in these different environments vary in the three formations (Table 8.1). Field and petrographic data suggest that carbonate–bearing lithologies are less abundant in the Nourpul Formation, where they represent 0–25% of the whole sequence, depending on the considered cross–section; magnesite–bearing protoliths are absent in this formation. The Dhading Dolomite Formation is dominated by dolomite–bearing lithologies, mainly derived from impure

dolostones and dolomitic marls, with minor amounts of dolomitic pelites. Volumetrically less abundant magnesite deposits are locally associated to these dolomitic lithologies. Overall, carbonatic rocks represent 70–90% of the whole Dhading Dolomite Formation. The Benighat Slates Formation contains a moderate proportion of carbonatic lithologies (15–35% of the whole sequence), mostly derived from dolomitic and magnesitic pelites, and from minor dolomitic and magnesitic marls.

Table 8.1 - Volume (%vol) of carbonate-bearing lithologies in Upper-LHS formations

	Nourpul Fm.			Dhading Dolomite Fm.			Benighat Slates Fm.		
	min	max	average	min	max	average	min	max	average
Dolomitic pelite	5%	10%	8%	5%	10%	7.5%	10%	15%	12.5%
Dolomitic marl	5%	10%	8%	25%	30%	27.5%	1%	5%	3.0%
Impure dolostone	1%	5%	3%	40%	45%	42.5%	-	-	-
Magnesitic pelite	-	-	-	-	-	-	5%	10%	7.5%
Magnesitic marl	-	-	-	-	-	-	1%	5%	3.0%
Magnesite ore	-	-	-	1%	5%	3.0%	-	-	-
Total	11%	25%	18.0%	71%	90%	81%	17%	35%	26%

8.1.1.2 Volumes of CO_2–producing lithologies

Although the correlation at the regional scale among the different stratigraphic units from western to eastern Nepal is not easy (different names are used for the same formations in different areas, see Chapter 2), our data combined with those of the literature suggest that the ***thickness*** of the Nourpul Formation, Dhading Dolomite Formation and Benighat Slates Formation (and their equivalents in western and eastern Nepal) varies along strike. This is especially evident for the Dhading Dolomite Formation and Benighat Slates Formation, whose thickness decreases from west to east, and which are not exposed in eastern Nepal (i.e. in the Arun and Tamor tectonic windows) (Table 8.2a). The general impression is that the thickness of the Dhading Dolomite Formation and Nourpul Formation are complementary (the thicker is the Dhading Dolomite Fm., the less thick is the Nourpul Fm. and vice versa). This could reflect: (1) original variations in the geometry of the margin where the sedimentary protoliths were deposited (e.g. occurrence of structural heights or lows, which could have favoured/hampered the development of a more or less developed carbonate platform), and/or (2) the result of a tectonic elision due to the propagation of the MCT juxtaposing the Lower–GHS over the Upper–LHS. Our own data about the thickness of each formation are quite detailed for central and eastern Nepal (Figs. 8.1 and 8.2), whereas for western Nepal literature data are used (DeCelles et al., 2001; Robinson et al., 2006) (Table 8.2a).

Table 8.2a - Thickness (km) of Upper-LHS formations

	Nourpul Fm.			Dhading Dolomite Fm.			Benighat Slates Fm.		
	min	max	average	min	max	average	min	max	average
Western Nepal	0.1	0.5	0.3	1.0	2.0	1.5	0.5	1.5	1.0
Central Nepal	1.0	2.0	1.5	1.0	2.0	1.5	3.0	4.0	3.5
Eastern Nepal	1.5	2.5	2.0	-	-	-	-	-	-

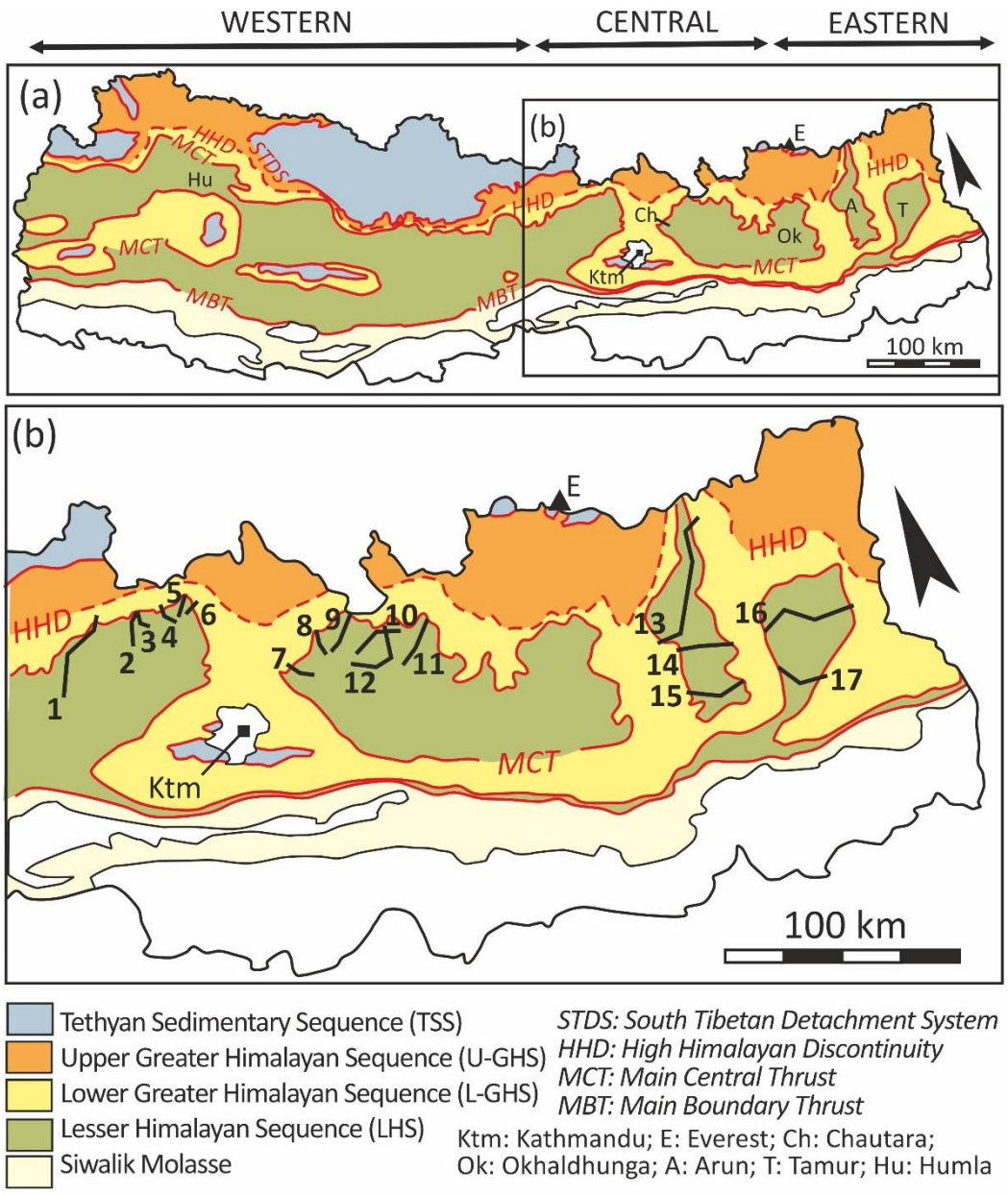

Figure 8.1: (a) Geological sketch map of the Nepal Himalaya showing the major tectono–metamorphic units (modified from Dithal, 2015; He et al., 2015), same figure as Fig. 2.1. (b) Detail of (a) showing the location of the cross sections reported in Fig. 8.2a–d and used for estimating the thickness of the Nourpul, Dhading Dolomite and Benighat Slate Formations along the central and eastern segments of the Nepal Himalaya.

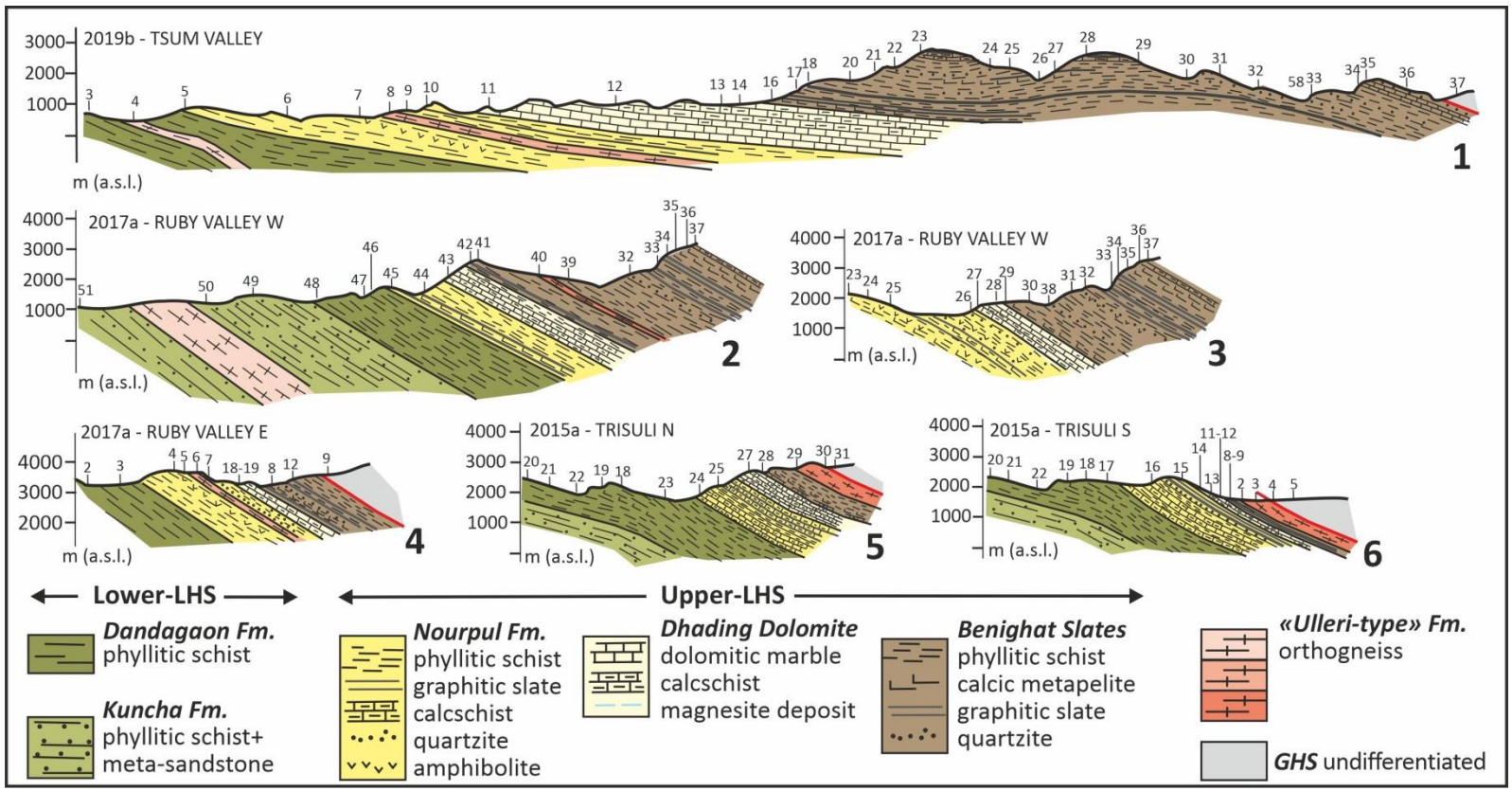

Figure 8.2a – Representative cross–sections across the Lower– and Upper–LHS in central Nepal, NW of Kathmandu. The location of each cross–section is reported in Fig. 8.1. Numbers along each cross section refer to samples collected during different field campaigns, identified by the year reported at the top (e.g. 2019b refers to fieldwork done in 2019; "a" and "b" are used to distinguish between spring and winter seasons, if two field campaigns have been done in the same year). For all the samples, the petrographic characterization is available.

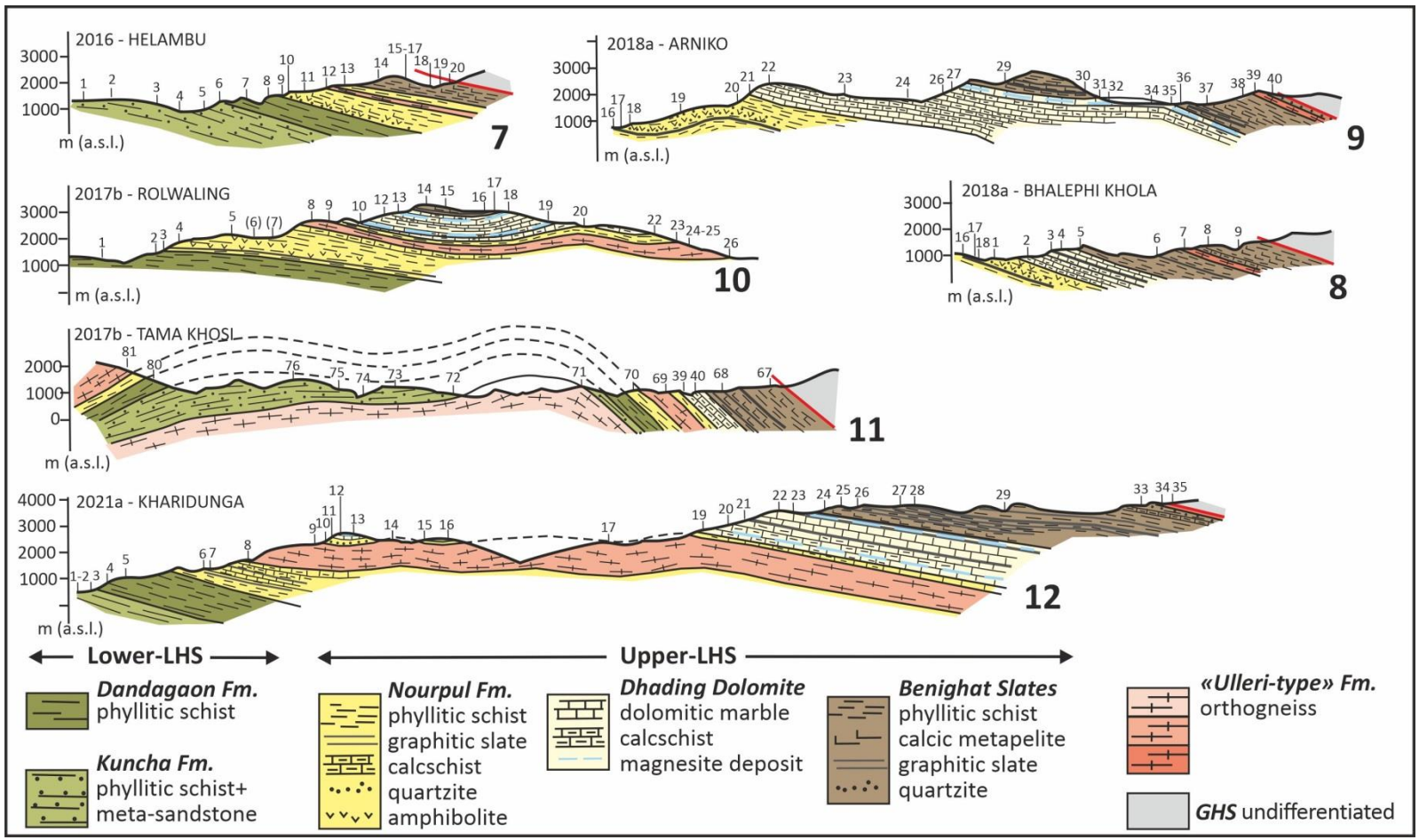

Figure 8.2b – Representative cross–sections across the Lower– and Upper–LHS in central Nepal, NE of Kathmandu. The location of each cross–section is reported in Fig. 8.1. All details as in Fig. 8.2a.

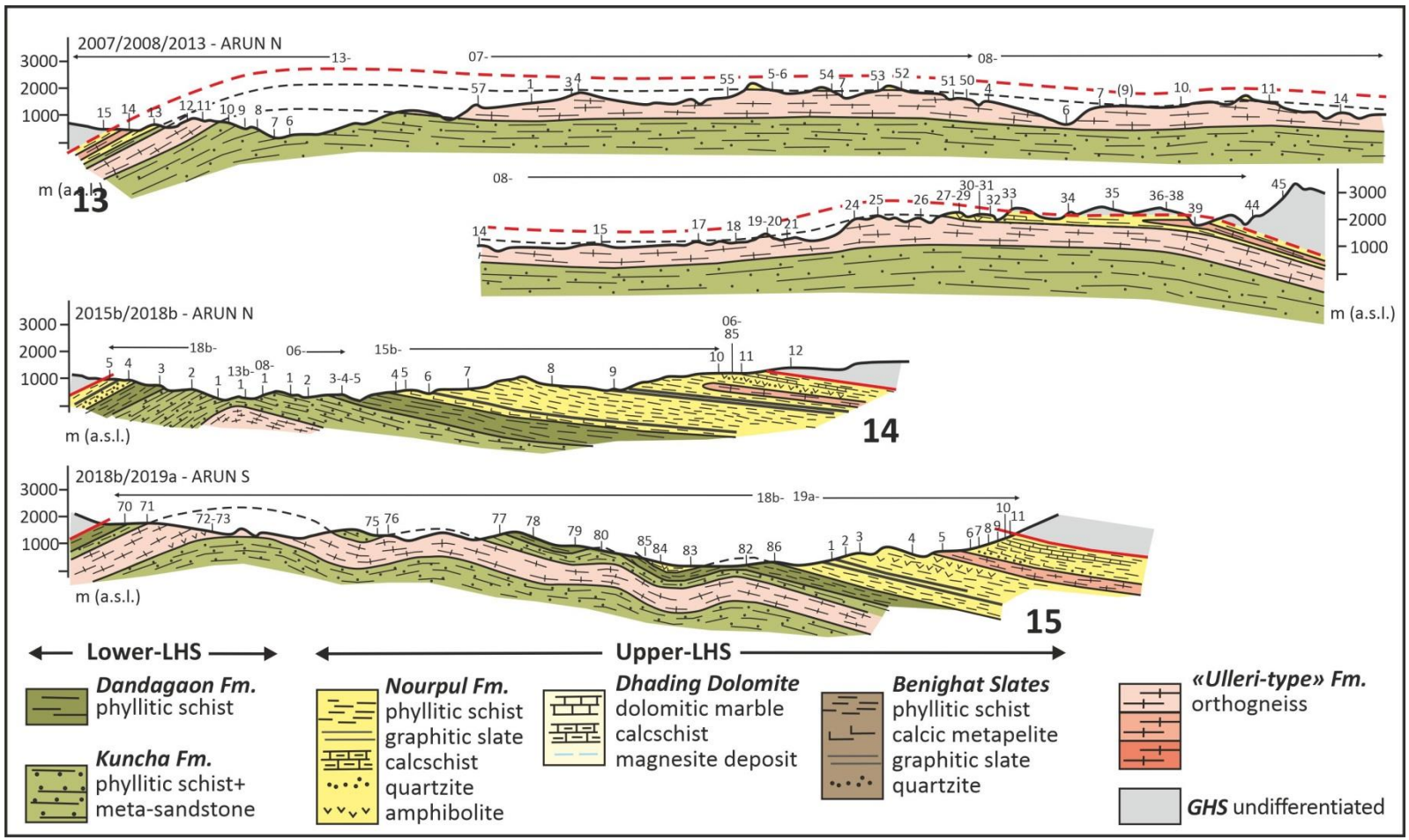

Figure 8.2c – Representative cross–sections across the Lower– and Upper–LHS in eastern Nepal, Arun tectonic window. Location of each cross–section is reported in Fig. 8.1. All details as in Fig. 8.2a.

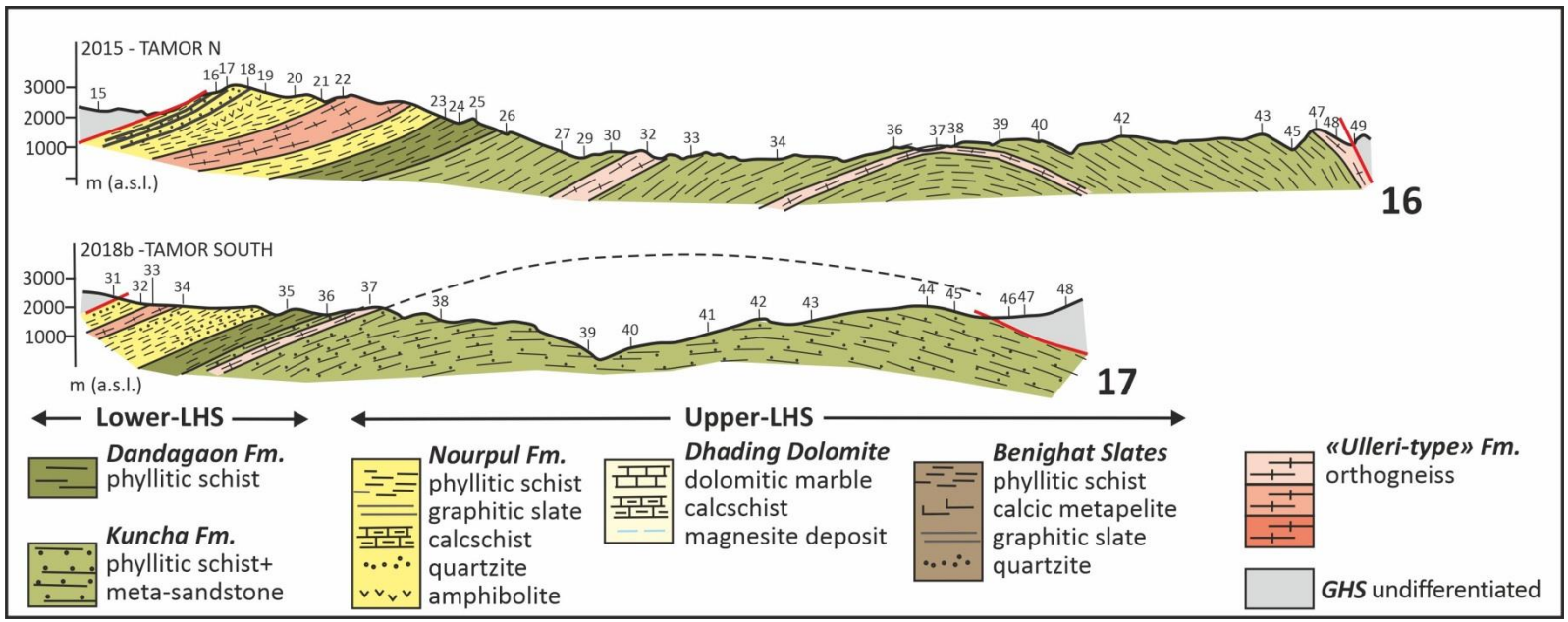

Figure 8.2d – Representative cross–sections across the Lower– and Upper–LHS in eastern Nepal, Tamor tectonic window. Location of each cross–section is reported in Fig. 8.1. All details as in Fig. 8.2a.

Estimating the volumes of the carbonate–bearing lithologies also requires considering the ***magnitude of the LHS shortening***, which varies across different north–south cross–sections from western to eastern Nepal. Long & Robinson (2021) demonstrated that the north–south cross–sectional length of the LHS thrust belt, magnitude of LHS shortening, accretion and structural elevation, and dimension of the LHS duplex culmination all increase westward along the orogen. This results in an increasing complexity of the LHS duplex architecture from east to west (i.e. the westernmost LHS duplexes are characterized by a greater number of imbricates with respect to the eastern duplexes). The magnitude of LHS shortening in western, central and eastern segments of the Nepal Himalaya, as defined by Long & Robinson (2021), and the length of each segment of the belt (Fig. 8.1) are reported in Table 8.2b:

Table 8.2b - Shortening and length (km) of LHS thrust belt

	LHS shortening			LHS lenght
	min	max	average	
Western Nepal	175	522	348.5	450
Central Nepal	220	284	252	200
Eastern Nepal	70	100	85	200

Combining the magnitude of the LHS shortening with the lengths of the western, central and eastern segments of the Nepal Himalaya, the ***LHS surfaces*** are obtained for each segment of the belt (Table 8.2c):

Table 8.2c - Surface (km^2) of LHS thrust belt

	min	max	average
Western Nepal	78750	234900	156825
Central Nepal	44000	56800	50400
Eastern Nepal	14000	20000	17000

The ***total volume of each formation*** in the western, central and eastern segments of Nepal Himalaya are derived by multiplying the LHS surfaces for the thickness of each formation (Table 8.2d). These volumes also comprise the amount of eroded material due to overburden, because they are derived using the magnitude of the shortening, rather than the north–south width of the exposed LHS thrust belt.

Table 8.2d - Total volume (km^3) of each formation

	Nourpul Fm.			Dhading Dolomite Fm.			Benighat Slates Fm.		
	min	max	average	min	max	average	min	max	average
Western Nepal	7875	117450	47047.5	78750	469800	235238	39375	352350	156825
Central Nepal	44000	113600	75600	44000	113600	75600	132000	227200	176400
Eastern Nepal	21000	50000	34000	-	-	-	-	-	-

The ***volumes of carbonate–bearing lithologies within each formation*** are obtained by multiplying their volume percentages (Table 8.1) for the total volume of each formation (Table 8.2d):

Table 8.3a - Total volume (km^3) of carbonate-bearing lithologies in each formation

	Nourpul Fm.			Dhading Dolomite Fm.			Benighat Slates Fm.		
	min	max	average	min	max	average	min	max	average
Western Nepal									
Dolomitic pelite	393.75	11745	3529	3938	46980	17643	3938	52853	19603
Dolomitic marl	393.75	11745	3529	19688	140940	64690	394	17618	4705
Impure dolostone	78.75	5873	1411	31500	211410	99976	-	-	-
Magnesitic pelite	-	-	-	-	-	-	1969	35235	11762
Magnesitic marl	-	-	-	-	-	-	394	17618	4705
Magnesite ore	-	-	-	788	23490	7057	-	-	-
Central Nepal									
Dolomitic pelite	2200	11360	5670	2200	11360	5670	13200	34080	22050
Dolomitic marl	2200	11360	5670	11000	34080	20790	1320	11360	5292
Impure dolostone	440	5680	2268	17600	51120	32130	-	-	-
Magnesitic pelite	-	-	-	-	-	-	6600	22720	13230
Magnesitic marl	-	-	-	-	-	-	1320	11360	5292
Magnesite ore	-	-	-	440	5680	2268	-	-	-
Eastern Nepal									
Dolomitic pelite	1050	5000	2550	-	-	-	-	-	-
Dolomitic marl	1050	5000	2550	-	-	-	-	-	-
Impure dolostone	210	2500	1020	-	-	-	-	-	-
Magnesitic pelite	-	-	-	-	-	-	-	-	-
Magnesitic marl	-	-	-	-	-	-	-	-	-
Magnesite ore	-	-	-	-	-	-	-	-	-

Finally, using an average density of 2.7 g/cm^3 (=2700 Mt/km^3), ***the volumes of carbonate–bearing lithologies in each formation are converted in weights (Mt)*** (Table 8.3b):

Table 8.3b - Total weight (Mt) of carbonate-bearing lithologies in each formation

	Nourpul Fm.			Dhading Dolomite Fm.			Benighat Slates Fm.		
	min	max	average	min	max	average	min	max	average
Western Nepal									
Dolomitic pelite	1.1E+06	3.2E+07	9.5E+06	1.1E+07	1.3E+08	4.8E+07	1.1E+07	1.4E+08	5.3E+07
Dolomitic marl	1.1E+06	3.2E+07	9.5E+06	5.3E+07	3.8E+08	1.7E+08	1.1E+06	4.8E+07	1.3E+07
Impure dolostone	2.1E+05	1.6E+07	3.8E+06	8.5E+07	5.7E+08	2.7E+08	-	-	-
Magnesitic pelite	-	-	-	-	-	-	5.3E+06	9.5E+07	3.2E+07
Magnesitic marl	-	-	-	-	-	-	1.1E+06	4.8E+07	1.3E+07
Magnesite ore	-	-	-	2.1E+06	6.3E+07	1.9E+07	-	-	-
Central Nepal									
Dolomitic pelite	5.9E+06	3.1E+07	1.5E+07	5.9E+06	3.1E+07	1.5E+07	3.6E+07	9.2E+07	6.0E+07
Dolomitic marl	5.9E+06	3.1E+07	1.5E+07	3.0E+07	9.2E+07	5.6E+07	3.6E+06	3.1E+07	1.4E+07
Impure dolostone	1.2E+06	1.5E+07	6.1E+06	4.8E+07	1.4E+08	8.7E+07	-	-	-
Magnesitic pelite	-	-	-	-	-	-	1.8E+07	6.1E+07	3.6E+07
Magnesitic marl	-	-	-	-	-	-	3.6E+06	3.1E+07	1.4E+07
Magnesite ore	-	-	-	1.2E+06	1.5E+07	6.1E+06	-	-	-
Eastern Nepal									
Dolomitic pelite	2.8E+06	1.4E+07	6.9E+06	-	-	-	-	-	-
Dolomitic marl	2.8E+06	1.4E+07	6.9E+06	-	-	-	-	-	-
Impure dolostone	5.7E+05	6.8E+06	2.8E+06	-	-	-	-	-	-
Magnesitic pelite	-	-	-	-	-	-	-	-	-
Magnesitic marl	-	-	-	-	-	-	-	-	-
Magnesite ore	-	-	-	-	-	-	-	-	-

8.1.2 CO_2–producing processes

8.1.2.1 Amounts of CO_2 produced, depths and times at which CO_2 was produced

The results of thermodynamic modelling of carbonate–bearing lithologies discussed in Chapter 6 demonstrate that CO_2 production in specific volumes of CO_2–source rocks occurs in pulses rather than being a continuous process. The ***P–T conditions (and depths) at which these pulses occur*** vary according to the involved lithology: (1) rocks originally containing low amounts of carbonates (dolomitic and magnesitic pelites) produce CO_2 during burial, i.e. during the early prograde evolution (T≈500–550 °C, P≈8.1–8.9 kbar). During the same event, CO_2 is also produced by the small bodies of magnesite ore, if infiltrated by aqueous external fluids; (2) rocks originally containing higher amounts of carbonates (dolomitic and magnesitic marls) produce CO_2 during early decompression, i.e. at the thermal peak (T=610–630 °C, P=7.9–9.1 kbar). In both cases CO_2 is mostly produced at depths of about 25–30 km, but in two different geodynamic regimes (i.e. burial vs exhumation).

The amounts (wt%) of CO_2 produced by each carbonate–bearing lithology is constrained by the results of the thermodynamic modelling (Chapter 6) and are summarized in Table 8.4:

Table 8.4 - Average CO_2 (wt%) produced from carbonate-bearing lithologies

	min	max	average
Dolomitic pelite	2%	7%	5%
Dolomitic marl	1%	7%	4%
Impure dolostone	0%	1%	1%
Magnesitic pelite	3%	6%	5%
Magnesitic marl	5%	10%	8%
Magnesite ore	4%	8%	6%

The ***total amount of CO_2 produced in each formation*** is obtained by multiplying these wt% of CO_2 (Table 8.4) for the total weight of each carbonate–bearing lithology (Table 8.3b):

Table 8.5a - Weight (Mt) of CO_2 produced by each carbonate-bearing lithology in each formation

	Nourpul Fm.			Dhading Dolomite Fm.			Benighat Slates Fm.		
	min	max	average	min	max	average	min	max	average
Western Nepal									
Dolomitic pelite	2.1E+04	2.2E+06	4.3E+05	2.1E+05	8.9E+06	2.1E+06	2.1E+05	1.0E+07	2.4E+06
Dolomitic marl	1.1E+04	2.2E+06	3.8E+05	5.3E+05	2.7E+07	7.0E+06	1.1E+04	3.3E+06	5.1E+05
Impure dolostone	0.0E+00	1.6E+05	1.9E+04	0.0E+00	5.7E+06	1.3E+06	-	-	-
Magnesitic pelite	-	-	-	-	-	-	1.6E+05	5.7E+06	1.4E+06
Magnesitic marl	-	-	-	-	-	-	5.3E+04	4.8E+06	9.5E+05
Magnesite ore	-	-	-	8.5E+04	5.1E+06	1.1E+06	-	-	-
Central Nepal									
Dolomitic pelite	1.2E+05	2.1E+06	6.9E+05	1.2E+05	2.1E+06	6.9E+05	7.1E+05	6.4E+06	2.7E+06
Dolomitic marl	5.9E+04	2.1E+06	6.1E+05	3.0E+05	6.4E+06	2.2E+06	3.6E+04	2.1E+06	5.7E+05
Impure dolostone	0.0E+00	1.5E+05	3.1E+04	0.0E+00	1.4E+06	4.3E+05	-	-	-
Magnesitic pelite	-	-	-	-	-	-	5.3E+05	3.7E+06	1.6E+06
Magnesitic marl	-	-	-	-	-	-	1.8E+05	3.1E+06	1.1E+06
Magnesite ore	-	-	-	4.8E+04	1.2E+06	3.7E+05	-	-	-
Eastern Nepal									
Dolomitic pelite	5.7E+04	9.5E+05	3.1E+05	-	-	-	-	-	-
Dolomitic marl	2.8E+04	9.5E+05	2.8E+05	-	-	-	-	-	-
Impure dolostone	0.0E+00	6.8E+04	1.4E+04	-	-	-	-	-	-
Magnesitic pelite	-	-	-	-	-	-	-	-	-
Magnesitic marl	-	-	-	-	-	-	-	-	-
Magnesite ore	-	-	-	-	-	-	-	-	-

Summing up the contributions of the different CO_2–source lithologies, the following amounts (Mt) of CO_2 are obtained for each segment of the LHS thrust belt (Table 8.5b):

Table 8.5b - Weight (Mt) of CO_2 produced by each segment of the LHS thrust belt

	All Formations		
	min	max	average
Western Nepal	1.3E+06	7.5E+07	1.8E+07
Central Nepal	2.1E+06	3.1E+07	1.1E+07
Eastern Nepal	8.5E+04	2.0E+06	6.0E+05
Whole Nepal	3.5E+06	1.1E+08	2.9E+07

In order to constrain the **timing of CO_2 production**, geochronological data from the literature are used. Basing on the review of Kohn (2014), the Upper–LHS rocks now exposed at the surface experienced early prograde metamorphism at 17–13 Ma, whereas the late prograde evolution is dated at 10–13 Ma. These time constraints can be applied, to a first approximation, to the two main pulses of CO_2 production inferred for the studied lithologies, i.e. early prograde pulse occurred at 17–13 Ma, and peak pulse at 10–13 Ma. This applies to the Upper–LHS rocks now exposed to the surface.

However, the India–Asia collision is still active today; the intense background seismicity that characterizes the Himalayan orogen (Sapkota et al., 2013), with 4–5 events of local magnitude > 5 per year concentrated between 10 and 25 kilometres depth (Pandey et al., 1995; Adhikari et al. 2023), documents the still active underthrusting of the LHS beneath the front of the Himalayan orogen. At present, the LHS material now residing at 25–30 km depth beneath the major active thrust fault (Main Himalayan Thrust) is experiencing prograde metamorphism at P–T conditions comparable to those estimated from the

studied samples. This implies that decarbonation within the LHS is a long lasting process, started less than 20 Ma ago and still operating today.

8.1.2.2 Toward an estimate of past CO_2 fluxes from the LHS at the orogen–scale

Converting the estimated amounts of CO_2 (Mt of CO_2, Table 8.5b) into CO_2 fluxes (Mt/year of CO_2) is a complex task, which would require knowledge of the mechanisms which control the transport of CO_2 from the deep source to the surface. What we can do with the available data is to provide a minimum estimate of these fluxes in the (extremely unlikely) hypothesis that, once produced at depth, the CO_2 is passively transported to the surface due to the simple exhumation of its source–rocks. Assuming that the Upper–LHS rocks took 10 Ma to be exhumed, minimum CO_2 fluxes of 0.3–10.8 Mt/yr (average: 2.9 Mt/yr) are obtained for the whole Nepal Himalaya (Table 8.6), with **average fluxes decreasing eastward from 1.8–1.1 Mt/yr in western and central Nepal to 0.06 Mt/yr in eastern Nepal**.

Table 8.6 - Fluxes (Mt/yr) of CO_2 from each segment of the LHS thrust belt

	Interval 10 Ma		
	min	max	average
Western Nepal	0.13	7.47	1.77
Central Nepal	0.21	3.10	1.06
Eastern Nepal	0.01	0.20	0.06
Whole Nepal	0.3	10.8	2.9

Previous studies, however, demonstrated that the migration of fluids from the deep source to the surface might be a step–like process, characterized by the alternation of periods in which CO_2 accumulates within the pores and periods in which, once that fluid–overpressure is reached within the pores, the CO_2–rich fluids induce carbo–fracturing of the host rocks and migrate upward through a network of fractures and/or through faults (e.g. Irving & Barnes, 85; Chiodini et al., 2004, 2020; Girault et al., 2018; Groppo et al., 2021). In this framework, it is substantially impossible to realistically predict the timing of CO_2 ascent towards the surface; however, the CO_2 ascent through this process is certainly faster than the passive rise of CO_2 by simple exhumation.

8.2 Overview of current CO_2 emissions in the Nepal Himalaya

8.2.1 Total CO_2 emission per region and spatial organization

In Nepal Himalaya, a total of 40 sites (Girault et al., 2022) from Central, Western, and Mid–Western Nepal including 3 sites (our study) from eastern and Far Western Nepal have been studied for the gaseous emissions. Among them, 11 sites in Central and Western Nepal are characterized by strong degassing in the form of tectonic fumaroles and diffusive degassing structures. The CO_2 fluxes in the main studied sites in Central Nepal (Syabru–Bensi, Timure and Chilime) and Western Nepal (Bahundanda) range over more than five orders of

magnitude and show a bi–modal distribution: low flux values (≈20 g m^{-2} d^{-1}) vs. large flux values (≈1000 g m^{-2} d^{-1}). The mean surface CO_2 fluxes (*n*=3267) vary from 0.3 to 140,000 g m^{-2} d^{-1} when the entire data set is considered, with overall geometric and arithmetic averages of 2400±200 and 87.1±0.3 g m^{-2} d^{-1}, respectively (Girault et al., 2022). The CO_2 concentration of the gaseous emissions ranges from 2 to 98 % (*n*=105). The mean carbon isotopic compositions of CO_2 bubbles in water and gaseous CO_2 emissions range from –11.2 to –1.9 ‰ and from –11.7 to –0.4 ‰, respectively (*n*=128) (Girault et al., 2022).

In eastern Nepal, the CO_2 emission was not measured at Sekhathum due to inaccessibility but was measured at Nundhaki. Considering the whole data set from Nundhaki, with overall arithmetic and geometric averages of 29.2 ± 4.7 and 23.5 ± 1.2 g m^{-2} d^{-1} respectively, mean surface CO_2 fluxes (n=31) vary from 7.62 to 64.4 g m^{-2} d^{-1}. Similarly, in Far Western Nepal, the overall arithmetic and geometric averages are 27.3 ± 3.47 and 24.4 ± 1 g m^{-2} d^{-1} respectively. The value obtained from the recent data for Eastern and War Western Nepal is compatible with the background value.

According to the data collected from Girault et al. (2022) and our own data, the total amount of gaseous CO_2 released in Eastern, Central, Western, and Mid–Western Nepal are $(2.5\pm0.6)\times10^4$, $(3.3\pm0.5)\times10^8$, $(1.6\pm0.5)\times10^7$ and $(2.4\pm0.5)\times10^5$ mol yr^{-1}, respectively.

8.2.2 Estimation of the total present–day CO_2 emission at the scale of the Nepal Himalaya

After having quantified the amounts of gaseous CO_2 released in each specific site, extrapolation to the regional scale is tentatively proposed with the aim of constraining the current CO_2 emissions from the whole Himalaya. Both the gaseous CO_2 and the CO_2 from the hot spring (C_{DIC}) are considered. The Nepal Himalaya has been divided into 5 different segments (Fig. 8.3), and the emissions of CO_2 from each of them have been extrapolated using the available data from the hot springs in each segment.

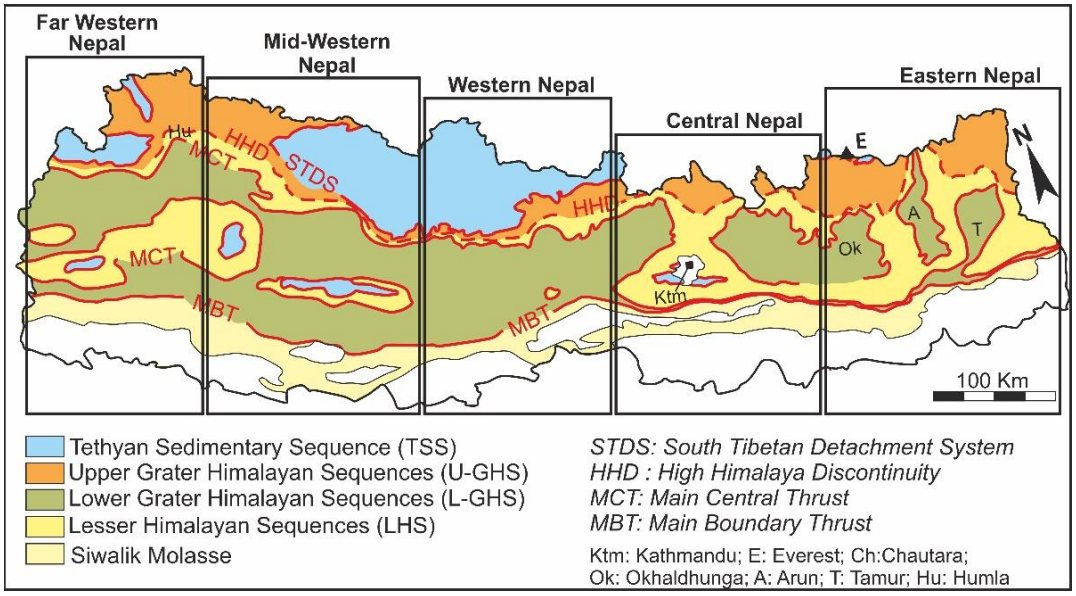

Fig. 8.3: Geological sketch map of Nepal, showing the 5 segments used for the extrapolation; Eastern Nepal, Central Nepal, Western Nepal, Mid–Western Nepal and Far Western Nepal, from right to left.

8.2.2.1 Extrapolation

The Nepal Himalaya has been divided into five segments: Eastern Nepal, Central Nepal, Western Nepal, Mid–Western Nepal and Far Western Nepal (Fig. 8.3). The area of each segment has been calculated from Google Earth™ using a polygon (Table 8.7), and the extrapolation factor for each segment has been calculated considering the following intermediate parameters: the area effectively investigated, the fraction of the area investigated with respect to the area of each segment, the total area occupied by the hot springs, the fraction of the area with hot springs over the investigated area, and the total area assumed to bear hot springs. The values of each parameter are reported in Table 8.7.

Table 8.7: Calculation for the extrapolation factor, of all five segments of Nepal.

Segments	Area of Each Segments (km^2)	Area effectively investigated (km^2)	Fraction of area investigated	Total area occupied by the Hot Springs(km^2)	Fraction of area with hot springs over the investigated area	Area supposed to bear hot springs (km^2)	Extrapolation factor
Far western Nepal	19500	255.7	0.0131	3.62	0.0142	276.0657	76.2612
Mid-Western Nepal	42400	456	0.0108	4.4	0.0096	409.1228	92.9825
Western Nepal	29400	719	0.0245	3	0.0042	122.6704	40.8901
Central Nepal	27400	745	0.0272	5.2	0.0070	191.2483	36.7785
Eastern Nepal	28500	261	0.0092	0.7	0.0027	76.4368	109.1954

Hot springs data and gaseous CO_2 flux measurements for Eastern and Far western segments are those collected in this study (Table 7.1 and 7.2), with the addition of data set from Girault et al., (2022) (Eastern Nepal: Arun valley; far–western Nepal: Mahakali valley and Chamliya valley). All the data for Central, Western and Mid–western segments are from Girault et al. (2022) (Dataset 10a and 10b). The gaseous CO_2 was calculated using kringing and interpolation procedures from the dataset of flux, while the CO_2 from the thermal spring was calculated in terms of Dissolved Inorganic Carbon (C_{DIC}). The CO_2 emissions from both gaseous discharges and waters (C_{DIC}) are calculated for the site and then extrapolated

to each segment. The total area occupied by each hot spring site is calculated and reported in dataset 10b.

Table 8.8. Calculation of the total CO_2 emission from the measured sites

Segments	Measured CO_2 emission (water) (mmol/s)	unc	Measured CO_2 emission (gas) (mmol/s)	unc	Total CO_2 emission (mmol/s)	unc
Far western Nepal	203.935	16.3148	100.4	50.1	304.335	66.415
Mid-Western Nepal	165.455	10.238	8	1.7	173.455	11.938
Western Nepal	1501.634258	72.9663	517.7	141.8	2019.33426	214.77
Central Nepal	1551.004153	57.042	10482.8	1695.7	12033.8042	1752.7
Eastern Nepal	74.337	5.95496	1.2	0.3	75.537	6.255

The total CO_2 emission from each site is calculated as the sum of the CO_2 emissions from water and gas (see Table 8.8) and then extrapolated over the whole segment by multiplying it for the extrapolation factor (Table 8.9). The obtained values of CO_2 expressed in $mmols^{-1}$ are then converted to mol y^{-1} for each segment. After the extrapolation over each segment in mol y^{-1}, the amount of CO_2 from each segment is added to obtain the total amount of CO_2 from the whole Nepal Himalaya (Table 8.9).

Table 8.9: Extrapolation of total CO_2 emission from the whole Nepal Himalaya

Segments	Total CO_2 emission from whole segment (mmol s^{-1})	unc	mol/year	unc	gCO_2/year	unc
Far western Nepa	2.32E+04	5.06E+03	7.32E+08	1.60E+08	3.22E+10	7.03E+09
Mid-Western Nep	1.61E+04	1.11E+03	5.09E+08	3.50E+07	2.24E+10	1.54E+09
Western Nepal	8.26E+04	8.78E+03	2.61E+09	2.77E+08	1.15E+11	1.22E+10
Central Nepal	4.43E+05	6.45E+04	1.40E+10	2.03E+09	6.15E+11	8.95E+10
Eastern Nepal	8.25E+03	6.83E+02	2.60E+08	2.16E+07	1.15E+10	9.49E+08
	Total for Nepal		**1.81E+10**	**2.53E+09**	**7.95E+11**	**1.11E+11**

8.3 Preliminary comparison between past and present–day CO_2 emissions in the Nepal Himalaya

Although the extrapolation of both the past and present–day total CO_2 emissions at the scale of the whole Nepal Himalayan must be considered as preliminary, a first order comparison between these results is tentatively proposed. Fig. 8.3 summarizes the extrapolated fluxes of CO_2 for the western, central and eastern segments of the Nepal Himalaya (i.e. for the present–day CO_2 emission the western segment is the sum of far–western, mid–western and western segments discussed in section 8.2). From the comparison it emerges that:

- The extrapolated present–day CO_2 fluxes are about one order of magnitude lower than the extrapolated past CO_2 fluxes
- The past CO_2 fluxes are affected by very large uncertainties, especially those estimated for the western segment of the belt. The major source of uncertainties

for the western segment is related to the estimate of the LHS shortening which is highly variable over the ca. 400 km length of the segment.

- Both the present–day and past CO_2 emissions are significantly lower in the eastern segment of the belt compared to the central and western segments.

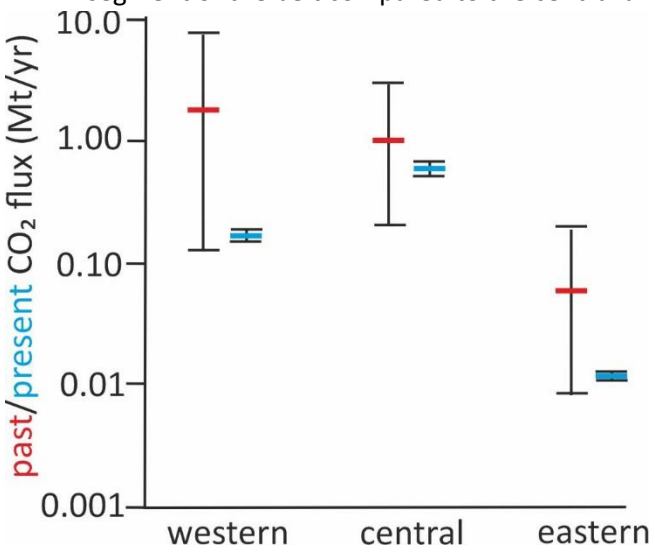

Fig. 8.3. Comparison between the past (in red) and present–day (in blue) CO_2 emissions extrapolated at the regional scale along the western, central and eastern segments of the Nepal Himalaya

These first estimates of past CO_2 production and current CO_2 emission from the Nepal Himalaya suggest that more work is needed to draw a more exhaustive overview of the current CO_2 emission and open numerous perspectives on the carbon sink/source duality of large orogens and on the global carbon cycle.

References

Ague, J. J. (2000). Release of CO_2 from carbonate rocks during regional metamorphism of lithologically heterogeneous crust. *Geology*, 28(12), 1123–1126.

Arita, K. (1983). Origin of the inverted metamorphism of the Lower Himalayas Central Nepal. *Tectonophysics*, 95, 43–60.

Auzanneau, E., Schmidt, M. W., Vielzeuf, D., & Connolly, J.A.D. (2010). Titanium in phengite: a geobarometer for high temperature eclogites. *Contributions to Mineralogy and Petrology*, *159*, 1–24.

Baker, J., Holland, T. J. B., & Powell, R. (1991). Isograds in internally buffered systems without solid solutions: principles and examples. *Contributions to Mineralogy and Petrology,* 106, 170–182.

Barnes, I., Evans, W. C., & White, L. D. (1988). The role of mantle CO_2 in volcanism. *Applied geochemistry*, 3(3), 281–285.

Bashyal, R. P. (1981). Geology of Dhangarhi–Dandeldhura road section and its regional significance. *Journal of Nepal Geological Society*, 1(1).

Becker, J.A. (2005). Quantification of Himalayan Metamorphic CO_2 Fluxes: Impact on Global Carbon Budgets. Unpublished Ph.D. thesis, *University of Cambridge*, Cambridge.

Becker, J.A., Bickle, M.J. Galy, A., & Holland, T.J.B. (2008). Himalayan metamorphic CO_2 fluxes: Quantitative constraints from hydrothermal springs. *Earth and Planetary Science Letters*, 265, 616–629.

Berner, R.A. (1999). A new look at the long–term carbon cycle. *GSA Today*, 9, 1–6.

Besse, J., Courtillot, V., Pozzi, J., Westphal, M., & Zhou, Y. X. (1984). Palaeomagnetic estimates of crustal shortening in the Himalayan thrusts and Zangbo suture. *Nature,* 311, 621–626.

Beyssac, O., Bollinger, L., Avouac, –P. J., & Groffé, B. (2004). Thermal metamorphism in the Lesser Himalaya of Nepal determined from Raman spectroscopy of carbonaceous material. *Earth and Planetary Science Letters*, 225, 233–241.

Bhattarai, D.R. (1980). Some geothermal springs of Nepal. *Tectonophysics*, 62, 7–11.

Bhattarai, D. R. (1986). Geothermal manifestations in Nepal. *Geothermics*, 15(5–6), 715–717.

Bhowmik, S., & Ao, A. (2016). Subduction initiation in the Neo–Tethys: constraints from counterclockwise P–T paths in amphibolite rocks of the Nagaland Ophiolite Complex, India. *Journal of Metamorphic Geology*, 34, 17 – 44.

Bickle, M.J. (1996). Metamorphic decarbonation, silicate weathering and the long–term carbon cycle. *Terra Nova*, 8, 270–276.

Bilham, R., Larson, K., & Freymuller, J., (1997). Indo–Asian convergence rates in the Nepal Himalaya. *Nature*, 386, 61 – 64.

Bollinger, L., Avouac, –P. J., Beyssac, O., Catlos, E. J., Harrison, T. M., Grove, M., Groffé, B., & Sapkota, S. (2004). Themal structure and exhumation history of the Lesser Himalaya in central Nepal. *Tectonics*, 23, 1–19.

Burchfield, B. C., Chen, Z., Hodges, K. V., Liu, Y., Royden, L. H., Deng, C., & Xu, J. (1992). The South Tibetan Detachment System, Himalayan orogen: extension contemporaneous with and parallel to shortening in a collisional mountain belt. *Geological Society of America Special Paper*, 269, 41.

Burg, J.P., & Chen, G.M. (1984). Tectonics and structural zonation of southern Tibet, China. *Nature*, 311, 219–223.

Burton, M.R., Sawyer, G.M., & Granieri, D. (2013). Deep Carbon Emissions from Volcanoes. *Reviews in Mineralogy & Geochemistry*, 75, 323–354.

Carlson, W. D. (1989). The significance of intergranular diffusion to the mechanisms and kinetics of porphyroblast crystallization. *Contributions to Mineralogy and Petrology*, *103*, 1–24.

Carlson, W. D., Pattison, D. R. M., & Caddick, M. J. (2015). Beyond the equilibrium paradigm: How consideration of kinetics enhances metamorphic interpretation. *American Mineralogist, 100*, 1659–1667.

Carosi, R., Lombardo, B., Molli, G., Musumeci, G., & Pertusati, P.C. (1998). The South Tibetan Detachment System in the Rongbuk valley, Everest region. Deformation features and geological implications. *Journal of Asian Earth Sciences,* 16**,** 299–311.

Castro, A. E., & Spear, F. S. (2016). Reaction overstepping and re–evaluation of peak P–T conditions of the blueschist unit Sifnos, Greece: implications for the Cyclades subduction zone. *International Geology Review, 59*, 548–562.

Catlos E. J., Lovera, O. M., Kelly, E. D., Ashley, K. T., Harrison, T. M., & Etzel, T. (2018). Modeling High–Resolution Pressure–Temperature Paths Across the Himalayan Main Central Thrust (Central Nepal): Implications for the Dynamics of Collision. *Tectonics, 37*, 2363–2388.

Catlos, E. J., Harrison, T. M., Grove, M., Ryerson, F. J., Manning, C. E., & Upreti, B. N. (2001). Geochronologic and thermobarometric constrains on the evolution of the Main Central Thrust, central Nepal Himalya. *Journal of Geophysical Research, Solid Earth, 106*, 16177–16204.

Catlos, E. J., Perez, T. J., Lovera, O. M., Dubey, C. S., Schmitt, A. K., & Etzel, T. M. (2020). High–resolution P–T–Time paths across himalayan faults exposed along the bhagirathi transect NW India: Implications for the construction of the Himalayan orogen and ongoing deformation. *Geochemistry, Geophysics, Geosystems, 21*, e2020GC009353.

Chamberlain, C.P., Koons, P.O., Meltzer, A.S., Park, S.K., Craw, D., Zeitler, P., & Poage, M.A. (2002). Overview of hydrothermal activity associated with active orogenesis and metamorphism: Nanga Parbat, Pakistan Himalaya. *American Journal of Science*, 302, 726–748.

Chiodini, G., Cardellini, C., Amato, A., Boschi, E., Caliro, S., Frondini, F., & Ventura, G. (2004). Carbon dioxide Earth degassing and seismogenesis in central and southern Italy. *Geophysical Research Letters*, 31(7).

Chiodini, G., Cardellini, C., Di Luccio, F., Selva, J., Frondini, F., Caliro, S., Rosiello, A., & Ventura, G. (2020). Correlation between tectonic CO2 Earth degassing and seismicity is revealed by a 10–year record in the Apennines, Italy. *Science advances*, 6(35), eabc2938.

Chatterjee, N., & Ghose, N.C. (2010). Metamorphic evolution of the Naga Hills eclogite and blueschist, Northeast India: implications for early subduction of the Indian plate under the Burma microplate. *Journal of Metamorphic Geology*, 28, 209–225.

Coggon, R., & Holland, T. J. B. (2002). Mixing properties of phengitic micas and revised garnet–phengite thermobarometers. *Journal of Metamorphic Geology*, *20*, 683–698.

Colchen, M., Le Fort, P., & Pêcher, A. (1980). Notice explicative de la carte géologique Annapurna–Manaslu–Ganesh (Himalaya du Népal) au 1:200 000e (bilingual: French–English), CNRS, Paris, 1986.

Colchen, M., LeFort, P., & Pecher, A. (1986). Notice explicative de la carte geologique Annapurna–Manaslu–Ganesh (Himalaya du Nepal) au 1:200.000e. *Cent. National de la Recherche Scientifique,* Paris, 137.

Connolly, J. A. D. (2009). The geodynamic equation of state: what and how. *Geochemistry, Geophysics, Geosystems, 10*, Q10014.

Connolly, J. A. D., & Cesare B. (1993). C–O–H–S fluid compositions and oxygen fugacity in graphitic metapelites. *Journal of Metamorphic Geology, 11*, 379–388

Connolly, J. A. D., & Trommsdorff, V. (1991). Petrogenetic grids for metacarbonate rocks: pressure–temperature phase diagrams for mixed–volatile systems. *Contributions to Mineralogy and Petrology*, 108, 93–105.

Connolly, J. A. D. (1990). Multivariable phase diagrams: an algorithm based on generalize thermodynamics. *American Journal of Science, 290*, 666–718.

Copley, A., Avouac, J. –P., & Royer, J. –Y. (2010). India–Asia and Cenozoic slowdown of the Indian plate: Imolications for the forces driving plate motions, *Journal of Geophysical Research*, 115, B03410.

Corfield, R.I., Searle, M. P., & Green, O.R. (1999). Photang thrust sheet: an accretionary complex structurally below the Spontang ophiolite constraining timing and tectonic environment of ophiolite obduction, Ladakh Himalaya, NW India. *Journal of the Geological Society*, 156, 1031–1044.

Corrie, S. L., & Kohn, M. J. (2011). Metamorphic history of the central Himalaya, Annapurna region, Nepal, and implications for tectonic models. *Geological Society of America Bulletin, 123*, 1863–1879.

Corvinus G. (1988). The Mio–Plio–Pleistocene litho– and biostratigraphy of the Surai Khola Siwaliks in West–Nepal: first results, *Comptes Rendus de l'Académie des Sciences, Paris*, 306/II, 1471–1477.

DeCelles P. G., Gehrels G. E., Quade J., & Ojha T.P. (2000). Eocene–early Miocene foreland basin development and the history of Himalayan thrusting, western and central Nepal. *Tectonics, 17*, 741–765.

DeCelles, P.G., Gehrels, G.E., Quade, J., & Ojha, T.P. (1998b). Eocene–early Miocene foreland basin development and the history of Himalayan thrusting, western and central Nepal. *Tectonics,* 17, 741 – 765.

DeCelles, P.G., Gehrels, G.E., Quade, J., Ojha, T.P., Kapp, P.A., & Upreti, B.N. (1998a). Neogene foreland basin deposits erosional unroofing and the kinematic history of the Himalayan fold–thrust belt, western Nepal. *Geological Society of America Bulletin*, 110, 2–21.

DeCelles, P.G., Robinson, D.M., Quade, J., Ojha, T.P., Garzione, C.N., Copeland, P., & Upreti, B.N. (2001). Stratigraphy, structure and tectonic evolution of the Himalayan fold–thrust belt in western Nepal. *Tectonics*, 20, 487–509.

Dewey, J.F., Cande, S., & Pitman III, W.C. (1989). Tectonic evolution of the India/ Eurasia collision zone. *Eclogae Geologicae Helvetiae*, 82, 717–734.

Dhital, M. R. (2015). Geology of Nepal Himalaya. Regional perspective of the classic collided orogen. *Regional Geology Review*. Springer International Publishing Switzerland, 498 pp.

Dhital, M. R., & Kizaki, K. (1987b). Lithology and Stratigraphy of the northern Dang, Lesser Himalaya. *Bulletin of the College of Science, University of the Ryukyus*, 45, 183–244.

Diener, C. (1895) Ergebnisse einer geologischen expedition in den Central–Himalaya von Johar, Hundes, und Painkhanda. *Denkschriften der Kaiserlichen Akademie der Wissenschaften, Wien*, 62:533–608.

Diener, C. (1898) Notes on the geological structure of the Chitichun region. *Memoirs of the Geological Survey of India.* XXVIII (Part 1):1–27

Diener, J.F.A., & Powell, R. (2012). Revised activity–composition models for clinopyroxene and amphibole. *Journal of Metamorphic Geology*, 30, 131–142.

Diener, J.F.A., Powell, R., White, R.W., & Holland, T.J.B. (2007). A new thermodynamic model for clino– and orthoamphiboles in the system Na2O–CaO–FeO–MgO–Al2O3–SiO2–H2O–O. *Journal of Metamorphic Geology*, 25, 631–656.

Ding, L., Kapp, P., Wan XQ. (2005) Paleocene–Eocene record of ophiolite obduction and initial India–Asia collision, south central Tibet. *Tectonics*, 24, TC3001

Eberhard, L., & Pettke, T. (2021). Antigorite dehydration fluids boots carbonate mobilisation and crustal CO_2 outgassing in collisional orogens. *Geochimica et Cosmochimica Acta*, 300, 192–214.

Evans, K.A. (2011). Metamorphic carbon fluxes: how much and how fast? *Geology*, 39, 95–96.

Evans, M.J., Derry, L.A., & France–Lanord, C. (2004). Geothermal fluxes of alkalinity in the Narayani river system of central Nepal, *Geochemistry Geophysics Geosystems*, 5, Q08011.

Evans, M.J., Derry, L.A., & France–Lanord, C. (2008). Degassing of metamorphic carbon dioxide from the Nepal Himalaya. *Geochemistry, Geophysics, Geosystems,* 9, Q04021.

Frank, W., & Fuchs, G.R. (1970). Geological investigations in West Nepal and their significance for the geology of the Himalayas. *Geologische Rundsch*au, 59, 552–580.

Frank, W., Gansser, A., & Trommsdorff, V. (1977). Geological observations in the Ladakh area (Himalayas) – A preliminary report. *Schweizerische Mineralogische und Petrographische Mitteilungen*, 57, 89–133.

Frank, W., Miller, C., & Grasemann, B. (1995). Ar/Ar ages of detrital micas and paleogeographic provenance of Proterozoic clastic sediments in the Himalayas. In: Spencer, D. A., Burg, J.–P. & Spencer–Cervato, C. (eds.), 10th Himalaya–Karakoram–Tibet Workshop Abstract Volume, Zürich, Mitteilungen aus dem Geologischen Institut der ETH und der Universität Zürich, 298.

Fuhrman, M. L., & Lindsley, D. H. (1988). Ternary–feldspar modeling and thermometry. *American Mineralogist, 73*, 201–215.

Gaetani, M., & Garzanti, E. (1991). Multicyclic history of the northern India continental margin (north– western Himalaya). *AAPG Bulletin*, 75, 1427–1446.

Gaidies, F., & George, F. R. (2021). The interfacial energy penalty to crystal growth close to equilibrium. *Geology, 49*, 988–992.

Gaidies, F., Krenn, E., De Capitani, C., & Abart, R. (2008). Coupling forward modelling of garnet growth with monazite geochronology: An application to the Rappold Complex (Austroalpine crystalline basement). *Journal of Metamorphic Geology, 26*, 775–793.

Gaidies, F., Petley–Ragan, A., Chakraborty, S., Dasgupta, S., & Jones, P. (2015). Constraining the conditions of Barrovian metamorphism in Sikkim, India: P–T–t paths of garnet crystallization in the Lesser Himalayan Belt. *Journal of Metamorphic Geology, 33*, 23–44.

Gaillardet, J., & Galy, A. (2008). Himalaya–carbon sink or source? *Science,* 320, 1727–1728.

Galy, A., & France–Lanord, C. (1999)**.** Weathering processes in the Ganges–Brahmaputra basin and the riverine alkalinity budget. *Chemical Geology,* 159, 31–60.

Gansser, A. (1964). Geology of the Himalayas. Interscience, John Wiley and Sons, London, 289 pp.

Gansser, A. (1977). The great suture zone between Himalaya and Tibet: A preliminary account.

Garzanti, E. (1999). Stratigraphy and sedimentary history of the Nepal Tethys Himalaya passive margin. *Journal of Asian Earth Sciences*, 17, 805–827.

Gehrels, G., Kapp, P., DeCelles, P., Pullen, A., Blakey, R., Weislogel, A., Ding, L., Martin, A., McQuarrie, N., & Yin, A. (2011). Detrital zircon geochronology of pre-Tertiary strata in the Tibetan-Himalayan orogen. *Tectonics*, 30, TC5016.

George, F. R., & Gaidies, F. (2017). Characterisation of a garnet population from the Sikkim Himalaya: Insights into the rates and mechanisms of porphyroblast crystallisation. *Contributions to Mineralogy and Petrology, 172*, 1–22.

Ghezzi, L., Petrini, R., Montomoli, C., Carosi, R., Paudyal, K., & Cidu, R. (2017). Findings on water quality in Upper Mustang (Nepal) from a preliminary geochemical and geological survey. *Environmental Earth Sciences*, 76(19), 1–13.

Ghezzi, L., Iaccarino, S., Carosi, R., Montomoli, C., Simonetti, M., Paudyal, K. R., ... & Petrini, R. (2019). Water quality and solute sources in the Marsyangdi River system of Higher Himalayan range (West–Central Nepal). *Science of The Total Environment*, 677, 580–589.

Ghose, N.C., & Singh, R.N. (1980). Occurrence of blueschist facies in the ophiolite belt of Naga Hills, east of Kiphire, N.E., India. *Geologische Rundschau*, 69, 41–43.

Giggenbach, W.F., Gonfiantini, R., Jangi, B.L., & Truesdell, A.H. (1983). Isotopic and chemical composition of Parbati valley geothermal discharges, north–west Himalaya, India. *Geothermics* 12, 199–222.

Girault, F., Adhikari, L. B., France–Lanord, C., Agrinier, P., Koirala, B.P., Bhattarai, M., Mahat, S., Groppo, C., Rolfo, F., Bollinger, L., & Perrier, F. (2018). Persistent CO_2 emissions and

hydrothermal unrest following the 2015 earthquake in Nepal. *Nature Communications*, 9, 1–10.

Girault, F., Bollinger, L., Bhattarai, M., Koirala, B.P., France–Lanord, C., Rajaure, S., Gaillardet, J., Fort, M., Sapkota, S.N., & Perrier, F. (2014). Large–scale organization of carbon dioxide discharge in the Nepal Himalayas. *Geophysical Research Letters,* 41, 6358–6366.

Girault, F., Perrier, F., Crockett, R., Bhattarai, M., Koirala, B.P., France–Lanord, C., Agrinier, P., Ader, M., Fluteau, F., Gréau, C., & Moreira, M. (2014b). The Syabru–Bensi hydrothermal system in central Nepal: 1. Characterization of carbon dioxide and radon fluxes. *Journal of Geophysical Research: Solid Earth,* 119, doi:10.1002/2013JB010301.

Girault, F., Koirala, B.P., Bhattarai, M., & Perrier, F. (2016). Radon and carbondioxide around remote Himalayan thermal springs. G*eological Society, London, Special Publications*, 451.

Girault, F., Lanord, C. –F., Adhikari, L. B., Upreti, B. N., Paudyal, K. R., Gajurel, A., Agrinier, P., Losno, R., Groppo, C., Rolfo, F., Thapa, S., Tamang, S..... & Perrier, F. (2022). Overview of Hydrothermal System in the Nepal Himalaya. (Submitted to) Himalaya, Dynamics of a Giant 3

Godard, G. (2009). Two orogenic cycles in eclogite–facies gneisses of the Southern Armorican Massif (France). *European Journal Mineralogy*, 21, 1173–1190.

Goscombe, B., Gray, D., & Foster, D. A. (2018). Metamorphic response to collision in the Central Himalayan Orogen. *Gondwana Research, 57*, 191–265.

Goscombe, B., Gray, D., & Hand, M. (2006). Crustal architecture of the Himalayan metamorphic front in eastern Nepal. *Gondwana Research, 10*, 232–255.

Grabczak, J., & Kotarba, M. (1985). Isotopic composition of the thermal waters in the central part of the Nepal Himalayas. *Geothermics*, 14(4), 567–575

Greenwood, H.J. (1975). Buffering of pore fluids by metamorphic reactions. *American Journal of Science***,** 275, 573–593.

Groppo, C., Rapa, G., Frezzotti, M. L., & Rolfo, F. (2021). The fate of calcareous pelites in collisional orogens. *Journal of Metamorphic Geology,* 39, 181‐207.

Groppo, C., Rapa, G., Rolfo, F., & Frezzotti, M. L. (2022). CO_2 outgassing during collisional orogeny is facilitated by the generation of immiscible fluids. *Communications Earth & environment,* 3.1, 1–11.

Groppo, C., Rolfo, F., & Mosca, P. (2013). The cordierite–bearing anatectic rocks of the Higher Himalayan Crystallines (eastern Nepal): low–pressure anatexis, melt–productivity, melt loss and the preservation of cordierite. *Journal of Metamorphic Geology, 31*, 187–204.

Groppo, C., Rolfo, F., & Indares, A. (2012). Partial melting in the Higher Himalayan Crystallines of Eastern Nepal: the effect of decompression and implications for the "channel flow" model. *Journal of Petrology, 53*, 1057–1088.

Groppo, C., Rolfo, F., & Lombardo, B. (2009). P–T evolution across the Main Central Thrust Zone (Eastern Nepal): hidden discontinuities revealed by petrology. *Journal of Petrology, 50*, 1149–1180.

Groppo, C., Rolfo, F., Castelli, D., & Mosca, P. (2017). Metamorphic CO_2 production in collisional orogens: petrologic constraints from phase diagram modeling of Himalayan, scapolite–bearing, calc–silicate rocks in the NKC(F)MAS(T)–HC system. *Journal of Petrology,* 58, 53–83.

Groppo, C., Rubatto, D., Rolfo, F., & Lombardo, B. (2010). Early Oligocene partial melting in the Main Central Thrust Zone (Arun Valley, eastern Nepal Himalaya). *Lithos, 118*, 287–301.

Guillot, S., Mahéo, G., de Sigoyer, J., Hattori, K.H., & Pecher, A. (2008). Tethyan and Indian subduction viewed from the Himalayan high– to ultrahigh–pressure metamorphic rocks. *Tectonophysics*, 451, 225–241.

Guiraud, M., Powell, R., & Rebay, G. (2001). H_2O in metamorphism and the preservation of metamorphic mineral assemblages. *Journal of Metamorphic Geology, 19*, 445–454

He, D., Webb, A. A. G., Larson, K. P., Martin, A. J., & Schmitt, A.K. (2015). Extrusion cs. Duplexing models of Himalayan Mountain building. 3: duplexing dominants from the Oligocene to Present. *International Geology Review, 57*, 1–27.

Heim, A., & Gansser, A. (1939). Central Himalaya: geological observations of the Swiss expedition 1936. *Denkschriften der Schweizerischen Naturforschenden Gesellschaft, Band LXXIII*, 1, 245.

Hodges, K. (2000). Tectonics of Himalaya and southern Tibet from two perspectives. *Geological Society of American Bullettin*, 112, 324–350.

Hofer, G., Wagreich, M., & Neuhuber, S. (2013). Geochemistry of fine grained sediments of the upper Cretaceous to Paleogene Gosau Group (Austria, Slovakia): Implications for paleoenvironmental and provenance studies. *Geosciences Frontiers*, 4, 449–468.

Holland, T. J. B., & Powell, R. (1998). An internally consistent thermodynamic data set for phases of petrologic interest. *Journal of Metamorphic Geology, 16*, 309–343.

Holland, T., Baker, J., & Powell, R. (1998). Mixing properties and activity-composition relationships of chlorites in the system $MgO\text{-}FeO\text{-}Al_2O_3\text{-}SiO_2\text{-}H_2O$. *European Journal of Mineralogy, 10*, 395–406

Hollister, L. S. (1969). Metastable paragenetic sequence of andalusite, kyanite, and sillimanite, Kwoiek Area, B.C. *American Journal of Science, 267*, 352–370.

Honegger, K., Le Fort, P., Mascle, G., & Zimmerman, J.L. (1989). The blueschists along the Indus Suture zone in Ladakh, NWHimalaya. *Journal of Metamorphic Geology*, 7, 57–72.

Hu, X., Garzanti, E., Wang, J., Huang, W., An, W., & Webb, A. (2016). The timing of India–Asia collision onset – Facts, theories, controversies. *Earth–Science Reviews*, 160, 264–299.

Imayama, T., Takeshita, T., & Arita, K. (2010). Metamorphic P–T profile and P–T path discontinuity across the far–eastern Nepal Himalaya: investigation of channel flow models. *Journal of Metamorphic Geology*, *28*, 527–549.

Irwin, W. P., & Barnes, I. (1980). Tectonic relations of carbon dioxide discharges and earthquakes. *Journal of Geophysical Research: Solid Earth*, *85*(B6), 3115–3121.

Jaeger, J. –J., Courtillot, V., & Tapponnier, P. (1989). Paleontological view of the ages of the Devvan Traps, the Cretaceous/Tertiary boundary, and the India–Asia collision. *Geology*, 17(4), 316–319.

Joshi, P.R., Khan, H.R., Singh, S., Khadka, D.R., & Napt, D.K. (2003). Map N° E–2. Geothermal hot springs resources in Nepal. *DMG Mineral Resources Division*.

Kellett, D.A., Grujic, D., Warren, C., Cottle, J., Jamieson, R., & Tenzin, T. (2010). Metamorphic history of a syn–convergent orogen–parallel detachment: the south Tibetan detachment system, eastern Himalaya. *Journal of Metamorphic Geology*, 28, 785–808.

Kerrick, D.M., & Caldeira, K. (1998). Metamorphic CO_2 degassing from orogenic belts. *Chemical Geology*, 145, 213–232.

Ketcham, R. A., & Carlson, W. D. (2012). Numerical simulation of diffusion–controlled nucleation and growth of porphyroblasts. *Journal of Metamorphic Geology*, *30*, 489–512.

Khanal, G. P., Wang J. M., Wu F. Y., Wang J. G., & Yang L. (2020). In–sequence buoyancy extrusion of the Himalayan Metamorphic Core, central Nepal: Constraints from monazite petrochronology and thermobarometry. *Journal of Asian Earth Sciences, 199*, 104406.

Klootwijk, C., Sharma, M.L., Gergan, J., Shah, S.K. & Tirkey, B. (1984). The Indus–Tsangpo suture zone in Ladakh, Northwest Himalaya: Further palaeomagnetic data and implications. *Tectonophysics*, 106(3–4), 215–238.

Kohn, M. J. (2008). PTt data from central Nepal support critical taper and repudiate large–scale channel flow of the Grater Himalayan Sequence. *Geological Society of America Bulletin, 120*, 259–273.

Kohn, M. J., Catlos, E. J., Ryerson, F. J., & Harrison, T. M. (2001). Pressure–temperature–time path discontinuity in the Main Central thrust zone, central Nepal. *Geology, 29*, 571–574.

Kohn, M. J., Paul, S. K., & Corrie, S. L. (2010). The lower Lesser Himalayan sequence: a Paleoproterozoic arc on the northern margin of the Indian plate. *Geological Society of America Bulletin, 122*, 323–335.

Kohn, M. J., Wieland, M. S., Parkinson, C. D., & Upreti, B. N. (2004). Miocene faulting at plate tectonic velocity in the Himalaya of central Nepal. *Earth and Planetary Science Letters, 228*, 299– 310.

Kohn, M.J. (2014). Himalayan metamorphism and its tectonic implications. *Annual Review of Earth and Planetary Sciences, 42*, 381–419.

Kotarba, M. (1986). Hydrogeological investigations in Seti Khola and Trisuli thermal springs area (Nepal Himalayas). 37–51.

Kuhn, B.K., Reusser, E., & Powell, R. (2005). Metamorphic evolution of calc–schists in the Central Alps, Switzerland. *Schweizerische Mineralogische und Petrographische Mitteilungen*, 85, 175–190.

Lanari, P., & Duesterhoeft, E. (2019). Modeling metamorphic rocks using equilibrium thermodynamics and internally consistent databases: Past achievements, problems and perspectives. *Journal of Petrology, 60,* 19–56.

Lanord, C. F., Evans, M., Hurtrez, J. –E., & Riotte, J. (2003). Annual dissolved fluxes from Central Nepal rivers: budget of chemical erosion in the Himalayas. *C. R Geosciences*, 335, 1131–1140.

Larson, K. M., Burgmann, R., Bilham, R., & Freymueller, J.T. (1999). Kinematics of the India–Eurasia collision zone from GPS measurements, *Journal of Geophysical Research*, 104, 1077 – 1093.

Larson, K. P., Cottle, J. M., Lederer, G., & Rai, S. M. (2017). Defining shear zone boundaries using fabric intensity gradients: an example from the East–Central Nepal Himalaya. *Geosphere, 13,* 771–781

Larson, K. P., Piercey, S., & Cottle, J. (2019). Preservation of a Paleoproterozoic rifted margin in the Himalaya: insight from the Ulleri–Phaplu–Melung orthogneiss. *Geoscience Frontiers, 10*, 873–883.

Larson, K.P., Gervais, F., & Kellett, D.A. (2013). A P–T–t–D discontinuity in east–central Nepal: Implications for the evolution of the Himalayan mid–crust. *Lithos*, 179, 275–292.

Lavé, J., & Avouac, J. P. (2000). Active folding of fluvial terraces across the Siwaliks Hills, Himalayas of central Nepal. *Journal of Geophysical Research*, 105, 5735–5770.

Le Fort, P., & Rai, S.M. (1999). Pre–Tertiary felsic magmatism of the Nepal Himalaya. Recycling of continental crust. *Journal of Asian Earth Sciences,* 17, 607 628.

Le Fort, P. (1975), Himalayas: The collided range: Present knowledge of the continental arc. *American Journal of Science*, 275–A, 1–44.

Leech, M.L., Singh, S., Jain, A.K., Klemperer, S.L., & Manickavasagam, R.M. (2005). The onset of India–Asia continental collision: early, steep subduction required by the timing of UHP metamorphism in the western Himalaya. *Earth and Planetary Science Letters*, 234, 83–97.

LePichon, X., Fournier, M., & Jolivet, L. (1992). Kinematics, topography, shortening, and extrusion in the India–Eurasia collision. *Tectonics*, 11, 1085–1098.

Lombardo, B., Pertusati, P., & Borghi, A. (1993). Geology and tectono–magmatic evolution of the eastern Himalaya along the Chomolungma–Makalu transect. In: Treloar, P. J. & Searle, M. P. (eds.), Himalayan Tectonics. *Geological Society of London, Special Publication,* 74, 341–355.

Long, S. P., & Robinson, D. M. (2021). Construction of the Lesser Himalayan–Subhimalayan thrust belt: The primary driver of thickening, exhumation, and high elevations in the Himalayan orogen since the middle Miocene. *Geology*, 49(11), 1283–1288.

Macfarlane, A. M. (1995). An evaluation of the inverted metamorphic gradient at Langtang National Park, central Nepal Himalaya. *Journal of Metamorphic Geology, 13*, 595–612.

Märki, L., Lupker, M., France–Lanord, C., Lavé, J., Gallen, S., Gajurel, A. P., Haghipour, N., West, F. L., & Eglinton, T. (2021). An unshakable carbon budget for the Himalaya. *Nature Geoscience*, 14(10), 745–750.

Martin, A. J., Burgya, K. D., Kaufmanb, A. J., & Gehrels, G. E. (2011). Stratigraphic and tectonic implications of field and isotopic constraints on depositional ages of Proterozoic Lesser Himalayan rocks in central Nepal. *Precambrian Research, 185*, 1–17.

Martin, A. J., DeCelles, P. G., Gehrels, G. H., Patchett, P. J., & Isachsen, C. (2005). Isotopic and structural constraints on the location of the Main Central Thrust in the Annapurna Range, central Nepal Himalaya. *Geological Society of America Bulletin, 117*, 926–944.

Martin, A. J., Ganguly, J., & DeCelles, P. G. (2010). Metamorphism of Greater and Lesser Himalayan rocks exposed in the Modi Khola valley, central Nepal. *Contribution to Mineralogy and Petrology, 159*, 203–223.

Marty, B., & Tolstikhin, I.N. (1998). CO_2 fluxes from mid–ocean ridges, arcs and plumes. *Chemical Geology*, 145, 233–248.

Massonne, H. J. (2010). Phase relations and dehydration behaviour of calcareous sediments at very–low to low grade metamorphic conditions. *Periodico di Mineralogia*, *79*(2), 21–43.

McLennan, S.M., Hemming, S., McDaniel, D.K., & Hanson, G.N. (1993). Geochemical approaches to sedimentation, provenance, and tectonics. In: Johnsson, M. J. & Basu, A.,

(eds.), Processes Controlling the Composition of Clastic Sediments: Boulder, Colorado. *Geological Society of America Special Paper,* 284, 21–40.

Montomoli, C., Iaccarino, S., Carosi, R., Langone, A., & Visonà, D. (2013). Tectonometamorphic discontinuities within the Greater Himalayan Sequence in Western Nepal (Central Himalaya): Insights on the exhumation of crystalline rocks. *Tectonophysics, 608*, 1349–1370.

Mosca, P., Groppo, C., & Rolfo, F. (2012). Structural and metamorphic features of the Main Central Thrust Zone and its contiguous domains in the eastern Nepalese Himalaya. *Journal of Virtual Explorer, Electronic Edition, 41*, paper 2.

Moynihan, D. P., & Pattison, D. R. M. (2013). An automated method for the calculation of P–T paths from garnet zoning, with application to metapelitic schist from the Kootenay Arc, British Columbia, Canada. *Journal of Metamorphic Geology, 31*, 525–548.

Munthe, J., Dongol, B., Hutchison, J. H., Kean, W. F., Munthe, K., & West, R. M. (1983). New fossil discoveries from the Miocene of Nepal include a hominoid. *Nature*, 303(5915), 331–333.

Murphy, M. A., & Copeland, P. (2005). Transtensional deformation in the central Himalaya and its role in accommodating growth of the Himalayan orogen. *Tectonics*, 24(4).

Nagurney, A. B., Caddick, M. J., Dragovic, B., & Busse, K. (2021). The (chemical) potential for understanding overstepped garnet nucleation and growth. *American Mineralogist, 106*, 812–829.

Najman, Y., Appel, E., Boudagher-Fadel, M., Bown, P., Carter, A., Garzanti, E., ... & Vezzoli, G. (2010). Timing of India-Asia collision: Geological, biostratigraphic, and palaeomagnetic constraints. *Journal of Geophysical Research: Solid Earth*, 115(B12).

Parrish, R. R., & Hodges, K. V. (1996). Isotopic constraints on the age and provenance of the Lesser Himalaya. *Geological Society of America Bulletin, 108*, 904–911.

Patriat, P., & Achache, J. (1984). The chronology of the India–Eurasia collision. Implications for crustal shortening and the driving mechanism of plates. *Nature*, 311, 615–621.

Pattison, D. R. M., & Tinkham, D. K. (2009). Interplay between equilibrium and kinetics in prograde metamorphism of pelites: an example from the Nelson aureole, British Columbia. *Journal of Metamorphic Geology, 27*, 249–279.

Pattison, D. R. M., de Capitani, C., & Gaidies, F. (2011). Petrological consequences of variations in metamorphic reaction affinity. *Journal of Metamorphic Geology, 29*, 953–977.

Pandey, M. R., Tandukar, R. P., Avouac, J. P., Lave, J., & Massot, J. P. (1995). Interseismic strain accumulation on the Himalayan crustal ramp (Nepal). *Geophysical Research Letters*, 22(7), 751–754

Paudel, L. P., & Arita, K. (2000). Tectonic and polymetamorphic history of the Lesser Himalaya in central Nepal. *Journal of Asian Earth Sciences*, 18, 561–584.

Paudel, L. P., & Arita, K. (2006a). Thermal evolution of the Lesser Himalaya, central Nepal: Insights from K–white micas compositional variation. *Gondwana Research*, 9, 409–425.

Paudel, L. P., & Arita, K. (2006b). The b–spacing values of white micas and their metamorphic implications in the Lesser Himalaya of central Nepal. *Journal of Asian Earth Science*, 27, 10–24.

Pearson, O. N., & DeCelles, P. G. (2005). Structural geology and regional tectonic significance of the Ramgarh thrust, Himalayan fold–thrust belt of Nepal. *Tectonics, 24*, TC4008.

Pêcher, A. (1989). The metamorphism in Central Himalaya. *Journal of Metamorphic Geology, 7*, 31–41.

Pécher, A. (1975). The Main Central Thrust of the Nepal Himalaya and the related metamorphism in the Modi–Khola cross–section (Annapurna Range). *Himalayan Geology*, 5, 115–132.

Pécher, A. (1977). Geology of the Nepal Himalaya: deformation and petrography in the Main Central Thrust zone, vol. 268. Ecologie et géologie de l'Himalaya. *C.N.R.S. Paris coll.int., Paris Sciences de la Terre Ed. Cent. Natl. Rech. Sci. Paris*, 301–318.

Pécher, A. (1991). The contact between the Higher Himalayan crystallines and the Tibetan Sedimentary series : Miocene large–scale dextral shearing. *Tectonics*, 10, 587–598.

Perrier, R., Chitrakar, G. R., Froidefond, T., Tiwari, D., Gautam, U., Kafle, B., & Trique, M. (2002). Estimating streaming potentials associated with geothermal circulation at the Main Central Thrust: an example from Tatopani–Kodari hot spring in central Nepal. *Journal of Nepal Geological Society*, 26, 17–27.

Perrier, F., Richon, P., Byrdina, S., France–Lanord, C., Rajaure, S., Koirala, B.P., Shrestha, P.L., Gautam, U.P., Tiwari, D.R., Revil, A., Bollinger, L., Contraires, S., Bureau, S., & Sapkota, S.N. (2009). A direct evidence for high carbon dioxide and radon–222 discharge in Central Nepal. *Earth and Planetary Science Letters*, 278, 198–207.

Perugini, D., & Poli, G. (2007). Tourmaline nodules from Capo Bianco aplite (Elba Island, Italy): an example of diffusion limited aggregation growth in a magmatic system. *Contributions to Mineralogy and Petrology*, *153*(5), 493–508.

Pouchou, J. L., & Pichoir, F. (1988). Determination of mass absorption coefficients for soft X-rays by use of the electron microprobe. In: Newbury, D. E. (eds.) Microbeam Analysis. San Francisco, CA, San Francisco Press, 319-324.

Powell, R., & Holland, T. J. B. (2008). On thermobarometry. *Journal of Metamorphic Geology, 26*, 155–179.

Powell, R., Guiraud, M., & White, R.W. (2005). Truth and beauty in metamorphic phase–equilibria: conjugate variables and phase diagrams. *Canadian Mineralogist, 43*, 21–33.

Powers, P.M., Lillie, R.J., & Yeates, R.S. (1998). Structure and shortening of the Kangra and Dehra Dun reentrants, Sub–Himalaya, India. *Geological Society of America Bulletin*, **110**, 1010 – 1027.

Quade, J., English, N., & DeCelles, P. G. (2003). Silicate versus carbonate weathering in the Himalaya: a comparison of the Arun and Seti River watersheds. *Chemical Geology*, *202*(3–4), 275–296.

Rai, S. M., Bhattarai, T. N., & Khatiwada, D. (2020). Hot Water Springs (Therma Springs) in Nepal: A review on Their Location, Origin, and Importance. *Journal of Development Innovations*, *4*(2), 24–42.

Rai, S. M., Guillot, S., Le Fort, P., & Upreti, B.N. (1998). Pressure–temperature evolution in the Kathmandu and Gosainkund regions, Central Nepal. *Journal of Asian Earth Sciences, 16*, 283–298.

Rapa, G., Groppo, C., Mosca, P., & Rolfo, F. (2016). Petrological constrains on the tectonic setting of the Kathmandu Nappe in the Langtang–Gosainkund–Helambu regions, Central Nepal Himalaya. *Journal of Metamorphic Geology, 34*, 999–1023.

Rapa, G., Groppo, C., Rolfo, F., Petrelli, M., Mosca, P., & Perugini, D. (2017). Titanite–bearing calc–silicate rocks constrain timing, duration, and magnitude of metamorphic CO_2 degassing in the Himalayan belt. *Lithos, 292–293*, 364–378.

Rapa, G., Mosca, P., Groppo, C., & Rolfo, F. (2018). Detection of tectonometamorphic discontinuities within the Himalayan orogen: Structural and petrological constraints from the Rasuwa district, central Nepal Himalaya. *Journal of Asian Earth Sciences*, 158, 266–286.

Robertson, A. (2000). Formation of mélanges in the Indus Suture Zone, Ladakh Himalaya by successive subduction–related, collisional and post–collisional processes during Late Mesozoic–Late Tertiary time. In: Khan, M.A., Treolar, P.J., Searle, M.P., Jan, Q. (eds.), Tectonics of the Nanga Parbat Syntaxis and the Western Himalaya. *Geological Society of London, Special Publication*, 170, 333–374.

Robinson, D. M., DeCelles, P. G., & Copeland, P. (2006). Tectonic evolution of the Himalayan thrust belt in western Nepal: Implications for channel flow models. *Geological Society of America Bulletin*, 118(7–8), 865–885.

Robinson, D. M., DeCelles, P. G., Patchett, P. J., & Garzione, C. N. (2001). The kinematic history of the Nepalese Himalaya interpreted from Nd isotopes. *Earth and Planetary Science Letters,* 192, 507–521.

Rolfo F., Groppo C., & Mosca P. (2017). Metamorphic CO_2 production in calc–silicate rocks from the eastern Himalaya. *Italian Journal of Geosciences,* 136, 28–38.

Rolfo, F., Groppo, C., & Mosca, P. (2015). Petrological constraints of the "Channel Flow" model in eastern Nepal. In: Mukherjee, S., Carosi, R., van der Beek, P. A., Mukherjee, B. K., & Robinson, D. M. (eds), "Tectonics of the Himalaya". *Geological Society of London, Special Publications, 412*, 177–197.

Sakai H. (1983). Geology of the Tansen Group of the Lesser Himalaya in Nepal. Memoirs of the Faculty of Science, Kyushu University (Japan), *Series D, Geology,* 25, 27–74.

Sakai, H. (1985). Geology of the Kali Gandaki Supergroup of the Lesser Himalayas in Nepal.

Sakai, H., Iwano, H., Danhara, T., Takigami, Y., Rai, S. M., Upreti, B. N., & Hirata, T. (2013). Rift-related origin of the Paleoproterozoic Kuncha Formation, and cooling history of the Kuncha nappe and Taplejung granites, eastern Nepal Lesser Himalaya: a multichronological approach. *Island Arc*, 22(3), 338–360.

Sapkota, S. N., Bollinger, L., Klinger, Y., Tapponnier, P., Gaudemer, Y., & Tiwari, D. (2013). Primary surface ruptures of the great Himalayan earthquakes in 1934 and 1255. *Nature Geoscience*, 6(1), 71–76

Schelling, D., & Arita, K. (1991). Thrust tectonics, crustal shortening, and the structure of the far–eastern Nepal, Himalaya. *Tectonics,* **10**, 851–862.

Schelling, D. (1992). The tectonostratigraphy and structure of the eastern Nepal Himalaya. *Tectonics*, 11, 925–943.

Searle, M. P., Law, R. D., Godin, L., Larson, K. P., Streule, M. J., Cottle, J. M., & Jessup, M. J. (2008). Defining the Himalayan Main Central Thrust in Nepal. *Journal of the Geological Society of London, 165*, 523–534.

Sengör, A. C., & Natal'In, B. A. (1996). Turkic–type orogeny and its role in the making of the continental crust. *Annual Review of Earth and Planetary Sciences*, 24(1), 263–337.

Sharma, T., Kansakar, D.R., & Kizaki, K. (1984). Geology and tec–tonics of the region between Kali Gandaki and Bheri rivers in central west Nepal. *Bulletin of the College of Science University of the Ryukyus* 38, 57–102.

Shrestha, S. B., & Shrestha, J. N. (1984). Geological map of eastern Nepal (scale 1:250,000). *Department of Mines and Geology,* Kathmandu.

Shrestha, S.B., Shrestha, J.N., & Sharma, S.R. (1987). Geological map of mid–western Nepal (scale: 1250,000). *Department of Mines and Geology, Kathmandu*.

Singh, R., et al. (2004). Geochemistry of thermal springs from Bhutan Himalaya. *Journal of the Geological Society of India*, 64, 191–198.

Spear, F. S. (1993). Metamorphic phase equilibria and pressure–temperature–time paths. *Mineralogical Society of America Monograph, 1*, 799 pp.

Spear, F. S., & Wolfe, O. M. (2018). Evaluation of the effective bulk composition (EBC) during growth of garnet. *Chemical Geology, 491*, 39–47.

Spear, F. S., & Wolfe, O.M. (2019). Implications of overstepping of garnet nucleation for geothermometry, geobarometry and P–T path calculations. *Chemical Geology, 530*, 119323

Spear, F. S., Thomas, J. B., & Hallett, B. W. (2014). Overstepping the garnet isograd: a comparison of QuiG barometry and thermodynamic modeling. *Contributions to Mineralogy and Petrology, 168*, 1–15.

Stöcklin, J. (1980). Geology of Nepal and its regional frame. *Journal of the Geological Society of London, 137,* 1–34.

Tamang, S., Groppo, C., Girault, F., & Rolfo, F (2022). Implications of garnet nucleation overstepping for the P–T evolution of the Lesser Himalayan Sequence of central Nepal. *Journal of Metamorphic Geology*. 10.1111/jmg.12695.

Tapponier, P., Peltzer, G., & Armijo, R. (1986). On the mechanics of the collision between India and Asia. *Geological Society of London, Special Publication*, 19, 115–157.

Tapponier, P., Peltzer, G., Le Dain, A. Y., Armijo, R., & Cobold, P. (1982). Propagation extrusion tectonics in Asia: New insights from simple experiments with plasticine. *Geology*, 10 (12), 611–616.

Terry, M. P., & Heidelbach, F. (2006). Deformation-enhanced metamorphic reactions and the rheology of high-pressure shear zones, Western Gneiss Region, Norway. *Journal of Metamorphic Geology, 24*, 3–18.

Tinkham, D.K., & Ghent, E. D. (2005) Estimating P–T conditions of garnet growth with isochemical phase–diagram sections and the problem of effective bulk–composition. *Canadian Mineralogist*, *43*, 35–50.

Tiwari, S. K., Rai, S. K., Bartarya, S. K., Gupta, A. K., & Negi, M. (2016). Stable isotopes ($\delta^{13}C_{DIC}$, δD, $\delta^{18}O$) and geochemical characteristics of geothermal springs of Ladakh and Himachal (India): Evidence for CO2 discharge in northwest Himalaya. *Geothermics*, 64, 314–330.

Ulmer, P. (1986). NORM. Program for cation and oxygen mineral norms. Computer Library, Institut für Mineralogie und Petrographie, ETH–Zentrum, Zürich, Switzerland.

Upreti B.N., & Yoshida M. (2005). Giudebook for Himalayan trekkers. Geology and natural hazard along the Kaligandaki Valley, Nepal. *Tribhuvan University Press, Lalipur, Nepal*, 165.

Upreti, B. N. (1999). An overview of the stratigraphy and tectonics of the Nepal Himalaya. *Journal of Asian Earth Science, 17*, 577–606.

Upreti, B. N., Rai, S. M., Sakai, H., Koirala, D. R., & Takigami, Y. (2003) Early Proterozoic granite of the Taplejung Window, far eastern Lesser Nepal Himalaya. *Journal of Nepal Geological Society*, 28, 9–18.

Upreti, B.N. (1996). Stratigraphy of the western Nepal Lesser Himalaya: a synthesis. *Journal of Nepal Geological Society*, 13, 11–28.

Valdiya, K. S. (1998). *Dynamic himalaya*. Universities press.

Valdiya, K.S. (1980). Geology of the Kumaun Lesser Himalaya. Wadia Institute of Himalayan Geology, Dehradun, India, 289.

Valdiya, K.S. (1995). Proterozoic sedimentation and Pan–African geo– dynamic development in the Himalaya. *Precambrian Research*, 74, 35–55.

Valdiya, K.S. (1998). In: Dynamic Himalaya. Universities Press (India) Ltd, Hyderabad 178 pp.

von Krafft A. (1902) Notes on the "Exotic Blocks" of Malla Johar in the Rhot Mahals of Kumaon. *Memoirs of the Geological Survey of India,* XXXII(Part 3):127–183 (with map and sections).

Wadia, D.N. (1933). Note on the Geology of Nanga Parbat (Mt. Diamir), and adjoining portions of Chilas, Gilgit District, Kashmir. *Records of the Geological Survey of India*, 66–2, Calcutta.

Wang, J.–M., Zhang, J.–J., Liu, K., Wang, X.–X., Rai, S., & Scheltens, M. (2016). Spatial and temporal evolution of tectonometamorphic discontinuities in the Central Himalaya: Constraints from P–T paths and geochronology. *Tectonophysics, 679*, 41–60.

Waters, D. J. (2019). Metamorphic constraints on the tectonic evolution of the High Himalaya in Nepal: the art of the possible. In: Himalayan Tectonics: A Modern Synthesis (Treloar, P. J. & Searle M. P., eds), *Geological Society, London, Special Publications, 483*, 325–375.

Waters, D. J., & Lovegrove, D. P. (2002). Assessing the extent of disequilibrium and overstepping of prograde metamorphic reactions in metapelites from the Bushveld complex aureole, South Africa. *Journal of Metamorphic Geology, 20*, 135–149.

Webb, A.A.G., Schmitt, A.K., He, D., & Weigand, E.L. (2011). Structural and geochronological evidence for the leading edge of the Greater Himalayan Crystalline complex in the central Nepal Himalaya. *Earth and Planetary Science Letters*, 304, 483–495.

West, R. M., & Munthe, J. (1981). Neogene vertebrate paleontology and stratigraphy of Nepal. *Journal of Nepal Geological Society*, 1(1), 1–14.

West, R.M., Lukacs, J.R., Munthe, J., & Hussain, S.T. (1978). Vertebrate fauna from Neogene Siwalik group Dang valley, western Nepal. *Journal of Paleontology,* 52, 1015–1022.

White, R. W., Powell, R., & Holland, T. J. B. (2007). Progress relating to calculation of partial melting equilibria for metapelites. *Journal of Metamorphic Geology, 25*, 511–527.

White, R. W., Powell, R., & Johnson, T. E. (2014). The effect of Mn on mineral stability in metapelites revisited: New a–x relations for manganese–bearing minerals. *Journal of Metamorphic Geology, 32*, 809–828.

Whitney, D. L., & Evans, B. W. (2010). Abbreviations for names of rock–forming minerals. *American Mineralogist, 95,* 185–187.

Wolfe, O. M., & Spear, F. S. (2018). Determining the amount of overstepping required to nucleate garnet during Barrovian regional metamorphism, Connecticut Valley Synclinorium. *Journal of Metamorphic Geology, 36*, 79–94.

Yavuz, F. (2007). WinAmphcal: A Windows program for the IMA-04 amphibole classification. *Geochemistry, Geophysics, Geosystems*, *8*(1).

Yin, A. (2006). Cenozoic tectonic evolution of the Himalayan orogen as constrained by along-strike variation of structural geometry, exhumation history, and foreland sedimentation. *Earth Science Reviews*, 76, 11–131.

Yin, A., & Harrison, T.M. (2000). Geologic evolution of the Himalayan–Tibetan orogen. *Earth and Planetary Sciences Letters, 28*, 211–280.

Zhu, B., Kidd, W. S., Rowley, D. B., Currie, B. S., & Shafique, N. (2005). Age of initiation of the India–Asia collision in the east–central Himalaya. *The Journal of Geology*, 113(3), 265–285.

Zhu, B., Kidd, W.S.F., Rowley, D.B., Currie, B.S., & Shafique, N. (2005). Age of initiation of the India–Asia collision in the east–central Himalaya. *Journal of Geology*, 113, 265–285.

Zhu, D.C., Zhao, Z.D., Niu, Y., Dilek, Y., Hou, Z.Q., & Mo, X.X. (2013). The origin and pre–Cenozoic evolution of the Tibetan Plateau. *Gondwana Research*, 1429–1454.

APPENDIXES

Appendixes include the following supplementary figures and tables:

Appendix 1 – List of collected samples

Table S1a – Kharidunga – Tingsa La Pass transect

Table S1b – Jumla – Rara Lake – Simikot transect

Appendix 2 – Bulk compositions

Table S2a – Bulk compositions of metapelites

Table S2a – Bulk compositions of dolomite and magnesite –bearing lithologies

Table S2a – Bulk compositions of calcite –bearing lithologies

Appendix 3 – Protoliths' and observed assemblages and modes

Table S3 – Protoliths' and observed assemblages and modes

Appendix 4 – Compositional profiles of representative garnet porphyroblasts in metapelite samples

Fig. S1a: Sample 17a–33

Fig. S1b: Sample 17a–22

Fig. S1c: Sample 15a–15b

Fig. S1d: Sample 15a–28b

Fig. S1e: Sample 17a–42

Appendix 5 – Processed X–ray maps of the investigated metapelite samples

Fig. S2a: Sample 17a–34

Fig. S2b: Sample 17a–33

Fig. S2c: Sample 17a–22

Fig. S2d: Sample 15a–15b

Fig. S2e: Sample 15a–28b

Fig. S2f: Sample 17a–42

Appendix 6 – Unfractionated and fractionated P–T pseudosections modelled for metapelite samples

Fig. S3: Sample 17a–34

Fig. S4: Sample 17a–33

Fig. S5: Sample 17a–22

Fig. S6: Sample 15a–15b

Fig. S7: Sample 15a–28b

Fig. S8: Sample 17a–42

Appendix 7 – P–T pseudosections modelled for metapelite samples contoured with the compositional isopleths of the main mineral phases

Appendix 8 – Processed X–ray maps of the investigated dolomite–bearing samples

Appendix 9 – Processed X–ray maps of the investigated magnesite –bearing samples

Appendix 10 – Cathodoluminescence maps of some dolomite– and magnesite– bearing lithologies

Appendix 11 – Mineral stability fields predicted by the P/T–X(CO_2) pseudosections modelled for carbonate–bearing lithologies

APPENDIX 1

List of collected samples along the Kharidunga – Tingsa La Pass transect (Table S1a) and the Jumla – Rara Lake – Simikot transect (Table S1b)

Table S1a. List of samples collected along the Kharidunga - Tingsa La Pass transect

Sample	Date	Lithology	GPS coordinates
21a-1	06/04/2021	Muscovitic phyllitic schist	[N27°45'10.9"; E85°51'38.0" - 770 m]
21a-2	06/04/2021	Graphitic phyllite	[N27°45'11.9"; E85°51'52.6" - 905 m]
21a-3	06/04/2021	Phylitic schist	[N27°45'07.7'; E85°52'13.7" - 1130 m]
21a-4	06/04/2021	Grt-bearing phylitic schist with garnet	[N27°45'05.0"; E85°52'20.3" - 1240 m]
21a5	07/04/2021	Grt-bearing phylitic schist	[N27°45'10.9"; E85°51'38.0" - 770 m]
21a-6	07/04/2021	Graphitic schist	[N27°43'57.9"; E85°53'37.8" - 1625 m]
21a-7a	07/04/2021	Impure marble/dolostone	[N27°43'52.2"; E85°53'57.0" - 1895 m]
21a-7b	07/04/2021	Calcschist with Mu and Phl	[N27°43'52.2"; E85°53'57.0" - 1895 m]
21a-7c	07/04/2021	Graphitic phyllite with Mu and Phl	[N27°43'52.2"; E85°53'57.0" - 1895 m]
21a-8	07/04/2021	Mylonitic two mica gneiss	[N27°43'18.9"; E85°54'49.1" - 2040 m]
21a-9	07/04/2021	Two mica leucogneiss	[N27°42'50.8"; E85°55'52.4" - 2541 m]
21a-10a	07/04/2021	Grt-bearing graphitic schist	[N27°42'46.2"; E85°55'59.9" - 2645 m]
21a-10b	07/04/2021	Impure marble with schist parting	[N27°42'46.2"; E85°55'59.9" - 2645 m]
21a-11	08/04/2021	Impure marble with phyllitic intercalations	[N27°42'41.4"; E85°56'04.4" - 2673 m]
21a-12a	08/04/2021	Talc + magnesite rock	[N27°42'39.7"; E85°56'05.8" - 2676 m]
21a-12b	08/04/2021	Talc + magnesite rock	[N27°42'39.7"; E85°56'05.8" - 2676 m]
21a-12c	08/04/2021	Talc + magnesite rock	[N27°42'39.7"; E85°56'05.8" - 2676 m]
21a-13	08/04/2021	Phyllitic schist	[N27°42'46.9"; E85°56'48.2" - 2612 m]
21a-14	08/04/2021	Two mica leucogneiss	[N27°42.0'49.0"; E85°57'40.2" - 2462 m]
21a-15a	08/04/2021	Amphibolite	[N27°42.0'49.0"; E85°57'40.2" - 2462 m]
21a-15b	08/04/2021	Graphitic schist	[N27°42.0'49.0"; E85°57'40.2" - 2462 m]
21a-16	08/04/2021	Bt-bearing amphibolite	[N27°42'02.2"; E85°57'53.4" - 2300 m]
21a-17	09/04/2021	Mylonitic orthogneiss	[N27°41'04.5"; E86°21'29.9" - 2315 m]
21a-18	09/04/2021	Chloritic-muscovitic schist	[N27°41'40.5"; E86°01'10.0" - 2405 m]
21a-19a	09/04/2021	Impure marble with phyllitic intercalations	[N27°43'07.8"; E85°00'59.1" - 2945 m]
21a-19b	09/04/2021	Muscovitic calcschist	[N27°43'07.8"; E85°00'59.1" - 2945 m]
21a-20	10/04/2021	Calcschist	[N27°43'27.5"; E86°01'17.8" - 3080 m]
21a-21	10/04/2021	Graphitic phyllite	[N27°44'01.3"; E86°01'30.6" - 3240 m]
21a-22a	10/04/2021	Impure marble	[N27°44'01.3"; E86°01'30.6" - 3240 m]
21a-22b	10/04/2021	Amp-bearing impure marble	[N27°44'01.3"; E86°01'30.6" - 3240 m]
21a-23a	10/04/2021	Graphitic phyllite	[N27°44'37.8"; E86°01'57.7" - 3420 m]
21a-23b	10/04/2021	Talcschist	[N27°44'37.8"; E86°01'57.7" - 3420 m]
21a-24	10/04/2021	Impure marble with phyllitic intercalations	[N27°45'16.9'; E86°02'01.6" - 3530 m]

Table S1a (continue). List of samples collected along the Kharidunga - Tingsa La Pass transect

Sample	Date	Lithology	GPS coordinates
21a-25a	10/04/2021	Graphitic schist	[N27°45'16.9"; E86°02'01.6" - 3530 m]
21a-25b	10/04/2021	Two mica Grt-bearing schist	[N27°45'16.9"; E86°02'01.6" - 3530 m]
21a-26a	11/04/2021	Graphitic phyllite	[N27°45'42.6"; E86°01'44.4" - 3730 m]
21a-26b	11/04/2021	Two mica Grt-bearing schist	[N27°45'42.6"; E86°01'44.4" - 3730 m]
21a-27	11/04/2021	Graphitic schist	[N27°46'28.6"; E86°01'16.1" - 3565 m]
21a-28	11/04/2021	Graphitic schist	[N27°47'04.0"; E86°01'29.0" - 3490 m]
21a-29	11/04/2021	Quartzitic schist	[N27°48'10.0"; E86°01'15.0" - 3600 m]
21a-30	12/04/2021	Two mica schist	[N27°49'45.9"; E86°00'09.4" - 3500 m]
21a-31	12/04/2021	Grt-bearing phylitic schist	[N27°50'01.8"; E86°00'24.1" - 3000 m]
21a-32	12/04/2021	Impure marble with phyllitic intercalations	[N27°50'17.3"; E86°00'31.6" - 3706 m]
21a-33	12/04/2021	Two mica schist	[N27°50'32.9"; E86°00'58.5" - 3535 m]
21a-34	12/04/2021	Phyllitic schist	[N27°50'48.0"; E86°01'19.9" - 3480 m]
21a-35	12/04/2021	Two mica Grt-bearing schist	[N27°50'54.4"; E86°01'37.7" - 3570 m]
21a-36	13/04/2021	Phyllitic schist	[N27°49'46.0"; E85°59'38.7" - 3350 m]
21a-37a	13/04/2021	Graphitic phyllite	[N27°49'46.3"; E85°59'23.3" - 3260 m]
21a-37b	13/04/2021	Impure marble	[N27°49'46.3"; E85°59'23.3" - 3260 m]
21a-38a	13/04/2021	Talc + magnesite rock	[N27°49'40.0"; E85°58'35.7" - 3225 m]
21a-38b	13/04/2021	Magnesitic marble	[N27°49'40.0"; E85°58'35.7" - 3225 m]
21a-39a	13/04/2021	Amphibolite	[N27°49'40.0"; E85°58'35.7" - 3225 m]
21a-39b	13/04/2021	Phyllitic schist	[N27°49'40.0"; E85°58'35.7" - 3225 m]
21a-40	14/04/2021	Dolomitic marble	[N27°49'46.4"; E85°57'26.3" - 3120 m]
21a-41	14/04/2021	Phyllitic schist	[N27°49'57.4"; E85°57'17.0" - 2985 m]
21a-42	14/04/2021	Two mica leucogneiss	[N27°49'42.3"; E85°55'54.8" - 2780 m]
21a-43a	14/04/2021	Amp-bearing calcschist	[N27°49'33.4"; E85°55'54.8" - 2015 m]
21a-43b	14/04/2021	Graphitic phyllite	[N27°49'33.4"; E85°55'54.8" - 2015 m]
21a-44	14/04/2021	Phyllitic schist	[N27°49'40.5"; E85°55'14.1" - 2285 m]
21a-45	15/04/2021	Phyllitic schist	[N27°50'26.6"; E85°54'39.4" - 2410 m]
21a-46	15/04/2021	Phyllitic schist	[N27°50'26.4"; E85°53'53.2" - 2880 m]
21a-47	15/04/2021	Graphitic schist	[N27°50'11.5"; E85°57'01.5" - 2960 m]
21a-48	15/04/2021	Phyllitic schist	[N27°50'18.0'; E85°56.0'09.5" - 3000 m]
21a-49a	16/04/2021	Graphitic phyllite	[N27°50'40.2"; E85°54'22.2" - 2245 m]
21a-49b	16/04/2021	Impure banded marble	[N27°50'40.2"; E85°54'22.2" - 2245 m]
21a-50	16/04/2021	Impure marble	[N27°51'40.7'; E85°53'51.4" - 1900 m]

Table S1b. List of samples collected along the Jumla - Rara Lake - Simikot transect

Sample	Date	Lithology	GPS coordinates
21b-1	05/11/2021	Muscovitic quartzite	[N29°17'21.3"; E82°10'2.5"-2400 m]
21b-2	05/11/2021	Dolomitic marble	[N29°18'26.8"; E82°10'42.7" - 2555 m]
21b-3	05/11/2021	Dolomitic marble	[N29°19'10.2"; E82°10'40.1" 2860 m]
21b-4	06/11/2021	Dolostone	[N29°20'06.4"; E82°09'57.5" - 3310 m]
21b-5	06/11/2021	Sligthly recrystallized dolostone	[N29°20'18.1"; E82°09'42.6" - 3530 m]
21b-6	06/11/2021	Black slate	[N29°21'17.1"; E82°09'39.1" - 3590 m]
21b-7	06/11/2021	Banded dolostone, poorly recrystallized	[N29°22'13.7"; E82°09'16.6" - 3365 m]
21b-8	06/11/2021	Banded marble with graphitic phyllitic layers	[N29°23'47.0"; E82°08'49.6" - 2665 m]
21b-9	07/11/2021	Black slate	[N29°24'05.9"; E82°08'11.7" - 2700 m]
21b-10	07/11/2021	Carbonatic phyllite	[N29°24'39.6"; E82°07'20.3" - 2710 m]
21b-11	07/11/2021	Brecciated dolostone	[N29°25'01.4"; E82°06'11.9" - 2945 m]
21b-12	07/11/2021	White dolomitic marble	[N29°26'03.2"; E82°06'30.4" - 2880 m]
21b-13	07/11/2021	Grey dolomitic marble	[N29°27'02.4"; E82°07'25.1" - 3210 m]
21b-14	08/11/2021	White dolomitic marble	[N29°28'17.5"; E82°08'10.3" - 3320 m]
21b-15a	08/11/2021	Grey dolomitic marble	[N29°28'52.0"; E82°08'50.9" - 2640 m]
21b-15b	08/11/2021	Black dolomitic marble	[N29°28'52.0"; E82°08'50.9" - 2640 m]
21b-16	08/11/2021	Mu+Chl phyllite	[N29°29'28.6"; E82°08'40.7" - 2515 m]
21b-17a	08/11/2021	Fine-grained gneiss	[N29°29'57.6"; E82°08'08.2" - 2410 m]
21b-17b	08/11/2021	Amphibolite	[N29°29'57.6"; E82°08'08.2" - 2410 m]
21b-17c	08/11/2021	Chloritic phyllite with Ctd(?)	[N29°29'57.6"; E82°08'08.2" - 2410 m]
21b-18	09/11/2021	Mu+Chl phyllite	[N29°30'36.3"; E82°07'03.8" - 2635 m]
21b-19	09/11/2021	Graphitic muscovitic phyllite	[N29°30'39.0"; E82°06'41.3" - 2885 m]
21b-20	09/11/2021	Fine-grained gneiss	[N29°31'43.9"; E82°03'56.1" - 3000 m]
21b-21a	10/11/2021	Quartzitic muscovitic gneiss	[N29°32'44.4"; E82°07'25.9" - 2790 m]
21b-21a	10/11/2021	Amphibolite	[N29°32'44.4"; E82°07'25.9" - 2790 m]
21b-22	10/11/2021	Mu+Chl phyllite	[N29°32'48.2"; E82°08'04.1" - 2520 m]
21b-23	10/11/2021	Mu+Chl fine grained gneiss	[N29°33'12.5"; E82°09'23.0" - 2030 m]
21b-24	10/11/2021	Mu+Chl phyllite	[N29°33'48.3"; E82°09'28.6" - 1840 m]
21b-25	10/11/2021	Muscovitic gneissic micaschist	[N29°34'20.2"; E82°09'20.5" - 21401 m]
21b-26	11/11/2021	Mu+Chl Grt-bearing phyllite	[N29°34'34.2"; E82°09'27.3" - 2040 m]
21b-27	11/11/2021	Mu+Chl phyllite	[N29°35'17.1"; E82°08'50.0" - 2575 m]
21b-28	11/11/2021	Mu+Chl Grt-bearing phyllite	[N29°36'41.8"; E82°08'06.3" - 2685 m]
21b-29	11/11/2021	Two-micas orthogneiss	[N29°37'22.8"; E82°08'05.8" - 2835 m]
21b-30a	12/11/2021	Muscovitic phyliitic schist with Grt	[N29°37'53.5"; E82°07'11.3" - 3410 m]
21b-30b	12/11/2021	Muscovitic phyllitic schist	[N29°37'53.5"; E82°07'11.3" - 3410 m]

Table S1b (continue). List of samples collected along the Jumla - Rara Lake - Simikot transect

Sample	Date	Lithology	GPS coordinates
21b-31	12/11/2021	Graphitic phyllitic schist	[N29°38'16.6"; E82°06'51.4" - 3570 m]
21b-32a	12/11/2021	Two-micas gneissic micaschist	[N29°38'37.7": E82°06'58.0" - 3415 m]
21b-32b	12/11/2021	Amphibolite	[N29°38'37.7": E82°06'58.0" - 3415 m]
21b-33	12/11/2021	Mu+Chl micaschist with Grt porphyroblasts	[N29°39'06.3"; E82°07'28.5" - 3100 m]
21b-34a	12/11/2021	Muscovitic gneissic micaschist	[N29°40'30.4"; E82°06'20.9" - 2985 m]
21b-34b	12/11/2021	Grt-bearing amphibolite	[N29°40'30.4"; E82°06'20.9" - 2985 m]
21b-35	12/11/2021	Two-micas micaschist with Grt	[N29°42'04.8"; E82°05'58.0" - 2480 m]
21b-36	13/11/2021	Graphitic phyllites with Sulp	[N29°42'17.9"; E82°05'24.5" - 2550 m]
21b-37	13/11/2021	Two-micas gneissic micaschist	[N29°43'00.5"; E82°05'11.2" - 2540 m]
21b-38a	13/11/2021	Calc-silicate granofels	[N29°44'43.2"; E82°04'07.1" - 1795 m]
21b-38b	13/11/2021	Coarse grained marble	[N29°44'43.2"; E82°04'07.1" - 1795 m]
21b-38c	13/11/2021	Banded calc-silicate gneiss	[N29°44'43.2"; E82°04'07.1" - 1795 m]
21b-39	13/11/2021	Grt-bearing black slate	[N29°45'03.9"; E82°02'43.1" - 1600 m]
21b-40a	14/11/2021	Calc-silicate gneiss	[N29°45'35.9"; E82°00'45.2" - 1570 m]
21b-40b	14/11/2021	Phl-bearing amphibolite	[N29°45'35.9"; E82°00'45.2" - 1570 m]
21b-41	14/11/2021	Muscovitic phyllitic schist, with	[N29°47'32.1"; E81°55'14.2" - 1780 m]
21b-42	15/11/2021	Muscovitic phyllitic schist, with	[N29°47'34.3"; E81°54'05.7" - 1740 m]
21b-43	15/11/2021	Muscovitic-chloritic schist, with	[N29°48'47.0"; E81°51'41.4" - 1820 m]
21b-44	16/11/2021	Two-micas, Grr-bearing, quartzitic phyllite	[N29°50'39.5"; E81°53'18.4" - 1910 m]
21b-45a	16/11/2021	Phl+Tr marble	[N29°50'58.5"; E81°53'15.6" - 1915 m]
21b-45b	16/11/2021	Tlc-bearing marble	[N29°50'58.5"; E81°53'15.6" - 1915 m]
21b-45c	16/11/2021	Calc-silicate gneiss /Phl-bearing amphibolite	[N29°50'58.5"; E81°53'15.6" - 1915 m]
21b-46	16/11/2021	Two-micas, Grt+Ky -bearing micaschist	[N29°51'02.8"; E81°53'16.9" - 1915 m]
21b-47a	16/11/2021	Two-micas fine grained gneiss	[N29°51'39.3"; E81°52'34.7" - 1915 m]
21b-47b	16/11/2021	Two-micas gneissic micaschist with St	[N29°51'39.3"; E81°52'34.7" - 1915 m]
21b-48	16/11/2021	Two-micas anatectic gneiss	[N29°51'54.3"; E81°52'30.5" - 1915 m]
21b-49	16/11/2021	Two-micas, Grt-bearing, anatectic gneissic	[N29°52'33.7"; E81°52'11.7" - 2040 m]
21b-50a	16/11/2021	Fine-grained two-micas gneiss	[N29°53'17.8"; E81°51'44.2" - 2100 m]
21b-50b	16/11/2021	Calc-silicate granofels	[N29°53'17.8"; E81°51'44.2" - 2100 m]
21b-51	16/11/2021	Biotitic anatectic gneiss, with Grt-bearing	[N29°53'57.4"; E81°52'09.8" - 2135 m]
21b-52	16/11/2021	Biotitic anatectic gneiss, with Grt and Ky	[N29°54'27.8"; E81°52'16.3" - 2035 m]
21b-53	17/11/2021	Two-mica gneissic micaschist with Grt and Sil	[N29°56'05.7"; E81°51'54.6" - 2080 m]
21b-54	17/11/2021	Biotitic, Grt-bearing, anatectic gneiss	[N29°56'32.2"; E81°51'05.2" - 2100 m]
21b-55	17/11/2021	Two-micas, Grt-bearing, anatectic gneiss	[N29°57'45.0"; E82°49'44.9" - 2820 m]

APPENDIX 2

Bulk compositions of the investigated metapelites (Table S2a), dolomite– and magnesite –bearing lithologies (Table S2b) and calcite –bearing lithologies (Table S2c) from both the LHS and GHS

Table S2a. Bulk compositions of metapelites

Sample	Unit	SiO_2	TiO_2	Al_2O_3	FeO	MnO	MgO	CaO	Na_2O	K_2O	Reference
Pelites											
15a-15b	LHS	72.27	0.62	13.91	5.41	0.04	3.37	0.43	0.88	3.07	This Thesis
15a-28b	LHS	68.23	0.15	12.83	10.52	0.31	3.76	2.10	0.24	1.86	This Thesis
17a-22	LHS	68.21	0.49	14.52	7.48	0.04	4.04	0.76	1.19	3.26	This Thesis
17a-33	LHS	64.32	1.25	22.15	3.47	0.09	1.42	0.02	1.53	5.76	This Thesis
17a-34	LHS	81.54	0.19	11.52	1.80	0.00	2.03	0.00	0.36	2.56	This Thesis
17a-42	LHS	67.33	0.68	14.23	8.42	0.11	4.43	2.03	0.65	2.11	This Thesis
14-27a	LHS	67.45	0.62	16.42	6.60	0.15	1.96	0.88	0.80	5.24	Rapa et al., 2016
06-69	LHS	71.51	0.87	13.45	4.13	0.04	2.20	0.09	0.42	2.84	Groppo et al., 2009
14-25b	GHS	63.81	0.61	17.77	7.68	0.24	3.05	0.56	1.77	3.54	Rapa et al., 2016
14-24	GHS	70.70	0.61	14.01	6.12	0.21	2.59	3.28	0.72	3.65	Rapa et al., 2016
06-02	LHS	67.35	0.51	14.08	3.98	0.28	2.93	1.24	2.25	2.86	Groppo et al., 2009
14-44a	GHS	68.05	0.53	16.24	4.75	0.12	3.18	0.84	1.76	4.63	Rapa et al., 2016
14-61b	GHS	69.36	0.52	10.81	6.23	0.10	2.16	0.64	3.41	3.10	Rapa et al., 2016
14-71	GHS	75.57	0.60	11.63	5.49	0.12	1.74	0.32	1.00	3.53	Rapa et al., 2016
14-52	GHS	71.01	0.95	8.91	7.25	0.07	6.63	0.61	1.83	2.75	Rapa et al., 2016
14-03	GHS	71.27	0.69	13.82	6.10	0.20	2.85	0.45	0.72	3.91	Rapa et al., 2016
06-29	GHS	73.08	0.62	11.42	4.56	0.12	2.30	0.50	1.72	2.71	Groppo et al., 2009
06-38	GHS	75.74	0.72	9.60	5.65	0.10	1.87	0.88	1.23	2.99	Groppo et al., 2009

Table S2b. Bulk compositions of dolomite and magnesite -bearing lithologies

Sample	Unit	SiO_2	TiO_2	Al_2O_3	FeO	MnO	MgO	CaO	Na_2O	K_2O	Reference
Dolomitic pelites											
17a-29	LHS	65.17	0.24	11.51	6.14	0.32	8.36	6.04	0.50	1.73	This Thesis
17b-12	LHS	68.14	0.39	11.83	5.94	0.05	6.03	3.70	1.00	2.91	This Thesis
17b-15	LHS	71.89	0.49	12.03	5.54	0.02	4.69	0.72	0.74	3.87	unpublished
08-31	LHS	66.30	0.40	10.01	3.72	0.05	8.79	5.34	1.18	4.16	unpublished
10-38a	LHS	69.82	0.48	10.68	6.44	0.13	5.45	3.62	0.48	2.84	Groppo et al., 2020
05-41 (I)	LHS	67.14	0.46	8.45	5.49	0.15	9.31	6.62	0.12	2.23	unpublished
08-36	LHS	57.20	0.48	9.38	5.61	0.12	11.37	11.24	0.71	3.84	unpublished
Dolomitic marls											
18a-26	LHS	59.26	0.04	3.40	1.26	0.00	19.52	15.39	0.53	0.59	This Thesis
15a-28a	LHS	54.57	0.29	7.32	3.41	0.03	16.77	15.27	0.38	1.95	This Thesis
10-39	LHS	51.65	0.34	7.83	3.75	0.09	16.19	14.82	0.16	5.17	unpublished
12-1b	LHS	41.49	0.15	3.54	1.98	0.09	26.95	24.18	0.18	1.43	unpublished
13-82a	LHS	39.27	0.17	3.43	3.52	0.14	24.27	27.68	0.54	0.91	unpublished
15a-11	LHS	54.54	0.30	6.32	4.73	0.09	15.28	16.03	0.71	2.00	unpublished
15a-24	LHS	71.52	0.16	3.75	1.42	0.05	9.83	10.35	0.12	2.82	unpublished
17a-37	LHS	63.93	0.30	6.47	3.75	0.04	12.19	9.90	0.10	3.33	unpublished
Dolostones											
17b-10b	LHS	23.23	0.02	0.41	0.78	0.00	37.31	37.69	0.00	0.17	This Thesis
21-22a	LHS										This Thesis
13-72	LHS	2.77	0.00	0.04	0.40	0.04	47.84	48.82	0.04	0.02	unpublished
14-30	LHS	21.12	0.02	0.41	0.90	0.16	37.88	39.26	0.01	0.20	unpublished
10-59	LHS	45.24	0.21	3.99	2.48	0.09	22.99	22.98	0.67	1.31	unpublished
15a-12b	LHS	24.44	0.03	0.62	1.87	0.09	34.44	38.25	0.03	0.23	unpublished
15a-25a	LHS	25.38	0.02	0.58	0.77	0.04	36.57	36.36	0.03	0.25	unpublished
17b-10c	LHS	44.38	0.19	3.57	2.26	0.13	22.93	23.50	0.19	2.85	unpublished
Magnesitic pelite											
17a-36b	LHS	79.20	0.28	7.76	1.37	0.00	8.06	0.15	0.33	2.85	This Thesis
Magnesitic marl											
17a-35	LHS	61.50	0.16	10.53	7.31	0.01	18.26	1.13	0.20	0.90	This Thesis
Magnesite ores											
17b-7d	LHS	14.56	0.00	1.72	1.14	0.00	82.42	0.16	0.00	0.00	This Thesis
18a-31	LHS	13.89	0.00	0.32	1.16	0.00	83.61	1.02	0.00	0.00	This Thesis
17b-18	LHS	12.10	0.00	0.14	1.28	0.00	85.35	1.13	0.00	0.00	This Thesis

Table S2c. Bulk compositions of calcite -bearing lithologies

Sample	Unit	SiO_2	TiO_2	Al_2O_3	FeO	MnO	MgO	CaO	Na_2O	K_2O	Reference
Calcareous pelites											
13-38a	GHS	69.16	0.66	11.13	5.64	0.11	3.78	7.22	0.49	1.75	Groppo et al., 2021
14-38a	GHS	69.93	0.56	10.82	6.61	0.11	4.36	3.20	1.02	3.32	Groppo et al., 2021
15-46	GHS	79.12	0.46	6.86	2.74	0.07	3.42	5.12	1.12	1.08	Groppo et al., 2021
13-31	GHS	69.44	0.74	10.42	5.26	0.07	4.14	4.58	2.43	2.87	Groppo et al., 2021
07-40	GHS	71.00	0.61	11.12	5.22	0.08	3.71	5.13	1.72	1.33	Groppo et al., 2021
12-11b	GHS	72.14	0.66	9.73	4.77	0.07	3.61	3.50	2.82	2.63	Groppo et al., 2021
12-12b	GHS	72.17	0.65	8.70	4.79	0.07	3.54	6.70	1.40	1.98	unpublished
12-11a	GHS	71.53	0.73	9.56	5.42	0.11	3.74	3.23	2.78	2.91	unpublished
13-64	GHS	55.03	0.56	8.99	4.45	0.06	5.50	21.16	1.88	2.33	Groppo et al., 2021
04-28 (I)	GHS	61.68	0.52	8.02	3.57	0.08	3.23	18.95	1.56	2.33	Groppo et al., 2021
17b-21	GHS	71.46	0.72	9.81	5.71	0.09	3.69	3.35	2.59	2.58	unpublished
Marls s.s.											
17a-27a	LHS	63.50	0.43	7.24	4.49	0.10	5.05	14.64	1.07	3.47	unpublished
10-49c	LHS	48.87	0.23	5.99	3.47	0.10	7.29	30.01	1.91	2.07	Groppo et al., 2021
07-22	GHS	42.99	0.40	6.55	3.33	0.06	6.12	37.61	0.88	2.01	Groppo et al., 2021
14-20a	GHS	45.79	0.47	7.20	3.43	0.08	6.76	33.81	1.22	1.19	Groppo et al., 2021
09-25	GHS	57.80	0.59	9.89	4.84	0.09	5.77	18.32	1.25	1.40	Groppo et al., 2021
07-20	GHS	61.28	0.64	10.10	4.72	0.07	4.54	16.79	0.55	1.24	Groppo et al., 2017
08-57	GHS	60.21	0.55	9.01	4.54	0.07	5.05	16.33	1.04	3.14	Groppo et al., 2021
08-67	GHS	65.34	0.27	8.90	2.21	0.04	2.81	15.11	3.57	1.74	Groppo et al., 2021
12-65	GHS	66.13	0.63	8.25	3.81	0.07	4.29	13.55	1.35	1.87	Groppo et al., 2021
14-17	GHS	62.92	0.48	8.09	4.05	0.01	5.59	13.14	1.15	4.55	Groppo et al., 2021
14-53c	GHS	73.48	0.33	5.70	2.56	0.04	4.45	11.77	0.43	1.20	Rapa et al. 2017
10-4	GHS	72.37	0.57	7.83	3.19	0.04	3.30	9.49	1.06	2.07	Groppo et al., 2021
12-12a	GHS	70.14	0.64	8.11	3.54	0.06	3.43	9.21	1.21	3.58	Groppo et al., 2021
12-64b	GHS	72.05	0.57	8.00	3.26	0.05	2.71	9.04	1.26	2.99	Groppo et al., 2021
14-20b	GHS	43.96	0.42	6.65	4.46	0.16	5.26	38.06	0.93	0.05	Groppo et al., 2021
14-53d	GHS	66.14	0.40	7.71	4.79	0.21	1.99	18.08	0.59	0.06	Groppo et al., 2021
15b-50	GHS	35.84	0.32	5.31	3.07	0.04	6.50	46.54	0.85	1.55	unpublished
Impure limestones											
10-47b	LHS	12.41	0.07	1.29	1.37	0.03	7.10	76.91	0.03	0.75	Groppo et al., 2021
17a-27b	LHS	34.29	0.10	2.10	2.20	0.17	8.28	51.44	0.52	0.89	unpublished
05-55	GHS	31.10	0.33	3.96	2.02	0.13	5.43	54.79	1.45	0.75	Groppo et al., 2021
07-41	GHS	30.62	0.35	5.20	2.84	0.05	5.92	53.53	0.61	0.85	Groppo et al., 2021

APPENDIX 3

Protoliths' and observed assemblages and modes for the investigated samples (Table S3)

Table S3. Protoliths' and observed assemblages and modes

	Aluminous pelites					
Sample	17a-34	17a-33	17a-22	15a-15b	15a-28b	17a-42
Protolith's assemblages						
Kao	7	1	0	2	14	13
Ill	36	77	42	43	26	32
FeChl	3	6	13	9	18	15
MgChl	3	2	7	6	3	5
Qz	47	3	24	31	32	28
Ab	3	12	10	7	2	5
Kfs	0	0	3	0	0	0
An	3	0	3	2	1	3
Dol	-	-	-	-	-	-
Mgs	-	-	-	-	-	-
Cal	-	-	-	-	-	-
Observed assemblages						
Qz	55	13	30	38	40	35
Mu	37	80	47	42	24	20
Bt	-	4	2	9	6	14
Chl	5	0	9	1	3	0
Grt	-	2	4	5	21	16
St	2	0	1	3	2	0
Ky	2	0	-	-	3	8
Pl	-	0	5	1	-	7

	Dolomite series					
	Dolomitic pelites		Dolomitic marl		Dolostone	
Sample	17b-12	17a-29	15a-28a	18a-26	17b-10b	21a-22a
Protolith's assemblages						
Kao	-	11	-	-	-	-
Ill	29	24	20	3	-	4
FeChl	8	10	6	2	1	0
MgChl	5	5	3	-	-	0
Qz	33	31	28	47	16	1
Ab	8	4	3	5	-	0.2
Kfs	7	-	4	-	1	1
An	4	2	1	2	-	0
Dol	6	14	36	41	80	94
Mgs	-	-	-	-	-	0.3
Cal	-	-	-	-	0.5	-
Observed assemblages						
Qz	37	36	26	42	16	1
Mu	17	8	-	-	-	4.5
Bt/Phl	23	18	32	8	2	1
Chl	-	6	-	4	-	-
Grt	2	7	-	-	-	-
St	-	1	-	-	-	-
Ky	-	2	-	1	-	-
Pl	21	18	10	8	-	-
Zo/Ep	<1		-	-	-	-
Crd	-	-	-	-	-	-
Hbl	-	-	11	-	-	-
Oamp	-	-	-	-	-	-
Tlc	-	-	-	-	-	-
Cal	-	3	14	-	-	-
Dol	-	1	7	37	81	93.5
Mgs	-	-	-	-	-	-

	Magnesite series				
	Mgs-pelite	Mgs-marl	Magnesite ores		
Sample	17a-36b	17a-35	17b-7d	18a-31	17b-18
Protolith's assemblages					
Kao	-	21	5	0.3	-
Ill	25	12	-	-	-
FeChl	2	12	2	2	2
MgChl	-	-	-	-	-
Qz	50	32	9	11	10
Ab	3	2	-	-	-
Kfs	10	-	-	-	-
An	1	1	-	-	-
Dol	-	2	0.4	2	3
Mgs	9	18	84	85	86
Cal	-	-	-	-	-
Observed assemblages					
Qz	54	27	-	-	-
Mu	24	-	-	-	-
Bt/Phl	21	20	-	-	-
Chl	-	-	14	4	1
Grt	-	3	-	-	-
St	-	-	-	-	-
Ky	-	10	-	-	-
Pl	2	-	-	-	-
Zo/Ep	<1	-	-	-	-
Crd	-	5	-	-	-
Hbl	-	6	-	-	-
Oamp	-	29	-	-	-
Tlc	-	-	12	17	15
Cal	-	-	-	-	-
Dol	-	-	-	1	2
Mgs	-	-	74	78	82

APPENDIX 4

Compositional profiles of representative garnet porphyroblasts in metapelite samples 17a−33 (Fig. S1a), 17a–22 (Fig. S1b), 15a–15b (Fig. S1c), 15a−28b (Fig. S1d), 17a–42 (Fig. S1e)

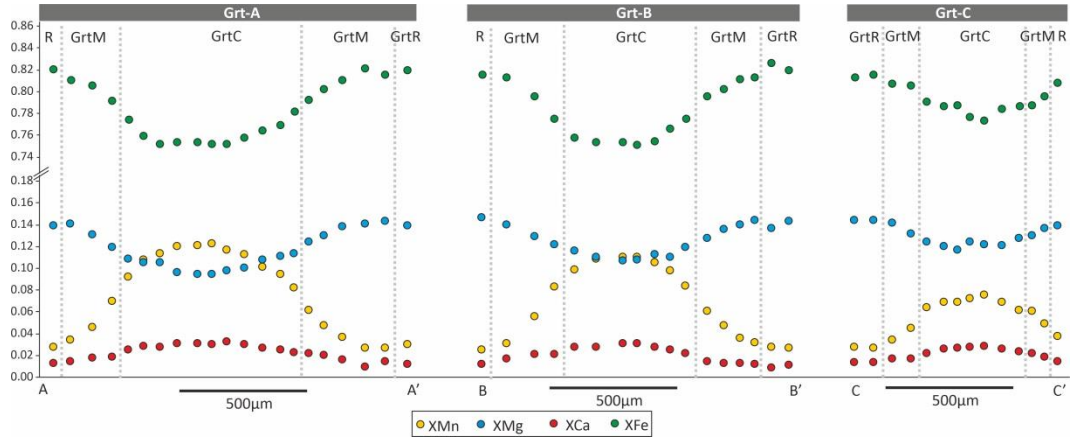

Fig. S1a – Compositional profiles of garnet porphyroblasts in sample 17a–33.

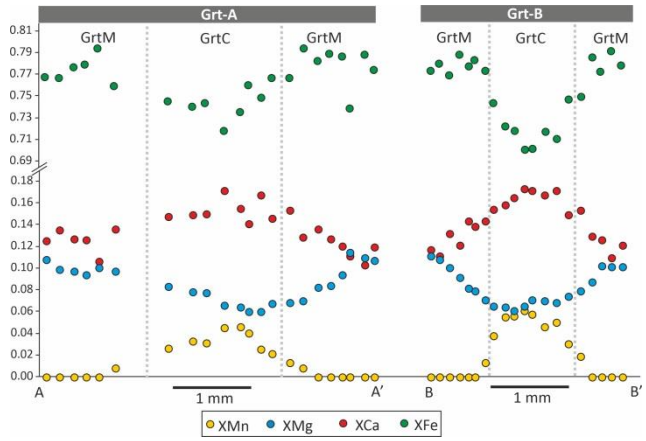

Fig. S1b – Compositional profiles of garnet porphyroblasts in sample 17a–22.

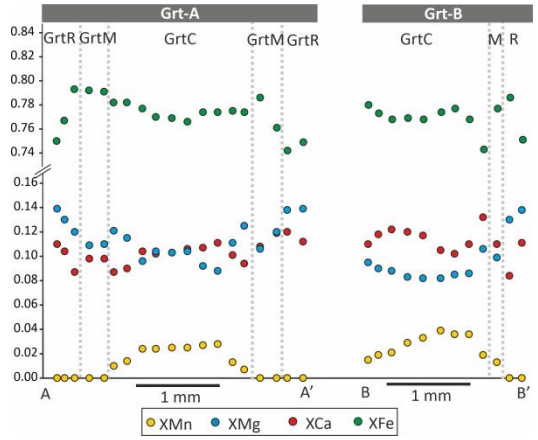

Fig. S1c – Compositional profiles of garnet porphyroblasts in sample 15a–15b.

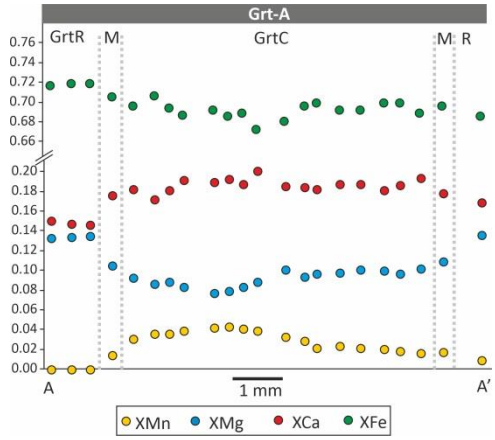

Fig. S1d – Compositional profile of garnet porphyroblast in sample 15a–28b.

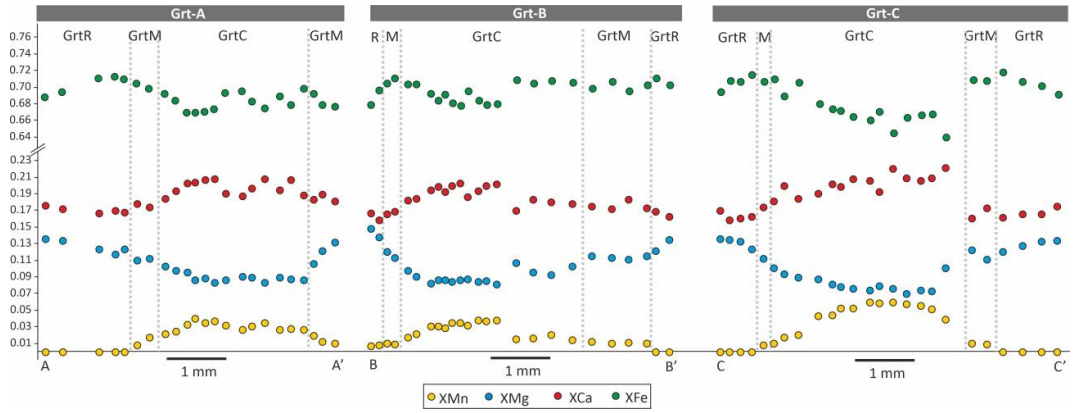

Fig. S1e – Compositional profiles of garnet porphyroblasts in sample 17a–42.

APPENDIX 5

Processed X−ray maps of the investigated metapelite samples (Fig. S2)

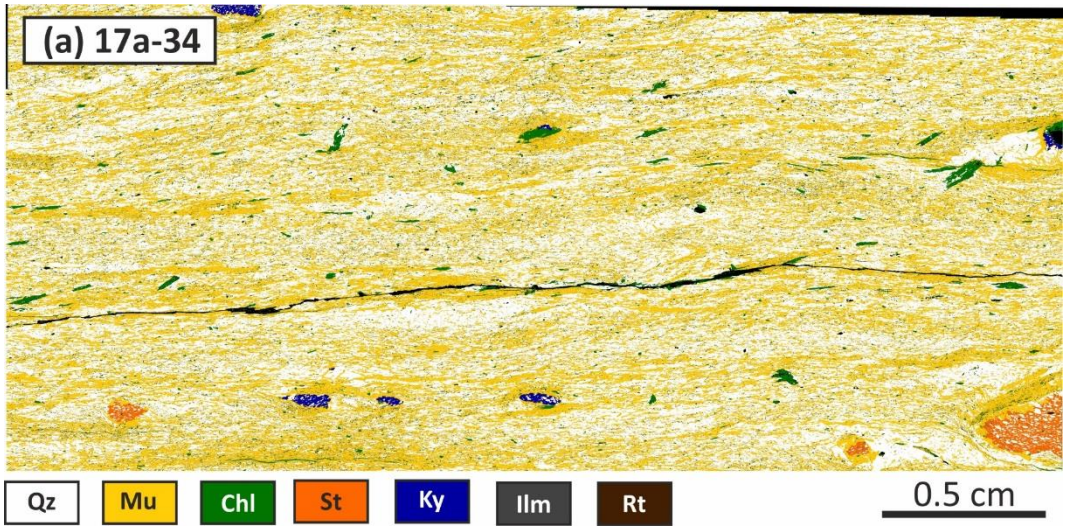

Fig. S2a – Processed X–Ray maps of metapelite sample 17a–34.

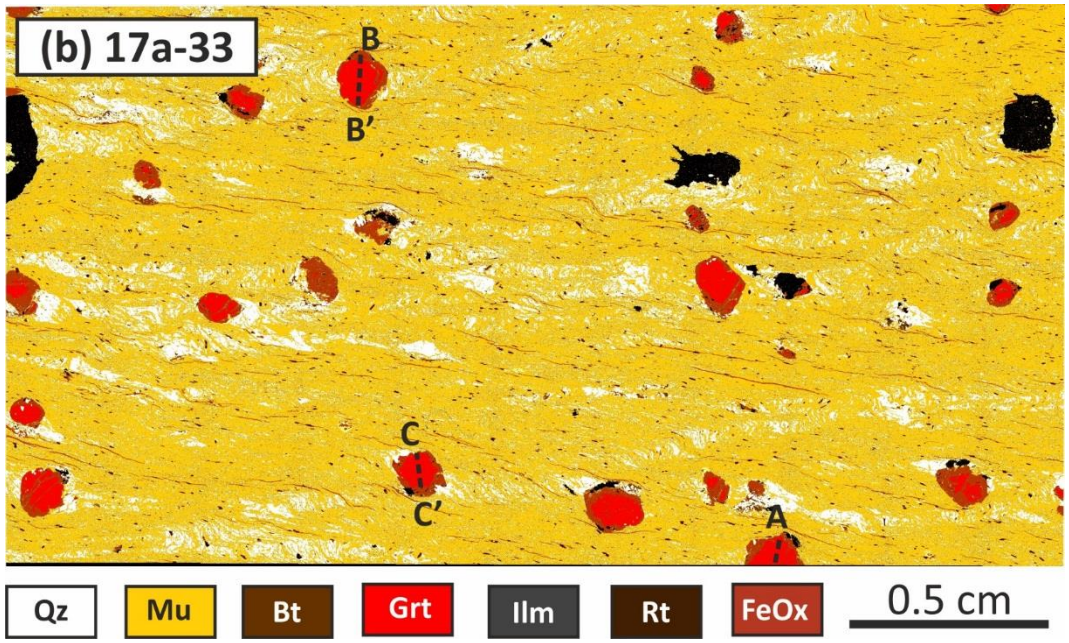

Fig. S2b – Processed X–Ray maps of metapelite sample 17a–33. Compositional profiles of garnet porphyroblasts carried out along the indicated transects are reported in Appendix 4 (Fig. S1a).

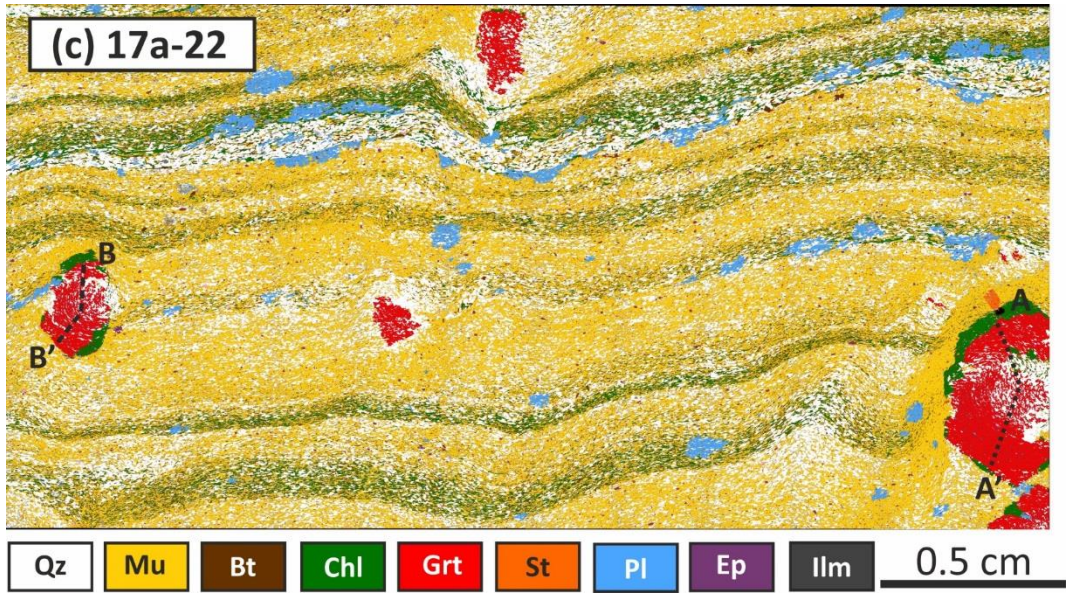

Fig. S2c – Processed X–Ray maps of metapelite sample 17a–22. Compositional profiles of garnet porphyroblasts carried out along the indicated transects are reported in Appendix 4 (Fig. S1b).

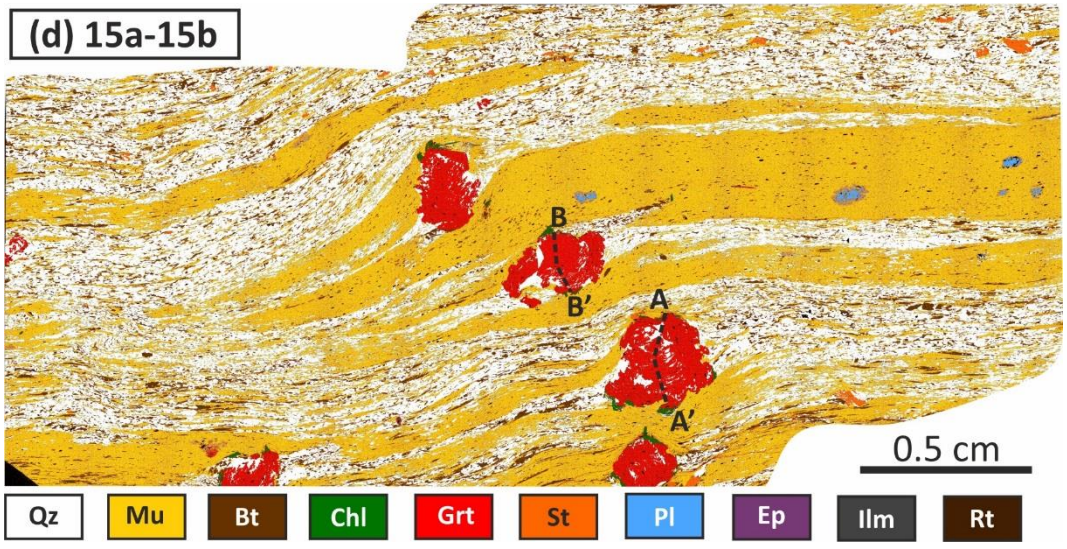

Fig. S2d – Processed X–Ray maps of metapelite sample 15a–15b. Compositional profiles of garnet porphyroblasts carried out along the indicated transects are reported in Appendix 4 (Fig. S1c).

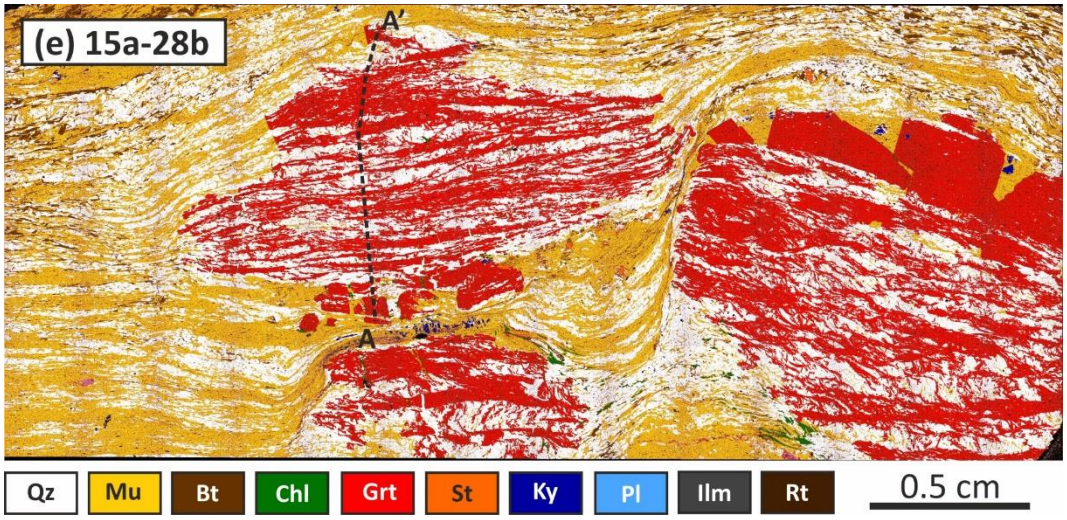

Fig. S2e – Processed X–Ray maps of metapelite sample 15a–28b. Compositional profiles of garnet porphyroblasts carried out along the indicated transects are reported in Appendix 4 (Fig. S1d).

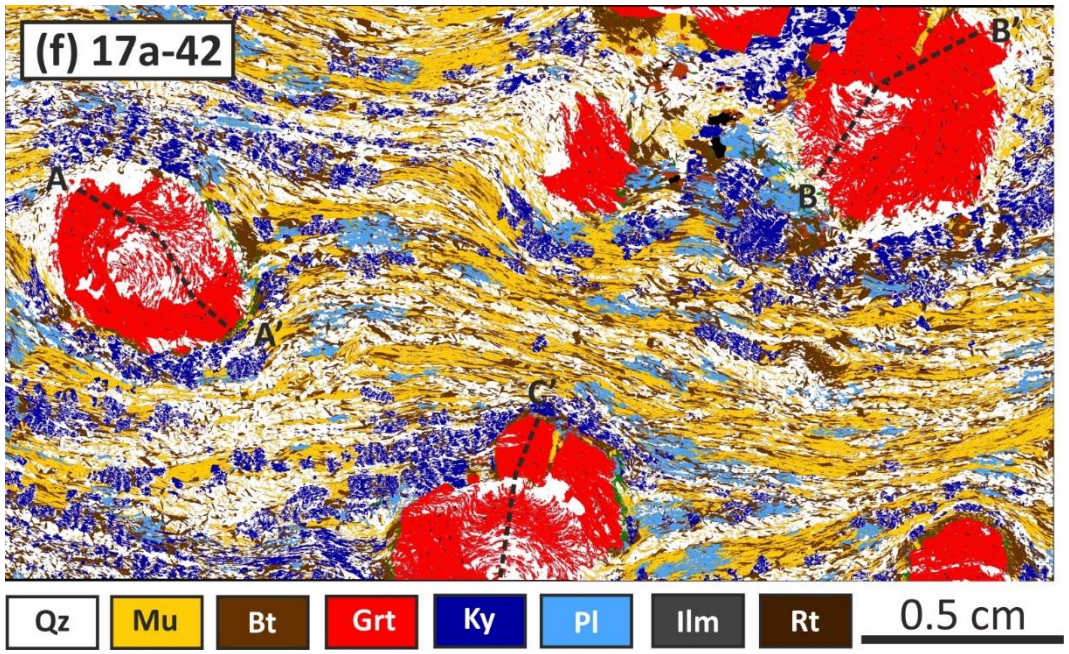

Fig. S2f – Processed X–Ray maps of metapelite sample 17a–42. Compositional profiles of garnet porphyroblasts carried out along the indicated transects are reported in Appendix 4 (Fig. S1e).

APPENDIX 6

Unfractionated and fractionated P–T pseudosections modelled for metapelite samples 17a–34 (Fig. S3), 17a–33 (Fig. S4), 17a–22 (Fig. S5), 15a–15b (Fig. S6), 15a–28b (Fig. S7) and 17a–42 (Fig. S8)

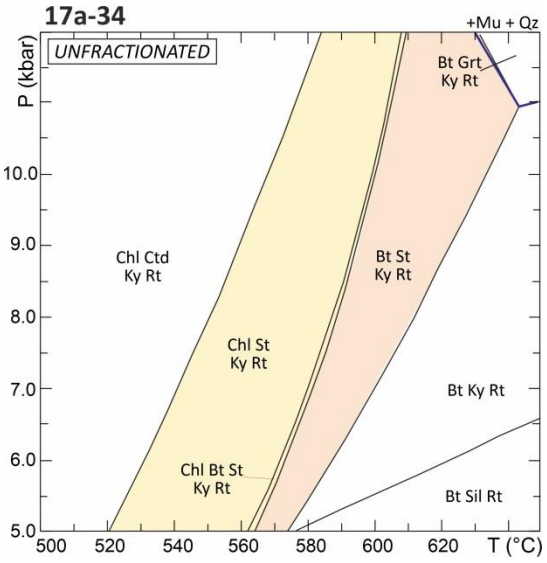

Fig. S3 – P–T isochemical phase diagram modelled for samples 17a–34. The thick blue line are the garnet–in boundaries. Early prograde and late prograde assemblages are indicated in yellow and orange, respectively.

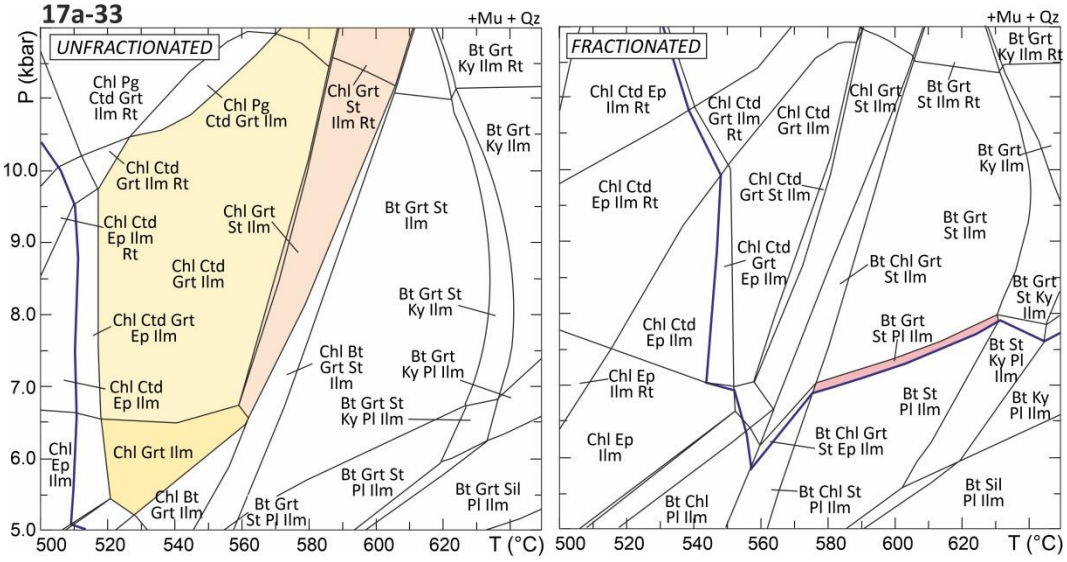

Fig. S4 – P–T isochemical phase diagrams modelled for samples 17a–33, using the unfractionated and fractionated bulk compositions. The thick blue lines in both the diagrams are the garnet–in boundaries. Early prograde, late prograde and peak assemblages are indicated in yellow, orange and red, respectively.

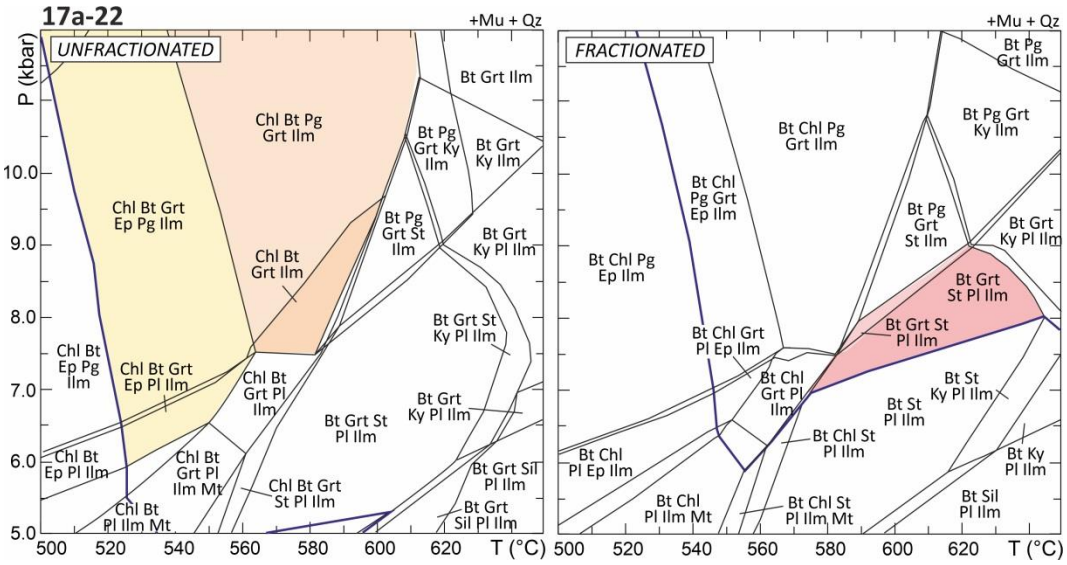

Fig. S5 – P–T isochemical phase diagrams modelled for samples 17a–22, using the unfractionated and fractionated bulk compositions.The thick blue lines in both the diagrams are the garnet–in boundaries. Early prograde, late prograde and peak assemblages are indicated in yellow, orange and red, respectively.

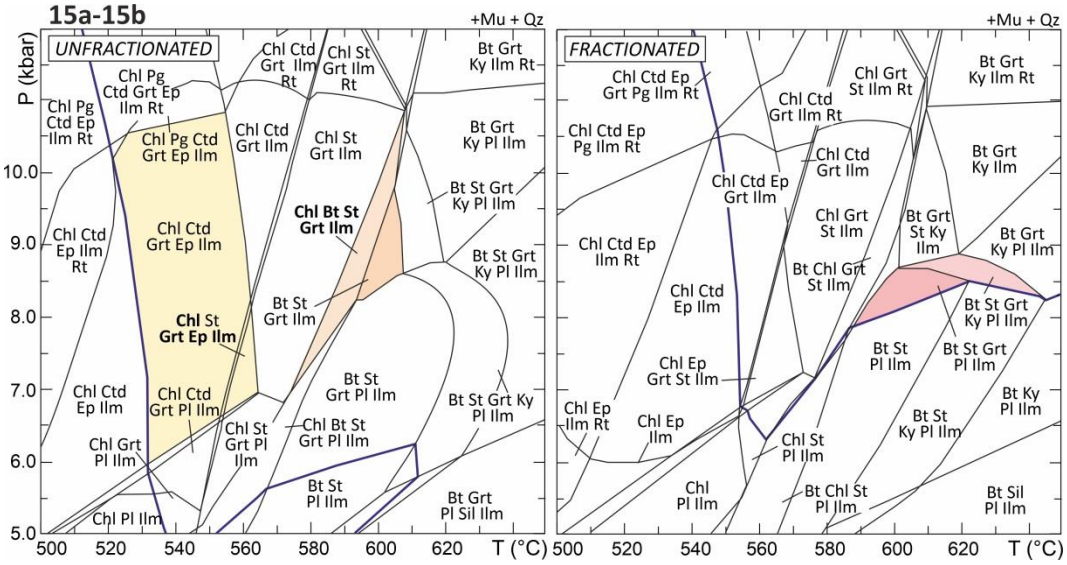

Fig. S6 – P–T isochemical phase diagrams modelled for samples 15a–15b, using the unfractionated and fractionated bulk compositions. The thick blue lines in both the diagrams are the garnet–in boundaries. Early prograde, late prograde and peak assemblages are indicated in yellow, orange and red, respectively.

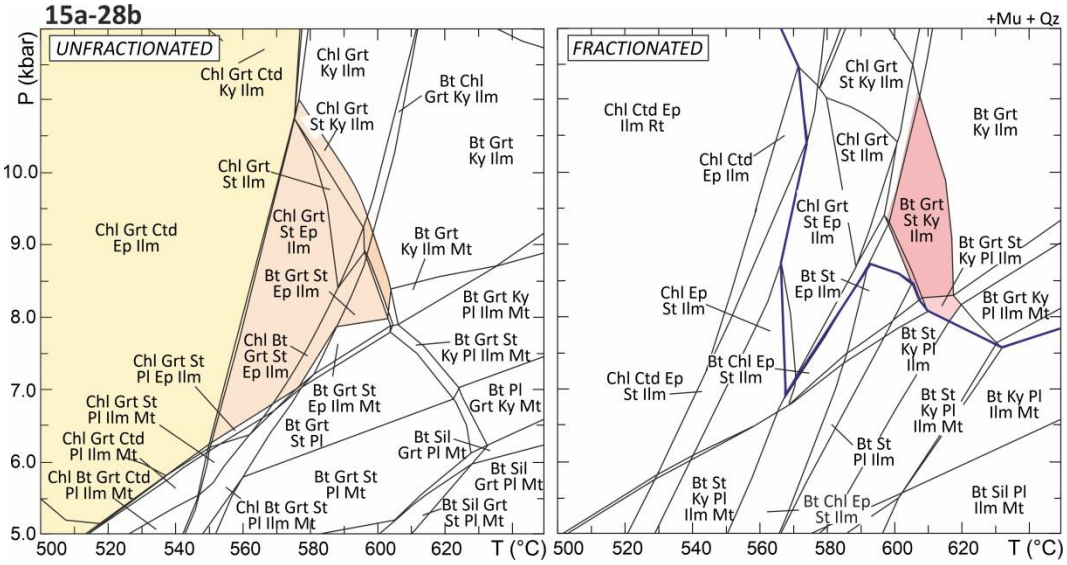

Fig. S7 – P–T isochemical phase diagrams modelled for samples 15a–28b, using the unfractionated and fractionated bulk compositions. The thick blue line in the diagram on the right is the garnet–in boundary. Early prograde, late prograde and peak assemblages are indicated in yellow, orange and red, respectively.

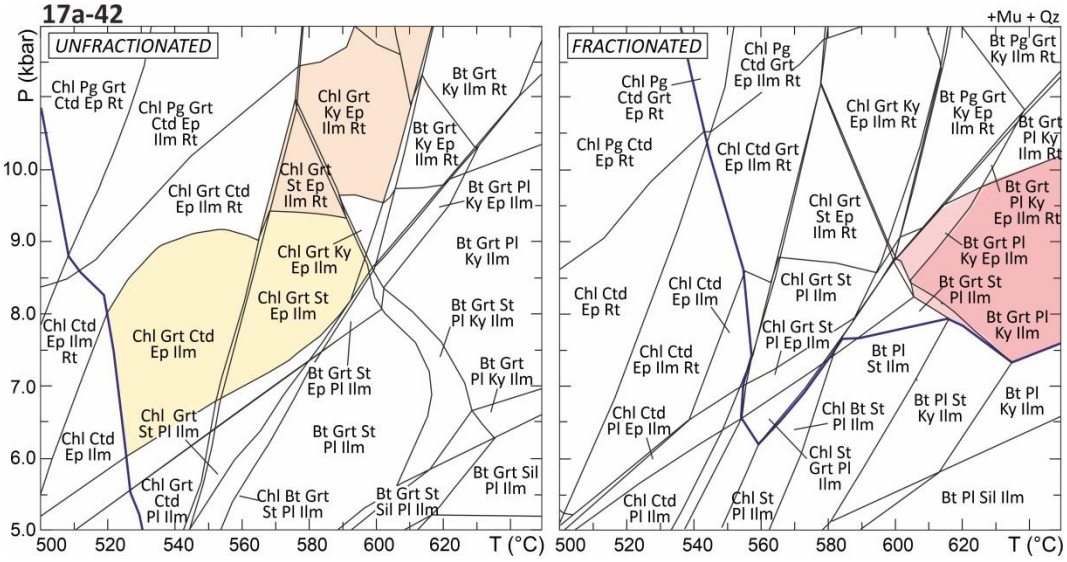

Fig. S8 – P–T isochemical phase diagrams modelled for samples 17a–42, using the unfractionated and fractionated bulk compositions. The thick blue lines in both the diagrams are the garnet–in boundaries. Early prograde, late prograde and peak assemblages indicated in yellow, orange and red, respectively.

APPENDIX 7

P–T pseudosections modelled for metapelite samples 17a–34 (Fig. S9a), 17a–33 (Fig. S9b,c), 17a–22 (Fig. S10), 15a–15b (Fig. S11), 15a–28b (Fig. S12) and 17a–42 (Fig. S13) contoured with the compositional isopleths of the main mineral phases

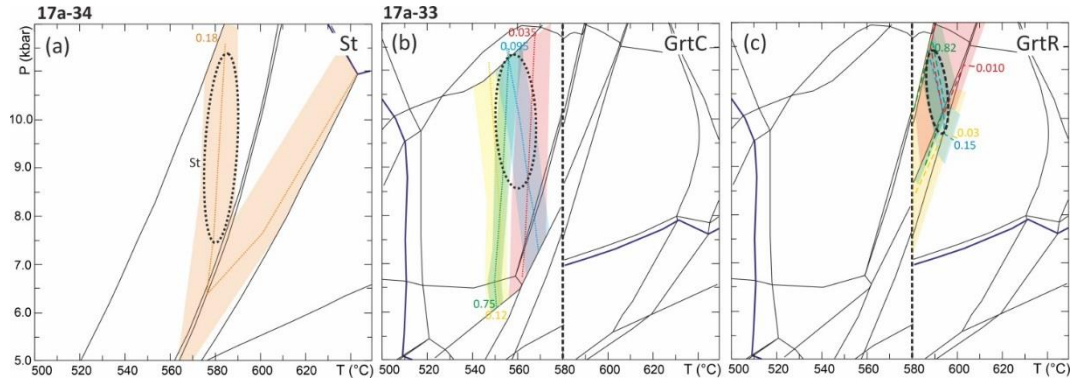

Fig. S9 – P–T isochemical phase diagrams modelled for samples 17a–34 (a) and 17a–33 (b,c), contoured with the compositional isopleths of staurolite (St), garnet core (GrtC) and garnet rim (GrtR), each one with the correspondent uncertainties (shaded areas).

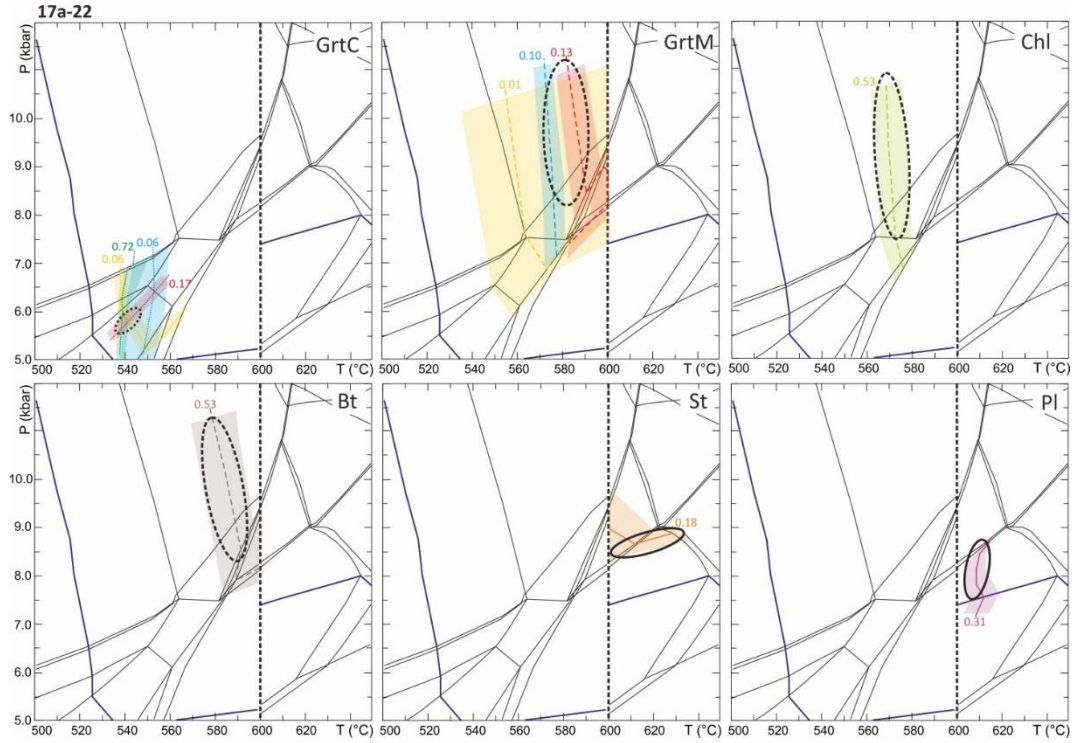

Fig. S10 – P–T isochemical phase diagram modelled for samples 17a–22, contoured with the compositional isopleths of garnet core (GrtC), garnet mantle (GrtM), chlorite (Chl), biotite (Bt), staurolite (St) and plagioclase (Pl), each one with the correspondent uncertainties (shaded areas).

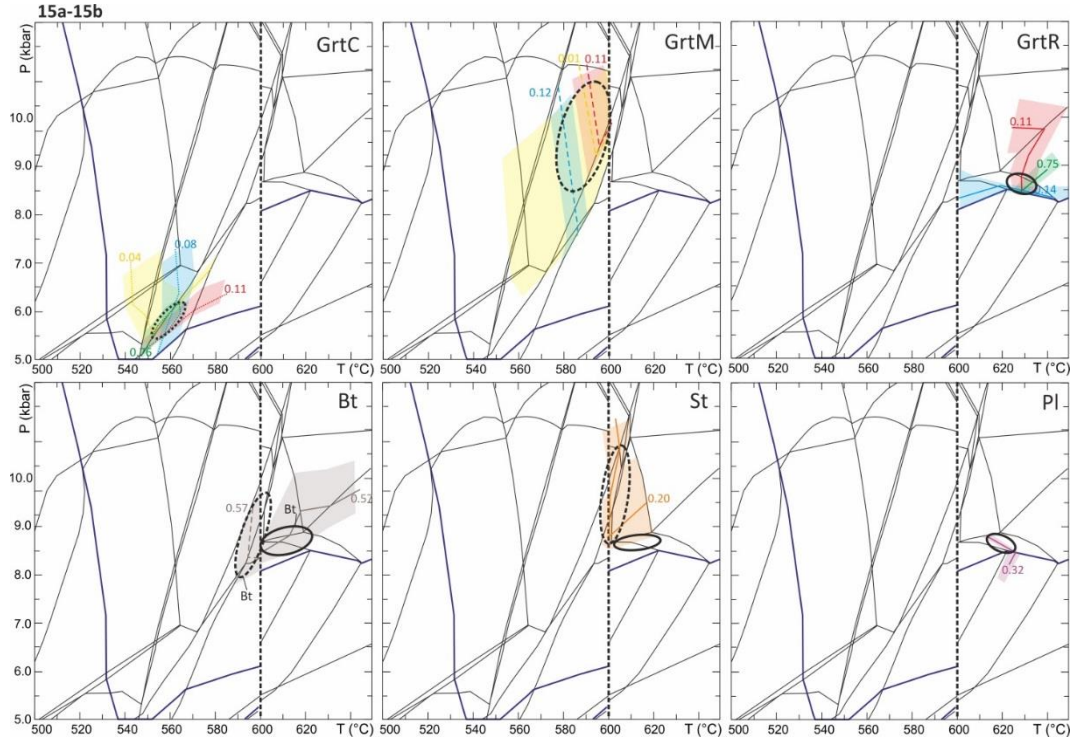

Fig. S11 – P–T isochemical phase diagram modelled for samples 15a–15b, contoured with the compositional isopleths of garnet core (GrtC), garnet mantle (GrtM), garnet rim (GrtR), biotite (Bt), staurolite (St) and plagioclase (Pl), each one with the correspondent uncertainties (shaded areas).

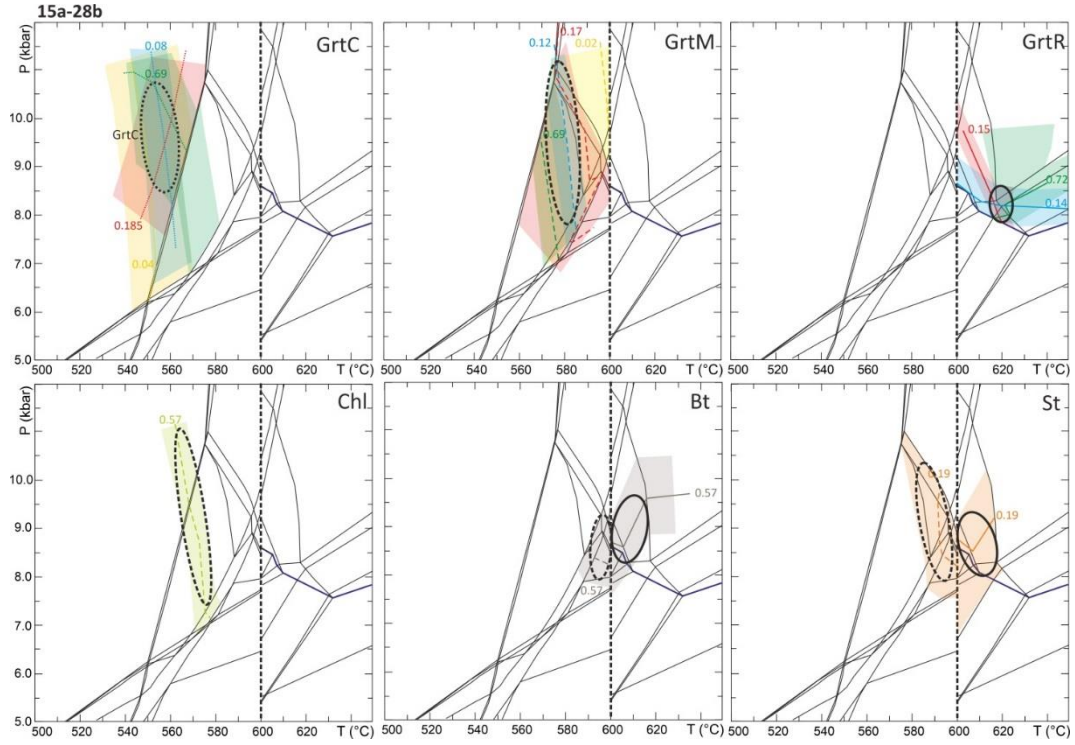

Fig. S12 – P–T isochemical phase diagram modelled for samples 15a–28b, contoured with the compositional isopleths of garnet core (GrtC), garnet mantle (GrtM), garnet rim (GrtR), chlorite (Chl), biotite (Bt), and staurolite (St), each one with the correspondent uncertainties (shaded areas).

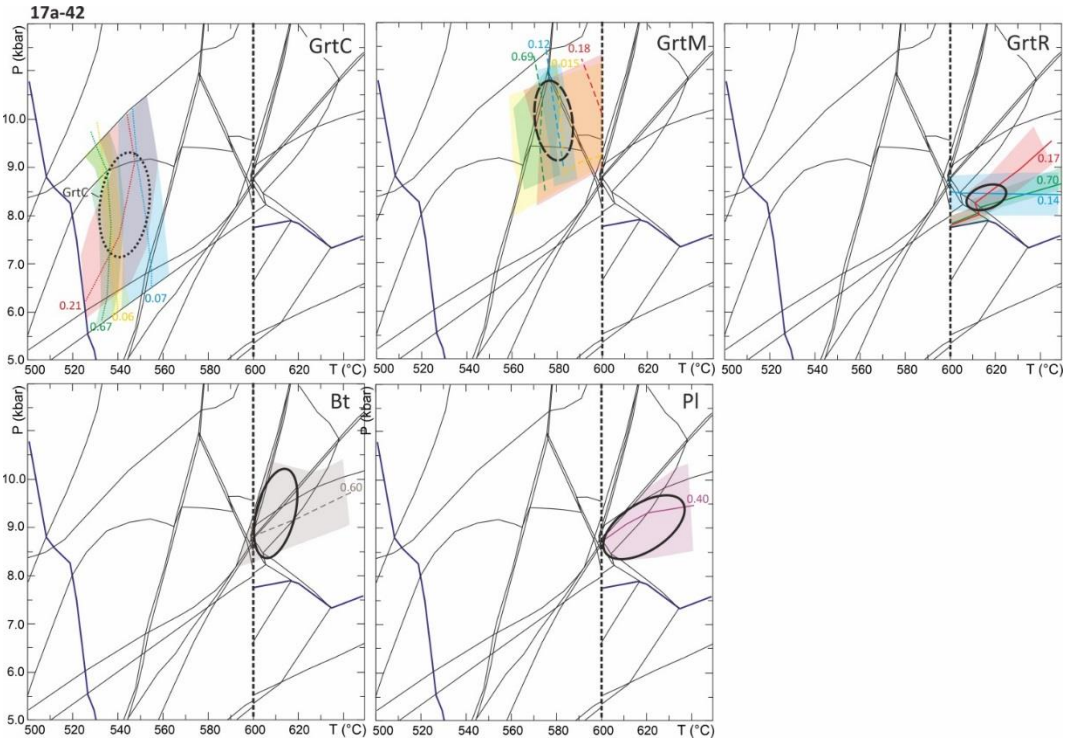

Fig. S13 – P–T isochemical phase diagram modelled for samples 17a–42, contoured with the compositional isopleths of garnet core (GrtC), garnet mantle (GrtM), garnet rim (GrtR), biotite (Bt), and plagioclase (Pl), each one with the correspondent uncertainties (shaded areas).

APPENDIX 8

Processed X−ray maps of the investigated dolomite− bearing lithologies, samples 17b−12 (Fig. S12a), 17a−29 (Fig. S12b), 15a−28a (Fig. S12c), 18a−26 (Fig. S12d), 17b−10b (Fig. S12e), 21a−22a (Fig. S12f)

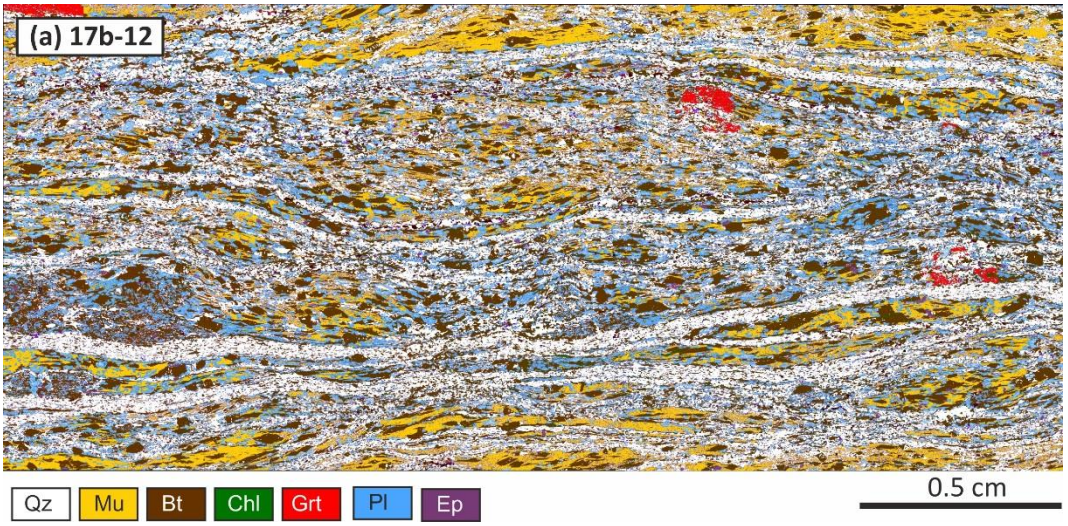

Fig. S12a – Processed X–Ray maps of sample 17b–12.

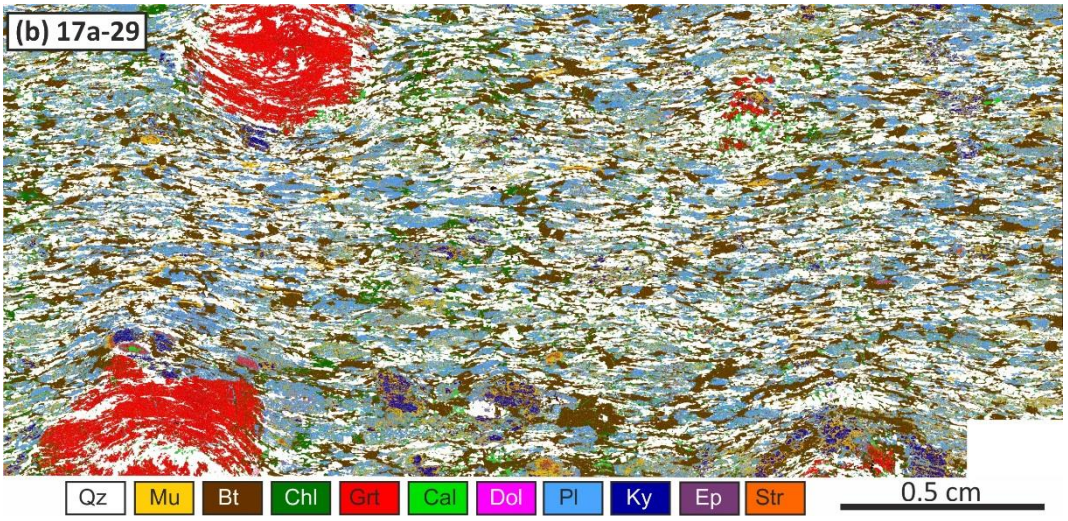

Fig. S12b – Processed X–Ray maps of sample 17a–29.

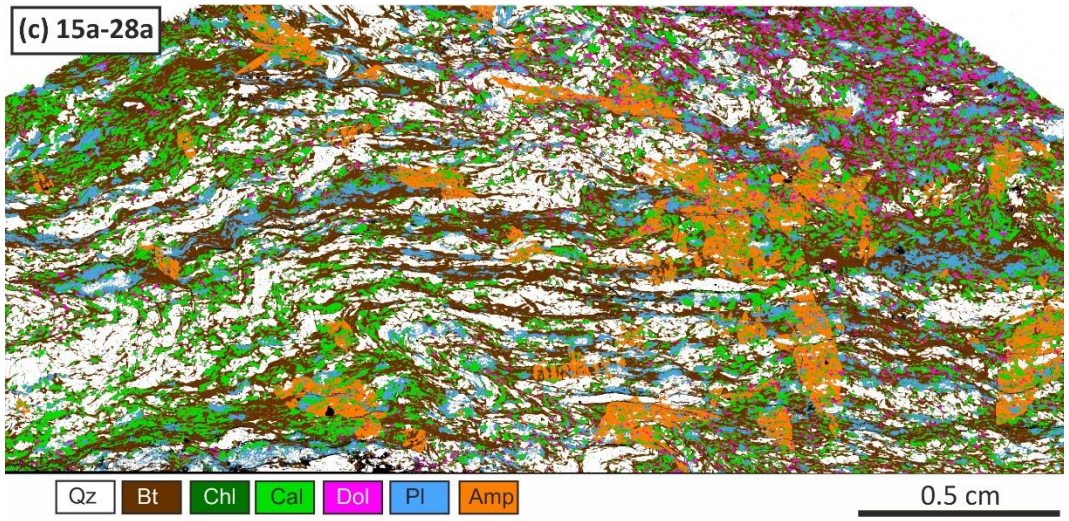

Fig. S12c – Processed X–Ray maps of sample 15a–28a.

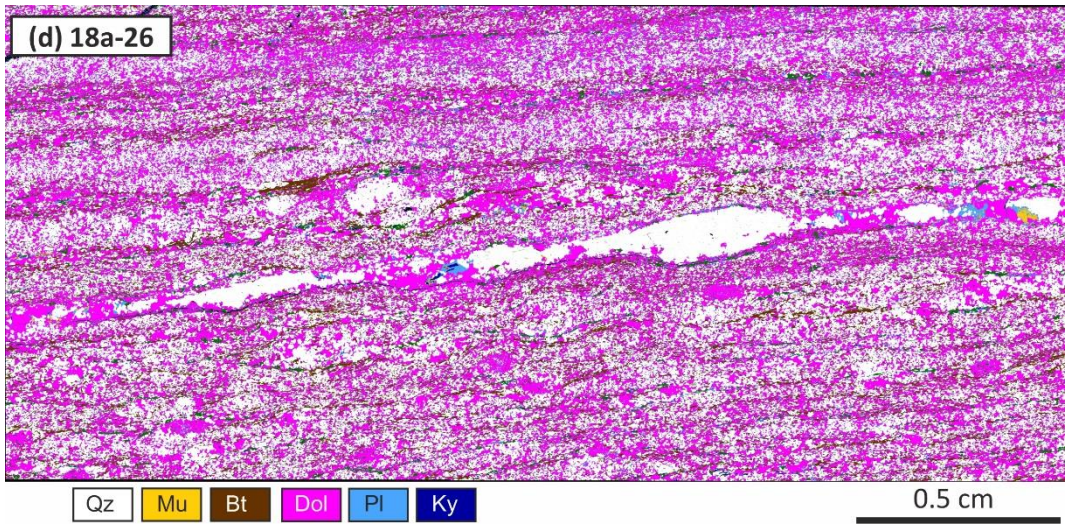

Fig. S12d – Processed X–Ray maps of sample 18b–26.

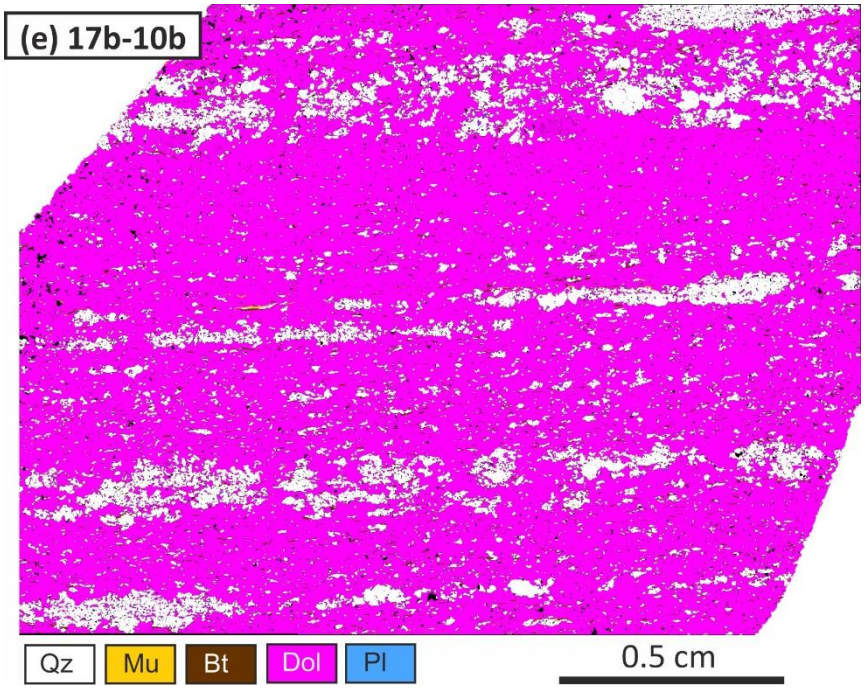

Fig. S12e – Processed X–Ray maps of sample 17b–10b.

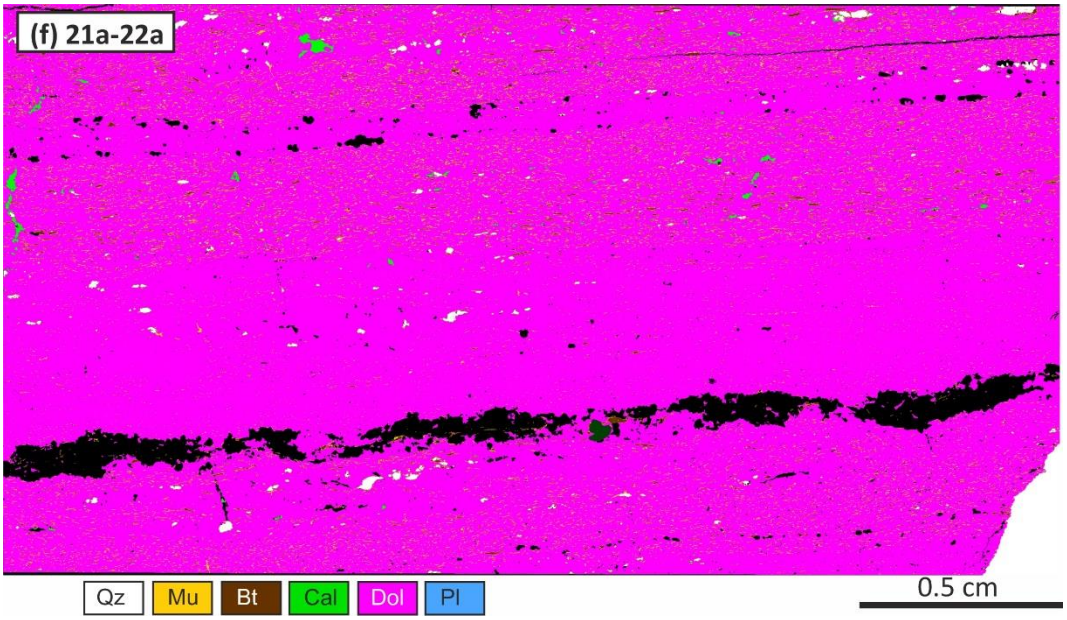

Fig. S12f – Processed X–Ray maps of sample 21a–22a.

APPENDIX 9

Processed X–ray maps of the investigated magnesite–bearing lithologies, samples 17a–36b (Fig. S13a), 17a–35 (Fig. S13b), 17b–7d (Fig. S13c), 18a–31 (Fig. S13d), 17b–18 (Fig. S13e)

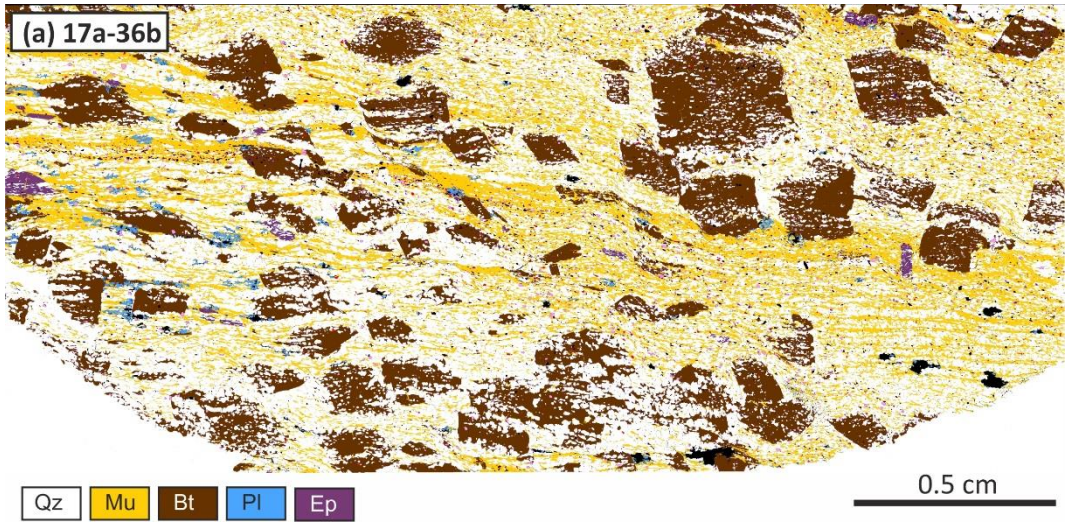

Fig. S13a – Processed X–Ray maps of sample 17a–36b.

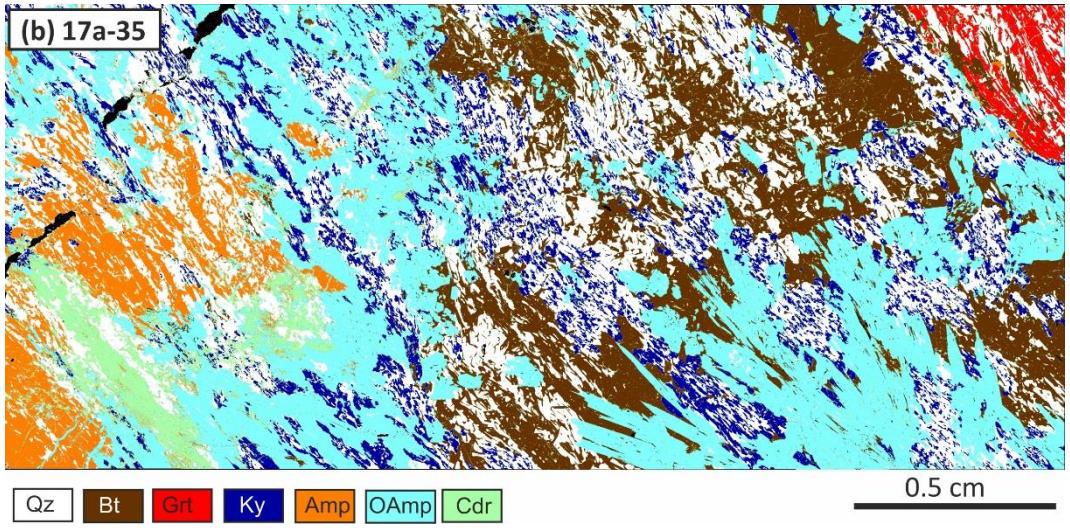

Fig. S13b – Processed X–Ray maps of sample 17a–35.

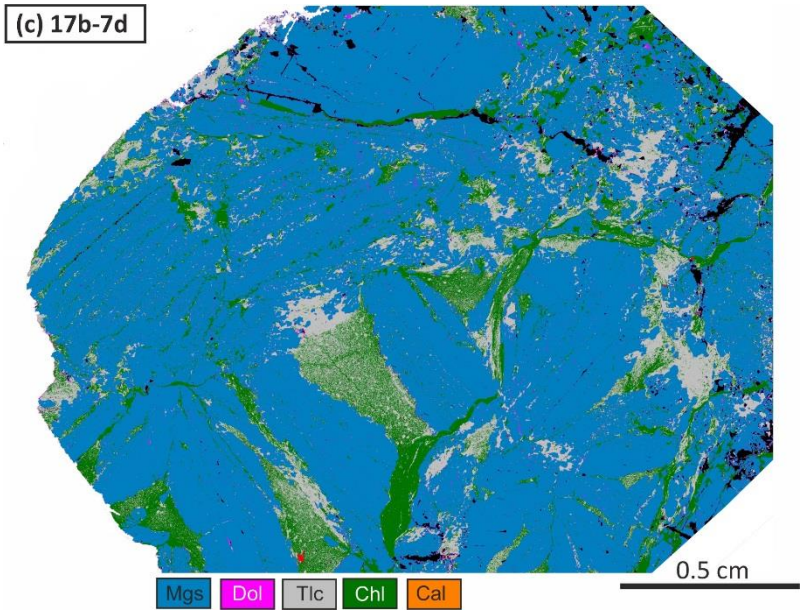

Fig. S13c – Processed X–Ray maps of sample 17b–7d.

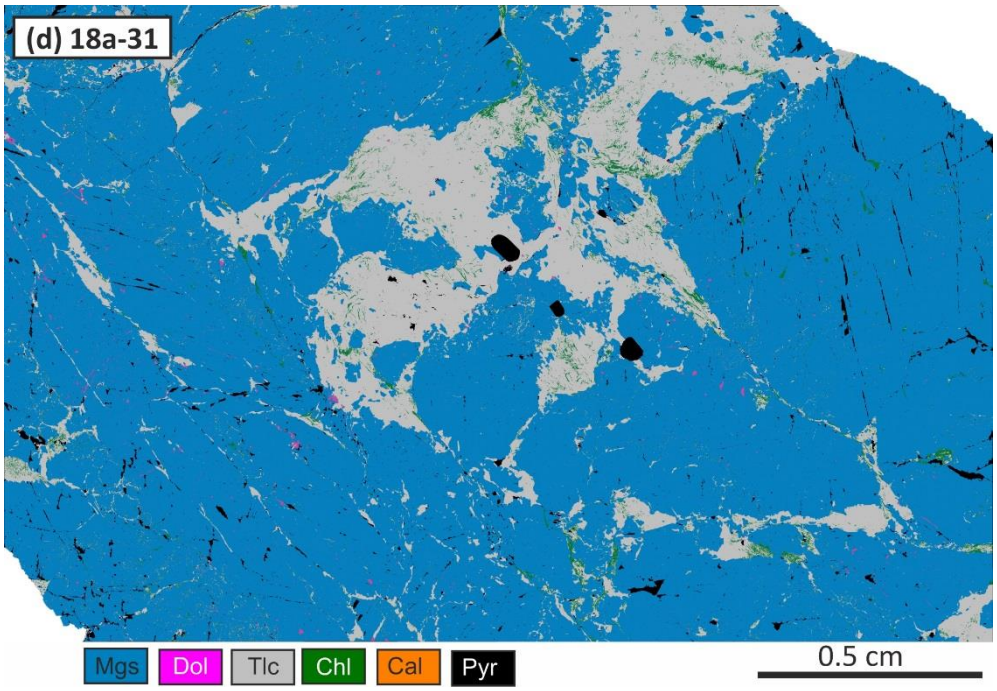

Fig. S13d – Processed X–Ray maps of sample 18a–31.

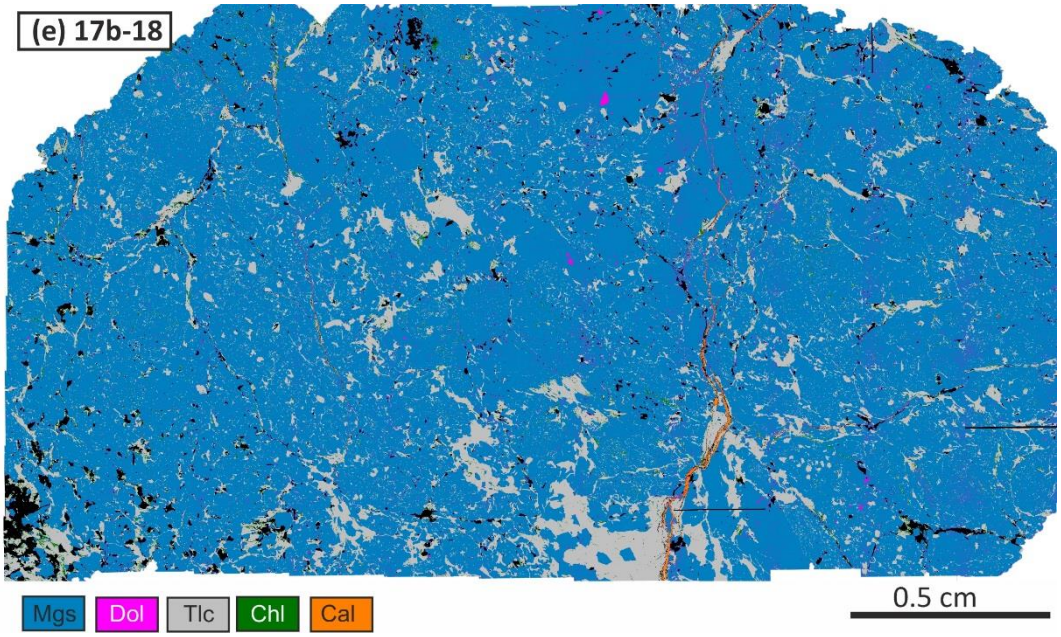

Fig. S13e – Processed X–Ray maps of sample 17b–18.

APPENDIX 10

Cathodoluminescence maps of some dolomite– and magnesite– bearing lithologies, samples 18a–26 (Fig. S14a), 17b–10b (Fig. S14b), 21a–22a (Fig. S14c), 17b–7b (Fig. S14d)

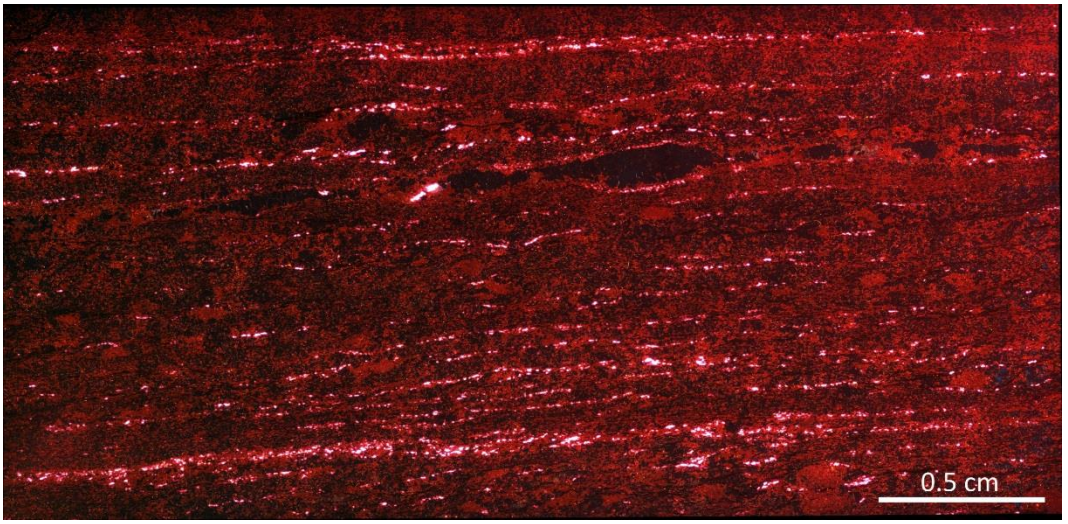

Fig. S14a – CL map of sample 18a–26.

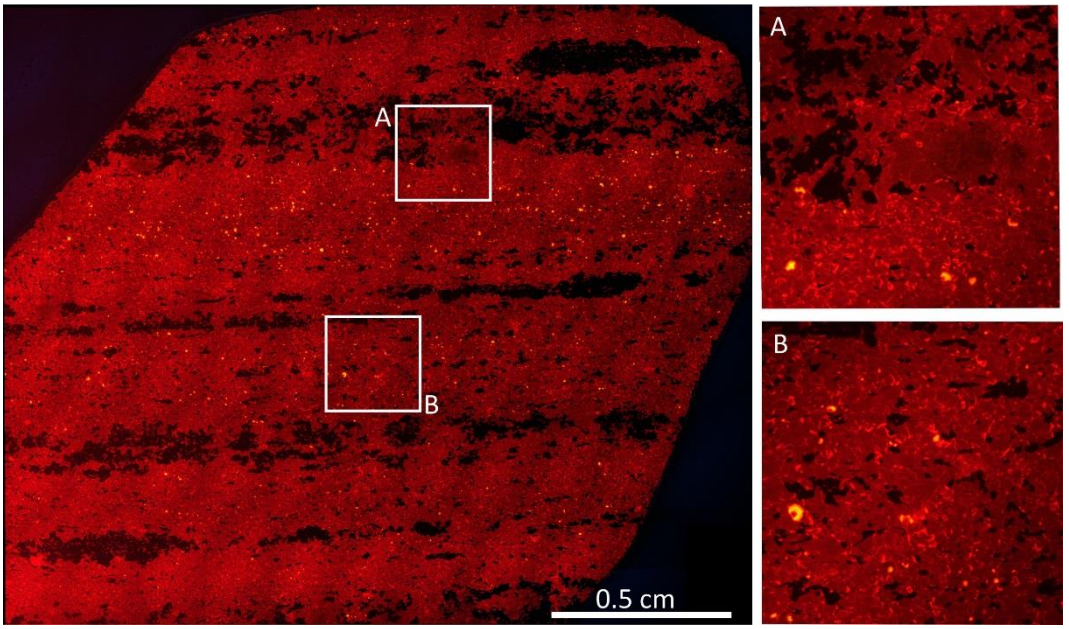

Fig. S14b – CL map of sample 17b–10b.

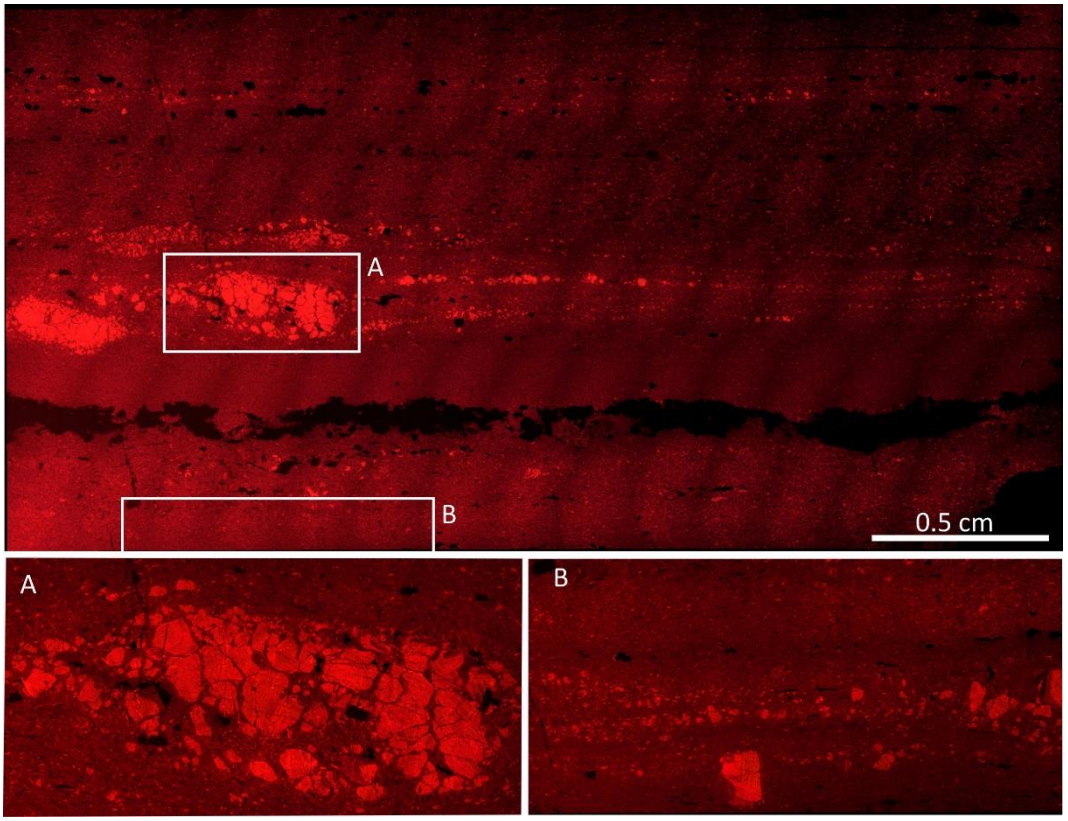

Fig. S14c – CL map of sample 21a–22a

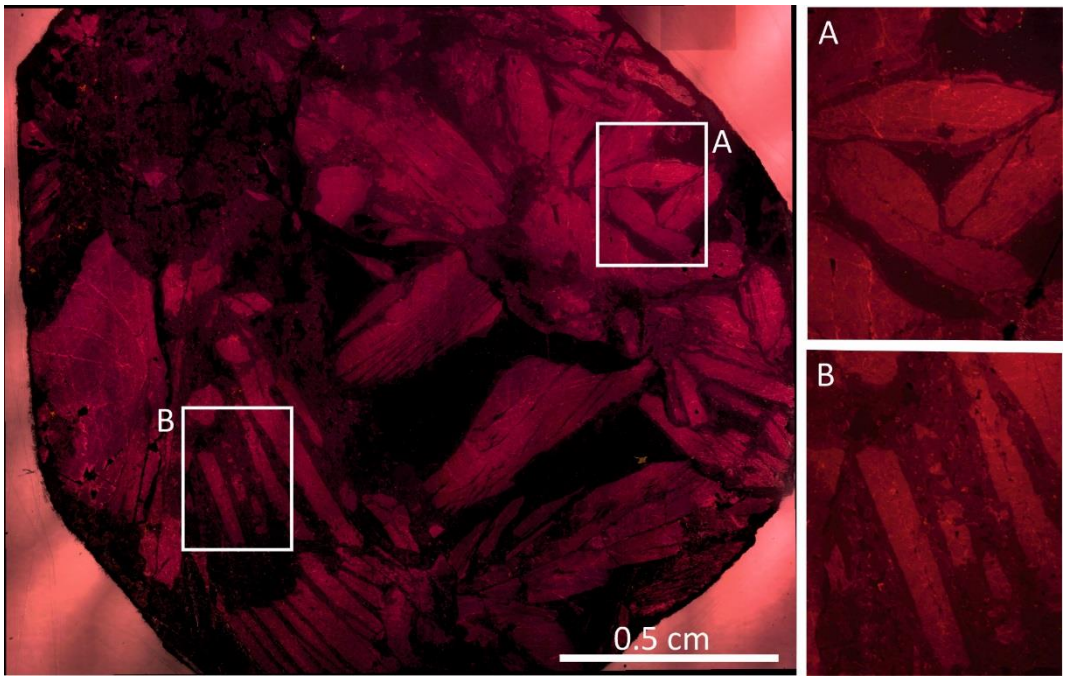

Fig. S14d – CL map of sample 17b–7d.

APPENDIX 11

Mineral stability fields predicted by the P/T–X(CO_2) pseudosections modelled for carbonate–bearing lithologies: samples 17b–12 (Fig. S15), 17a–29 (Fig. S16), 15a–28a (Fig. S17), 18a–26 (Fig. S18), 17a–36b (Fig. S19), 17a–35 (Fig. S20), 17b–7d (Fig. S21)

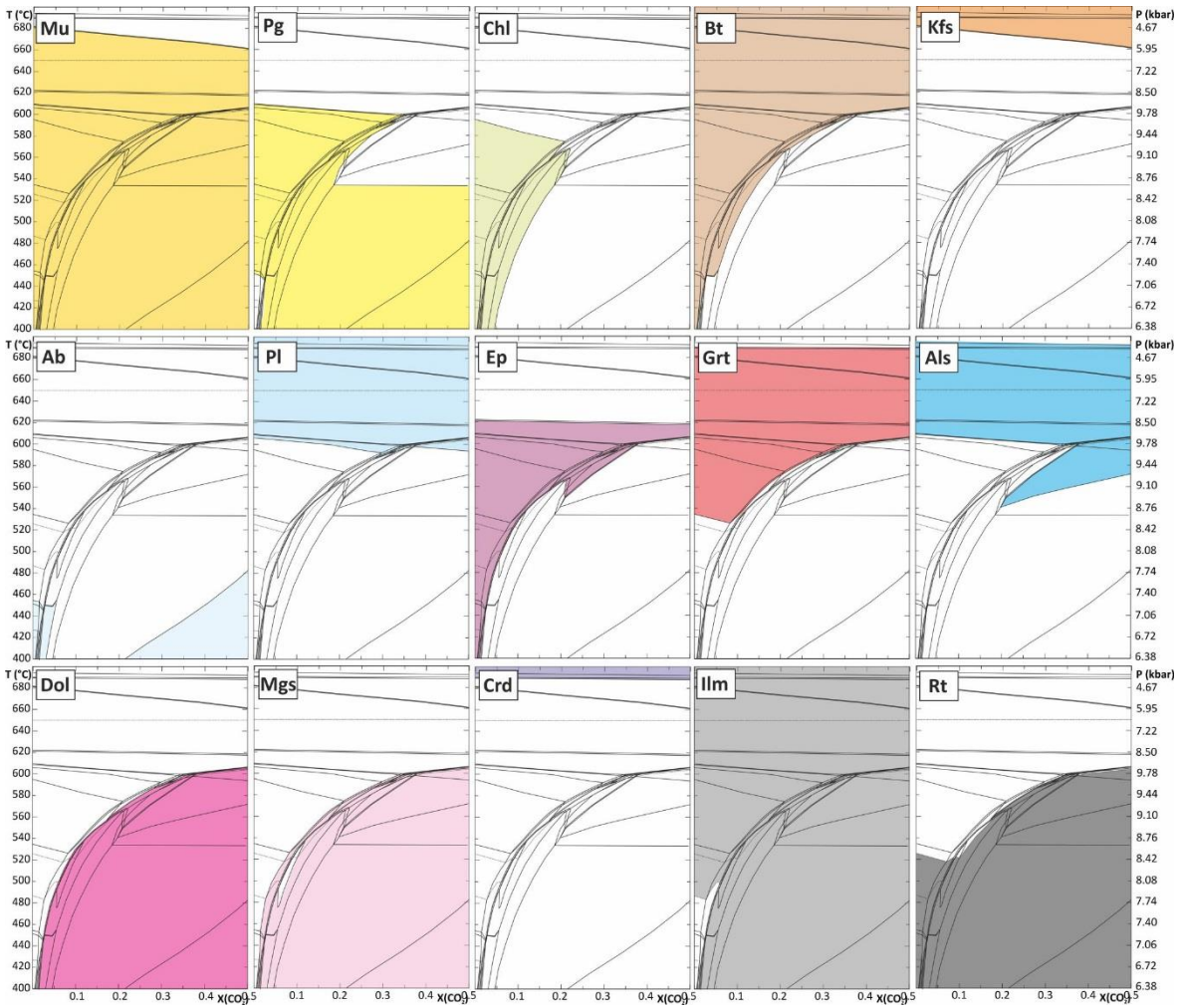

Fig. S15 – P/T–X(CO_2) pseudosection modelled for sample 17b–12 showing the stability fields of the main minerals.

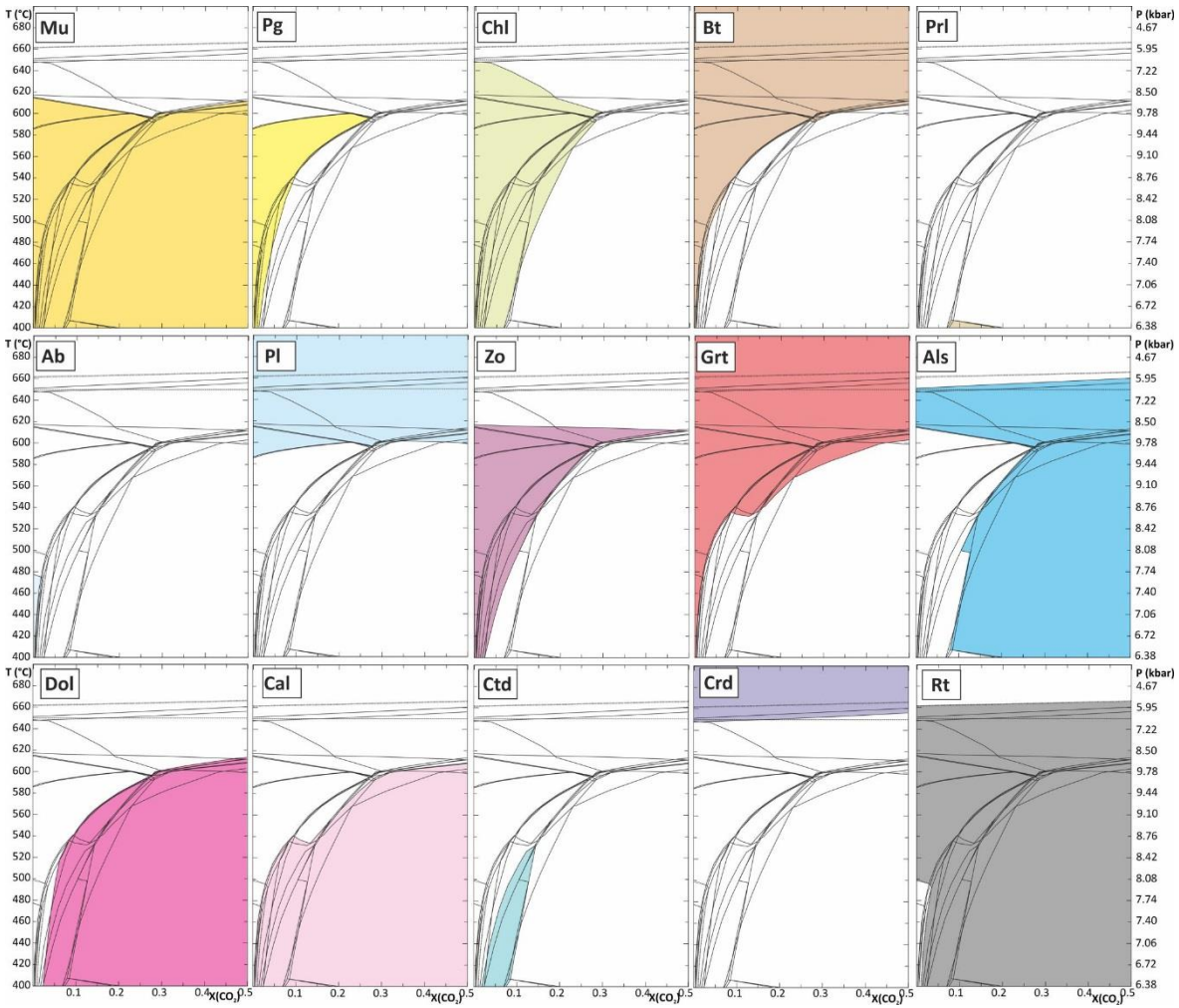

Fig. S16 – P/T–X(CO_2) pseudosection modelled for sample 17a–29 showing the stability fields of the main minerals.

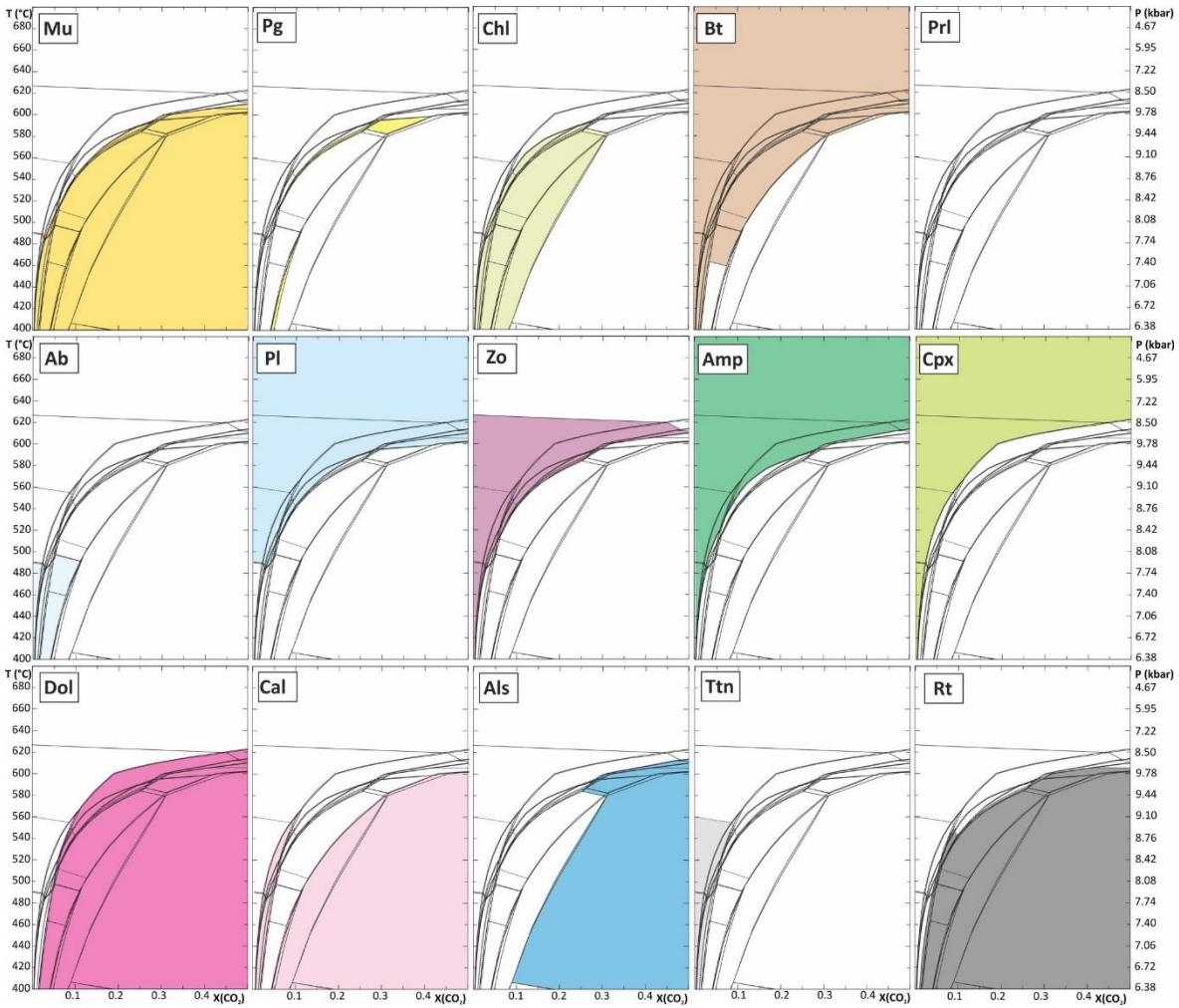

Fig. S17 – P/T–X(CO_2) pseudosection modelled for sample 15a–28a showing the stability fields of the main minerals.

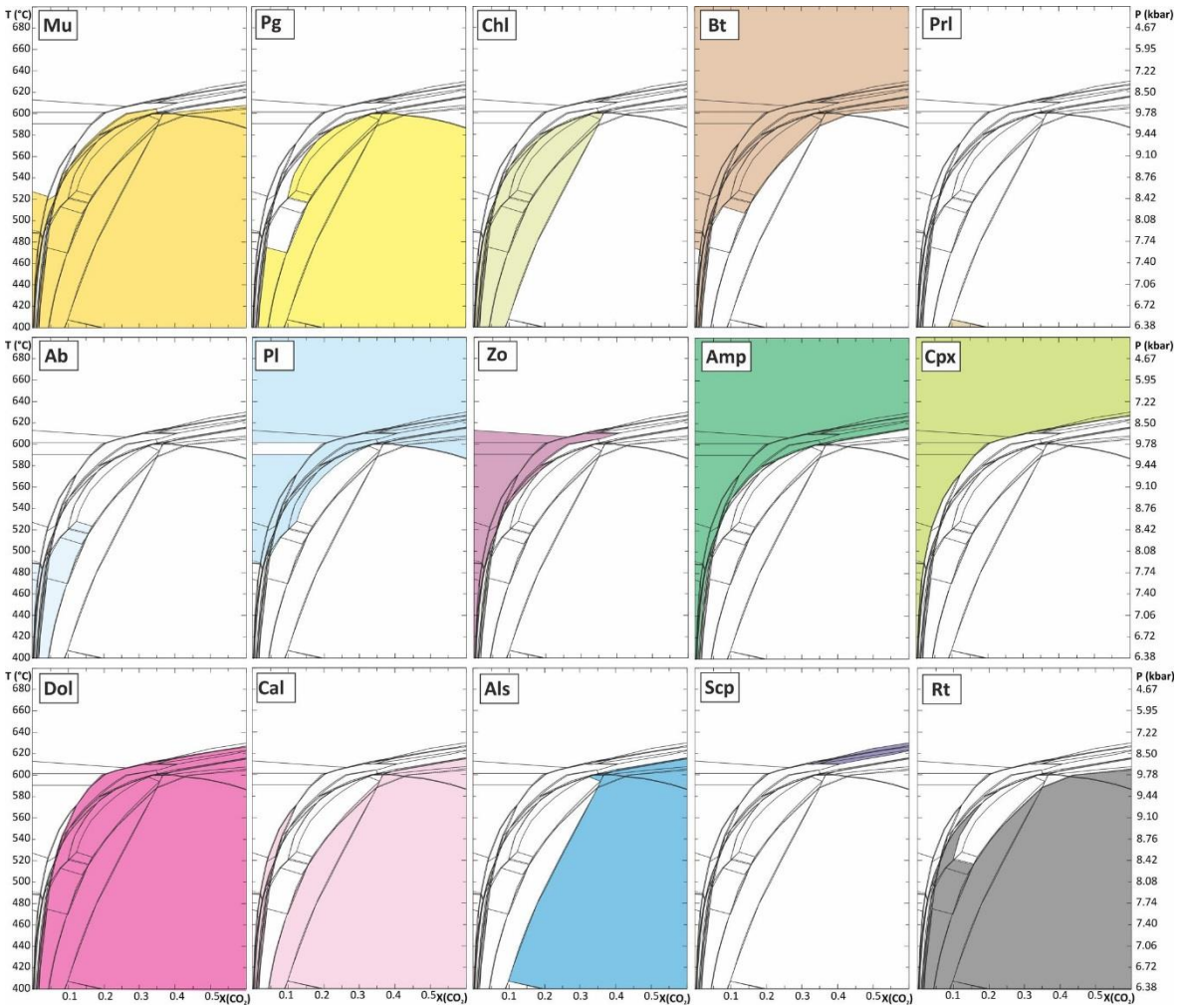

Fig. S18 – P/T–X(CO_2) pseudosection modelled for sample 18a–26 showing the stability fields of the main minerals.

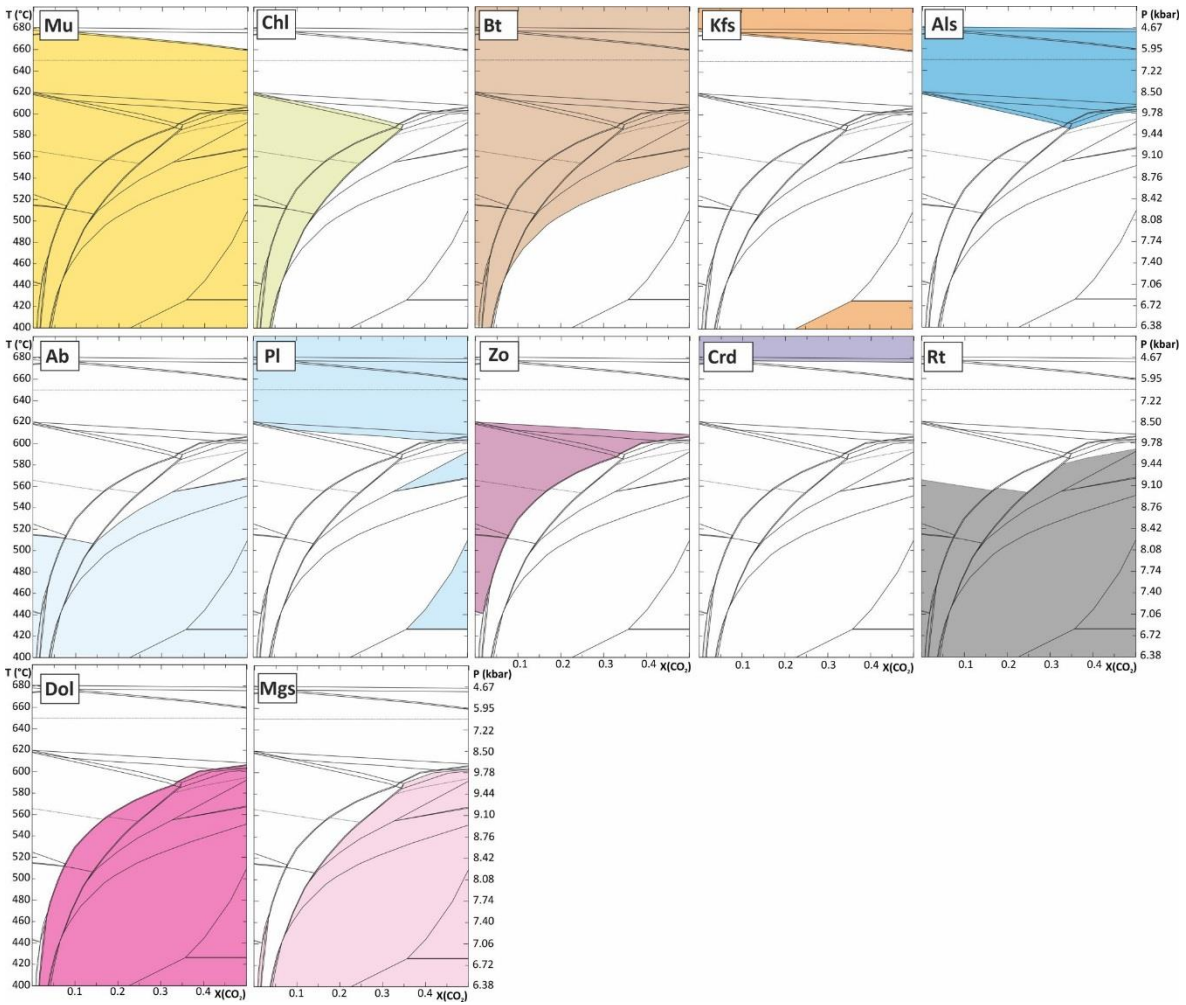

Fig. S19 – P/T–X(CO_2) pseudosection modelled for sample 17a–36b showing the stability fields of the main minerals.

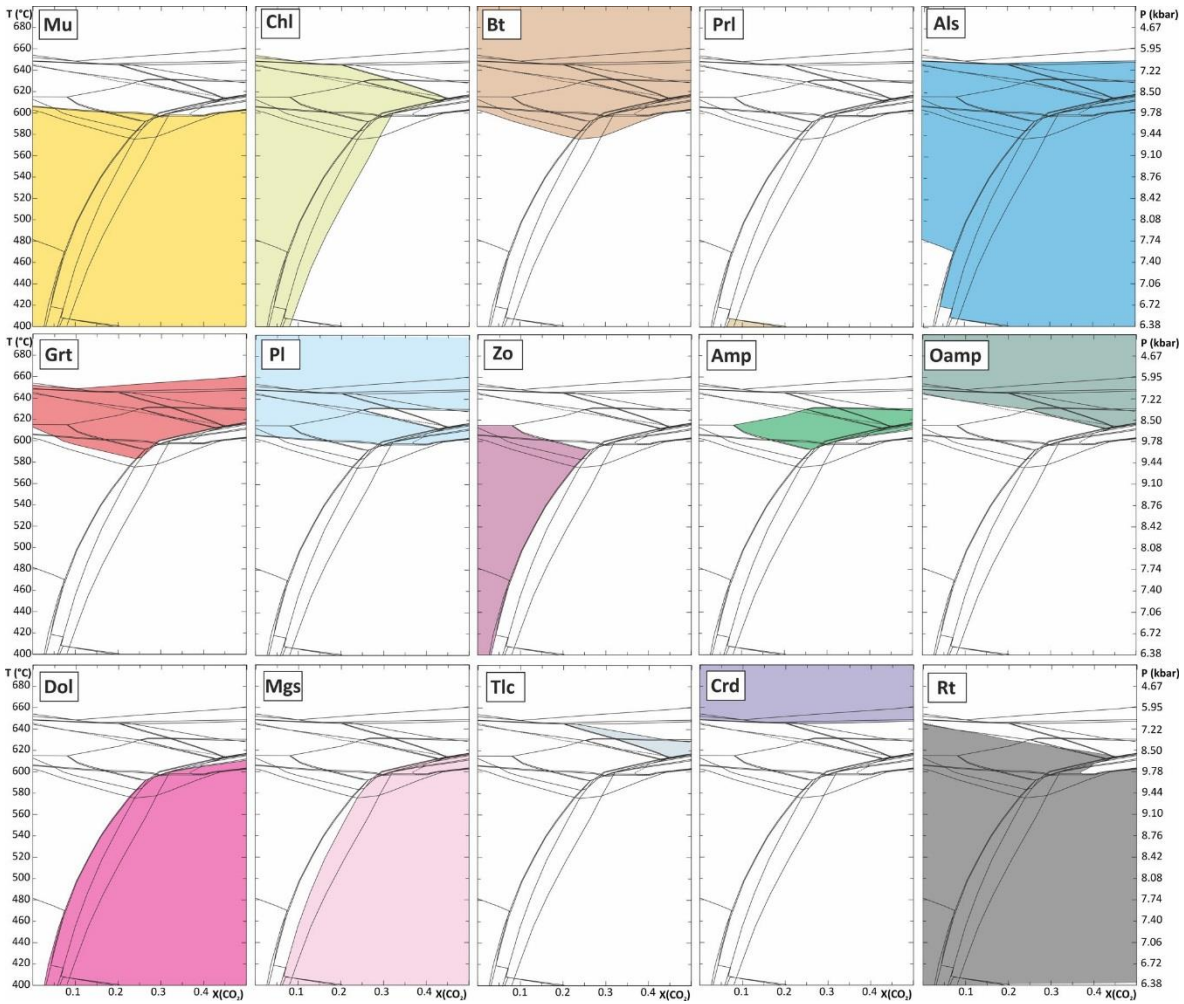

Fig. S20 – P/T–X(CO_2) pseudosection modelled for sample 17a–35 showing the stability fields of the main minerals

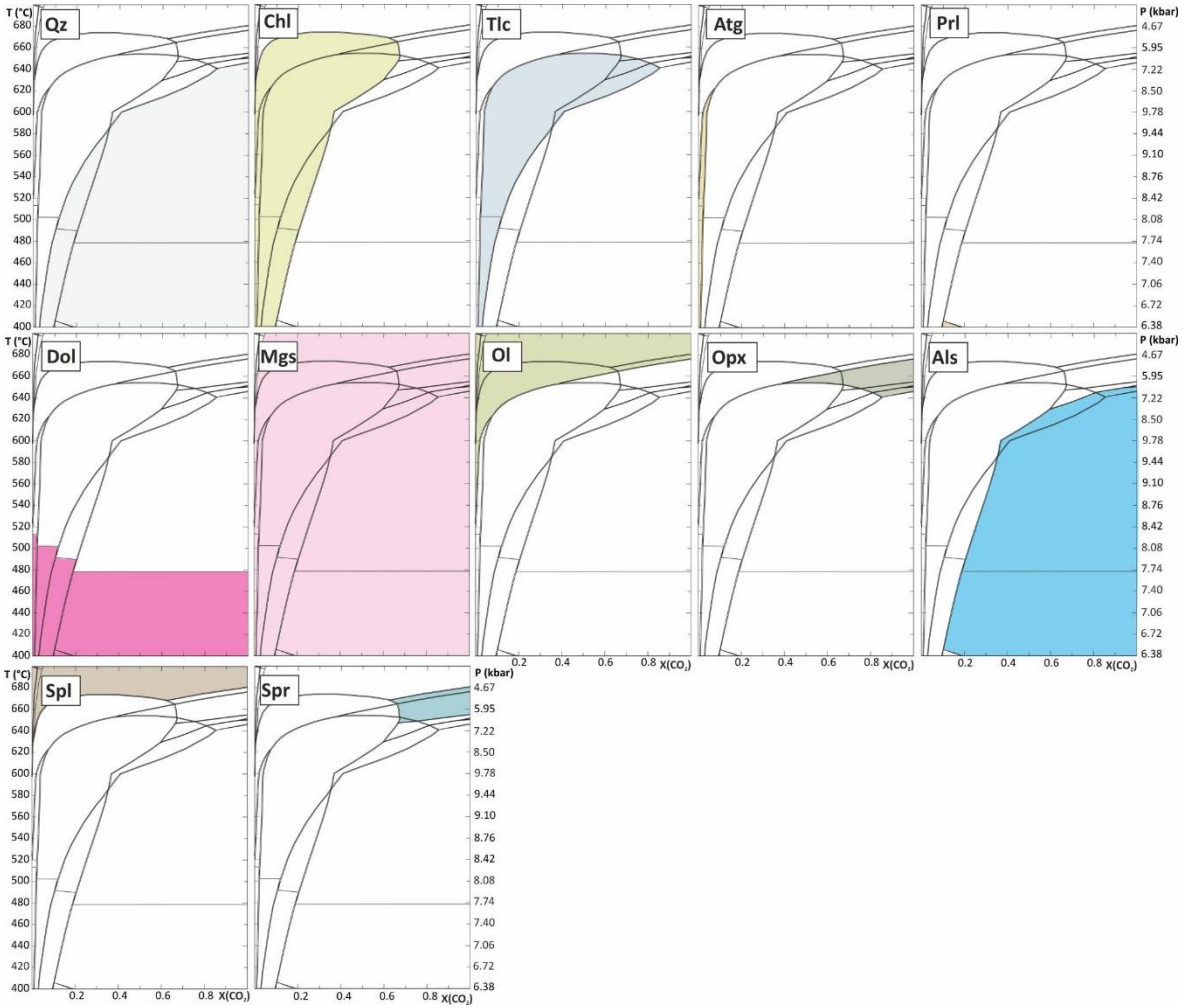

Fig. S21 – P/T–X(CO_2) pseudosection modelled for sample 17b–7d showing the stability fields of the main minerals

DATASETS

Datasets are provided as separate Excel spreadsheets and include

Dataset 1 – Mineral chemistry of metapelites
Dataset 1a: Mineral chemistry – sample 17a–34
Dataset 1b: Mineral chemistry – sample 17a–33
Dataset 1c: Mineral chemistry – sample 17a–22
Dataset 1d: Mineral chemistry – sample 15a–15b
Dataset 1e: Mineral chemistry – sample 15a–28b
Dataset 1f: Mineral chemistry – sample 17a–42

Dataset 2 – Spreadsheets used for bulk composition calculation of metapelites
Dataset 2a: Bulk composition calculation – sample 17a–34
Dataset 2b: Bulk composition calculation (unfractionated/fractionated) – sample 17a–33
Dataset 2c: Bulk composition calculation (unfractionated/fractionated) – sample 17a–22
Dataset 2d: Bulk composition calculation (unfractionated/fractionated) – sample 15a–15b
Dataset 2e: Bulk composition calculation (unfractionated/fractionated) – sample 15a–28b
Dataset 2f: Bulk composition calculation (unfractionated/fractionated) – sample 17a–42

Dataset 3 – Spreadsheets used for the reconstruction of the protoliths' assemblages for metapelites
Dataset 3a: Protolith's assemblage calculation – sample 17a–34
Dataset 3b: Protolith's assemblage calculation – sample 17a–33
Dataset 3c: Protolith's assemblage calculation – sample 17a–22
Dataset 3d: Protolith's assemblage calculation – sample 15a–15b
Dataset 3e: Protolith's assemblage calculation – sample 15a–28b
Dataset 3f: Protolith's assemblage calculation – sample 17a–42

Dataset 4 – Mineral chemistry of dolomite–bearing lithologies
Dataset 4a: Mineral chemistry – sample 17b–12
Dataset 4b: Mineral chemistry – sample 17a–29
Dataset 4c: Mineral chemistry – sample 15a–28a
Dataset 4d: Mineral chemistry – sample 18a–26
Dataset 4e: Mineral chemistry – sample 17b–10b
Dataset 4f: Mineral chemistry – sample 21a–22a

Dataset 5 – Mineral chemistry of magnesite–bearing lithologies
Dataset 5a: Mineral chemistry – sample 17a–36b
Dataset 5b: Mineral chemistry – sample 17a–35
Dataset 5c: Mineral chemistry – sample 17b–7d

Dataset 6 – Spreadsheets used for bulk composition calculation of dolomite–bearing lithologies

Dataset 6a: Bulk composition calculation – sample 17b–12
Dataset 6b: Bulk composition calculation – sample 17a–29
Dataset 6c: Bulk composition calculation – sample 15a–28a
Dataset 6d: Bulk composition calculation – sample 18a–26
Dataset 6e: Bulk composition calculation – sample 17b–10b
Dataset 6f: Bulk composition calculation – sample 21a–22b

Dataset 7 – Spreadsheets used for bulk composition calculation of magnesite–bearing lithologies

Dataset 7a: Bulk composition calculation – sample 17a–36b
Dataset 7b: Bulk composition calculation – sample 17b–35
Dataset 7c: Bulk composition calculation – sample 17b–7d
Dataset 7d: Bulk composition calculation – sample 18a–31
Dataset 7e: Bulk composition calculation – sample 17b–18

Dataset 8 – Spreadsheets used for the reconstruction of the dolomite–bearing protoliths' assemblages

Dataset 8a: Protolith's assemblage calculation – sample 17b–12
Dataset 8b: Protolith's assemblage calculation – sample 17a–29
Dataset 8c: Protolith's assemblage calculation – sample 15a–28a
Dataset 8d: Protolith's assemblage calculation – sample 18a–26
Dataset 8e: Protolith's assemblage calculation – sample 17b–10b
Dataset 8f: Protolith's assemblage calculation – sample 21a–22b

Dataset 9 – Spreadsheets used for the reconstruction of the magnesite–bearing protoliths' assemblages

Dataset 9a: Protolith's assemblage calculation – sample 17a–36b
Dataset 9b: Protolith's assemblage calculation – sample 17b–35
Dataset 9c: Protolith's assemblage calculation – sample 17b–7d
Dataset 9d: Protolith's assemblage calculation – sample 18a–31
Dataset 9e: Protolith's assemblage calculation – sample 17b–18

Dataset 10 – Spreadsheets used for calculation of total emission of CO_2

Dataset 10a: Summary of gaseous emission zones in Nepal. Taken from our recent original work and the literature (Girault et al. 2014a,b, 2018b,c, 2022).

Dataset 10b: Summary of thermal springs in Nepal. Takenfrom our recent original work and the literature (Girault et al. 2022 and reference their in.)